

ELEMENTARY AND TOPOLOGICAL EXCITATIONS IN ULTRACOLD
DIPOLAR BOSE GASES

THOMAS BLAND

Thesis submitted for the degree of
Doctor of Philosophy



*School of Mathematics, Statistics & Physics
Newcastle University
Newcastle upon Tyne
United Kingdom*

December 2018

ACKNOWLEDGEMENTS

First and foremost I am hugely thankful to my supervisor, Nick Parker, for being an excellent mentor and friend throughout the last five years, ever since we met forcing Christmas decorations into condoms (for science).

I would also like to thank my second supervisor Nick Proukakis for his expertise and advice throughout my studies. Serendipity also brought me Matthew Edmonds, who taught me a lot during my first few years of the PhD. I'd also like to thank other Newcastle collaborators George Stagg, Andrew Baggaley, and Luca Galantucci.

My gratitude goes out to those who have supported me during research visits, and to EPSRC for financially supporting this project. Firstly to Kazik Rzażewski and Krzysiek Pawłowski for hosting me in Warsaw, and to Andy Martin, Sri Prasad and Abhi Chopra for hosting me in Melbourne. I'd also like to thank Boris Malomed for his wisdom during our collaboration.

In the department I'd like to thank all of those I've shared offices with: Amit Seta, Wael Al-Taie, Tom Fisher, Safwan Ibrahim, David Cushing, Yameng Ji, Can Evirgen, Matthew Robinson, David Robertson, Joe Matthews, David Pescod, Ste Johnson, Mae Mesgarnezhad, Tom Lowe, and Paolo Comaron. Honourable mentions from other offices include: Jack Walton, Liam Dobson, Rathish Ratnasingam, Alex Svalova, Robert Pattinson, Hayley Moore, Sophie Harbisher, Francesca Fedele, Joe Reid, Marios Bounakis, Sarah Jowett, David Stewart, Stewart Hall, Richard Boys, Ryan Doran, Dmitris Chiotis, Robbie Bickerton, Amos Ajibo, Nick Loughlin, Sam James, Anne-Kathleen Malchow, Em Rickinson, Georgina Kay-Black, James Hollins, Keith Newman, Lewis Clark, and Naomi Hannaford.

Thanks to those outside of the department who kept me sane for the past four years. As a minimum I need to thank Imogen Large, Harry Robinson, Neil Wilyman, Katie Connor for organising maths get togethers, and all the Kendalians for the reunions. There are those who have joined me on travels around the world, so thanks to Liam Atkinson and Dale Harper for the weirdest holiday I've had in my life, Michael Wharton, Michael Lee and Lewis Chaytor for trying their best to match it, Fabrizio Larcher for "accidentally" making us Mr and Mr Larcher for the weekend, Matthew Smith, David Fujiwara, Hassan Tahir, Liam Dury and Nick Waterton for the many continuing adventures¹.

Huge thanks to my family for their love and support throughout my studies, particularly in the last few months for taking care of me whilst I wrote this thesis in a dark room, only appearing to steal lovely food they made for me.

Finally, thanks to the one with whom I share my biscuits, Clarissa, for providing the beginning of an adventure.

¹Of course the above lists are not exhaustive, and if you are looking for your name then I thank you too, random citizen.

ABSTRACT

QUANTUM gases are an exemplar for exploring quantum phenomena; dipolar quantum gases only enriches the pool of potential experiments, exhibiting long-range and anisotropic interactions. In this thesis, we perform extensive numerical and theoretical studies of the dipolar Gross-Pitaevskii equation, exposing new intriguing phenomena of solitons and vortices in these systems.

Firstly, we map out the stability diagram as a function of strength and polarisation direction of the atomic dipoles in a quasi-one-dimensional dipolar gas, identifying both roton and phonon instabilities. Then we obtain the family of dark soliton solutions supported in this system. Away from these instabilities dark solitons collide elastically. Varying the polarisation direction relative to the condensate axis enables tuning of this non-local interaction between repulsive and attractive; the latter case supports unusual dark soliton bound states. Remarkably, these bound states are themselves shown to behave like solitons, emerging unscathed from collisions with each other. In trapped gases the oscillation frequency of the dark soliton is strongly dependent on the atomic interactions, in stark contrast to the non-dipolar case. Considering parameter regimes allowing the existence of bright solitons we map out the existence of the soliton solutions and show three collisional regimes: free collisions, bound state formation and soliton fusion. We examine the solitons in their full three-dimensional form through a variational approach; along with regimes of instability to collapse and runaway expansion, we identify regimes of stability which are accessible to current experiments.

Then, we undertake a theoretical analysis of the stability of a Thomas-Fermi density profile for a dipolar gas in a rotating frame of reference and find that the theoretical prediction for "anti-dipoles" is only experimentally realisable for short periods of time. We compare this theory against numerical simulations of the governing equation for these systems and find excellent agreement.

Finally, we study the elementary characteristics of turbulence in a quantum ferrofluid through the context of a dipolar Bose gas condensing from a highly non-equilibrium thermal state. Our simulations reveal that the dipolar interactions drive the emergence of polarised turbulence and density corrugations. The superfluid vortex lines and density fluctuations adopt a columnar or stratified configuration, with the vortices tending to form in the low density regions to minimise kinetic energy. When the interactions are dominantly dipolar, the decay rate of vortex line length is enhanced. This system poses exciting prospects for realising stratified quantum turbulence and new levels of generating and controlling turbulence using magnetic fields.

Contents

I Introduction and theory

1	Introduction	2
1.1	Bose-Einstein condensation	2
1.2	The dipole-dipole interaction	6
1.3	Ferrofluids	7
1.4	Ultra-cold dipolar systems	8
1.4.1	Electric dipoles	9
1.4.2	Magnetic dipoles	10
1.4.3	Comparison of dipolar strengths	11
1.5	Topological excitations	13
1.5.1	Vortices	13
1.5.2	Solitons	16
1.6	Thesis overview	20
1.7	List of publications	22
2	Experimental progress and theoretical groundwork	23
2.1	Modelling and tuning interactions	23
2.1.1	Feshbach resonance	25
2.1.2	Tuning the dipole-dipole interaction	26
2.1.3	Fourier transform of the dipole-dipole interaction	27
2.2	Gross-Pitaevskii theory	28
2.2.1	Bose gases	28
2.2.2	Mean-field approximation	30
2.2.3	The dipolar Gross-Pitaevskii equation	30

2.3	Time-independent solutions	35
2.3.1	Non-interacting regime	35
2.3.2	Contact interactions	35
2.3.3	Dipolar interactions	37
2.3.4	Unusual ground states	39
2.4	Excitations in BECs	43
2.4.1	Elementary excitations	44
2.4.2	Dipolar vortices	48
2.4.3	Dipolar solitons	49
2.5	Instability	50
2.5.1	Collapse instability	50
2.5.2	Homogeneous dipolar gas	51
2.5.3	Trapped dipolar gas	52
2.5.4	Quantum Rosensweig instability	53
2.6	Beyond mean-field models	54
3	Numerical methods	57
3.1	Evaluation of the dipolar potential	57
3.2	Imaginary time propagation	58
3.3	Biconjugate gradient method	60
3.4	Crank-Nicolson scheme	62
3.5	Split-step Fourier method	63
 II Excitations in a quasi-one-dimensional dipolar Bose gas		
4	Introduction	68
5	Stability of the quasi-1D dipolar condensate	70
5.1	Derivation of the quasi-1D dipolar GPE	70
5.2	Stability of the homogeneous system	75
5.3	Stability of the harmonically trapped system	78
5.4	Summary	83
6	Dark solitons in homogeneous dipolar condensates	84
6.1	Dark soliton solutions	85
6.1.1	Non-dipolar dark solitons	85

6.1.2	Dipolar dark solitons	85
6.1.3	Integrals of motion	88
6.2	Dynamics of dipolar dark solitons	91
6.2.1	Propagation	91
6.2.2	Collisions	92
6.3	Two-soliton interaction potential and bound states	95
6.4	Summary	97
7	Dark solitons in confined dipolar condensates	99
7.1	Dipolar dark solitons in a trapped BEC	99
7.2	Soliton dynamics	101
7.3	Analytic consideration of the oscillation frequency	103
7.4	Summary	107
8	Dipolar bright solitons	109
8.1	Single dipolar solitons	109
8.2	Collisions	111
8.2.1	In-phase collisions	111
8.2.2	Out-of-phase collisions	113
8.2.3	Noise	113
8.3	3D stability	114
8.3.1	Gaussian variational approach	115
8.3.2	Stability analysis	116
8.4	Summary	120

III Rotation and turbulence

9	Stability analysis of a rotationally tuned dipolar BEC	122
9.1	Hydrodynamic equations in a rotating frame	123
9.2	Stationary solutions	126
9.3	Comparison to GPE simulations	128
9.4	Stability analysis	130
9.5	Summary	134

10	Quantum ferrofluid turbulence	135
10.1	Classical field method in non-dipolar gases	136
10.2	Polarised turbulence	137
10.3	Quantifying the polarisation	140
10.4	Line-length decay	142
10.5	Summary	144

IV Conclusions, outlook, and appendices

11	Conclusions and future work	147
11.1	Conclusions	147
11.2	Further work	149
A	Derivation of the dipolar Bogoliubov-de Gennes equations	151
B	Convolution theorem	155
C	Derivation of the Gross-Pitaevskii equation	156
D	Probing quasi-integrability of the GPE in the harmonic oscillator potential	158
D.1	Introduction	158
D.2	The Galerkin approximation and its validity	163
D.2.1	The four-mode truncated Hamiltonian and dynamical equations	165
D.2.2	Exploring the accuracy of the Galerkin approximation	168
D.3	Dark-soliton dynamics as the testbed for the validity of the Galerkin approximation	169
D.4	Probing quasi-integrability in the 1D harmonic oscillator potential	171
D.5	Summary	173
	Bibliography	176

I

Introduction and theory

1

Introduction

QUANTUM theory predicts that particles can be separated into two categories: bosons and fermions. Fermions, particles with half-integer spin, follow Fermi-Dirac statistics and are bound by Pauli's exclusion principle. Bosons, particles with integer spin, follow Bose-Einstein statistics and, importantly, are free to populate a single quantum state. Under precise conditions a macroscopic population of bosons occupy the ground state, a phenomenon called Bose-Einstein condensation (BEC) [1, 2].

1.1 Bose-Einstein condensation

The road to BEC began with Satyendra Nath Bose, who in 1924 showed that it was possible to derive Planck's empirical formula for black-body radiation (which was famously inconsistent with classical physics) by modelling a gas of photons under two key assumptions: that the photons were indistinguishable from each other (rather than the distinguishable particles of classical physics) and that each occupied a finite-sized volume in phase space (rather than the points in phase space of classical particles) [1]. Albert Einstein recognised that this model could be extended to particles, and broadened this idea to a gas of atoms in two papers. In the second of these papers he predicted BEC [2].

Physical realisations of a system of this type remained in obscurity for the remainder of the century. In order to create the weakly-interacting dilute Bose gas, experimentalists needed to be able to engineer temperatures very close to absolute zero (zero Kelvin (0K) or -273°C), which was an obstacle for nearly 70 years. However, with advancements in cooling techniques the first BEC was observed in 1995 when, now Nobel prize winners Cornell and Wieman, succeeded in creating a condensate with rubidium-87 atoms (^{87}Rb) [3], see Fig. 1.1, and Ketterle with sodium-23 atoms (^{23}Na) [4]¹.

A BEC is an unusual state of matter that can consist of millions of atoms, yet behave in synchrony as a single giant atom. The effect is purely quantum mechanical. In the quantum world each particle in an ensemble in thermal equilibrium at temperature T

¹To date BEC has been achieved in Rb [3], Na [4], Li [5, 6], H [7], He [8], K [9], Cs [10], Yb [11], Cr [12], Ca [13], Sr [14], Dy [15], and Er [16]. Degenerate Fermi gases have been realised for K [17], Li [18, 19], He [20], Sr [21], Yb [22], Dy [23], Er [24], and Cr [25].

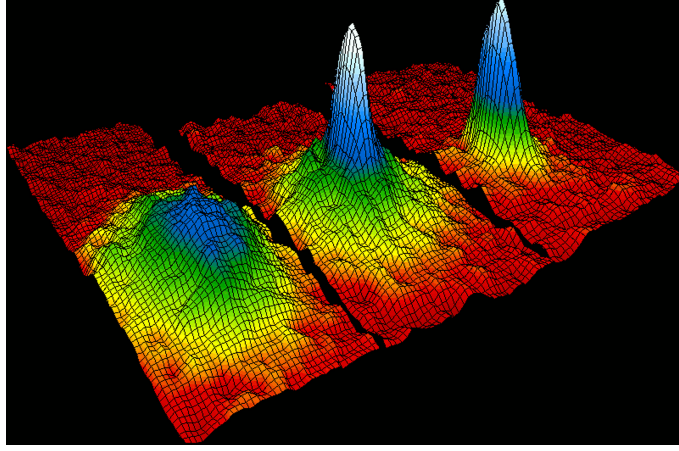


Figure 1.1: The first weakly-interacting gaseous BEC produced using ^{87}Rb atoms at the JILA lab. These figures show the initial velocity distribution - taken after removing the external trapping potential and letting the BEC expand. The macroscopic population of a single momentum state is a signature of BEC. From left to right the temperatures are just above, at, and just below the critical temperature for BEC. (Copyright (2002) by The American Physical Society [3]).

is described by a localised wavepacket. The size of this wavepacket is given by the de Broglie wavelength $\lambda_{\text{dB}} \propto T^{-1/2}$. At low temperatures the spatial extent of the wavepacket increases and can become comparable to the average distance between the particles. When this is achieved, the individual wavepackets overlap and a quantum degenerate gas is formed. In an ideal 3D Bose gas the criterion for BEC is fulfilled when $n\lambda_{\text{dB}}^3 \approx 2.612$, where n is the particle density [26]. This criterion allows for high temperature BECs, for large densities, such as in neutron stars where temperature is roughly 10^8 Kelvin [27].

Quantum fluids exhibit superfluidity, where the fluid flows with zero viscosity, and superconductivity, where an electric current flows without resistance [28]. The phrase superfluidity was coined after observations of inviscid flow in ^4He by Kapitza [29] and Allen and Misener [30] in 1938. The origin of these superfluid properties was a cause of controversy for many years, with the first suggestion from Fritz London [31, 32] that despite the inherent strong particle interactions the origin is due to Bose-Einstein condensation. This idea was later backed up by results from a "two fluid model" for liquid helium — originally introduced by Tisza [33] that formed the basis for a more rigorous model from his former post-doc supervisor Landau [34] — which allows for a normal component and a superfluid component to mutually exist in the same system. Despite Landau himself being vehemently against the link between BEC and superfluidity², Landau's two fluid model suggested that the superfluid behaviour could be accounted for by a dispersion

²Landau *refused* to cite the work by F. London, and when Tisza linked his two fluid model to the presence of BEC Landau said "[Tisza's] entire quantitative theory (microscopic as well as thermodynamic-hydrodynamic) is in my opinion entirely incorrect" [35].

relation which is linear at low momenta. A further six years later Bogoliubov showed that the dispersion relation for Bose gases exhibit precisely this [36], providing the first tangible evidence between superfluidity and BEC.

A problem with Landau's theory was that the critical velocity for dissipation was larger than observed in experiments. In 1951, Penrose [37] generalised the description of BEC as "off-diagonal long range order" (ODLRO) in the formalism of a density matrix — showing that BEC is a consequence of coherence over infinite distances — an approach extended by Penrose and Onsager in 1956 [38]. Their work allows the condensate fraction to be much smaller than one, and irrotational dissipationless motion to occur below a critical velocity, smaller than Landau's. These works collectively show that the existence of superfluidity is really linked to BEC³.

Theoretical works into BECs have touted improvements to fields such as ultra-precise clocks, quantum computing and metrology [40]. There are a swathe of excellent reviews on the progress of the field so far including Dalfovo *et al.* [41], Leggett [42], and Bloch *et al.* [43], and some comprehensive books by Pethick and Smith [44] and by Pitaevskii and Stringari [45]. Studies into Bose-Einstein condensation carry a weight of importance in the field of physics because of the close analogies to many observable systems in nature, such as aforementioned neutron stars, or even black holes, but most importantly because it is highly controllable in laboratory experiments.

The zero temperature dynamics of a BEC are accurately described by the celebrated Gross-Pitaevskii equation (GPE) [46–49] as derived in the early 1960s. The GPE is a partial differential equation describing the temporal evolution of the fluid density and phase through the *wavefunction* $\psi(\mathbf{r}, t)$. The wavefunction is trivially related to the fluid density n through $n(\mathbf{r}, t) = |\psi(\mathbf{r}, t)|^2$. In its simplest form the GPE can be stated as

$$i\hbar \frac{\partial \psi(\mathbf{r}, t)}{\partial t} = \left(-\frac{\hbar^2 \nabla^2}{2m} + V_{\text{ext}}(\mathbf{r}, t) + g|\psi(\mathbf{r}, t)|^2 \right) \psi(\mathbf{r}, t), \quad (1.1)$$

where m is the mass of the atomic species under consideration, V_{ext} gives the trapping potential confining the condensate, and the size and sign of the constant g characterises the strength and nature of the effective atom-atom interactions.

The most common form of trapping potential used in experiments is the harmonic trap, given by

$$V_{\text{ext}}(\mathbf{r}) = \frac{1}{2}m \left(\omega_x^2 x^2 + \omega_y^2 y^2 + \omega_z^2 z^2 \right), \quad (1.2)$$

with trapping frequencies ω_j . A potential of this form is easy to implement with magnetic

³The rich history of the discovery of superfluidity has been compiled in a recent article by Sébastien Balibar [39].

fields, as in earlier experiments, and now employable through optical fields. Through tuning of the trap frequencies one can control the geometry of the system under consideration. If $\omega_x = \omega_y \gg \omega_z$ the system is prolate (cigar shape) or if $\omega_x = \omega_y \ll \omega_z$ the system is oblate (pancake shape). Box-like traps are also increasingly being employed in experiments [50–53].

In the zero temperature limit the only interactions considered are those of short-range s-wave scattering, which for most of the experiments to date is sufficient to reproduce observed physical phenomena. The interaction potential used to model these scattering effects is given by

$$U_s(\mathbf{r} - \mathbf{r}') = g \delta(\mathbf{r} - \mathbf{r}') = \frac{4\pi\hbar^2 a_s}{m} \delta(\mathbf{r} - \mathbf{r}') , \quad (1.3)$$

where a_s is the s-wave scattering length, a parameter describing the strength (through magnitude) and nature of the effective interactions; $a_s > 0$ describes repulsive interactions, whereas $a_s < 0$ describes attractive interactions. A rigorous derivation of the GPE and a justification for the interaction potential are given in Ch. 2 of this thesis.

In 1998 Ketterle’s group observed that the s-wave scattering length can be tuned in sodium through *Feshbach resonances* [54], and now tuning the interaction strength and sign is commonplace throughout BEC experiments worldwide, regardless of the atom considered.

The GPE can be transformed into a set of equivalent hydrodynamical equations through the Madelung transformation [55], which is akin to separating the density and phase contributions as

$$\psi(\mathbf{r}, t) = \sqrt{n(\mathbf{r}, t)} \exp[iS(\mathbf{r}, t)] , \quad (1.4)$$

where $S(\mathbf{r}, t)$ is the macroscopic phase factor. The velocity of the condensate is defined as

$$\mathbf{v}(\mathbf{r}, t) = \frac{\hbar}{m} \nabla S(\mathbf{r}, t) . \quad (1.5)$$

After substitution of these equations into the GPE (1.1) the ensuing classical fluid equations — a continuity equation and an Euler equation — depict a compressible inviscid fluid, albeit with a quantum pressure term arising from zero-point kinetic energy. These fluid properties are discussed in more detail in Sec. 2.2.3.

Extensions to the early GPE model go beyond pure zero temperature dynamics. Much effort has been put into making experimentally comparable predictions of finite temperature dynamics using stochastic methods. These introduce an element of random perturbation to the GPE by considering fluctuations, e.g. such as those arising from particle interactions between the condensate and thermal particles [56–58].

The aforementioned experiments and results were limited to BECs comprising of local effective interactions, however a range of exotic long-range interactions are possible. Tailored long-range potentials are theoretically possible through the engineering of dressed rotational states of strongly dipolar molecules with static microwave fields [59–61]. Realised long-range atomic systems include gravity analogues through a $1/r$ potential [62], laser induced oscillating dipoles [63], spin-orbit coupling (interaction between a quantum particle’s spin and orbital angular momentum) [64], and magnetic dipole-dipole interactions (DDIs). The focus of this thesis is on the latter.

The creation of condensates with atoms possessing significant magnetic dipole moments — ^{52}Cr [12, 65], ^{164}Dy [15, 66] and ^{168}Er [16] — affords a new opportunity to explore the interplay of magnetic effects with the coherent nature of the condensate. The dipole-dipole interaction (DDI) is anisotropic and long-ranged, contributing a non-local nonlinearity to the mean-field equation of motion for the condensate [67]. Importantly, the relative strength of the local to non-local interactions can be precisely tuned using Feshbach resonances, allowing the creation of condensates possessing a dominantly dipolar character [68].

The long-range dipolar potential makes analytic work exceptionally difficult, and theoretical progress has been slow. However, this thesis makes use of many numerical methods available for dealing with the integro-differential equations derived for these systems.

1.2 The dipole-dipole interaction

The general dipole-dipole interaction potential between two dipoles with arbitrary polarisation takes the form

$$V_{\text{dd}}(\mathbf{r}) = \frac{C_{\text{dd}}}{4\pi} \left(\frac{(\hat{\mathbf{e}}_1 \cdot \hat{\mathbf{e}}_2)r^2 - 3(\hat{\mathbf{e}}_1 \cdot \mathbf{r})(\hat{\mathbf{e}}_2 \cdot \mathbf{r})}{r^5} \right), \quad (1.6)$$

where C_{dd} is $\mu_0\mu_m^2$ (the permeability of free space multiplied by the dipole moment squared) for magnetic dipoles and d^2/ϵ_0 (electric dipole moment squared over the permittivity of free space) for electric dipoles, \mathbf{r} is the vector joining the dipoles, while $r = |\mathbf{r}|$, and $\hat{\mathbf{e}}_j$ is the orientation of dipole j . See Fig. 1.2 for a schematic of this setup.

We will be considering dipoles that are polarised along a specified axis, $\hat{\mathbf{e}}_1 = \hat{\mathbf{e}}_2$, implemented by an external magnetic or electric field. The DDI then takes the form

$$V_{\text{dd}}(\mathbf{r}) = \frac{C_{\text{dd}}}{4\pi} \left(\frac{1 - 3\cos^2\theta}{r^3} \right), \quad (1.7)$$

with θ being the angle between the polarising direction and \mathbf{r} . In this form it is clear that

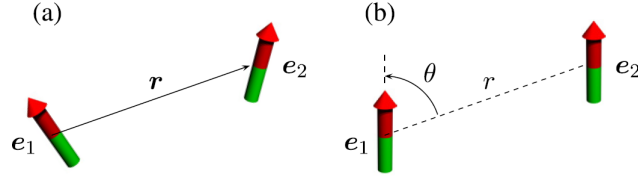


Figure 1.2: Schematic of the dipole-dipole interaction (DDI). (a) General case with arbitrary polarisation. (b) Polarised case, reducing the number of parameters to two: the distance between dipoles r and the angle between them θ . (Copyright IOP Publishing. Reproduced by permission of IOP Publishing. All rights reserved [67]).

the DDI is both long-ranged⁴ and anisotropic.

The behaviour of the DDI is analogous to two bar magnets. When $\theta = 0$ the dipoles are in an end-to-end configuration and the interaction energy is negative causing mutual attraction, whereas for $\theta = \pi/2$ dipoles are in a side-by-side configuration and the interaction energy is positive causing mutual repulsion, as shown in Fig. 1.3.

1.3 Ferrofluids

Returning to the classical world briefly, here we classify what properties a fluid must have to be called a *ferrofluid*. A ferrofluid is a collection of nanoscale ferromagnetic particles that have been suspended within a carrier solution, which coats each nanoparticle with a surfactant to inhibit aggregation [69]. These fluids do not fit the properties of a ferromagnet as they lose magnetisation in the absence of an external magnetic field, but are classified as a superparamagnet instead.

First patented in 1963 by Steve Papell [see his book chapter on the subject [70]], the ferrofluid now has uses in many different fields. In electronics a ferrofluid is used as

⁴A potential of the form r^{-m} ($m > 0$) is long-range when the dimension D of the system satisfies $D \geq m$ and non-local otherwise.

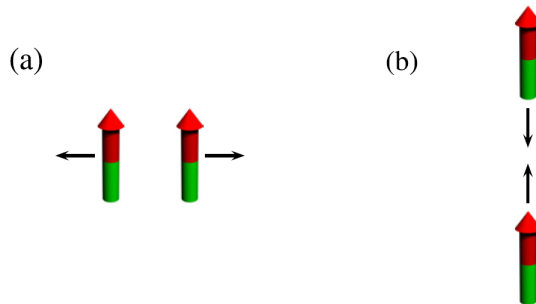


Figure 1.3: Anisotropic interactions due to the DDI. (a) Side-by-side polarisation leads to repulsion. (b) Head-to-tail configuration leads to mutual attraction. (Copyright IOP Publishing. Reproduced by permission of IOP Publishing. All rights reserved [67]).

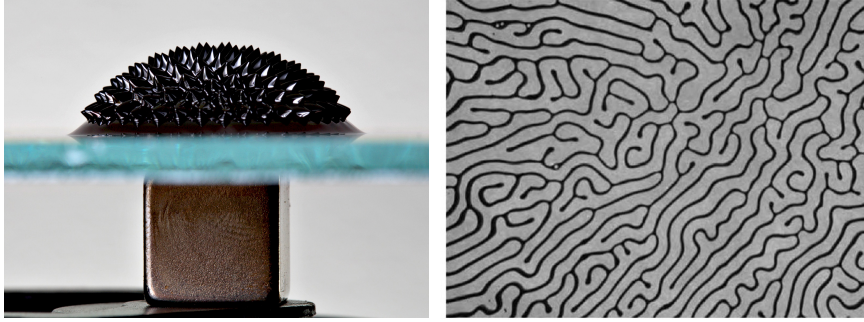


Figure 1.4: Left: The Rosensweig instability of a ferrofluid, activated by a magnet placed underneath a pane of glass. (Photo credit: Gregory F. Maxwell, 2006 [73]). Right: The labyrinth instability of a colloidal mixture of ferrofluid and water. Width of image is 3cm across. (Copyright (2001) Kluwer Academic Publishers [74]).

a liquid sealant preventing debris from entering a hard drive, in loudspeakers they are used for cooling the voice coil, making use of Curie's law that the fluid will become less magnetic at higher temperatures and will flow away from a magnet placed at the centre of the voice coil, giving an overall cooling effect. Proposed uses for ferrofluids in the future even include medical applications, enclosing drugs in a ferrofluid and using magnetic fields to target and selectively release drugs in specific places [71].

By adding an external polarising magnetic field the elusive beauty of ferrofluids shines through. The alignment of the dipoles causes an effect known as the Rosensweig instability [69] where corrugations form to minimise the magnetic energy in a peak and valley formation, but larger peaks increase the surface free energy and the gravitational energy cost, therefore small "spikes" appear out of a balance of forces. This effect is shown in Fig. 1.4 (left).

The mixing of two fluids in a quasi-two-dimensional scenario, one ferrofluid and one non-magnetic fluid, creates labyrinthine structures where the ferrofluid minimises the azimuthal repulsive forces by undergoing a fingering instability [72], resembling a labyrinth as seen in Fig. 1.4 (right).

These patterns illustrate the rich physics which can arise from the interplay between the fluidity and the magnetic forces. Analogous physics occurs when dipolar interactions are added to BECs, and we will be exploring this effect in this thesis.

1.4 Ultra-cold dipolar systems

Dipolar interactions fall into a dichotomy: electric and magnetic dipoles. In the following section we explore these two categories in the context of quantum gases and BECs, and the experimental progress that has been made on both.

1.4.1 Electric dipoles

Dipolar excitons

An electron in the valence band of an atom can be excited into a higher energy state, leaving behind a hole. The negative charge of the electron and net positive charge of the hole left behind creates a mutual attraction between the electron-hole pair; this is a quasi-particle called an *exciton*. Unlike the atomic gases explored in this thesis these systems undergo a continuous growth and decay process, where the atoms absorb a photon to create an exciton, then relax, emitting a photon and destroying the exciton. Through continuous pumping of light into a 2D gas of gallium arsenide (GaAs), for example, an equilibrium can be found determined by the interplay of drive and relaxation in the system.

Excitons that carry an electric dipole moment, dipolar excitons, display large interactions due to high energy blue-shifts of their emission line, and large collisional broadening [75–77]. These effects stem from the long-range dipole-dipole interactions.

Exciton gases are intimately affected by their internal spin structure. There exist two states: bright states, where the exciton can couple to light to create a polariton, and dark states, where the exciton is optically inactive. An exciton BEC is predicted to spontaneously form in the dark spin state if the excitons are considered non-interacting [78]. Short-range exchange interactions destroy this picture through a brightening instability, i.e. dark states becoming bright, at a critical density. Through adding an induced electric field, polarised perpendicularly to the 2D gas, this increases the repulsive side-by-side interactions and reduces short-range collisions, suppressing this instability; as seen experimentally [76, 77, 79], and explained in Ref. [80].

Rydberg atoms

These are atoms with at least one electron with a large principal quantum number n . The radius of an electron scales as n^2 , and thus the typical Rydberg atom has a radius $\sim 1\mu\text{m}$, leading to enormous dipole-dipole interactions scaling as n^4 . After one photon has been absorbed to create a Rydberg state further incident light is deflected by the now enormous radius of the atom, known as the *blockade radius*. This has been measured as a reduction in the g_2 correlation of emitted light. However, the lifetime of these states is very small, scaling as n^{-3} , and is worse for higher densities [81]. Recent experiments with Rydberg atoms have shown a strong link between these atoms and qubits, where considering the Rydberg state as "on" and the ground state as "off" a group in Harvard have been able to create a 51-atom quantum simulator [82].

Polar molecules

Degenerate mixtures of molecules have been the subject of a swathe of theoretical and experimental work in the last decade. Molecules share a strong connection to the atomic systems considered in this thesis, due to the strong permanent electric dipole moment, but with the advantage of a much stronger interaction strength. However, experimental creation of these systems comes with great difficulties. First, two atomic species (or the same species in two different spin states) have to be condensed simultaneously and separately in space. Once condensation has been achieved they are moved to overlap with each other in space. Finally, the atoms are bound to form a molecule through Feshbach resonances. To meet the criteria for BEC this gas of molecules has to be condensed into the degenerate molecular ground state. This step has yet to be achieved due to molecules having significantly more motional freedom than an atom, presenting major challenges to cool to the motional ground state. A further complication to these systems is whether the molecules are chemically reactive or non-reactive. Reactive 2-body losses are atom exchange interactions, e.g. $\text{KRb} + \text{KRb} \rightarrow \text{K}^2 + \text{Rb}^2$. This could be avoided by choosing chemically stable molecules, such as NaK or CsRb, or by manipulating external electric [83, 84] or microwave [60, 85] fields to shield against 2-body collisions.

1.4.2 Magnetic dipoles

The magnetic dipoles are our next topic of discussion. Current research into long-range interactions in a BEC setting are contained in this section, due to the *relative* ease of which these dipolar systems can be created and manipulated. Unlike the electric dipoles, where the effects require an external electric potential to become significant, these atoms have a permanent dipole moment, due to numerous unpaired electrons. In experiments, it is standard practice to polarise the dipoles with an external magnetic field.

Chromium

The first strongly dipolar degenerate gas was achieved in 2005 by the Pfau group [12] creating a BEC of ^{52}Cr atoms. This particular isotope of chromium has a ground state spin quantum number of 3, giving a large magnetic dipole moment of $6\mu_B$, where μ_B is the Bohr magneton. The non-zero quantum spin number at degeneracy also allows for a 2-body loss process — where the spin of a colliding atom is flipped, converting between spin and orbital angular momentum — known as dipolar relaxation. Zeeman splitting can be used to thermally freeze out spin flips, so this problem was overcome by optically pumping the atoms into the lowest energy spin state, $m_s = -3$ [12, 67].

The anisotropy of the DDI induces an effect called *magnetostriction*, i.e. a distortion in the density profile dependent on the polarisation angle of the dipoles. This was observed

in the first chromium experiment, through a distortion of the aspect ratio after taking a time-of-flight expansion image. The Pfau group moved to study one of the rare-earth metallic species, which we will cover in the next section. However, other experiments using chromium include a group in Paris [65]. This group have studied the effects of the DDI on collective excitations [86], spontaneous demagnetisation of a dipolar spinor BEC [87], and they reported on the anisotropic speed of sound due to the DDI [88]. In their most recent work they have created the first collective spin excitation, the *magnon* mode, generated by adding a linear magnetic field along the long axis of a quasi-1D gas [89]. This group have also branched into an optical lattice setup, using the long-range potential to explore interaction-induced spin exchanges in a lattice of chromium atoms (local interactions only allow for atom coupling through tunnelling-assisted processes) [90] and probing Mott insulator to superfluid transitions in this system [91].

Rare-earth metals

The rare-earth metals contain the largest permanent dipole moment, and thus have mostly replaced chromium experiments. Early work in cooling these heavy atoms was undertaken with ytterbium [11, 92] and erbium [93, 94], where temperatures of $T \approx 2\mu\text{K}$ were achieved. Ytterbium has a magnetic moment of $4\mu_B$, weaker than chromium, and is not explored in this thesis. However, the first strongly magnetic quantum degenerate bosonic gas was achieved in 2011 with dysprosium (^{164}Dy) in the Lev group in Stanford [15]. This atom has a magnetic dipole moment of $9.93\mu_B$, and has been the "gold standard" of studying dipolar interactions, with many other groups also achieving degeneracy including the group of Pfau [95] and Modugno [96]. The Lev group also were the first to create a degenerate dipolar Fermi gas of ^{161}Dy [23].

In 2012 came the first erbium BEC in Innsbruck [16]. This element also has a strong permanent dipole moment of $6.98\mu_B$. Recently, the first mixture of erbium and dysprosium has been created by the same group, being able to produce five bosonic and one Bose-Fermi mixture through the choice of different isotopes [97, 98]. The discoveries made in these experiments will be elucidated throughout this thesis, particularly in Ch. 2.

Other lanthanides have been cooled, including thulium [99] and holmium [100], though neither has reached degeneracy. Holmium is the best candidate for competing with dysprosium with a dipole moment of $9\mu_B$, whereas thulium only possesses a dipole moment of $4\mu_B$.

1.4.3 Comparison of dipolar strengths

In order to define which of the atomic species detailed in the last section have dominantly dipolar interactions we must consider the ratio of the long-range interactions to the short-

Species	a_s (a_0)	μ_m (μ_B)	a_{dd} (a_0)	ε_{dd}	References
^{87}Rb	100.4(1)	1	0.7	0.007	[101]
^{52}Cr	102.5(4)	6	15.1	0.15	[102]
^{162}Dy	122(10)	9.93	129.2	1.06	[103]
^{164}Dy	92(8)	9.93	130.8	1.42	[103, 104]
^{166}Er	72(13)	6.98	65.5	0.91	[105]
^{168}Er	137(1)	6.98	66.2	0.48	[106]
^{170}Er	-221(22)	6.98	67.0	-0.3	[105]

Table 1.1: Dipole strengths - darker shade of blue indicates strength. Lengths here are presented in units of the Bohr radius, $a_0 = 5.3 \times 10^{-10}\text{m}$.

range interactions. We follow Ref. [67] and define a characteristic lengthscale for dipolar interactions,

$$a_{dd} \equiv \frac{C_{dd}m}{12\pi\hbar^2}, \quad (1.8)$$

and subsequently define

$$g_{dd} = \frac{4\pi\hbar^2 a_{dd}}{m}. \quad (1.9)$$

We can compare this quantity to the s-wave scattering length a_s (see Sec. 2.1) by defining the quantity

$$\varepsilon_{dd} = \frac{a_{dd}}{a_s} \equiv \frac{g_{dd}}{g}. \quad (1.10)$$

We will explore the requirements for stability of a condensate with arbitrary ε_{dd} , however for now it is enough to consider $\varepsilon_{dd} > 1$ as dominantly dipolar, and $\varepsilon_{dd} < 1$ as dominantly s-wave.

In Table 1.1 we show these quantities for all of the bosonic isotopes experimentally created to date. Rubidium features on this table, with a value of $\varepsilon_{dd} = 0.007$, highlighting that it is safe to neglect dipolar interactions for modelling this species. The only dominantly dipolar species are the dysprosium isotopes, although through reducing the scattering length of ^{166}Er one could access the dominantly dipolar regime, like what has been seen in ^{52}Cr [68]. It is worth mentioning here that the equivalent value for ε_{dd} of alkali dimers is at least one order of magnitude larger than seen in Table 1.1. For example, the molecule KRb has $\varepsilon_{dd} = 37$, whereas NaRb boasts a value of $\varepsilon_{dd} = 229$ [107].

1.5 Topological excitations

1.5.1 Vortices

Vortices are ubiquitous in nature. In classical fluids they represent any degree of fluid rotation and occur during the breakdown of ordered fluid flow, leading to turbulence. In quantum fluids their existence causes the dissipation of superfluidity and their circulation is quantised, appearing as many singly charged vortices rather than one vortex with a high charge. These excitations are topological as they can only decay at a boundary or through collision (annihilation).

Destructive imaging techniques such as expansion imaging have revealed single vortices [108–111], vortex lattices [109, 112–114], and vortex rings [115, 116]. Recent developments in non-destructive imaging have also taken place, where a small portion of the atoms ($\sim 5\%$) are excited into a different hyperfine state and out-coupled from the main cloud, then imaged separately [117]. Repeated applications of this technique allows for near real-time observation of dynamics, such as vortex trajectories. A recent experiment in Trento used this technique to classify many different possible vortex reconnections and interactions in a cigar-shaped atomic BEC [118].

There are several techniques that can be employed in order to generate vortices, one method is to rotate the superfluid about a fixed axis. Above some critical rotation frequency, associated with the minimum velocity to create excitations, one or more vortices are nucleated in the system to lower the free energy [119, 120]. Another method commonly employed is to drag a repulsive Gaussian laser beam through a condensate faster than some critical velocity. Recently this method lead to the observation of a von Kármán vortex street [121].

Quantised circulation

The wavefunction must remain single-valued. In order to maintain this condition the phase $S(\mathbf{r}, t)$ around any closed contour C must be an integer multiple of 2π ,

$$\oint_C \nabla S \cdot d\mathbf{l} = 2\pi q, \quad (1.11)$$

where $q = 0, \pm 1, \pm 2, \dots$. Using the relationship between the phase and velocity, $\mathbf{v}(\mathbf{r}, t) = (\hbar/m)\nabla S(\mathbf{r}, t)$, we can rewrite the above equation as

$$\oint_C \mathbf{v} \cdot d\mathbf{l} = q \left(\frac{h}{m} \right). \quad (1.12)$$

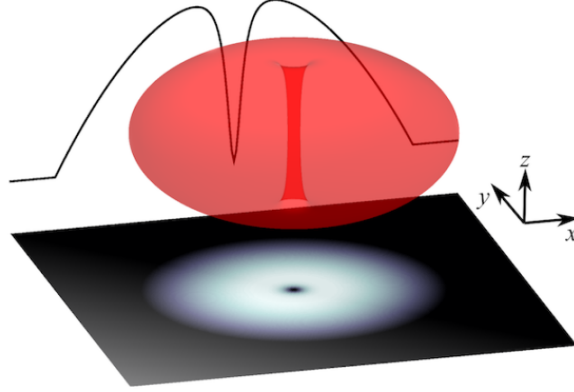


Figure 1.5: A vortex in a quasi-2D condensate. Shown is a vortex as a central tube in a 3D isosurface density, a 2D density profile column integrated along z (with the vortex appearing as a black dot), and a 1D density profile column integrated along y and z . Image courtesy of N. G. Parker.

So the above equation tells us the circulation of the fluid is quantised in units of $\kappa = h/m$. This constraint comes directly from the quantum mechanics of a highly occupied single state, any rotation of a superfluid must be held in the form of vortex lines with quantised circulation, and it can be proved that the presence of vortices becomes energetically favourable at some critical velocity [119, 120].

A quantised vortex can be represented by the wavefunction

$$\psi(r) = \sqrt{n_V(r)} \exp(iq\phi) , \quad (1.13)$$

with vortex density $n_V(r)$ and azimuthal angle around the vortex core ϕ , which does not have an analytic solution. In Fig. 1.5 we plot an example vortex in a quasi-2D system. From Eq. (1.12) it appears a vortex can have arbitrary quantisation, however it turns out that it is always energetically favourable for a vortex with charge $q > 1$ to decay into several singly charged vortices. This can be seen from the classical hydrodynamic approximation where the vortex energy per unit line length in a system of size L is given by,

$$E_V \approx \frac{mn\kappa^2}{4\pi} \ln\left(\frac{L}{\xi}\right) , \quad (1.14)$$

where it is energetically favourable to have q singly-charged vortices rather than one q charged vortex. Interestingly, for steeper-than-harmonic potentials this picture changes and multicharged vortices can become dynamically stable [122].

Classical turbulence

Classical turbulence is a term describing chaotic and highly irregular fluid dynamics on a large range of time and length scales. It is dominated by the appearance of vortices, or "eddies", interacting with one another. The largest length scale of these eddies is set by the system size, known as the integral length scale, and the shortest set by the scale at which viscosity dominates, dissipating the smallest eddies into heat. Note that, in practice, the smallest length scales which can be probed experimentally is set by the size of the measurement device, and in numerical simulations by the computational grid resolution.

The parameter used to characterise different flows is the *Reynolds number*, Re , defined as

$$Re = \frac{uL}{\nu},$$

where u is the flow velocity, L is the size of the system, and ν is the kinematic viscosity. For low Reynolds number (the precise values depending on the geometry of the flow) the flow is laminar, no vortices are seeded into the system, and the dynamics are deterministic. For large Reynolds number the flow is turbulent and unpredictable.

For flows with large Reynolds number, viscous forces dominate over inertial forces as eddies decay to smaller size. The length scale at which these forces balance is the Kolmogorov length scale, and at smaller length scales viscosity causes energy dissipation in the flow.

Much of the interest in turbulence stems from the transport of energy in the system. The transport of kinetic energy between length scales is a process known as energy cascade. In classical, isotropic turbulence most of the kinetic energy is contained in large-scale structures and is distributed across length scales following the famous Kolmogorov energy spectrum, where the kinetic energy density (in spherical shells of k) scales as $E_k \propto k^{-5/3}$ [123].

Quantum turbulence

The nature of quantum turbulence is very different than its classical counterpart; quantum turbulence is governed by the interactions of an irregular tangle of quantised vortex lines. The interest in quantum turbulence is dominantly at very low temperature, where thermal viscous dissipation is insignificant. It is believed that the dominant mechanisms for dissipating the flow is via the generation of sound waves (phonons) which occur when two vortex lines reconnect or when an element of a vortex line otherwise accelerates (e.g. under Kelvin wave excitation). The quantised circulation and inviscid flow properties of superfluidity makes these excellent testbeds to study turbulence, as is seen by the swathe of theoretical and experimental studies [124–128].

There are two distinct regimes of quantum turbulence, based on the observed energy spectrum [129]. In Vinen, or ultra-quantum, turbulence the vortices are essentially randomised. The flow velocity is typically correlated on lengthscales less than the inter-vortex spacing and the maximum kinetic energy lies at such intermediate lengthscales. In Kolmogorov, or quasi-classical, turbulence vortices tend to form coherent structures (bundles). The velocity correlations typically extend beyond the inter-vortex spacing and the maximum kinetic energy lies at larger scales. In this sense, this form of turbulence mimics classical flow and reveals energy spectra consistent with the classical Kolmogorov scaling [130, 131].

Turbulence in BECs

Atomic BECs provide an alternative platform for studying quantum turbulence due to the large vortex size, which is on the order of a micron (c.f. in liquid helium this is about one Angström, $1\text{\AA} = 10^{-10}\text{m}$), and bolstered by the extreme experimental control available in modern experiments. Theoretical proposals for studying quantum turbulence in BECs first arose at the beginning of the 21st century [132–135]. These proposals became reality soon after with observations of three [136] and two-dimensional turbulence [137, 138]. An exciting recent development is the observation of Onsager vortices, large clusters of vortices of the same polarity in a 2D gas, indicative of the inverse energy cascade [139, 140].

Due to the limitations in the number of vortices that can be induced into a BEC experiment there are a limited number of length scales available. This limits the number of comparisons available to make between BEC and classical turbulence where much of the theory is described by the distribution of kinetic energy between a large number of length scales. However, numerical simulations of the GPE have shown that quantum turbulence still distributes kinetic energy in accordance with Kolmogorov’s 5/3 law [130, 131, 141].

1.5.2 Solitons

Solitons are excitations of non-linear systems that possess both wave-like and particle-like qualities. These structures are localised one-dimensional wavepackets, and take on the form of a solitary wave when embedded into a three-dimensional system. They obey wave equations and yet do not disperse, maintaining their shape and speed by balancing dispersion with nonlinearity.

Solitons appear across a wide range of physical systems that include water, light, plasmas, liquid crystals, optical fibres, spin chains, the human circulatory system, and BECs [142], and have been touted as playing a fundamental role in the fabric of our universe [143]. Much of the soliton behaviour across these diverse systems, including their interactions and collisions, are universal [144]. The extreme controllability of the nonlinearity,

dimensionality and external potential in atomic BECs makes them an ideal playground for studying solitons [145–148].

Experiments confirm that solitons in BECs and in classical systems such as water or light are for many purposes the same phenomenon and share the same three particle-like defining properties, namely: permanent form, localisation within a region, and emergence from collisions with other solitons unaltered, except for a phase shift [149]. It is important to bear in mind, however, that in BECs the soliton relies on quantum mechanical coherence across the sample, and is at heart a probability wave [43].

There are two distinct categories of soliton in a BEC depending on the sign of the nonlinearity, a bright soliton is a matter-wave on a zero-density background with attractive/focussing short-range interactions, and a dark soliton is a density depletion on a homogeneous background with repulsive/defocussing interactions. These names were adapted from their discovery in optical fibres through their appearance of brighter or darker regions of light.

Bright solitons

For attractive contact interactions $a_s < 0$, a single bright soliton solution along a one-dimensional waveguide in z , which for simplicity we take to be initially positioned at the origin, is

$$\psi(z, t) = \frac{1}{2\sqrt{l_z}} \text{sech}\left(\frac{z - ut}{2l_z}\right) \exp[iS(z)] , \quad (1.15)$$

where u defines the velocity of the bright soliton, l_z is a lengthscale on the order of 5-10 microns, and S is the phase. In this form $|\psi|^2$ is normalised to unity. This solution describes a sech-shaped profile which propagates at constant velocity, an example solution is shown in Fig. 1.6(a).

Bright solitary waves are most common of the two soliton species. They are found in a smorgasbord of systems including optical physics [150], acoustics [151] and plasma physics [152, 153]. The classic story of their discovery is of John Scott Russell following a solitonic wave in a shallow canal by horseback in 1845 [154].

Under attractive van der Waals interactions, bright solitons have been observed in BECs [155–162]. They typically contain a few thousand atoms and are around 5-10 microns in length. In real 3D systems, 1D bright solitons can be approximated by confining them in elongated waveguides with strong transverse confinement. Nonetheless, significant differences can emerge in this 3D setting, the most prominent being the instability of the condensate to collapse when the attractive nonlinearity dominates (an effect not present in the 1D case). The critical atom number in a ^7Li condensate in a one-dimensional waveguide with $\omega_z = 0$, radial oscillator length $a_r \approx 3\mu\text{m}$ and scattering

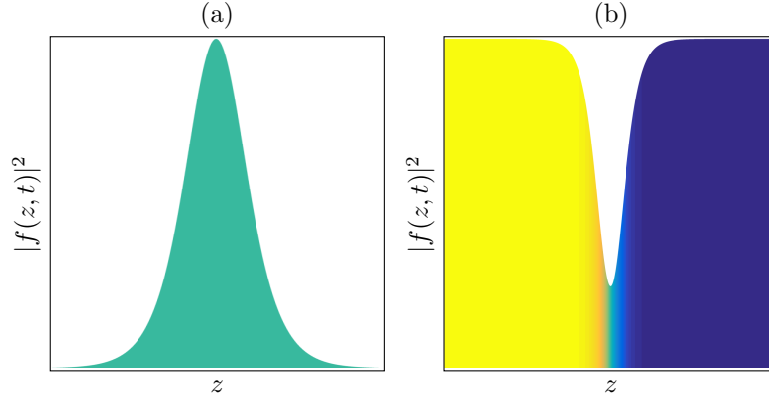


Figure 1.6: Simple soliton solutions. (a) Bright soliton solution, the condensate density is shaded. (b) Dark soliton solution for $v = 0.5c$. The condensate phase is shown as a colour gradient in the condensate density.

length $a_s \approx -1.45\text{nm}$ the critical atom number is $N_c \sim 1400$ [6]. We discuss process of condensate collapse in Sec. 2.5. Subsequent experiments have explored the effect of collisions with barriers [159, 163], and also the role of the relative phase for two trapped solitons [164]. Matter-wave interferometry using bright solitons has also been the focus of recent experimental [160] and theoretical [165] interest.

Powerful analytical tools such as the inverse scattering transform (IST) have allowed the investigation of higher-order solitons [166] and the derivation of a particle model for the soliton dynamics and interactions, based on the knowledge of the scattering phase shifts [167]. This, in turn, has lead to the identification of regimes of chaotic dynamics for three trapped bright solitons [168, 169] and the observed frequency shifts of trapped bright solitons in a recent experiment [170]. Examining collisions between bright solitons introduces an extra parameter, namely the relative phase. While these solitons collide freely in one dimension, numerical simulations [171–173] have demonstrated that in-phase collisions promote the collapse of the condensate in three dimensions, while a relative phase of π suppresses the collapse. Indeed, such π phase differences are believed to have existed between experimental bright solitons [155, 174, 158], critical to the observed stability of these states. A strategy to control the relative phase of the solitons has been proposed [175]. Attractive nonlinearities can also facilitate molecule-like bound states of two bright solitons [166, 176, 170], with these states being sensitive to both the relative phase and velocity of the solitons [176].

Dark solitons

It is known that the purely local Gross-Pitaevskii equation supports a family of dark soliton solutions for repulsive contact interactions ($a_s > 0$) [177, 178]. The solution of a dark

soliton at the origin on a background density n_0 is given by

$$\psi(z, t) = \sqrt{n_0} \left[\beta \tanh \frac{\beta(z - vt)}{\xi} + i \frac{v}{c} \right] e^{-i\mu t/\hbar}. \quad (1.16)$$

Here the soliton is shown moving at velocity v with respect to condensate speed of sound c , and $\beta = \sqrt{1 - v^2/c^2}$. Stationary solitons have a node of zero density and a phase slip of π , whereas a $v = c$ soliton has no phase or density contrast from the background fluid. The soliton energy decreases with increasing speed [178], leading to the analogue of a particle with negative effective mass [179]. Meanwhile the density minimum of the soliton scales as $n_{\min}/n_0 = \beta^2$ [147]. We present a solution to Eq. (1.16) in Fig. 1.6(b).

Dark solitary waves are not as ubiquitous as bright solitons, and have only been realised in a handful of systems, seminally in nonlinear optics in 1987 [180]. Experimental demonstrations of dark solitons in BECs are created through disturbing the gas. The most common method is to imprint a π phase jump into the BEC by shining a laser on half of the cloud; this phase defect then evolves into one or more dark solitons. This method was used to show the first dark solitons in 1999 [181] and has been used several times since [182, 113]. Dynamical experiments were quick to follow, with explorations of the soliton's decay dynamics [115, 183], interaction with sound waves [116], appearance after the collision of two species of BEC [184, 185] and collision dynamics [186, 187], in subsequent years.

In binary condensates unique two-soliton complexes coined "dark-bright" solitons have also been probed experimentally [188, 189]. A dark soliton is created in one species with overall repulsive interactions and the second species, with attractive interactions, forms a bright soliton in the generated density depletion.

Novel applications of solitons

Matter-wave solitons are still in their infancy from discovery, however optical bright solitons have already found applications in communications [190]. Dark solitons have been dubbed "quantum canaries", as they have the ability to provide insight into the interplay of solitons with quantum coherence [191], and have potential applications in interferometry [155, 192, 160, 165], surface force detection [193], as robust quantum-information carriers [194] and as long-lived matter-wave qubits [195].

1.6 Thesis overview

Part I - Introduction and theory

- In this Chapter we have introduced superfluidity, topological excitations, dipolar interactions, and their history.
- In Chapter 2 we introduce the theoretical framework from which we will build upon in the main parts of the thesis. We also give a thorough introduction to the experimental progress that has been undertaken thus far.
- In Chapter 3 we outline the basic numerical procedures utilised in our work.

Part II - Excitations in a quasi-one-dimensional dipolar Bose gas

- In Chapter 4 we introduce progress made on non-local interactions in nonlinear waves and motivate our work.
- In Chapter 5 we perform a stability analysis of the quasi-1D dipolar Gross-Pitaevskii equation in the Bogoliubov-de Gennes framework to investigate the onset of instability of excitations. Results of this chapter have been published in Physical Review A [196]. We are thankful for analytical and computational help from Matthew Edmonds for the homogeneous system analysis, and Matthew Edmonds and Stuart Szigeti for the trapped system analysis.
- In Chapter 6 we find dipolar dark soliton solutions in homogeneous systems and show how the dipole-dipole interactions modify the density and collisions of these excitations. Results of this chapter have been published in two papers in Physical Review A [197, 196]. We are thankful to Matthew Edmonds for analytical and computational help in these works.
- In Chapter 7 we assess the effect of dipolar interactions on the oscillation frequency of a dark soliton for a dipolar condensate under harmonic confinement. Results of this chapter have been published in Physical Review A [198]. We are thankful to Krzyszek Pawłowski for providing 3D simulations for this project.
- In Chapter 8 we find dipolar bright soliton solutions, and categorise interactions between two solitons. Results of this chapter have been published in New Journal of Physics [199]. The author's role in this project was to provide numerical and analytical assistance, and we are thankful for Matthew Edmonds and Ryan Doran for their efforts in preparing the manuscript.

Part III - Rotation and turbulence

- In Chapter 9 we assess the theoretical implications of attempting to access the anti-dipolar regime through fast rotation of a magnetic field. This work has been submitted to Physical Review Letters [200]. The author's role in this work was to provide GPE simulations and analytical aid. We are thankful to Srivatsa Badariprasad and Brendan Mulkerin for their work on the stability analysis.
- In Chapter 10 we undertake finite temperature simulations of a turbulent 3D homogeneous dipolar Bose gas. Results of this chapter have been published as the Editors' Suggestion in Physical Review Letters [201]. We are thankful to George Stagg for his computational expertise, and Luca Galantucci for his help in providing line-length calculations.

Part IV - Conclusions, outlook, and appendices

- In Chapter 11 we draw conclusions from the work presented and present some ideas for future work.
- In Appendix A we present a derivation of the dipolar Bogoliubov-de Gennes equations.
- In Appendix B we present the convolution theorem, and show how it is used in this thesis.
- In Appendix D we present work undertaken during the period this thesis was written, but not related to dipolar condensates. We investigate the quasi-integrability of BECs under harmonic confinement, using dark solitons as a probe. Results of this appendix have been published in Journal of Physics B [202].

1.7 List of publications

Work in this thesis has been partially covered in the following list of publications

- *Controllable nonlocal interactions between dark solitons in dipolar condensates*,
T. Bland, M. J. Edmonds, N. P. Proukakis, A. M. Martin, D. H. J. O'Dell and N. G. Parker,
Phys. Rev. A **92**, 063601 (2015).
- *Exploring the Stability and Dynamics of Dipolar Matter-Wave Dark Solitons*,
M. J. Edmonds, T. Bland, D. H. J. O'Dell and N. G. Parker,
Phys. Rev. A **93**, 063617 (2016).
- *Engineering Bright Matter-Wave Solitons of Dipolar Condensates*,
M. J. Edmonds, T. Bland, R. Doran and N. G. Parker,
New J. Phys. **17**, 023019 (2017).
- *Interaction-sensitive oscillations of dark solitons in trapped dipolar condensates*,
T. Bland, K. Pawłowski, M. J. Edmonds, K. Rzażewski and N. G. Parker,
Phys. Rev. A **95**, 063622 (2017).
- *Probing quasi-integrability of the Gross-Pitaevskii equation in a harmonic-oscillator potential*,
T. Bland, N. G. Parker, N. P. Proukakis and B. A. Malomed,
J. Phys. B **51**, 205303 (2018).
- *Quantum ferrofluid turbulence*,
T. Bland, G. W. Stagg, L. Galantucci, A. W. Baggaley and N. G. Parker,
Phys. Rev. Lett. **121**, 174501 (2018).
- *Instability of rotationally-tuned dipolar Bose-Einstein condensates*,
S. B. Prasad, T. Bland, B. C. Mulkerin, N. G. Parker and A. M. Martin,
Submitted to Phys. Rev. Lett. [arXiv:1810.09041].

2

Experimental progress and theoretical groundwork

2.1 Modelling and tuning interactions

MOST quantum gas experiments are dilute, containing a peak number density of $n \sim 10^{20} \text{m}^{-3}$ (c.f. the number density of air $n \sim 10^{25} \text{m}^{-3}$, water $n \sim 10^{28} \text{m}^{-3}$). The number density of the vacuum chamber, used for BEC experiments, is typically in the range $n \sim 10^8 - 10^{10} \text{m}^{-3}$). This means that the dominating interactions are two-body, given the low probability of three- or higher order interactions, called van der Waals (vdW) interactions. At small inter-particle separations r these are short-ranged, decaying proportionally as r^{-6} , and isotropic for large separations. The true inter-atomic two-body interaction potential in the ultra-cold Bose gas varies rapidly at small separations, making detailed calculations difficult. However, in the low energy regime the typical momentum is $k \ll 2\pi/R$, where R is the range of the interaction, and for low densities satisfying $n^{1/3}a_s \ll 1$, where a_s is the characteristic length scale over which interactions occur, the precise form of the interaction potential is not required, as long as the behaviour before and after the collision is correct.

The physics behind two-body interactions is well understood through scattering theory. Scattering experiments have unravelled everything known about nuclear and atomic physics, including Rutherford's discovery of the nucleus and the discovery of sub-atomic particles, such as quarks. The problem is that shown in Fig. 2.1 for finding the scattering cross section σ , defined by the proportion of particles scattered into an element of solid angle $d\Omega$.

If the wavefunction of the scattering problem is defined by $\psi(\mathbf{r}) \simeq e^{i\mathbf{k}\cdot\mathbf{r}} + f(\theta)e^{ikr}/r$ for an incoming plane wave $e^{i\mathbf{k}\cdot\mathbf{r}}$ and a scattered spherical wave e^{ikr}/r with amplitude $f(\theta)$ (dependent on the scattering angle θ) then the differential cross section is

$$\frac{d\sigma}{d\Omega} = |f(\theta)|^2. \quad (2.1)$$

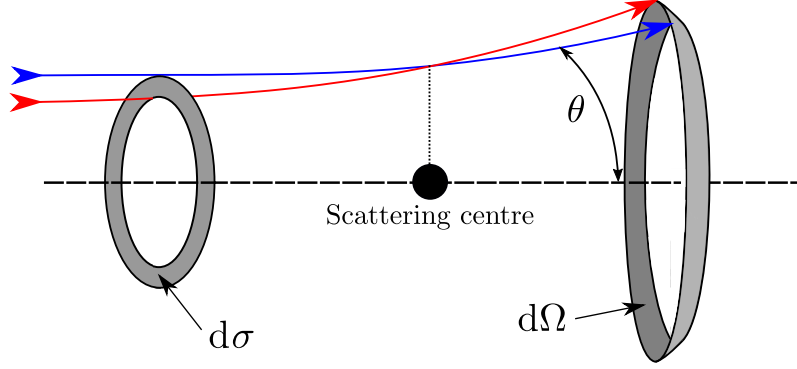


Figure 2.1: Incoming wavefunction considered over differential cross section $d\sigma$ scattered by an angle θ passed a scattering centre to new cross section defined by the solid angle $d\Omega$.

For a general central potential of the form r^{-n} the scattering phase shift, a quantity defining the effect of a scattering centre from the reference of a free particle $\delta_l(k) = 0$, in the limit $k \rightarrow 0$ can be derived as the following [204]

$$\delta_l(k) \propto \begin{cases} k^{2l+1}, & l < (n-3)/2, \\ k^{n-2}, & \text{otherwise,} \end{cases} \quad (2.2)$$

where $l = 0, 1, 2, \dots$ is the angular momentum quantum number. In this case the scattering amplitude is

$$f(\theta) = \frac{1}{2ik} \sum_l (2l+1) (e^{2i\delta_l} - 1) P_l(\cos \theta), \quad (2.3)$$

where the $P_l(\cos \theta)$ are the Legendre polynomials.

In the limit $k \rightarrow 0$ the term $(e^{2i\delta_l} - 1)/(2ik) \rightarrow \delta_l/k$, keeping only lowest order terms in k . Thus, using Eq. (2.2) for the van der Waals potential $n = 6$, the s-wave ($l = 0$) contribution to $f(\theta)$ is independent of k , the p-wave ($l = 1$) contribution is proportional to k^2 and for all $l > 1$ it scales as k^3 . Hence, in the limit of low energy scattering, $k \rightarrow 0$, only the s-wave channel contributes and the interaction potential can be approximated as a delta function pseudo-potential [44]

$$U_s(\mathbf{r}_1 - \mathbf{r}_2) = g\delta(\mathbf{r}_1 - \mathbf{r}_2), \quad (2.4)$$

where

$$g = \frac{4\pi\hbar^2 a_s}{m}, \quad (2.5)$$

with characteristic interaction length scale a_s . When $a_s > 0$ the interactions are repulsive,

but for $a_s < 0$ they are attractive. This approximation is unsuitable for studying correlations at length scales shorter than a_s .

The same analysis can reveal the long-range character of the dipole-dipole interaction. By considering $n = 3$ the scattering amplitude for all orders of l are independent of k and thus contribute in the $k \rightarrow 0$ limit. Consequently, a delta function is not appropriate as a pseudo-potential for the DDI. In fact in Ref. [205] the authors validate that the DDI pseudo-potential is merely the DDI itself but the scattering length becomes dependent on the dipolar interaction strength, $a_s \rightarrow a_s(C_{dd})$. As the results we present in this thesis are general we will ignore this dependence, however we direct the reader to Refs. [205–210] for further information. Thus, the full interaction pseudo-potential reads

$$U(\mathbf{r}_1 - \mathbf{r}_2) = g\delta(\mathbf{r}_1 - \mathbf{r}_2) + \frac{C_{dd}}{4\pi} \left(\frac{1 - 3\cos^2\theta}{|\mathbf{r}_1 - \mathbf{r}_2|^3} \right). \quad (2.6)$$

2.1.1 Feshbach resonance

Quantum gases are routinely used as a testbed for fundamental physical principles, aided by the extreme controllability in these systems. The Feshbach resonance is a tool used to precisely control the s-wave scattering length a_s , including the ability to change its sign. Predicted theoretically in 1976 [211] it was first successfully deployed in quantum gases in a plethora of experiments in 1998 [54, 212–214].

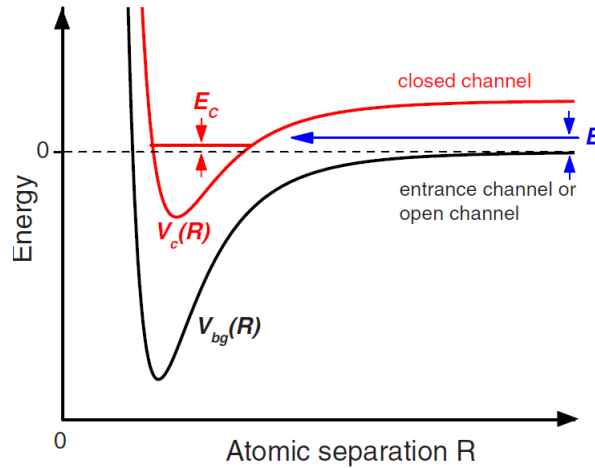


Figure 2.2: The basic two-channel model of a Feshbach resonance. A particle of energy E approaches an open channel close to $E \rightarrow 0$, which is resonantly coupled to a bound state in a closed channel with energy E_c . With the application of an external magnetic field B the bound state energy can be tuned to $E \sim E_c$ enabling full control of the scattering length, assuming the open and closed channels have differing magnetic moments (Copyright American Physical Society (2010) [215]).

Figure 2.2 shows a basic two-channel model of this process. At the ultracold temperatures required for BEC experiments collisions in the system occur near zero energy, $E \rightarrow 0$.

If there is a closed channel which contains a bound state with coupling energy E_c then there can be a resonant interaction if $E_c \sim E$. When the two channels have different magnetic moments then an externally applied magnetic field can be used to tune the bound state energy — by manipulating the electron orbitals of the atom, as process known as the Zeeman effect — and thus the asymptotic behaviour of the collision is very sensitive to this resonance and allows for the complete control of the scattering length.

In Ref. [216] a simple expression was derived for the effect of a magnetic field B on the background s-wave scattering length a_{bg} ,

$$a_s(B) = a_{\text{bg}} \left(1 - \frac{\Delta}{B - B_0} \right), \quad (2.7)$$

where $\Delta > 0$ is the width of the resonance and B_0 is the magnetic field at which $E = E_c$ and the scattering length diverges.

2.1.2 Tuning the dipole-dipole interaction

We have already discussed how the local interactions may be tuned by the application of an external magnetic field, however it is also theoretically possible to tune the DDI too, including being able to invert the sign [217].

To understand this first consider the interaction of two dipoles $\hat{\mathbf{e}}_1$ and $\hat{\mathbf{e}}_2$ separated by a distance \mathbf{r} , given by

$$V_{\text{dd}}(\mathbf{r}) = \frac{C_{\text{dd}}}{4\pi} \left(\frac{\hat{\mathbf{e}}_1 \cdot \hat{\mathbf{e}}_2 - 3(\hat{\mathbf{e}}_1 \cdot \hat{\mathbf{r}})(\hat{\mathbf{e}}_2 \cdot \hat{\mathbf{r}})}{r^3} \right). \quad (2.8)$$

Suppose that the orientation of the two dipoles is made to oscillate in time through the application of an external electric or magnetic field, as in Fig. 2.3, such that

$$\hat{\mathbf{e}}_1 = \hat{\mathbf{e}}_2 = (\sin \varphi \cos \Omega t, \sin \varphi \sin \Omega t, \cos \varphi). \quad (2.9)$$

Substituting Eq. (2.9) and $\hat{\mathbf{r}} = (\sin \theta, 0, \cos \theta)$ into Eq. (2.8) gives

$$V_{\text{dd}}(\mathbf{r}) = \frac{C_{\text{dd}}}{4\pi r^3} \left[1 - 3 \left(\sin^2 \theta \sin^2 \varphi \cos^2 \Omega t + \cos^2 \theta \cos^2 \varphi + 2 \sin \theta \sin \varphi \cos \theta \cos \varphi \cos \Omega t \right) \right], \quad (2.10)$$

which after averaging the result over one period of oscillation we obtain

$$\langle V_{\text{dd}}(\mathbf{r}, t) \rangle = \frac{C_{\text{dd}}}{4\pi} \left(\frac{1 - 3 \cos^2 \theta}{r^3} \right) \left[\frac{3 \cos^2 \varphi - 1}{2} \right]. \quad (2.11)$$

It is clear from Eq. (2.11) that through the choice of φ the magnitude of the dipolar po-

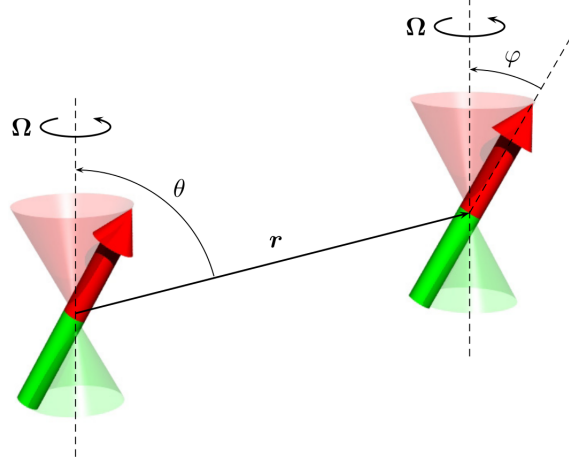


Figure 2.3: Using a rotating field about z the dipole-dipole interaction may be tuned. (IOP Publishing, all rights reserved [67]).

tential is altered by a factor of $(3 \cos^2 \varphi - 1)/2$. If the choice of φ is $\varphi = 0$ then this factor is 1, else for the choice $\varphi = \pi/2$ this factor is $-1/2$; leading to repulsion between dipoles for $\theta = 0$, and attraction between dipoles when $\theta = \pi/2$, converse to the standard dipole-dipole interaction. Thus, if the oscillation period is made to be smaller than the timescale for internal dynamics of the gas (e.g. phonons or collective modes), then the gas effectively experiences this time-averaged DDI. Recently, the Lev group [218] have reported the successful application of this method for a dysprosium gas over very short timescales. We will revisit this effect in Ch. 9.

2.1.3 Fourier transform of the dipole-dipole interaction

Obtaining an expression of the Fourier transform of the DDI involves evaluating the following expression

$$\tilde{V}_{dd}(\mathbf{k}) = \frac{C_{dd}}{4\pi} \int d^3\mathbf{r} \frac{1 - 3 \cos^2 \theta}{r^3} e^{i\mathbf{k} \cdot \mathbf{r}} = \frac{C_{dd}}{4\pi} \int_0^\infty \frac{dr}{r} \int d\Omega (1 - 3 \cos^2 \theta) e^{i\mathbf{k} \cdot \mathbf{r}}, \quad (2.12)$$

where the final expression has been transformed into spherical polar coordinates with $d\Omega = \sin \theta d\theta d\phi$. The integral over the solid angle $d\Omega$ can be carried out using a few substitutions. Firstly, we state an expansion of a plane wave in terms of spherical harmonics $Y_l^m(\hat{\mathbf{r}})$ and spherical Bessel functions $j_l(kr)$, given as

$$e^{i\mathbf{k} \cdot \mathbf{r}} = 4\pi \sum_{l=0}^{\infty} i^l j_l(kr) \sum_{m=-l}^l Y_l^m(\hat{\mathbf{k}})^* Y_l^m(\hat{\mathbf{r}}), \quad (2.13)$$

and the relation $(1 - 3 \cos^2 \theta) = -\sqrt{16\pi/5} Y_2^0(\hat{\mathbf{r}})$, where $\hat{\mathbf{r}} = (\sin \theta \cos \phi, \sin \theta \sin \phi, \cos \theta)$. Using the orthonormality relations for the spherical harmonic functions the only remaining terms over the integral are defined by $\int d\Omega Y_l^m(\hat{\mathbf{r}}) Y_2^0(\hat{\mathbf{r}}) = \delta_{l2} \delta_{m0}$. Thus, the solid angle integral in Eq. (2.12) becomes

$$\int d\Omega (1 - 3 \cos^2 \theta) e^{i\mathbf{k}\cdot\mathbf{r}} = -4\pi j_2(kr) \left[-\sqrt{\frac{16\pi}{5}} Y_2^0(\hat{\mathbf{k}})^* \right] = -4\pi j_2(kr) (1 - 3 \cos^2 \theta_k), \quad (2.14)$$

where θ_k is the angle between \mathbf{k} and the direction of the dipoles, i.e. if the dipoles are polarised along z this would read $\cos \theta_k = k_z/k$. The remaining integration over r can be evaluated with the relation

$$\int_0^\infty dr \frac{j_2(kr)}{r} = \frac{1}{3}. \quad (2.15)$$

Finally, we obtain

$$\tilde{V}_{dd}(\mathbf{k}) = \frac{C_{dd}}{3} (3 \cos^2 \theta_k - 1). \quad (2.16)$$

This form of the DDI will be particularly useful to us when evaluating the dipolar GPE.

2.2 Gross-Pitaevskii theory

2.2.1 Bose gases

We consider a gas of N bosons. A system of identical Bose particles is described by a state vector that is symmetric under exchange of any two particles. A Fock state is a symmetrised state vector $|n_1, n_2, \dots\rangle$, where n_j is the number of particles in the single particle state corresponding to $|\psi_j\rangle$, which itself is a member of some orthonormal basis of single particle states $\{|\psi_j\rangle\}_j$. The vectors $\{|n_1, n_2, \dots\rangle\}_{n_1, n_2, \dots}$ form an orthonormal basis for the symmetric subspace of the tensor product of the individual particle Hilbert spaces, known as the Fock space; hence, the state of a general system of identical Bose particles is described by a superposition of Fock states.

In order to construct general operators for the many-particle system, we define the following so-called creation and annihilation operators

$$\hat{a}_j^\dagger |n_1, n_2, \dots, n_j, \dots\rangle = \sqrt{n_j + 1} |n_1, n_2, \dots, n_j + 1, \dots\rangle, \quad (2.17)$$

$$\hat{a}_j |n_1, n_2, \dots, n_j, \dots\rangle = \sqrt{n_j} |n_1, n_2, \dots, n_j - 1, \dots\rangle. \quad (2.18)$$

The following commutation relations must hold

$$[\hat{a}_j, \hat{a}_k^\dagger] = \delta_{jk}, \quad (2.19)$$

$$[\hat{a}_j, \hat{a}_k] = 0, \quad (2.20)$$

$$[\hat{a}_j^\dagger, \hat{a}_k^\dagger] = 0. \quad (2.21)$$

The first relation tells us that a particle cannot be simultaneously destroyed and created in the same state, however this can happen simultaneously if the operators act on different states. The second (third) relation tells us that any two particles can be simultaneously destroyed (created).

With these ingredients we introduce the Bose field operators

$$\hat{\Psi}^\dagger(\mathbf{r}) = \sum_j \hat{a}_j^\dagger \psi_j^*(\mathbf{r}), \quad (2.22)$$

$$\hat{\Psi}(\mathbf{r}) = \sum_j \hat{a}_j \psi_j(\mathbf{r}). \quad (2.23)$$

The field operators are useful in describing the atomic ensemble, and can be interpreted as creation and annihilation operators for a particle in the position state $|\mathbf{r}\rangle$. In what follows we will evaluate the time-dependence of these operators, under the Heisenberg picture¹, which will eventually lead to the dynamics of the condensate. Following from Eqs. (2.19)-(2.21) the Bose field commutation relations are

$$[\hat{\Psi}(\mathbf{r}), \hat{\Psi}^\dagger(\mathbf{r}')] = \delta(\mathbf{r} - \mathbf{r}'), \quad (2.24)$$

$$[\hat{\Psi}(\mathbf{r}), \hat{\Psi}(\mathbf{r}')] = 0, \quad (2.25)$$

$$[\hat{\Psi}^\dagger(\mathbf{r}), \hat{\Psi}^\dagger(\mathbf{r}')] = 0. \quad (2.26)$$

The second-quantised Hamiltonian for the Bose field operators is given by,

$$\hat{\mathcal{H}} = \int d^3\mathbf{r} \hat{\Psi}^\dagger(\mathbf{r}) \hat{\mathcal{H}}_0 \hat{\Psi}(\mathbf{r}) + \frac{1}{2} \int d^3\mathbf{r} \int d^3\mathbf{r}' \hat{\Psi}^\dagger(\mathbf{r}) \hat{\Psi}^\dagger(\mathbf{r}') V_{\text{int}}(\mathbf{r}, \mathbf{r}') \hat{\Psi}(\mathbf{r}') \hat{\Psi}(\mathbf{r}). \quad (2.27)$$

Here, $V_{\text{int}}(\mathbf{r}, \mathbf{r}')$ is the two-body interaction potential, and

$$\hat{\mathcal{H}}_0 = -\frac{\hbar^2}{2m} \nabla^2 + V_{\text{ext}}(\mathbf{r}), \quad (2.28)$$

is the single-particle Hamiltonian, where $V_{\text{ext}}(\mathbf{r})$ is the external potential. In Eq. (2.27) we read these operators from right to left. So the first term destroys a particle in one state $\hat{\Psi}$, acts upon that particle with the operator $\hat{\mathcal{H}}_0$, which may change the state the particle lies

¹In the Heisenberg picture observables are time-dependent and state vectors are time-independent.

in, and recreates it in the new state with $\hat{\Psi}^\dagger$. Similarly for the second term we remove two particles from their initial states, they interact with some potential V_{int} , and they are then created in their new states.

Using Heisenberg's relation $i\hbar\partial\hat{\Psi}/\partial t = [\hat{\Psi}, \hat{\mathcal{H}}]$ and the commutation relations for the field operators, see Appendix C, we obtain the equation of motion

$$i\hbar\frac{\partial\hat{\Psi}(\mathbf{r}, t)}{\partial t} = \hat{\mathcal{H}}_0\hat{\Psi}(\mathbf{r}, t) + \int d^3\mathbf{r}' \hat{\Psi}^\dagger(\mathbf{r}', t)V_{\text{int}}(\mathbf{r}, \mathbf{r}')\hat{\Psi}(\mathbf{r}', t)\hat{\Psi}(\mathbf{r}, t). \quad (2.29)$$

2.2.2 Mean-field approximation

Bose-Einstein condensation requires macroscopic occupation of a single quantum state, thus it is appropriate to consider a *mean-field* approach. The Bose field operator is decomposed as

$$\hat{\Psi}(\mathbf{r}, t) = \psi(\mathbf{r}, t) + \delta\hat{\Psi}(\mathbf{r}, t), \quad (2.30)$$

where $\psi(\mathbf{r}, t) \equiv \langle\hat{\Psi}(\mathbf{r}, t)\rangle$ is the expectation value of the Bose field operator, and is a classical field approximation, and $\delta\hat{\Psi}$ represents quantum and thermal fluctuations around this value. In the context of BECs, the former quantity is a mean-field order parameter representing the condensed atoms, and is generally referred to as the macroscopic *wavefunction*. The latter quantity describes the dynamics of the non-condensed atoms, induced by thermal and quantum effects. A BEC is therefore a classical state of the atomic field, analogous to the laser being a classical state of the electromagnetic field.

We assume the limit of zero temperature, such that the thermal component of the system is non-existent. Furthermore, due to the weakly-interacting nature ($a_s \ll \lambda_{\text{dB}}$) of the condensate, quantum depletion at zero temperature is expected to be minimal. It is then reasonable to neglect the non-condensed atoms, and consider only the classical field $\hat{\Psi}(\mathbf{r}, t) \rightarrow \psi(\mathbf{r}, t)$. Note that the assumption of zero temperature is generally satisfied for temperatures much less than the transition temperature for condensation. For low-energy scattering the interaction potential $V_{\text{int}}(\mathbf{r}, \mathbf{r}')$ is well described by a pseudo-potential $U(\mathbf{r} - \mathbf{r}')$, hence we make the replacement $V_{\text{int}} \rightarrow U$, with U given by Eq. (2.6).

2.2.3 The dipolar Gross-Pitaevskii equation

Insertion of the classical field wavefunction and the pseudo-potential into Eq. (2.27) leads to the time-dependent equation of motion

$$i\hbar\frac{\partial\psi(\mathbf{r}, t)}{\partial t} = \hat{H}\psi(\mathbf{r}, t) = \left(-\frac{\hbar^2\nabla^2}{2m} + V_{\text{ext}}(\mathbf{r}, t) + gn(\mathbf{r}, t) + \Phi_{\text{dd}}(\mathbf{r}, t)\right)\psi(\mathbf{r}, t), \quad (2.31)$$

where the condensate density at a given point is $n(\mathbf{r}, t) = |\psi(\mathbf{r}, t)|^2$ and we denote the mean-field Hamiltonian \hat{H} . The dipole-dipole contribution to the mean-field energy is

$$\Phi_{\text{dd}}(\mathbf{r}, t) = \int d^3\mathbf{r}' U_{\text{dd}}(\mathbf{r} - \mathbf{r}') |\psi(\mathbf{r}', t)|^2. \quad (2.32)$$

The result of the mean-field treatment is the dipolar Gross-Pitaevskii equation (GPE), first written in this form by Góral and co-authors [219].

Time-independent dipolar Gross-Pitaevskii equation

The chemical potential μ , which is the energy required to add or remove a particle from the system, characterises the ground state energy of the condensate. The sign of the chemical potential tells us whether the local interactions are repulsive, $\mu > 0$, or attractive, $\mu < 0$. Time-independent solutions of the dipolar GPE can be written in the form $\psi(\mathbf{r}, t) = \psi(\mathbf{r}) \exp(-i\mu t/\hbar)$, which after substitution into Eq. (2.31) gives the resulting time-independent equation

$$\mu\psi(\mathbf{r}) = \left(-\frac{\hbar^2 \nabla^2}{2m} + V_{\text{ext}}(\mathbf{r}) + g|\psi(\mathbf{r})|^2 + \Phi_{\text{dd}}(\mathbf{r}) \right) \psi(\mathbf{r}). \quad (2.33)$$

Homogeneous chemical potential

For a homogeneous dipolar Bose gas ($V_{\text{ext}} = 0$), the density, and thus the chemical potential, is constant. This homogeneous density is given the value $|\psi(\mathbf{r})|^2 \equiv |\psi_0|^2 = n_0$ and upon substitution into Eq. (2.33) the homogeneous dipolar chemical potential μ_0 is given by

$$\mu_0 = n_0 g (1 - \varepsilon_{\text{dd}}), \quad (2.34)$$

where the factor $(1 - \varepsilon_{\text{dd}})$ is the correction due to dipoles.

Integrals of motion

There are an infinite number of integrals of motion in the Gross-Pitaevskii model, those with clear physical meaning are the total energy, particle number, and momentum. The inclusion of the latter will be elucidated when necessary, as both linear and angular momentum integrals are employed in this thesis. The total energy of the system can be derived using the variational relation

$$i\hbar \frac{\partial \psi}{\partial t} = \frac{\delta \mathcal{E}}{\delta \psi^*}, \quad (2.35)$$

where \mathcal{E} is the energy density, or energy functional, of the system, and the right-hand side is a functional derivative. Using the dipolar GPE Eq. (2.31) to evaluate the left-hand side of Eq. (2.35) and integrating over ψ^* gives

$$\mathcal{E}[\psi] = \left(\frac{\hbar^2}{2m} |\nabla \psi|^2 + V_{\text{ext}} |\psi|^2 + \frac{g}{2} |\psi|^4 + \frac{1}{2} \Phi_{\text{dd}} |\psi|^2 \right). \quad (2.36)$$

The total energy is then the integral of the energy density over all space

$$E = \int d^3\mathbf{r} \mathcal{E}[\psi]. \quad (2.37)$$

The total number of particles in the system is defined to be

$$N = \int d^3\mathbf{r} |\psi|^2. \quad (2.38)$$

The total momentum of the condensate is defined to be

$$P = \frac{i\hbar}{2} \int_{-\infty}^{\infty} d^3\mathbf{r} [\psi \nabla \psi^* - \psi^* \nabla \psi]. \quad (2.39)$$

Transforming the reference frame

Linear transformation

When describing moving objects in a system it is often useful to transform into a reference frame moving with the object. This is achieved by including the linear momentum operator in the GPE Hamiltonian defined by $\hat{\mathbf{p}} = -i\hbar\nabla$. Often a flow is taken to be along a single axis, with velocity vector \mathbf{u} . For example, to simulate a flow with velocity $\mathbf{u} = (0, 0, u_z)$ the GPE becomes

$$i\hbar \frac{\partial \psi}{\partial t} = \left[\hat{H} - i\hbar u_z \frac{\partial}{\partial z} \right] \psi. \quad (2.40)$$

Rotating frame

Similarly, to obtain rotating solutions the GPE is adjusted through addition of the angular momentum operator. In classical mechanics the angular momentum vector is defined as the cross product of the position and momentum vectors, i.e. $\mathbf{L} = \mathbf{r} \times \mathbf{p}$. In quantum mechanics these quantities are operators, defined as $\hat{\mathbf{r}} = \mathbf{r}$ and $\hat{\mathbf{p}} = -i\hbar\nabla$, thus the angular momentum operator becomes

$$\hat{\mathbf{L}} = \hat{\mathbf{r}} \times \hat{\mathbf{p}}, \quad (2.41)$$

which written out elementwise reads

$$\hat{L}_x = -i\hbar \left(y \frac{\partial}{\partial z} - z \frac{\partial}{\partial y} \right), \quad \hat{L}_y = -i\hbar \left(z \frac{\partial}{\partial x} - x \frac{\partial}{\partial z} \right), \quad \hat{L}_z = -i\hbar \left(x \frac{\partial}{\partial y} - y \frac{\partial}{\partial x} \right). \quad (2.42)$$

If the angular frequency is given by $\Omega = (0, 0, \Omega_z)$, corresponding to rotation about the z axis, then the GPE becomes

$$i\hbar \frac{\partial \psi}{\partial t} = \left[\hat{H} - i\hbar \Omega_z \left(x \frac{\partial}{\partial y} - y \frac{\partial}{\partial x} \right) \right] \psi. \quad (2.43)$$

Hydrodynamic equations

In Ch. 1 we touched upon the similarities between the GPE and classical fluid equations. This comparison is brought to light through the Madelung transformation [55], which is akin to separating the density and phase contributions as

$$\psi(\mathbf{r}, t) = \sqrt{n(\mathbf{r}, t)} \exp[iS(\mathbf{r}, t)], \quad (2.44)$$

where $n(\mathbf{r}, t)$ is the fluid density and $S(\mathbf{r}, t)$ is the macroscopic phase factor. The velocity of the condensate is defined as

$$\mathbf{v}(\mathbf{r}, t) = \frac{\hbar}{m} \nabla S(\mathbf{r}, t). \quad (2.45)$$

Substituting equations (2.44) and (2.45) into the GPE gives two equations, one from equating the imaginary contributions,

$$\frac{\partial n}{\partial t} + \nabla \cdot (n\mathbf{v}) = 0, \quad (2.46)$$

and the other from equating the real components,

$$m \frac{\partial \mathbf{v}}{\partial t} + \nabla \left(V_{\text{ext}} + n g + \Phi_{\text{dd}} + \frac{1}{2} m v^2 - \frac{\hbar^2}{2m\sqrt{n}} \nabla^2 \sqrt{n} \right) = 0. \quad (2.47)$$

Here, we may interpret Eq. (2.46) as the continuity equation and Eq. (2.47) as an inviscid compressible Euler equation for the superfluid². The final term appearing in the quantum Euler equation does not appear in its classical counterpart, which represents the quantum

²The flow is irrotational, $\nabla \times \mathbf{v} = 0$, so the $\mathbf{v} \cdot \nabla \mathbf{v}$ contribution to the Euler equation is zero and the material derivative becomes

$$\frac{D\mathbf{v}}{Dt} \equiv \frac{\partial \mathbf{v}}{\partial t}. \quad (2.48)$$

pressure³.

Extensions to the dipolar Gross-Pitaevskii equation

In 2016 studies into the collapse of dipolar Bose-Einstein condensates [221–223], the mechanism for which we will cover in more detail in Sec. 2.5, found that the mean-field theory did not accurately predict the behaviour when crossing into a parameter regime where one would expect collapse. Instead, after an instability was induced the condensate density did not increase indefinitely but rather saturated to a fixed value where the cloud became stable and self confined. In order to describe this effect we need to revisit the previous analysis keeping the quantum fluctuations contribution $\delta\hat{\Psi}$ we threw away in Eq. (2.30) as this is responsible for this new stabilisation mechanism [224]. If we consider energy corrections to first order they result in a positive energy contribution which adds to the repulsive interactions. This correction is the famous Lee-Huang-Yang correction [225] with an additional dependence on the dipolar strength ε_{dd} , and gives a shift of the ground state energy of [226, 227]

$$\Delta E(\mathbf{r}) = \frac{64}{15} g n^2(\mathbf{r}) Q_5(\varepsilon_{\text{dd}}) \sqrt{\frac{n(\mathbf{r}) a_s^3}{\pi}}, \quad (2.49)$$

where the auxiliary function $Q_l(x) = \int_0^1 du (1 - x + 3xu^2)^{l/2}$ is monotonic and grows from $Q_5(0) = 1$ up to $Q_5(1) = 3\sqrt{3}/2 \approx 2.6$. Often an approximation for this function is used, given as $Q_5(x) \approx 1 + \frac{3}{2}x^2$. This approximation works for $0 < \varepsilon_{\text{dd}} \lesssim 2$, as long as one discards the imaginary component of the $Q_5(\varepsilon_{\text{dd}})$ function for $\varepsilon_{\text{dd}} > 1$ [228]. This energy shift scales as $\Delta E \propto n^{5/2}$ and therefore has a dominating effect when the density is large, as one would expect during a collapse.

By taking the derivative of the energy density with respect to the number density one can derive the shifted chemical potential, and from this the often called generalised GPE (gGPE), given by

$$i\hbar \frac{\partial \psi(\mathbf{r}, t)}{\partial t} = \left(-\frac{\hbar^2 \nabla^2}{2m} + V_{\text{ext}}(\mathbf{r}, t) + g n(\mathbf{r}, t) + \Phi_{\text{dd}}(\mathbf{r}, t) + \gamma_{\text{QF}} |\psi|^3 \right) \psi(\mathbf{r}, t), \quad (2.50)$$

where

$$\gamma_{\text{QF}} = \frac{32}{3} g \sqrt{\frac{a_s^3}{\pi}} \left(1 + \frac{3}{2} \varepsilon_{\text{dd}}^2 \right). \quad (2.51)$$

The inclusion of this term significantly affects the condensate dynamics at high density,

³See Ref. [220] for a more detailed discussion on this.

for example, when in the regime of a collapse instability. However, it does not greatly affect the predicted parameter region for stability. Therefore, in this thesis we will not employ the gGPE unless stated.

2.3 Time-independent solutions

2.3.1 Non-interacting regime

For the ideal (non-interacting) gas the GPE reduces to the Schrödinger equation (the solutions of which are well documented and are dependent on the choice of potential). The free particle solution ($V_{\text{ext}} = 0$) has a continuous wavefunction solution given by a plane wave and energy

$$E = \frac{\hbar^2 k^2}{2m} . \quad (2.52)$$

Taking the harmonic oscillator potential in the non-interacting gas we obtain the standard harmonic oscillator eigenfunctions, the Hermite polynomials. It has been shown for non-dipolar gases that in the low interaction limit, meeting the condition $Na_s/\bar{l} \ll 1$, where $\bar{l} = \sqrt{\hbar/m\bar{\omega}}$ is the mean harmonic oscillator length and $\bar{\omega} = (\omega_x\omega_y\omega_z)^{1/3}$, the eigenstates are similar to the non-interacting case [41]. The harmonic oscillator groundstate for potential $V_{\text{ext}}(\mathbf{r}) = (m/2)(\omega_x^2 x^2 + \omega_y^2 y^2 + \omega_z^2 z^2)$ is

$$n(\mathbf{r}) = N \left(\frac{m\bar{\omega}}{\pi\hbar} \right)^{3/2} \exp \left[-\frac{m}{\hbar} (\omega_x x^2 + \omega_y y^2 + \omega_z z^2) \right] . \quad (2.53)$$

2.3.2 Contact interactions

The non-dipolar Gross-Pitaevskii equation was derived contemporaneously by Gross [46, 47] and Pitaevskii [48, 49] in 1961, and has since become the workhorse for quantum gas modelling. The GPE, written here as

$$i\hbar \frac{\partial \psi(\mathbf{r}, t)}{\partial t} = \left(-\frac{\hbar^2 \nabla^2}{2m} + V_{\text{ext}}(\mathbf{r}, t) + g|\psi(\mathbf{r}, t)|^2 \right) \psi(\mathbf{r}, t) , \quad (2.54)$$

can be related to its dipolar counterpart in the limit of $\varepsilon_{\text{dd}} = 0$.

The GPE resembles the Schrödinger equation with an added nonlinear $|\psi|^2$ term describing atomic interactions. The GPE is analogous to the cubic nonlinear Schrödinger equation (NLSE)⁴ employed in nonlinear optics to describe media with Kerr nonlinearity [229].

⁴Interestingly, the GPE (and hence NLSE) is not a nonlinear equation. It is semilinear, as the term with the highest order derivative is linear, but contains a nonlinear term.

Hard-wall solution

Consider stationary solutions of Eq. (2.54) in a homogeneous system ($V_{\text{ext}} = 0$) with repulsive interactions ($g > 0$), then the GP Hamiltonian consists of two terms: the kinetic and the self-interaction energies. On dimensional grounds these two terms are balanced by the length-scale

$$\xi = \frac{\hbar}{\sqrt{mn}g} = \frac{1}{\sqrt{4\pi n a_s}}. \quad (2.55)$$

This quantity is known as the *healing length* as it is the typical lengthscale over which the condensate density relaxes to its homogeneous value from a local perturbation. Typically ξ is on the order of $1\mu\text{m}$. For example, taking the boundary condition $\psi(0) = 0$, representing a hard-wall boundary, the fluid transitions from zero at the origin to a real homogeneous constant $\psi_0 = \sqrt{\mu_0/g}$ over a small distance on the order of ξ . For a boundary at $z = 0$, the solution in the z -direction has the form

$$\psi(z) = \sqrt{\frac{\mu_0}{g}} \tanh\left(\frac{z}{\xi}\right). \quad (2.56)$$

This constant is ubiquitous in the context of superfluids. Indeed, any perturbation to the fluid such as solitons in 1D systems and vortex lines and tubes in 3D systems will heal to the homogeneous density of the system over this naturally occurring distance. In fact, Eq. (2.56) is also the exact stationary dark soliton solution.

Thomas-Fermi solution

In the limit of large repulsive interactions $Na/\bar{l} \gg 1$ the effect of the kinetic energy term is negligible in comparison to the interaction energy, i.e.

$$gn(\mathbf{r})\psi(\mathbf{r}) \gg \left| \frac{\hbar^2 \nabla^2}{2m} \psi(\mathbf{r}) \right|, \quad (2.57)$$

and thus it becomes reasonable to neglect the kinetic energy entirely. This approximation is known as the Thomas-Fermi approximation and has analytic solution

$$n(\mathbf{r}) = \begin{cases} [\mu - V_{\text{ext}}(\mathbf{r})]/g, & \text{for } \mu \geq V_{\text{ext}}(\mathbf{r}), \\ 0, & \text{elsewhere.} \end{cases} \quad (2.58)$$

For the case of harmonic confinement the solution is an inverted paraboloid with width in each dimension independently set by the corresponding trap frequency. The perimeter of the condensate is found by setting $V_{\text{ext}}(\mathbf{r}) = \mu$, which is used to find the Thomas-Fermi

radii in each dimension. For example, for the spherically symmetric case with single trap frequency ω the Thomas-Fermi radius is $R_{\text{TF}} = \sqrt{2\mu/m\omega^2}$. Equation (2.58) is accurate up to the edges of the cloud, where this approximation becomes discontinuous, and in reality the density exhibits a smooth transition to zero density over the distance of a healing length. This solution is considerably wider than the non-interacting solution in Eq. (2.53) and broadens with increasing g and N .

2.3.3 Dipolar interactions

Dipolar Thomas-Fermi solution

Remarkably, the extension of the Thomas-Fermi analysis is possible when including the dipolar interaction. This relies on a clever trick allowing the dipolar potential to be rewritten in terms of an appropriate electrostatic potential. Upon evaluating the dot product in Eq. (2.8) we can write

$$\begin{aligned} U_{\text{dd}}(\mathbf{r}) &= C_{\text{dd}} \sum_{i,j}^3 \frac{\hat{e}_i \hat{e}_j \delta_{ij} - 3(\hat{r}_i \hat{e}_i)(\hat{r}_j \hat{e}_j)}{4\pi r^3} \\ &= C_{\text{dd}} \sum_{i,j}^3 \hat{e}_i \left(\frac{\delta_{ij} - 3\hat{r}_i \hat{r}_j}{4\pi r^3} \right) \hat{e}_j \\ &= C_{\text{dd}} \hat{\mathbf{e}}^T \mathbf{D}(\mathbf{r}) \hat{\mathbf{e}}, \end{aligned} \quad (2.59)$$

where we have defined the rank 2 tensor

$$[\mathbf{D}(\mathbf{r})]_{ij} = \frac{\delta_{ij} - 3\hat{r}_i \hat{r}_j}{4\pi r^3}. \quad (2.60)$$

In a book by Craig and Thirunamachandran [230], it is derived that \mathbf{D} can be rewritten as

$$[\mathbf{D}(\mathbf{r})]_{ij} = -\nabla_i \nabla_j \frac{1}{4\pi r} - \frac{1}{3} \delta_{ij} \delta(\mathbf{r}). \quad (2.61)$$

Upon substitution of this back into Eq. (2.59), the dipolar potential becomes

$$\Phi_{\text{dd}}[n(\mathbf{r})] = -C_{\text{dd}} \sum_{i,j}^3 \hat{e}_i \hat{e}_j \left(\nabla_i \nabla_j \phi[n(\mathbf{r})] + \frac{\delta_{ij}}{3} n(\mathbf{r}) \right), \quad (2.62)$$

with

$$\phi[n(\mathbf{r})] = \frac{1}{4\pi} \int d\mathbf{r}' \frac{n(\mathbf{r}')}{|\mathbf{r} - \mathbf{r}'|}. \quad (2.63)$$

The form of ϕ here is instantaneously recognisable as the electrostatic potential due to a charge distribution n , or the gravitational potential due to a mass distribution n . Writing the DDI in the form of Eq. (2.62) explicitly separates the potential into the long-range (first term) and short-range (second term) contributions, the latter of which contribute to the definition of the homogeneous chemical potential in Sec. 2.2.3. In its current form Eq. (2.62) doesn't seem like much of an improvement over the usual DDI, however when we consider dipoles polarised along the z -axis such that $\hat{\mathbf{e}} = (0, 0, 1)$, for example, the equation simplifies down to

$$\Phi_{\text{dd}}[n(\mathbf{r})] = -C_{\text{dd}} \left(\frac{\partial^2}{\partial z^2} \phi[n(\mathbf{r})] + \frac{1}{3} n(\mathbf{r}) \right). \quad (2.64)$$

The dipolar Thomas-Fermi density will be a solution to the time-independent equation

$$V_{\text{ext}}(\mathbf{r}) + \Phi_{\text{dd}}(\mathbf{r}) + g n(\mathbf{r}) = \mu. \quad (2.65)$$

In order to find the dipolar Thomas-Fermi solutions we start with an ansatz for the density

$$n(\mathbf{r}) = n_0 \left(1 - \frac{x^2}{R_x^2} - \frac{y^2}{R_y^2} - \frac{z^2}{R_z^2} \right), \quad \text{for } n(\mathbf{r}) \geq 0, \quad (2.66)$$

where $n_0 = 15N/8\pi R_x R_y R_z$ and here we expect the Thomas-Fermi radii to be distorted by magnetostriction (electrostriction), compared to their non-dipolar counterparts.

Substituting the above equation into Eq. (2.64) remarkably supports an analytic solution, which is also parabolic [231, 232]. This solution is an extension of 19th century astrophysics [233–235], showing that any polynomial density will yield a dipolar potential of the same degree. So, for the ansatz Eq. (2.66), Eq. (2.65) becomes [232, 236]

$$\begin{aligned} \mu = 3g\epsilon_{\text{dd}} \frac{n_0 \kappa_x \kappa_y}{2R_z^2} & \left[R_z^2 \beta_{001} - \beta_{101} x^2 - \beta_{011} y^2 - 3\beta_{002} z^2 \right] \\ & + \frac{1}{2} m (\omega_x^2 x^2 + \omega_y^2 y^2 + \omega_z^2 z^2) + \frac{g n_0}{R_z^2} \left(R_z^2 - \frac{x^2}{\kappa_x^2} - \frac{y^2}{\kappa_y^2} - z^2 \right), \end{aligned} \quad (2.67)$$

where $\kappa_x = R_x/R_z$ and $\kappa_y = R_y/R_z$ are the aspect ratios of the condensate and

$$\beta_{ijk} = \int_0^\infty \frac{ds}{(\kappa_x^2 + s)^{i+1/2} (\kappa_y^2 + s)^{j+1/2} (1+s)^{k+1/2}}, \quad (2.68)$$

for integers i, j, k . Comparing coefficients of x^2 , y^2 , and z^2 in Eq. (2.66) and (2.67) leads to

three self-consistency relations,

$$\kappa_x^2 = \frac{\omega_z^2}{\omega_x^2} \frac{1 + \varepsilon_{\text{dd}} \left(\frac{3}{2} \kappa_x^3 \kappa_y \beta_{101} - 1 \right)}{\zeta}, \quad (2.69)$$

$$\kappa_y^2 = \frac{\omega_z^2}{\omega_y^2} \frac{1 + \varepsilon_{\text{dd}} \left(\frac{3}{2} \kappa_y^3 \kappa_x \beta_{011} - 1 \right)}{\zeta}, \quad (2.70)$$

$$R_z^2 = \frac{2gn_0}{m\omega_z^2} \zeta, \quad (2.71)$$

where $\zeta = \left[1 - \varepsilon_{\text{dd}} \left(1 - 9\kappa_x \kappa_y \beta_{002}/2 \right) \right]$. Solving Eqs. (2.69)-(2.71) gives the dipolar Thomas-Fermi radii for this system.

2.3.4 Unusual ground states

Numerical simulations of the dipolar GPE have often found that the Thomas-Fermi approximation is inappropriate. As we will discuss in Sec. 2.5 the DDI can cause the condensate to become unstable, and in this case the kinetic energy term becomes important. Here we briefly review some of the numerical studies of the full dipolar GPE that have taken place, and relate to experiments when appropriate.

Red blood cell

The Bohn group found that for regimes with cylindrical symmetry the ground state density resembles a red blood cell [237], as shown in Fig. 2.4. Here, the polarising field is aligned the long axis of the trap and there is azimuthal repulsion pushing the region of high density radially outward, reducing the repulsive side-by-side DDI energy.



Figure 2.4: Isosurface of the biconcave ground state density for a condensate with dipoles polarised in the tight direction, with trap aspect ratio $\omega_z/\omega_\rho \approx 8$. (Copyright (2007) by The American Physical Society [237]).

Multi-peaked structures

The above work assumed cylindrical symmetry, however breaking that allows such ground states more generally known as "density-oscillating ground states", which the red blood cell state is an example of. Investigations into the effect of varying all three trap frequencies was undertaken by Refs. [238, 239], where they found density-oscillating ground state solutions of multiple types, visualised in Fig. 2.5, categorised into the following

Type I Normal (without density oscillations).

Type II Density-oscillating condensate with two peaks in the x direction. This is further sub-categorised into (a) simple two peak structures and (b) two peaks with a biconcave crater.

Type III Density-oscillating condensate with two peaks in the y direction. This can also be sub-categorised like Type II, but this is not shown.

Type IV Density-oscillating condensate with four peaks, two in both x and y .

Type V Density-oscillating condensate that is biconcave, but without additional peaks: the red blood cell state.

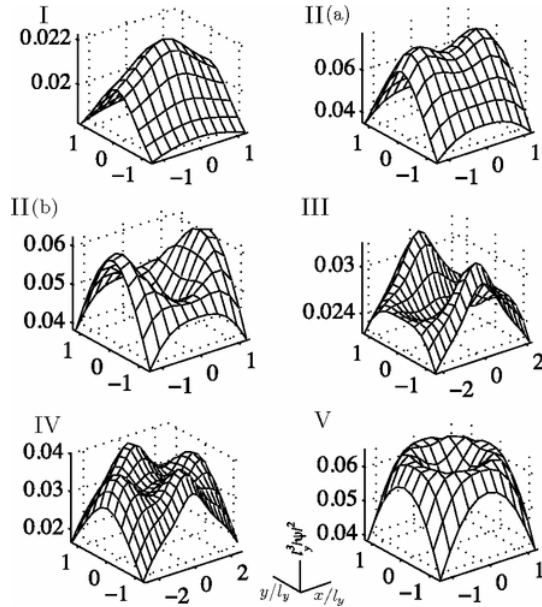


Figure 2.5: Central slice of the ground state density in the xy plane. The list of condensate types is in the main text. (Copyright (2012) by The American Physical Society [239]).

Interaction with a hard-wall

Spatial density oscillations also occur in other trap geometries, for example Ref. [240] considered an infinite square well along the x and y axes, with harmonic trapping in z . Such

a potential can be experimentally realised using a tightly focussed light sheet [50]. The result of their work is displayed in Fig. 2.6, they found that near to the hard-wall the condensate undergoes pronounced density oscillations.



Figure 2.6: Isosurface of the ground state density for a condensate with a box-trap potential in both x and y , and harmonic trapping in z . (Copyright (2010) by The American Physical Society [240]).

Dumbbell

There has also been investigation into the possible ground state solutions in the anti-dipole $C_{dd} < 0$ regime. Recall in this regime the general dipole behaviour is reversed, such that side-by-side dipoles attract one another. Reference [240] found that in a cigar shape geometry the ground state density can resemble a dumbbell-shape, as seen in Fig. 2.7. Here the interaction energy is reduced by the head-to-tail dipoles repelling each other, such that there is axial separation into two high density structures.



Figure 2.7: Isosurface of the ground state density for a condensate with anti-dipoles polarised in the long direction, with trap aspect ratio $\omega_z/\omega_\rho \approx 0.3$. (Copyright (2010) by The American Physical Society [240]).

Stable Rosensweig structure

Theoretical work has also explored two component systems, which highlighted the link between ferrofluids and dipolar BECs for the first time. Reference [241] found an exotic ground state which resembles the Rosensweig instability from Fig. 1.4 by solving a two

component dipolar GPE, where one component has strong DDIs and the other is a non-dipolar condensate, as shown in Fig. 2.8. They found by tuning the miscibility — a parameter describing how well the two components mix — of the two condensates they could find new types of ground state tuned entirely by the dipoles.

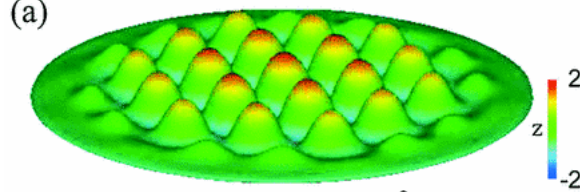


Figure 2.8: Isosurface of the dipolar component ground state, shown forming a hexagonal component reminiscent of the Rosensweig instability. (Copyright (2009) by The American Physical Society [241]).

Labyrinth structure

Other works on two-component condensates have also found labyrinthine structures between the two condensates. Reference [241] were the first to discover this effect in their two component work as described above. Since then the stability and miscibility of two component (both dipolar) two dimensional labyrinthine condensates has been assessed in Ref. [242], as shown in Fig. 2.9.

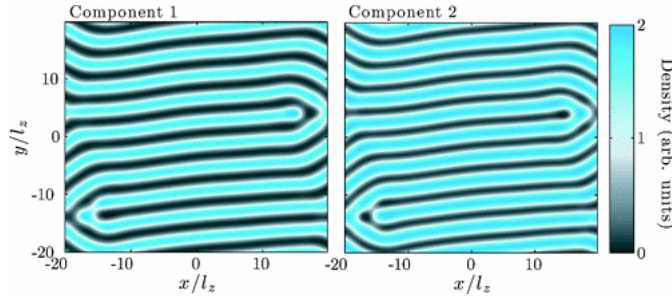


Figure 2.9: Ground state of a two component system showing immiscibility. (Copyright (2012) by The American Physical Society [242]).

Single quantum droplet

In 2015 Petrov showed that quantum fluctuations in a Bose-Bose gas are responsible for a quantum mechanical stabilisation of a collapsing gas [243], building on earlier work predicting the same behaviour from the competition between two- and three-body interactions [244]. This prediction requires a correction on the mean-field level, however quantum Monte-Carlo simulations show that this phenomenon is inherent in the many-body formalism of BECs [245].

The stabilisation quantum fluctuations provides gives a new type of state called a *droplet*. This state is a high density self-bound liquid stabilised by two competing contributions — an attraction from the inter-particle interactions and the repulsion arising from quantum fluctuations. By considering a toy model for the energy per unit volume as

$$\frac{E}{V} = \alpha n^2 + \beta n^{5/2}, \quad (2.72)$$

in the case of $\alpha/\beta < 0$ a liquid-like state is achieved. In dipolar gases this inequality is satisfied for $R_r/R_z \ll 1$ and $\varepsilon_{dd} > 1$, where R_r is the axial width and R_z is the long-axis length if the dipoles are oriented along z .

The first Bose-Bose “macrodroplet” — a single high density droplet — was observed in late 2017 by two independent groups using the same method [246, 247]. Starting with two ^{39}K Bose-Einstein condensates in hyperfine states $|\uparrow\rangle \equiv |F, m_F\rangle = |1, -1\rangle$ and $|\downarrow\rangle = |1, 0\rangle$, where F is the total angular momentum and m_F its projection, and by tuning the residual mean-field interaction $\delta a = a_{\uparrow\downarrow} + \sqrt{a_{\uparrow\uparrow}a_{\downarrow\downarrow}}$ to satisfy $\delta a < 0$ a long-lived self-bound droplet was observed. The findings of these experiments are also seen with quantum Monte-Carlo methods [248].

Returning to dipolar gases, quantum droplets arise from the competition from the mean-field and beyond mean-field effects, without having to consider two component gases. In 2016 macrodroplets were observed in dysprosium [222] and erbium [223]. Numerical work undertaken by Bisset *et al.* [228] showed that in order to obtain a single macrodroplet in the ground state, a specific experimental procedure had to be undertaken. First, a ground state gaseous BEC is created in a highly prolate geometry, then the trapping potential is reduced until the condensate is in a weakly prolate geometry — this step is introduced to avoid a bistable region — finally the scattering length is reduced until the condition $\alpha/\beta < 0$ is met. Once the condition for a droplet is met, the trapping potential is slowly turned off, and it is seen that the droplet is self-bound and stable in free space, as shown in Fig. 2.10. There have been a number of numerical studies into the stability [249] and collective excitation frequencies [250] of single droplets, and recently the scissors mode — the rocking back-and-forth of a BEC quickly rotated by an angle θ — of a quantum droplet has been experimentally probed [251].

2.4 Excitations in BECs

In this section we explore different types of excitations in a dipolar BEC. The elementary excitations are small surface perturbations and are carriers or dissipation in the superfluid. Theoretical progress on the effect of non-local interactions on shape excitations such as solitons and vortices is also reviewed.

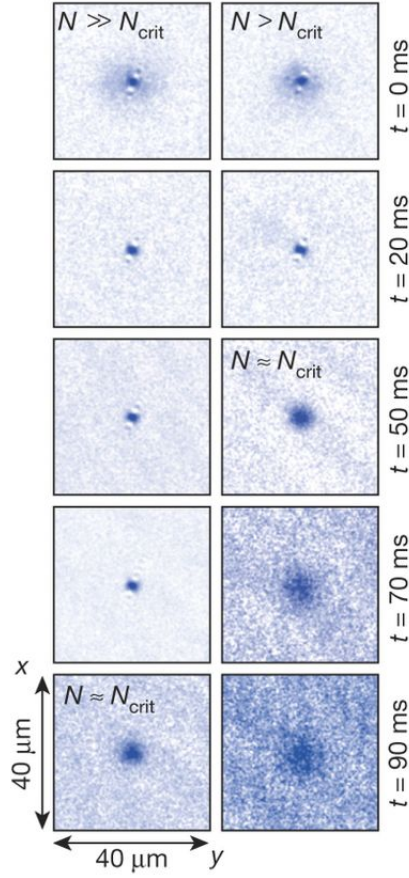


Figure 2.10: Time-of-flight expansion dynamics of a single quantum droplet in a dysprosium gas. For atom number greater than a critical number $N > N_{\text{crit}}$ the condensate is in the liquid phase. As the atom number decreases due to three-body interaction effects the droplet melts into a gas and expands. (Copyright (2016) by Springer Nature [222]).

2.4.1 Elementary excitations

In 1947 Bogoliubov proposed splitting the mean-field wavefunction into two contributions: the macroscopically occupied condensate described by a complex mean-field $\psi_0(\mathbf{r})$ and weak perturbations describing small-scale excitations to the background $\delta\psi(\mathbf{r}, t)$ [36], a theory later applied to superconductivity of metals by de Gennes [252]. This gives a trial wavefunction

$$\psi(\mathbf{r}, t) = [\psi_0(\mathbf{r}) + \delta\psi(\mathbf{r}, t)] e^{-i\mu t/\hbar}. \quad (2.73)$$

Substitution of (2.73) into (2.31) and linearising gives the dispersion relation for the low energy elementary excitations. We can link the energy of the excitations to their frequency through $E(\mathbf{k}) = \hbar\omega(\mathbf{k})$. This derivation is undertaken in full in Appendix A. Here, we state the result for the homogeneous BEC,

$$E(\mathbf{k}) = \sqrt{\frac{\hbar^2 k^2}{2m} \left\{ \frac{\hbar^2 k^2}{2m} + 2n_0 \tilde{U}(\mathbf{k}) \right\}}, \quad (2.74)$$

where n_0 is the density and $\tilde{U}(\mathbf{k})$ is the Fourier transform of the interparticle interaction pseudo-potential. Using Eq. (2.16) the dispersion relation becomes

$$E(\mathbf{k}) = \sqrt{\frac{\hbar^2 k^2}{2m} \left\{ \frac{\hbar^2 k^2}{2m} + 2n_0[g + g_{\text{dd}}(3 \cos^2 \theta_k - 1)] \right\}}. \quad (2.75)$$

Phonons and free particles

Consider two limiting cases of equation (2.75), firstly in the limit of large momenta $k \gg 1$ we obtain the free particle dispersion relation

$$E_{k \gg 1} = \frac{\hbar^2 k^2}{2m}. \quad (2.76)$$

i.e. the effects of particle interactions become negligible.

In the opposite limit, $k \ll 1$ the dispersion relation becomes

$$E_{k \ll 1} = \hbar k c, \quad (2.77)$$

where these excitations are phonons (sound waves) propagating at speed of sound

$$c = \sqrt{\frac{n}{m} [g + g_{\text{dd}}(3 \cos^2 \theta_k - 1)]}. \quad (2.78)$$

This speed of sound is anisotropic, as seen by the θ_k dependence above, a feature that has been experimentally measured in chromium [88] and dysprosium [253].

Rotons and maxons

In non-dipolar gases the story of elementary excitations ends with phonons and free particles. However, in dipolar gases there is another feature: the roton minimum. Studies on the theory of superfluidity in liquid ^4He by Landau in the 1940s brought forward the idea of phonons and rotons as elementary excitations of the superfluid phase. The “roton” is an elementary particle found at a local minimum in the dispersion relation $E = \Delta + \hbar^2(k - k_c)^2/2\mu$ where Δ is the height of the local minimum, k_c is the average roton wavenumber and μ is a constant determining the curvature. The next step that allowed for the accurate comparison between theory and experiments wasn’t made until 1954 when Feynman derived a relationship between the dispersion relation and the static structure factor $S(k)$, which relates the observed diffracted intensity per atom to that produced by a single scattering unit, to be $E = \hbar^2 k^2 / 2m S(k)$ [254]. Measurements from neutron diffraction experiments of the static structure factor were then used to support Landau’s prediction, as shown in Fig. 2.11. Rotons were originally named after their predicted man-

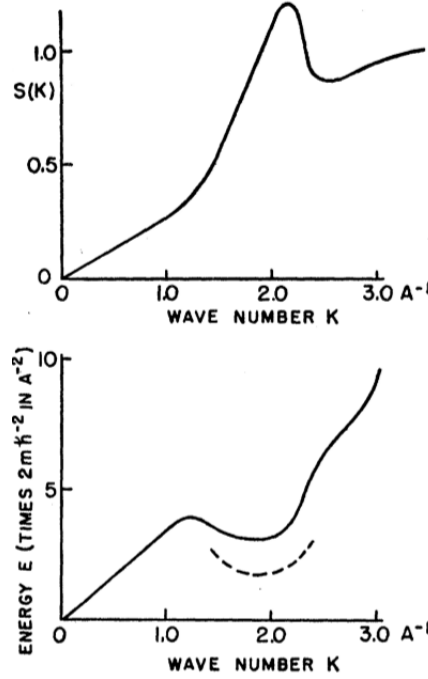


Figure 2.11: Top: The static structure factor as determined from neutron scattering experiments (the data was extrapolated to $k \rightarrow 0$). Bottom: The excitation spectrum obtained using $E = \hbar^2 k^2 / 2mS(k)$, which has a clear minimum corresponding to Landau's rotons. Theoretical predictions for the true minimum are given by the dashed line. (Copyright (1954) by The American Physical Society [254]).

ifestation as vortices, however this has never been experimentally confirmed. Excitations at the maximum occurring before the roton are known as maxons, completing the roton-maxon dispersion relation.

The roton minimum is a precursor to solidity. The critical wavelength, $\lambda_c = 2\pi/k_c$, tells us that the lowest energy configuration for the particles is a crystalline structure with lattice separation λ_c , called a supersolid⁵. A requirement for such systems is high density and strong interactions in order to reach the strongly correlated regime. If the interactions become so strong that the roton minimum touches zero energy the mode goes *soft*. This is how the system becomes unstable, which we will cover in Sec. 2.5.

Rotons in dipolar systems

In dipolar gases the roton can only appear if there is a trapping potential in at least one dimension. In 2003 it was shown that the roton minimum can occur in weakly interacting quasi-2D dipolar gases [256]. The roton minimum has also been shown to exist in fully trapped 3D pancake gases [237, 257] and in quasi-1D geometries [258]. The roton minimum in these systems originates from the fact that at intermediate momenta one has a local structure produced by the tendency of atoms to stay apart. In Fig. 2.12(a) we plot the typical excitation spectrum for a homogeneous quasi-1D condensate, with parameters

⁵Helium is a highly incompressible liquid and the strong inter-atomic forces would act against any crystallisation, however in the case of extremely high pressures (~ 25 atmospheres of pressure [255]) crystalline helium has been predicted.

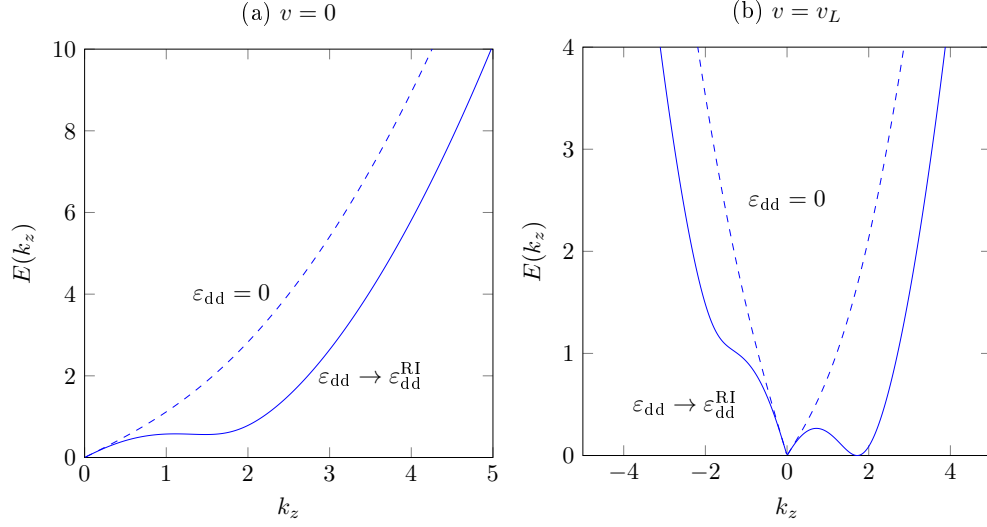


Figure 2.12: (a) Typical excitation spectrum of a quasi-1D condensate in a stationary frame. The value $\epsilon_{dd}^{\text{RI}}$ is representative of a typical value exhibiting a roton minimum. This spectrum is symmetric in k . (b) The same parameters as in (a) but the fluid is now flowing with some velocity $v = v_L$.

chosen to exhibit the roton minimum. The interplay between the short and long-range interactions required to generate this state is the discussion in Ch. 5.

In a landmark experiment undertaken in Innsbruck in 2018 the population of the roton mode was measured for the first time in a quantum gas [259]. The roton is observed after an s-wave interaction quench into an unstable regime, and through taking images of 2D density slices through the condensate they reconstruct the 2D momentum density. By measuring the population growth of a well-defined finite momentum at symmetric peaks in the momentum distribution the softening rate can be extracted and the authors find a universality constraint relating this time and the final scattering length [259].

Superfluidity

A superfluid is characterised by dissipationless flow, which was first observed in liquid ^4He experiments. Landau's proposal to explain the theory of superfluidity is the existence of some critical velocity,

$$v_L = \min_k \left[\frac{E(k)}{\hbar k} \right], \quad (2.79)$$

below which a moving obstacle cannot promote elementary excitations. This is due to the requirement of simultaneous momentum and energy conservation [34]. The breakdown of superfluidity occurs when a single mode touches the zero energy axis, thus inducing

dissipation, i.e. the creation of low energy quasi-particles. If a superfluid is flowing down a pipe with velocity v the excitation spectrum is rotated through

$$E(k) \rightarrow E(k) - \hbar k v, \quad (2.80)$$

where if the condition $E(k) - \hbar k v > 0$ is met the flow is dissipationless, however if broken elementary particles are promoted causing dissipation. A superfluid with a rotonic dip in the dispersion relation has a lower critical velocity than a superfluid with a linear dispersion, as seen in Fig. 2.12(b).

Theoretical works showed this effect is embedded in the dipolar GPE. Ref. [257] theoretically investigated the dragging of a blue-detuned laser beam through a trapped purely dipolar condensate at different speeds and observed the ensuing occupation of depleted atoms due to the presence of a roton lowering the critical velocity. The same group repeated this work with the dipoles polarised in the plane, they found an anisotropic dispersion relation and anisotropic superfluid critical velocity [260].

Anisotropy in the excitation spectrum has since been seen experimentally. Bismut et al. [88] performed Raman-Bragg spectroscopy for a ^{52}Cr BEC and found some experimental evidence for an anisotropic excitation spectrum. In 2018 the Pfau group [253] measured the same effect in ^{162}Dy , moving an attractive laser beam through the condensate observing anisotropy in superfluid flow.

2.4.2 Dipolar vortices

In dipolar condensates vortices have been found to exhibit novel behaviour arising from the anisotropy of the DDI and take on a modified density profile due to the presence of the roton [261], and the role of trap geometry on stability in fully 3D systems has been explored [262], as shown in Fig. 2.13. Exciting theoretical work exploring the generation of vortices inside dipolar quantum droplets has also been undertaken [263].

Generally speaking vortices in experiments are found through the fast rotation of the condensate, which leads to the generation of lattices. Dipolar vortices are no different; in non-dipolar condensates the vortices align themselves in a triangular, or Abrikosov, lattice, whereas in dipolar systems the orientation is dependent on the interaction strength, with vortices tending to align in lines along the polarisation angle. Ref. [264] solved the 3D dGPE and looked at the effect of changing the trap aspect ratio; upon breaking cylindrical symmetry they found that there is some critical rotation frequency where the condensate splits into stable high density fragments. Exploration of the low-lying excitations in dipolar vortex lattices have been undertaken [265]. Extensions to the dGPE have been explored with three-body interactions [266] and two-component systems — where both species are dipolar [267], or only one is dipolar [268]. For a recent review on the progress of dipolar

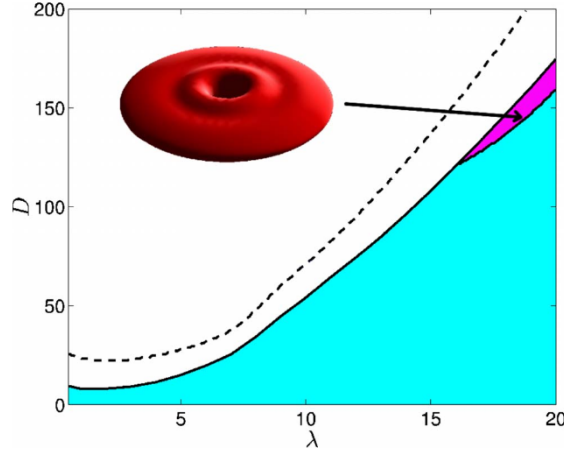


Figure 2.13: Vortex stability in a dipolar condensate as a function of vortex strength $D \equiv a_{dd}/a_0$ vs aspect ratio λ . Blue regions are stable, the pink region highlights where the vortex obtains ripple structures around the core, as shown by the isosurface density inset. (Copyright (2009) by The American Physical Society [262]).

vortices see Ref. [269].

2.4.3 Dipolar solitons

A series of theoretical investigations have indicated that dipolar interactions in BECs also considerably enrich the properties of solitons. In quasi-one-dimensional geometries the effect of varying the relative strength of the local and nonlocal interactions has revealed novel bright [270–272, 199] and dark dipolar matter wave solitons [273, 197, 196, 198]. Dark-in-bright and bright-in-dark dipolar solitons have also been predicted [274]. Yet perhaps the most interesting facet of solitons in general are their interactions and collisions [144], and in dipolar condensates the solitons themselves, considered as individual particle-like entities, inherit non-local soliton-soliton interactions in addition to the usual short-range soliton-soliton interaction [270, 197]. The play off between these two contributions can lead to the formation of unconventional bound states of bright [271] and dark solitons [273, 197]. Dipole-dipole interactions are also predicted to support two-dimensional bright solitons in quasi-2D geometries [275–279], and suppress the well-known transverse “snaking” instability of dark solitons in three-dimensional geometries [280]. These works highlight important prevailing physical characteristics, including the existence of bound states of multiple dipolar solitons due to the intrinsic long-ranged nature of the dipolar interaction.

It is worth elucidating that a bright soliton is not a quantum droplet, but each state does share some properties. The stability of a quantum droplet is purely due to the presence of quantum mechanical effects prevalent in Bose-Bose mixtures and dipolar BECs,

whereas bright solitons are stable in their own right below a threshold density. The critical density required for the transition of a Bose-Bose mixture from soliton-to-droplet has been experimentally studied [281], and further classified numerically by assessing the behaviour of collective modes through the transition [282].

2.5 Instability

Attractive interactions can cause a quantum gas to undergo a runaway collapse into a dense state. Due to the DDI anisotropy the criterion for collapse depends heavily on the trap geometry and the polarisation angle. In this section we review instability mechanisms for dipolar and non-dipolar gases.

2.5.1 Collapse instability

In 1995, Hulet's group reported (non-dipolar) ^7Li condensates containing $\sim 10^5$ atoms [5]. Theory predicted that such large condensates are not possible for this isotope of lithium, which has attractive contact interactions, and showed that only condensates with up to $\sim 1.5 \times 10^3$ atoms are stable [283] due to the runaway collapse of the negative interaction energy for large atom number. Proposals to account for this discrepancy included dominating repulsive three-body interactions [284] or a vortex [285]. The answer turned out to be an imaging error, due to spherical aberration, as explained in an erratum in 1997 [6], and matching theoretical predictions in Refs. [286, 287]. Importantly, the original report of a ^7Li BEC was correct, just with a smaller atom number than first reported.

In 1998 Kagan et al. [288] showed that including three-body losses causes a ^7Li condensate to undergo a series of collapses and revivals. The collapse is induced by exceeding the critical atom number, but this is halted by the large three-body loss rate. Then the condensate atom number is allowed to grow again, with atoms being drawn in from the surrounding thermal cloud completing the cycle.

Bosenova

In 2001 Refs. [289, 290] employed Feshbach resonances to suddenly change the size and magnitude of the scattering length in a ^{85}Rb condensate at less than 6nK. The initially positive scattering length became instantaneously negative causing a sudden collapse and subsequent explosion of the condensate, as shown in Fig. 2.14. This phenomenon has since been termed the "bosenova", due to its similarities with supernovae; the appearance of bursts and jets — complex patterns of the exploding condensate — were also reported.

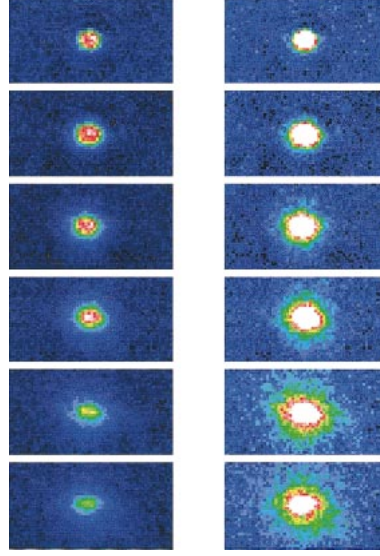


Figure 2.14: Bosenova explosion. Each row shows the time evolution of the cloud from 0.2 to 4.8 ms after the interaction was made negative. The right column shows a three times amplified image of the left, done to highlight the 200nK explosion products. (Copyright (2002) by The American Physical Society [291]).

2.5.2 Homogeneous dipolar gas

Now we return to discussion of the DDI, introducing instabilities that arise from the long-range and anisotropic interactions. First, let us restate the Bogoliubov dispersion relation for the homogeneous gas in the phonon limit

$$E(\mathbf{k}) \approx \hbar k \sqrt{\frac{n}{m} [g + g_{\text{dd}}(3 \cos^2 \theta_k - 1)]}. \quad (2.81)$$

A gas will become unstable when this quantity becomes imaginary, signalling a mode softening. For a gas to become unstable only a single mode has to go soft. If we fix $g_{\text{dd}} > 0$, as is the case for all conventional dipole-dipole systems, then considering the most attractive \mathbf{k} direction $\theta_k = \pi/2$, where \mathbf{k} is aligned perpendicular to the polarisation axis giving,

$$E(\mathbf{k}) \propto \sqrt{g - g_{\text{dd}}}. \quad (2.82)$$

Soft modes grow when $g < g_{\text{dd}}$, which when $g > 0$ is simply the condition $\varepsilon_{\text{dd}} > 1$. See Fig. 2.15 for the qualitative explanation as to why these particular modes become unstable.

For the case of inverted dipoles, see Sec. 2.1.2, $g_{\text{dd}} < 0$, the most attractive \mathbf{k} direction is $\theta_k = 0$ and the energy in the phonon limit is

$$E(\mathbf{k}) \propto \sqrt{g + 2g_{\text{dd}}}. \quad (2.83)$$

In this case the equivalent instability condition is given by $\varepsilon_{\text{dd}} < -1/2$. The combination of these criteria give the general statement that the homogeneous dipolar Bose gas is stable in the range $-1/2 < \varepsilon_{\text{dd}} < 1$.

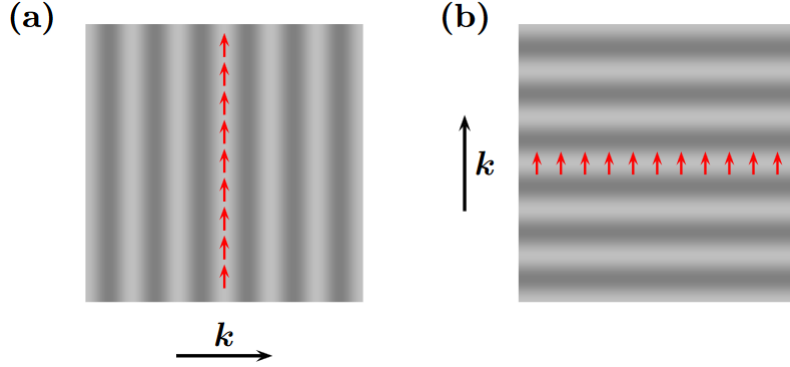


Figure 2.15: (a) A phonon with \mathbf{k} oriented perpendicularly to the polarisation creates planes of high density where the dipoles are in a end-to-end configuration, causing an instability. (b) If \mathbf{k} is parallel to the polarisation direction the dipoles point out of the plane of high density, and remain stable. (Copyright (2009) IOP Publishing. Reproduced by permission of IOP Publishing. All rights reserved [67]).

The pure homogeneous dipole gas ($g = 0$, $g_{dd} \neq 0$) is always unstable, due to there always being a \mathbf{k} direction that is dominantly attractive.

2.5.3 Trapped dipolar gas

When considering trapped gases with contact interactions the increase in complexity from the homogeneous case is small, with most problems being tractable using *local density approximations*⁶. However, as we will see in the upcoming section this is often not the case when considering DDIs. This is due to the complex dependence of polarisation direction relative to the orientation of the anisotropic trap.

The d-wave collapse and explosion

Early experimental work looking at the instability dynamics of ^{52}Cr found that the well known bosenova phenomenon takes on a different shape in dipolar gases [292, 293]. By starting with a chromium gas in the ground state of an almost spherical trap ($\omega_x, \omega_y, \omega_z \approx 2\pi \times (600, 400, 530)$ Hz the scattering length was quenched via Feshbach resonances from $a_s = 30a_0$ ($\varepsilon_{dd} = 0.53$), in the stable regime, to $a_s = 5a_0$ ($\varepsilon_{dd} = 3.2$), pushing the condensate into the unstable regime. This new scattering value is held for a time t_{hold} , then the trap is turned off and the condensate is imaged after 8ms of expansion time. Figure 2.16 shows the result of varying the time t_{hold} . The ensuing dynamics are reminiscent of the bosenova, however with a clear d-wave shape in the explosion.

⁶The local density approximation surmounts to replacing the homogeneous chemical potential with one that varies in space as $\mu \rightarrow \mu(\mathbf{r}) - V(\mathbf{r})$. As long as the potential is slowly varying in space the kinetic energy contribution can be ignored.

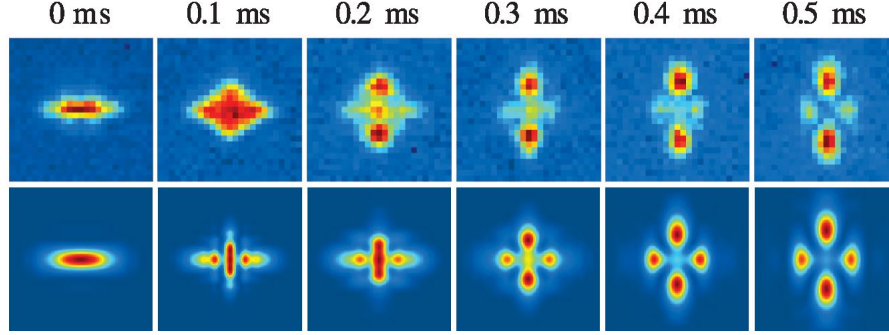


Figure 2.16: The collapse dynamics of a ^{52}Cr condensate for increasing hold times t_{hold} , for dipoles oriented horizontally. Top: experimental images averaged over 5 runs. The thermal cloud has been removed. Bottom: numerical simulation of the dipolar GPE. (Copyright (2008) by The American Physical Society [292]).

Collapse mechanism

Here we uncover the mechanism for collapse inherent in dipolar BECs by following the rhetoric of the Bohn group in Ref. [294]. We cover three different trapping potentials, as shown in Fig. 2.17:

- (a) When the trap is near spherical ($\lambda \sim 1$) the collapse happens globally, causing the whole condensate to collapse as a narrow rod-shape along the axis of polarisation in order to maximise the head-to-tail attractive interactions and not significantly increase the trap or kinetic energy.
- (b) Stability is increased in slightly oblate geometries ($\lambda > 1$) due to the trap creating a greater energy barrier preventing the global rod-like behaviour from occurring.
- (c) In highly oblate geometries ($\lambda \gg 1$) a global collapse isn't possible [231, 232], instead local density fluctuations produce series of locally prolate high density regions. The separation between these prolate regions is intrinsically linked to the roton wavelength, and this instability is triggered by a softening of roton modes.

2.5.4 Quantum Rosensweig instability

The earliest experiments on dipolar droplets actually mimicked the set-up as described in Fig. 2.17(c). By rapidly quenching the scattering length into a roton unstable regime the system breaks into a series of small droplets, rather than one single macrodroplet. This was first seen in dysprosium [95], where they found that by increasing the atom number they could increase the number of droplets that appear after the quench. This observation is the quantum analogue of the classical Rosensweig instability, as can be seen from

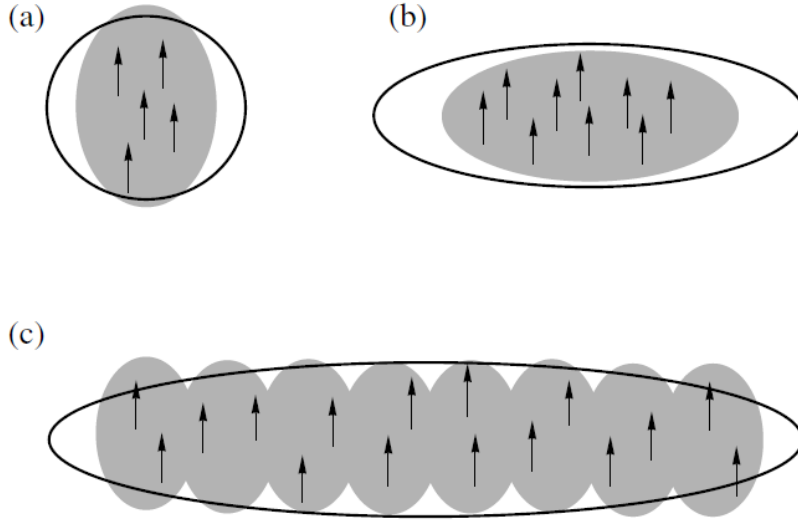


Figure 2.17: A cartoon of a collapsing dipolar BEC. In all figures the arrows represent the dipole polarisation, the grey shaded region shows the density and the black solid line is the trapping potential. A full description of each figure can be found in the main text. (Copyright (2009) by Laser Physics [294]).

Fig. 2.18. Exact path integral ground-state Monte-Carlo simulations match these experiments nicely [295]. The Pfau group also proved that these droplets are stable due to quantum mechanical effects and not three-body interactions [221]. Theoretical studies into these many-droplet states have been undertaken by the Santos group [224, 296], where they showed that the gGPE also predicts the same observed experimental behaviour of an increase in droplet number with atom number, and a full exploration of the predicted phase diagram has recently been experimentally undertaken [251]. They also calculate the modifications of the excitation frequencies due to the LHY correction, which have been experimentally probed in [297]. Due to the non-adiabatic nature of generating these many-droplet states the coherence length does not extend further than a single droplet, and cannot be called a supersolid. Similar experiments in quasi-1D geometries have since been undertaken [298].

2.6 Beyond mean-field models

Gross-Pitaevskii theory is a zero temperature theory, and the GPE describes the experimentally impossible scenario of a zero temperature BEC. A number of finite-temperature theories have now been created in order to incorporate the effects of temperature in the description of Bose gases. Some theories build on the mean-field theory as a base, continuing to treat the Bose gas as a classical object, separated from the thermal field [299–302]. The common feature of these methods is to describe the condensate and thermal clouds

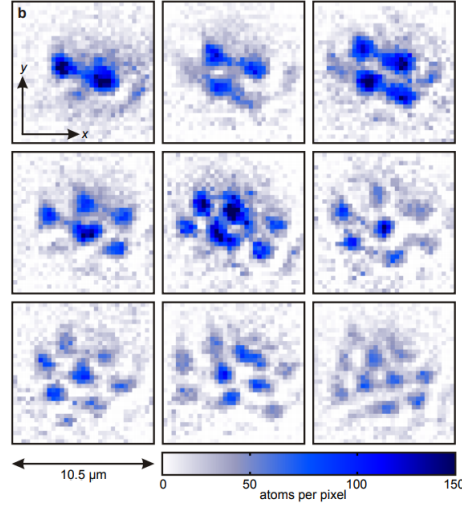


Figure 2.18: Expansion images of a dipolar BEC after a quench into a roton unstable regime. Each figure has an increase of atom number, ranging from $N \approx 5000$ to $N \approx 15000$, which increases the number of created droplets from $N_d = 2$ to $N_d = 10$. (Copyright (2016) by Springer Nature [95]).

by coupled dynamical equations, incorporating mean-field and particle-exchange interactions. In this scenario the condensate is described by an appropriately generalised GPE and the non-condensate is coupled to a Boltzmann equation [303–305]; this model has been extensively developed by Zaremba, Nikuni and Griffin, labelled the ZNG method [299]. This approach requires modifications to accurately reproduce low dimensional experiments, where phase fluctuations are large [306–308].

Other approaches tackle the problem in a fully dynamical manner, making use of the classical field methodology. The GPE should be able to describe all classical aspects of a Bose gas. As long as the occupation all k modes is large the creation and annihilation field operators can be approximated by c-number amplitudes [309]. Through taking an initial condition

$$\psi(\mathbf{r}, 0) = \sum_{\mathbf{k}} a_{\mathbf{k}} \exp(i\mathbf{k} \cdot \mathbf{r}), \quad (2.84)$$

where $a_{\mathbf{k}}$ are the c-numbers that are uniform with a random phase distribution, the classical field method boils down to solving the GPE with this highly non-equilibrium finite temperature initial state and subsequently allowing for equilibration at some temperature [309]. This method imposes a fixed particle number and energy, and the equilibrium temperature is an output of the initial condition, and thus is useful as a qualitative model for finite temperature simulations that can accurately capture equilibrium dynamics. In order to gain a qualitative understanding of finite temperature in dipolar Bose gases we use this method in Ch. 10 of this thesis. The classical field method has been used to model many

beyond-mean-field effects, including thermal equilibration dynamics [132, 310–312], condensate fractions [313], critical temperatures [314], correlation functions [315], spontaneous production of vortex-antivortex pairs in quasi-2D gases [316], thermal dissipation of vortices [317], and related effects in binary condensates [318–320].

Improvements to the classical field theory are achieved through the Truncated Wigner method [321]; the key element of this method is to incorporate quantum effects through the addition of a prescribed amount of quantum noise to the wavefunction initial conditions, and generalising the GPE to a Langevin type equation, often called the Stochastic (Projected) Gross Pitaevskii equation (SPGPE) [56, 57]. The SPGPE describes the stochastic evolution of the condensate plus highly occupied low-lying thermal modes [58].

In dipolar gases theoretical progress has been few and far between. Early works had computational limitations and neglected exchange interactions between excited modes [322], or included these interactions but only in quasi-2D geometries [323]. Ref. [324] included the exchange interactions but were computationally limited to only consider very low temperatures. Theoretical studies on the stability of gases at temperatures $T > T_c$ [325] and $0 < T < T_c$ [326] have been undertaken, where they found that the unusual ground states we describe in Sec. 2.3.4 can be enhanced at higher temperatures [327].

3

Numerical methods

NUMERICAL simulations of BECs allow us to explore regimes beyond the scope of current theory, thus a large portion of this thesis is given to numerics in order to probe stationary and time-dependent dynamics of a complex array of systems. A collection of the numerical techniques used throughout are introduced in this Chapter. For each case, we give a general introduction to the numerical method, and then describe the specific details of how it is applied to dipolar BECs in this thesis.

3.1 Evaluation of the dipolar potential

The dipolar potential is efficiently evaluated in Fourier space through application of the convolution theorem (see Appendix B). Recall the dipolar interaction term $\Phi_{\text{dd}}(\mathbf{r}, t)$, stated again here as

$$\Phi_{\text{dd}}(\mathbf{r}, t) = \int d^3\mathbf{r}' U_{\text{dd}}(\mathbf{r} - \mathbf{r}') |\psi(\mathbf{r}', t)|^2. \quad (3.1)$$

The convolution theorem allows us to rewrite this as

$$\Phi_{\text{dd}}(\mathbf{r}, t) = \mathcal{F}^{-1} \left[\tilde{U}_{\text{dd}}(\mathbf{k}) \tilde{n}(\mathbf{k}, t) \right], \quad (3.2)$$

where \mathcal{F} (\mathcal{F}^{-1}) denotes the (inverse) Fourier transform, $\tilde{U}_{\text{dd}}(\mathbf{k}) = \mathcal{F}[U_{\text{dd}}(\mathbf{r})]$ is the k -space dipolar pseudo-potential from Eq. (2.16) and $\tilde{n}(\mathbf{k}, t) = \mathcal{F}[n(\mathbf{r}, t)]$ is the density in k -space. The numerical calculation of Eq. (3.2) is handled simply through fast Fourier transforms (FFTs). However, FFT algorithms are naturally periodic and introduce alias copies that interact with the system of interest through the long-range DDI. In order to offset this effect we use two truncated variants of the DDI to reduce the effect of these phantom copies.

The first variant introduces a spherical cut-off, and is employed in Ch. 9. Restricting

the range of the DDI potential to a sphere of radius R_c gives us the real-space DDI

$$U_{\text{dd}}^{R_c}(\mathbf{r}) = \begin{cases} \frac{C_{\text{dd}}}{4\pi} \frac{1-3\cos^2\theta}{r^3}, & r < R_c, \\ 0, & \text{otherwise.} \end{cases} \quad (3.3)$$

As long as we choose $R_c > L$, where L is the system size, this potential is physically reasonable. The analytical Fourier transform is [209]

$$\tilde{U}_{\text{dd}}^{R_c}(\mathbf{k}) = \frac{C_{\text{dd}}}{3} \left[1 + 3 \frac{\cos(R_c k)}{R_c^2 k^2} - 3 \frac{\sin(R_c k)}{R_c^3 k^3} \right] (3 \cos^2 \theta_k - 1), \quad (3.4)$$

which reduces to the full DDI in the limit $R_c \rightarrow \infty$.

The spherical cut-off works exceptionally for near-spherical traps. However, when the trap potential is highly oblate or prolate the grid size in each dimension must still extend beyond L . The number of grid points in the tight direction is then required to be large to maintain resolution. A fix to this problem is to introduce a cylindrical cut-off to the DDI, given as

$$U_{\text{dd}}^{\rho_c, Z_c}(\mathbf{r}) = \begin{cases} \frac{C_{\text{dd}}}{4\pi} \frac{1-3\cos^2\theta}{r^3}, & \rho < \rho_c \text{ and } |z| < Z_c, \\ 0, & \text{otherwise.} \end{cases} \quad (3.5)$$

The Fourier transform is semi-analytic [240],

$$\begin{aligned} \tilde{U}_{\text{dd}}^{\rho_c, Z_c}(\mathbf{k}) = & \frac{C_{\text{dd}}}{3} (3 \cos^2 \theta_k - 1) \\ & + C_{\text{dd}} e^{-Z_c k_\rho} \left[\sin^2 \theta_k \cos(Z_c k_z) - \sin \theta_k \cos \theta_k \sin(Z_c k_z) \right] \\ & - C_{\text{dd}} \int_{\rho_c}^{\infty} \rho d\rho \int_0^{Z_c} dz \cos(k_z z) \frac{\rho^2 - 2z^2}{(\rho^2 + z^2)^{5/2}} J_0(k_\rho \rho), \end{aligned} \quad (3.6)$$

where J_0 is the zeroth order Bessel function of the first kind. The final line requires numerical integration, which is computationally costly but only required once as part of the simulation setup.

3.2 Imaginary time propagation

We introduce a handy trick which we will use for numerically finding groundstates to the Gross-Pitaevskii equation, known as the imaginary time method [328]. Consider the wavefunction as a superposition of eigenstates, where $\psi_m(\mathbf{r})$ is an eigenstate of the wave-

function $\Psi(\mathbf{r}, t)$ expressed in terms of eigenenergies E_m . We write

$$\Psi(\mathbf{r}, t) = \sum_m \psi_m(\mathbf{r}) e^{-iE_m t/\hbar}, \quad (3.7)$$

where it is important to note that each next eigenstate has higher energy than the previous one, or $E_m > E_{m-1}$. Now make the substitution $t \rightarrow -i\tau$, then we have

$$\Psi(\mathbf{r}, -i\tau) = \sum_m \psi_m(\mathbf{r}) e^{-E_m \tau/\hbar}. \quad (3.8)$$

Crucially, the eigenenergy governs the decay rate, and so the eigenstate with the lowest energy (the ground state of the system) decays slowest. This can be easily seen by taking $\exp(-E_0 \tau/\hbar)$ out as a factor of Eq. (3.8), then

$$\Psi(\mathbf{r}, -i\tau) = e^{-E_0 \tau/\hbar} \left(\psi_0 + \psi_1 e^{-(E_1-E_0)\tau/\hbar} + \psi_2 e^{-(E_2-E_0)\tau/\hbar} + \dots \right), \quad (3.9)$$

and here it is clear that the terms with larger magnitude exponents will decay quicker as τ increases. Thus by taking an approximation of the initial profile of the wavefunction during propagation in imaginary time the thermal states will dissipate, leaving behind the ground state. However, as the factor of $\exp(-E_0 \tau/\hbar)$ is also tending towards zero as $\tau \rightarrow \infty$ we have to renormalise appropriately. This is either achieved by fixing the chemical potential and allowing the atom number to vary, usually employed for homogeneous systems, or by fixing the atom number and allowing the chemical potential to vary, usually used in trapped systems.

In this thesis

In the following Part we extensively use the imaginary time method to generate stationary dark and bright soliton solutions, and Thomas-Fermi profiles. Bright solitons are found with ease as they are ground state solutions. The initial guess is taken to be the non-dipolar solution, and this is allowed to evolve under the dipolar Hamiltonian, converging to the dipolar soliton solution. Dark solitons are excitations, and the use of imaginary time may seem controversial. However, by repeated application of the soliton phase at the beginning of each time-step, i.e. mapping $\psi \rightarrow |\psi| \exp(iS)$, where ψ is the current wavefunction and S is the target phase, a dark soliton solution is found. The disadvantage in using this method is that an a priori knowledge of the phase is required. It transpires that the stationary black soliton phase is a sharp π phase jump, even in dipolar gases, but to find dark soliton solutions with $v \neq 0$ more sophisticated methods are required.

3.3 Biconjugate gradient method

In this section, we describe a method of finding stationary solutions that, unlike the imaginary time method, are not restricted to the groundstate of the condensate and may in fact include excitations. These are obtained by numerically solving the time-independent GPE (see Sec. 2.2.3), and is particularly useful for finding solutions that are stationary in a moving reference frame (see Sec. 2.2.3). This is performed using the biconjugate gradient method [329] (BCGM). This technique has been used to obtain moving-frame vortex solutions in the 2D/3D GPE [330, 331].

The BCGM is an iterative method based on the Newton-Raphson method for finding roots of equations. For a function $f(x)$, Newton's method uses an initial guess, $x^{(1)}$, and the following iteration

$$x^{(p+1)} = x^{(p)} - \frac{f(x^{(p)})}{f'(x^{(p)})} \quad (3.10)$$

to minimise the Taylor expansion $f(x^{(p+1)}) \approx f(x^{(p)}) + f'(x^{(p)})(x^{(p+1)} - x^{(p)}) = 0$ at step p . Generalising this to a system of N coupled equations, $\mathbf{f}(\mathbf{x}) = \mathbf{0}$ (here \mathbf{x} denotes the vector $\{x_u\}_{u=1,\dots,N}$ and $\mathbf{f}(\mathbf{x})$ the vector of functions $\{f_u\}_{u=1,\dots,N}$), the same minimisation procedure can be applied.

Defining $\mathbf{f}(\psi) = (\hat{H} - \mu)\psi$, for appropriate Hamiltonian \hat{H} , the linearised system of equations we seek to solve is

$$f_u(\psi^{(p+1)}) \approx f_u(\psi^{(p)}) + \sum_{v=1}^N J_{u,v} \delta\psi_v \approx 0, \quad (3.11)$$

where $J_{u,v} = \partial f_u(\psi^{(p)}) / \partial \psi_v^{(p)}$ defines the elements of the Jacobian matrix and $\delta\psi = \psi^{(p+1)} - \psi^{(p)}$. This method is akin to solving the equation $\mathbf{J}\delta\psi = -\mathbf{f}$ for $\delta\psi$, then setting $\psi^{(p+1)} = \psi^{(p)} + \delta\psi$ at each step p . The advantage of using the BCGM is that we only require knowledge of the transpose of the Jacobian, which is numerically faster to obtain than matrix inversion.

In this thesis

In this thesis the BCGM is employed to find dark solitons in the presence of nonlocal interactions. It is worth noting that this approach provides the true dipolar dark soliton solutions for arbitrary speed.

Let us show the example of a quasi-1D system in the moving frame¹. Position z is discretised onto a grid z_i , with $i = 1, \dots, \mathcal{N}$ and grid spacing Δz . Similarly, the spatial

¹The dipolar quasi-1D Hamiltonian is derived in Ch. 5 and the moving frame term is introduced in Sec. 2.2.3.

wavefunction is denoted ψ_j ($j = 1, \dots, \mathcal{N}$). We further define the real and imaginary parts of ψ_j as $\psi_{j,0} = \text{Re}[\psi(z_j)]$ and $\psi_{j,1} = \text{Im}[\psi(z_j)]$. The discretised version of the function \mathbf{f} can then be written down in terms of its composite real and imaginary parts as

$$f_{j,r} = -\frac{\hbar^2}{2m} \frac{\psi_{j-1,r} - 2\psi_{j,r} + \psi_{j+1,r}}{(\Delta z)^2} + \left[\frac{g}{2\pi l_{\perp}^2} (\psi_{j,0}^2 + \psi_{j,1}^2) + \Phi_{\text{dd}}^{j,r} - \mu \right] \psi_{j,r} + (2r-1)v\hbar \frac{\psi_{j+1,1-r} - \psi_{j-1,1-r}}{2\Delta z} = 0, \quad (3.12)$$

where the spatial derivatives have been evaluated through the finite-difference scheme. The computation of the dipolar potential $\Phi_{\text{dd}}^{j,r}$ is handled via the convolution theorem as

$$\Phi_{\text{dd}}^{j,r} = \mathcal{F}^{-1}[\mathcal{F}[U_{1\text{D}}(z)]\mathcal{F}[|\psi(z)|^2]]_{j,r}, \quad (3.13)$$

where $U_{1\text{D}}(z)$ is the one-dimensional dipolar pseudo-potential, as derived in Ch. 5. The Jacobian $J_{u,v}$ in Eq. (3.11) is formed as the discrete functional derivative of $f_{j,r}$ with respect to $\psi_{k,s}$. Making use of the relation $\partial\psi_{j,r}/\partial\psi_{k,s} = \delta_{j,k}\delta_{r,s}$, we obtain

$$\begin{aligned} \frac{\partial f_{j,r}}{\partial \psi_{k,s}} = & -\frac{\hbar^2}{2m} \frac{\delta_{j+1,k} - 2\delta_{j,k} + \delta_{j-1,k}}{(\Delta z)^2} \delta_{r,s} + \delta_{j,k} \delta_{r,s} \left[\frac{g}{2\pi l_{\perp}^2} (\psi_{j,0}^2 + \psi_{j,1}^2) + \Phi_{\text{dd}}^{j,r} - \mu \right] \\ & + 2\psi_{j,r} \psi_{k,s} \left[\frac{g}{2\pi l_{\perp}^2} \delta_{j,k} + U_{1\text{D}}(|z_j - z_k|)\Delta z \right] + (2r-1)v\hbar \delta_{1-r,s} \frac{\delta_{j+1,k} - \delta_{j-1,k}}{2\Delta z}. \end{aligned} \quad (3.14)$$

Numerical implementation was handled in MATLAB with the function `bicgstab`. In practice, it is convenient to concatenate the real and imaginary components of \mathbf{f} into a single vector of length $2\mathcal{N}$, and similarly for ψ . \mathbf{J} is then of size $2\mathcal{N} \times 2\mathcal{N}$. Taking the non-dipolar soliton solution, as defined by Eq. (6.1), as the initial guess for ψ (centered at the origin), we find that the BCGM robustly converges to the required dipolar soliton solution (also centered at the origin). Note that a different choice for initial guess may lead instead to the homogeneous ground state.

The absolute value of the phase is arbitrary, and to aid convergence we fix the value of the phase at one end of the grid. The grid spacing Δz is typically 0.1ξ . Away from the phonon/roton instabilities, we employ a box of typical length 100ξ . However, close to these instabilities, box sizes of up to 1600ξ were required to ensure good approximation to the infinite limit (that is, for the mean-field dipolar potential to reach its homogeneous value at the boundaries). The solutions were deemed converged when the relative residual, calculated as $\|\mathbf{J}\delta\psi + \mathbf{f}\|/\|\mathbf{f}\|$, had fallen below an arbitrary tolerance of 10^{-5} .

3.4 Crank-Nicolson scheme

The Crank-Nicolson method uses finite differences to numerically solve partial differential equations. It was developed by John Crank and Phyllis Nicolson in the 1950s [332]. For a partial differential equation, in one dimension, it can be said

$$\frac{\partial u}{\partial t} = F\left(u, x, t, \frac{\partial u}{\partial x}, \frac{\partial^2 u}{\partial x^2}\right). \quad (3.15)$$

Letting $u(j\Delta x, n\Delta t) = u_j^n$ the Crank-Nicolson method is the calculation of

$$\frac{u_j^{n+1} - u_j^n}{\Delta t} = \frac{1}{2} \left[F_j^{n+1}\left(u, x, t, \frac{\partial u}{\partial x}, \frac{\partial^2 u}{\partial x^2}\right) + F_j^n\left(u, x, t, \frac{\partial u}{\partial x}, \frac{\partial^2 u}{\partial x^2}\right) \right]. \quad (3.16)$$

Note that the numerical calculation of a second order derivative is given by

$$\frac{\partial^2 u_j^n}{\partial x^2} = \frac{u_{j+1}^n - 2u_j^n + u_{j-1}^n}{(\Delta x)^2} + O(\Delta x^2). \quad (3.17)$$

Rearranging Eq. (3.16) for $\mathcal{A}u^{n+1} = \mathcal{B}u^n$ for some matrices \mathcal{A} and \mathcal{B} gives the iterative problem to solve. In many cases the algebraic problem is a tridiagonal matrix, which is zero everywhere except in the main diagonal and the diagonals above and below (often referred to as sup- and sub-diagonals). These matrices can be inverted with the tridiagonal matrix, or Thomas, algorithm [332]. From this reference we note that the method only converges if the relation $\Delta t/(\Delta x)^2 < 1/2$ holds.

The Gross-Pitaevskii equation introduces a new complication however, due to the presence of the nonlinear term that depends on the value of ψ^{n+1} in \mathcal{A} . A workaround for this is to set $\psi^{n+1} = \psi^n$ for one iteration to obtain an approximation for the next step, then substitute this newly obtained ψ^{n+1} back into the original equation. This intermediate process is repeated until convergence of the new wavefunction, although we find that one iteration gives sufficient accuracy.

In this thesis

Consider once again the quasi-1D dipolar GPE in the form $i\partial\psi(x, t)/\partial t = \hat{H}\psi(x, t)$, for the Hamiltonian \hat{H} . Direct integration gives

$$\psi(x, t + \Delta t) = \exp\{-i\Delta t\hat{H}/\hbar\}\psi(x, t) + O(\Delta t^2), \quad (3.18)$$

assuming the Hamiltonian is fixed during the time interval. We can replace the exponential function using a finite difference approximation called Cayley's form [333]

$$\exp\{-i\Delta t \hat{H}\} = \frac{1 - \frac{i\Delta t}{2\hbar} \hat{H}}{1 + \frac{i\Delta t}{2\hbar} \hat{H}} + \mathcal{O}(\Delta t^2). \quad (3.19)$$

We now have the tools to evolve our solution in time and space. After substituting Eq. (3.19) into (3.18) and letting $\psi(j\Delta x, n\Delta t) = \psi_j^n$ the full time evolution step is

$$\begin{aligned} & -\frac{i\hbar\Delta t}{4m(\Delta x)^2} (\psi_{j-1}^{n+1} + \psi_{j+1}^{n+1}) \\ & + \left[1 - \frac{i\Delta t}{2\hbar} \left(\mu - \frac{\hbar^2}{m(\Delta x)^2} - V_{\text{ext}}(x_j) - \frac{g}{2\pi l_{\perp}^2} |\psi_j^{n+1}|^2 - \Phi_{\text{dd}}[\psi_j^{n+1}] \right) \right] \psi_j^{n+1} \\ & = \frac{i\hbar\Delta t}{4m(\Delta x)^2} (\psi_{j-1}^n + \psi_{j+1}^n) \\ & + \left[1 + \frac{i\Delta t}{2\hbar} \left(\mu - \frac{\hbar^2}{m(\Delta x)^2} - V_{\text{ext}}(x_j) - \frac{g}{2\pi l_{\perp}^2} |\psi_j^n|^2 - \Phi_{\text{dd}}[\psi_j^n] \right) \right] \psi_j^n. \end{aligned} \quad (3.20)$$

The left-hand side is nothing more than the tridiagonal matrix introduced in the last section, which can be inverted using the Thomas algorithm [332], leaving ψ_j^{n+1} on the left hand side.

3.5 Split-step Fourier method

The split-step Fourier method (SSFM) [334, 335] is well-established for numerically solving the time-dependent Schrödinger equation. Here we write the GPE as

$$i\hbar \frac{\partial}{\partial t} \psi(\mathbf{r}, t) = \hat{H} \psi(\mathbf{r}, t). \quad (3.21)$$

The Hamiltonian \hat{H} can be decomposed as $\hat{H} = \hat{T} + \hat{V}$, where $\hat{T} = -\hbar^2 \nabla^2 / (2m)$ and $\hat{V} = V_{\text{ext}}(\mathbf{r}) + g|\psi|^2 + \Phi_{\text{dd}}$. Integrating from t to $t + \Delta t$ leads to the time-evolution equation,

$$\psi(\mathbf{r}, t + \Delta t) = \exp\{-i\Delta t \hat{H} / \hbar\} \psi(\mathbf{r}, t). \quad (3.22)$$

The operators \hat{T} and \hat{V} do not commute, hence $\exp\{-i\Delta t \hat{H} / \hbar\} \neq \exp\{-i\Delta t \hat{T} / \hbar\} \exp\{-i\Delta t \hat{V} / \hbar\}$. Nonetheless, the following approximation,

$$\exp\{-i\Delta t \hat{H} / \hbar\} \psi \approx \exp\{-i\Delta t \hat{V} / 2\hbar\} \exp\{-i\Delta t \hat{T} / \hbar\} \exp\{-i\Delta t \hat{V} / 2\hbar\} \psi, \quad (3.23)$$

or equivalently,

$$\exp\{-i\Delta t \hat{H}/\hbar\}\psi \approx \exp\{-i\Delta t \hat{T}/2\hbar\} \exp\{-i\Delta t \hat{V}/\hbar\} \exp\{-i\Delta t \hat{T}/2\hbar\}\psi, \quad (3.24)$$

holds with error $\mathcal{O}(\Delta t^3)$. In position space \hat{V} is diagonal, and so the operation $\exp\{-i\Delta t \hat{V}/2\hbar\}\psi$ simply corresponds to multiplication of $\psi(\mathbf{r}, t)$ by $\exp\{-i\Delta t \hat{V}/2\hbar\}$. Although \hat{T} is not diagonal in position space, it becomes diagonal in momentum space. Conversion to momentum space is achieved by taking the Fourier transform \mathcal{F} of the wavefunction $\tilde{\psi}(\mathbf{k}, t) = \mathcal{F}[\psi(\mathbf{r}, t)]$, where \mathbf{k} denotes the wavevector. Then the kinetic energy operation corresponds to multiplication of $\tilde{\psi}(\mathbf{k}, t)$ by $\exp\{-i\hbar\Delta t k^2/2m\}$. Equation (3.23) is more commonly employed as it requires the fewest Fourier transforms.

Thus the algorithm to achieve one time step of the SSFM, using Eq. (3.23), reads

- 1) Apply half of the potential operator on input $\psi(\mathbf{r}, t)$, giving

$$\psi_1(\mathbf{r}, t) = \exp\{-i\Delta t \hat{V}/2\hbar\}\psi(\mathbf{r}, t).$$

- 2) Calculate the Fourier transform

$$\tilde{\psi}_1(\mathbf{k}, t) = \mathcal{F}[\psi_1(\mathbf{r}, t)].$$

- 3) Apply the kinetic operator

$$\tilde{\psi}_2(\mathbf{k}, t) = \exp\{-i\hbar\Delta t k^2/2m\}\tilde{\psi}_1(\mathbf{k}, t).$$

- 4) Calculate the inverse Fourier transform

$$\psi_3(\mathbf{r}, t) = \mathcal{F}^{-1}[\tilde{\psi}_2(\mathbf{k}, t)].$$

- 5) Apply half of the potential operator again

$$\psi(\mathbf{r}, t + \Delta t) = \exp\{-i\Delta t \hat{V}/2\hbar\}\psi_3(\mathbf{r}, t).$$

- 6) Repeat from step 1) until desired time is reached, or if running in imaginary time the desired solution has been found to within an appropriate tolerance.

In practice, the computational expense of performing forward and backward Fourier transforms to evaluate Eq. (3.23) is small (particularly when using numerical fast Fourier transform (FFT) techniques) compared to the significant expense of evaluating the kinetic energy term directly in position space. The above method was developed for the linear

Schrödinger equation with time-independent Hamiltonian. Remarkably, it holds for the GPE (despite its nonlinearity and time-dependent Hamiltonian). Errors of $O(\Delta t^3)$ are maintained, providing the most up-to-date ψ is always employed during the sequential operations in the above algorithm [336]. A bonus of using this method is not only speed, but FFT algorithms are naturally periodic, which we take advantage of here.

In this thesis

The method as described above is used in Ch. 10 to explore 3D homogeneous dipolar turbulence. However, we employ a variation of this technique to solve the 3D dipolar GPE in a rotational frame in Ch. 9. The variation we use is called the Strang alternating direction implicit time-splitting spectral (ADI-TSSP) method [337]. The "ADI" allows the addition of the rotational term into the Hamiltonian, by splitting the kinetic operator into three operations, one for each dimension. In order to symmetrise the scheme, the ordering of the kinetic operations is reversed after the application of the potential operator in each time step. This means we are forced to use the approximation from Eq. (3.24). Concretely, this means we sequentially apply the operations

$$\hat{T}_x/2 \rightarrow \hat{T}_y/2 \rightarrow \hat{T}_z/2 \rightarrow \hat{V} \rightarrow \hat{T}_z/2 \rightarrow \hat{T}_y/2 \rightarrow \hat{T}_x/2,$$

The full algorithm is given below:

- 1) Take the x Fourier transform of input $\psi(\mathbf{r}, t)$, apply half of the kinetic operator in x , then take the inverse x Fourier transform

$$\begin{aligned}\tilde{\psi}(\mathbf{k}, t) &= \mathcal{F}_x[\psi(\mathbf{r}, t)], \\ \tilde{\psi}_1(\mathbf{k}, t) &= \exp\left\{-\frac{i\Delta t}{2}\left(\frac{\hbar k_x^2}{2m} + i\Omega y k_x\right)\right\} \tilde{\psi}(\mathbf{k}, t), \\ \psi_1(\mathbf{r}, t) &= \mathcal{F}_x^{-1}[\tilde{\psi}_1(\mathbf{k}, t)].\end{aligned}$$

- 2) Take the y Fourier transform, apply half of the kinetic operator in y , then take the inverse y Fourier transform

$$\begin{aligned}\tilde{\psi}_1(\mathbf{k}, t) &= \mathcal{F}_y[\psi_1(\mathbf{r}, t)], \\ \tilde{\psi}_2(\mathbf{k}, t) &= \exp\left\{-\frac{i\Delta t}{2}\left(\frac{\hbar k_y^2}{2m} - i\Omega x k_y\right)\right\} \tilde{\psi}_1(\mathbf{k}, t), \\ \psi_2(\mathbf{r}, t) &= \mathcal{F}_y^{-1}[\tilde{\psi}_2(\mathbf{k}, t)].\end{aligned}$$

- 3) Take the z Fourier transform, apply half of the kinetic operator in z , then take the

inverse z Fourier transform

$$\begin{aligned}\tilde{\psi}_2(\mathbf{k}, t) &= \mathcal{F}_z[\psi_2(\mathbf{r}, t)] , \\ \tilde{\psi}_3(\mathbf{k}, t) &= \exp \left\{ -\frac{i\hbar\Delta t k_z^2}{4m} \right\} \tilde{\psi}_2(\mathbf{k}, t) , \\ \psi_3(\mathbf{r}, t) &= \mathcal{F}_z^{-1}[\tilde{\psi}_3(\mathbf{k}, t)] .\end{aligned}$$

4) Apply the potential operator

$$\psi_4(\mathbf{r}, t) = \exp \left\{ -\frac{i\Delta t}{\hbar} \left(V_{\text{ext}}(\mathbf{r}) + g|\psi|^2 + \Phi_{\text{dd}} \right) \right\} \psi_3(\mathbf{r}, t) .$$

5) Repeat step 3), with input $\psi_4(\mathbf{r}, t)$,

$$\begin{aligned}\tilde{\psi}_4(\mathbf{k}, t) &= \mathcal{F}_z[\psi_4(\mathbf{r}, t)] , \\ \tilde{\psi}_5(\mathbf{k}, t) &= \exp \left\{ -\frac{i\hbar\Delta t k_z^2}{4m} \right\} \tilde{\psi}_4(\mathbf{k}, t) , \\ \psi_5(\mathbf{r}, t) &= \mathcal{F}_z^{-1}[\tilde{\psi}_5(\mathbf{k}, t)] .\end{aligned}$$

6) Repeat step 2), with input $\psi_5(\mathbf{r}, t)$,

$$\begin{aligned}\tilde{\psi}_5(\mathbf{k}, t) &= \mathcal{F}_y[\psi_5(\mathbf{r}, t)] , \\ \tilde{\psi}_6(\mathbf{k}, t) &= \exp \left\{ -\frac{i\Delta t}{2} \left(\frac{\hbar k_y^2}{2m} - i\Omega x k_y \right) \right\} \tilde{\psi}_5(\mathbf{k}, t) , \\ \psi_6(\mathbf{r}, t) &= \mathcal{F}_y^{-1}[\tilde{\psi}_6(\mathbf{k}, t)] .\end{aligned}$$

7) Repeat step 1), with input $\psi_6(\mathbf{r}, t)$,

$$\begin{aligned}\tilde{\psi}_6(\mathbf{k}, t) &= \mathcal{F}_x[\psi_6(\mathbf{r}, t)] , \\ \tilde{\psi}_7(\mathbf{k}, t) &= \exp \left\{ -\frac{i\Delta t}{2} \left(\frac{\hbar k_x^2}{2m} + i\Omega y k_x \right) \right\} \tilde{\psi}_6(\mathbf{k}, t) , \\ \psi(\mathbf{r}, t + \Delta t) &= \mathcal{F}_x^{-1}[\tilde{\psi}_7(\mathbf{k}, t)] .\end{aligned}$$

8) Repeat from step 1) until desired time is reached, or if running in imaginary time the desired solution has been found to within an appropriate tolerance.

II

Excitations in a quasi-1D dipolar Bose gas

Phonons, rotons, and solitons

4

Introduction

A current direction in soliton research is the addition of a non-local nonlinearity. This enriches the soliton behaviour, e.g., promoting non-local interactions between solitons, and offers prospects for studying wave analogues of particles with long-range interactions and emulating complex nonlinear networks [338]. To date, such “non-local solitons” have been observed in liquid crystals [339–341], thermo-nonlinear optical fibres [338] and liquids [342], and optical ring fibres [343]. In these cases, the non-local response is provided by molecular re-orientations, heat conduction and acoustic waves, respectively. Typically these nonlinearities lead to retarded interactions.

The physical system worth the most elucidation is nonlinear optical fibres, where the interaction of the electric field of light with the material gives rise to a defocussing Kerr-type non-local nonlinearity [178]. In this context a mathematical analogy can be drawn between such a system and dipolar condensates, since both are studied with a similar underlying model [344]. However, the response function that characterises the nonlocal optical medium differs to that responsible for the magnetic dipolar interactions, as the former is not truly long-ranged, and instead is of exponential form [345, 346]. Studies of these systems have focussed on their stability [347], and the interaction forces between dark solitons [348, 349]. This has in turn lead to the observation [342] of both repulsion and attraction between dark solitons, with the latter supporting bound states in the optical context. The generation of dark solitons from shocks in these systems has also been experimentally studied [350].

The local cubic defocussing Schrödinger equation represents a solvable model within the framework of the inverse scattering method [351, 352]. The inclusion of a cubic non-local potential to this model greatly complicates its analytical treatment within this method, there currently being no-known exact solutions. Nevertheless, approximate methods including series approximations for the non-local potential [353] and variational calculations [354] have been successfully employed within this context to illuminate the physics of these models, with the latter capturing the existence of dark soliton bound-states.

A series of theoretical investigations have indicated that dipolar interactions in BECs also considerably enrich the properties of solitons. In quasi-one-dimensional geometries

the effect of varying the relative strength of the local and non-local interactions has revealed novel bright [270–272, 199] and dark dipolar matter wave solitons [273, 197, 196, 198]. Dark-in-bright and bright-in-dark dipolar solitons have also been predicted [274]. Yet perhaps the most interesting facet of solitons in general are their interactions and collisions [144], and in dipolar condensates the solitons themselves, considered as individual particle-like entities, inherit non-local soliton-soliton interactions in addition to the usual short-range soliton-soliton interaction [270, 197]. The play off between these two contributions can lead to the formation of unconventional bound states of bright [271] and dark solitons [273, 197]. Dipole-dipole interactions are also predicted to support two-dimensional bright solitons in quasi-2D geometries [275–278], and suppress the well-known transverse “snaking” instability of dark solitons in three-dimensional geometries [280]. These works highlight important prevailing physical characteristics, including the existence of bound states of multiple dipolar solitons due to the intrinsic long-ranged nature of the dipolar interaction.

The main body of this Part is organised into four Chapters.

1. In Chapter 5 we derive the mean-field equation of motion for the quasi-one-dimensional dipolar condensate, and we analyse the stability of the homogeneous system, obtaining analytical expressions for the position of the phonon and roton instabilities, and the trapped system, comparing numerical simulations of the dipolar GPE to the solutions of the Bogoliubov-de Gennes equations.
2. Chapter 6 describes single dipolar dark soliton properties and solutions on homogeneous condensates across the full parameter space of the problem and explores their collision dynamics, including the formation and interaction of bound states close to and away from the systems two instabilities.
3. Chapter 7 introduces a trapping potential and explores the role of dipolar interactions on dark solitons in a Thomas-Fermi like condensate, highlighting the interaction sensitive oscillations of a dark soliton in this system.
4. In Chapter 8 we instead investigate dipolar condensates with dominantly attractive interactions, allowing the creation of bright solitons. Their shape and interactions are categorised across the whole parameter space, and their stability analysed from a fully 3D variational approach.

5

Stability of the quasi-1D dipolar condensate

IN this Chapter we derive the quasi-1D dipolar Gross-Pitaevskii equation, allowing for arbitrary potential in the axial dimension. The confinement in the transverse directions is assumed to be harmonic with the form, $V_{\text{ext}}(x, y) = m\omega_{\perp}^2(x^2 + y^2)/2$, where ω_{\perp} is the corresponding trap frequency. The quasi-1D limit is reached when this confinement is sufficiently strong ($\hbar\omega_{\perp} \gg \mu$, where μ is the BEC chemical potential) that the condensate wavefunction approaches the harmonic oscillator state in the transverse direction [306, 355], with lengthscale $l_{\perp} = \sqrt{\hbar/m\omega_{\perp}}$. In this regime the 3D condensate can be parameterised via a 1D mean-field wavefunction $\psi(z, t)$ which obeys an effective 1D Gross-Pitaevskii equation (GPE) [258, 356].

By assessing the fate of small perturbations in the quasi-1D model we categorise the stability of the condensate, identifying regions of phonon and roton instability for arbitrary parameter choices. We undertake this analysis first in the axially uniform system, then under harmonic confinement.

5.1 Derivation of the quasi-1D dipolar GPE

In three-dimensional geometries, dark solitons are prone to transverse excitation of the nodal line, the so-called “snake instability”. However, in quasi-one-dimensional geometries this instability is prevented and dark solitons become long-lived [147, 187, 357]. In order to model a one dimensional condensate we reduce the dimensions of the full 3D dipolar GPE, given in Sec. 2.2.3. First, we will concentrate on dimensionally reducing the dipolar potential term Φ_{dd} .

Real space dipolar pseudo-potential

Within the single-mode approximation (SMA), we take the condensate radial wavefunction to be in the ground state of the harmonic oscillator, i.e.

$$\Psi(x, y, z, t) = \psi(z, t)\psi_r(x, y) = \psi(z, t) \exp \left[- (x^2 + y^2) / 2l_\perp^2 \right] / \left(\sqrt{l_\perp} \sqrt{\pi} \right). \quad (5.1)$$

Upon integrating out the radial degrees of freedom the one-dimensional pseudo-potential will be given by

$$U_{1D}(z_1 - z_2) = \int_{-\infty}^{\infty} dx_1 \int_{-\infty}^{\infty} dx_2 \int_{-\infty}^{\infty} dy_1 \int_{-\infty}^{\infty} dy_2 U(\mathbf{r}_1 - \mathbf{r}_2) \psi_r^2(x_1, y_1) \psi_r^2(x_2, y_2). \quad (5.2)$$

For brevity, the 3D dipolar pseudo-potential is given by

$$U(\mathbf{r}_1 - \mathbf{r}_2) = \frac{C_{dd}}{4\pi} \left(\frac{1 - 3 \cos^2 \theta}{|\mathbf{r}_1 - \mathbf{r}_2|^3} \right), \quad (5.3)$$

where $\cos \theta = \mathbf{r} \cdot \mathbf{d} / rd$ is the angle between the dipole axis \mathbf{d} and the vector joining two dipoles \mathbf{r} .

Switching to centre of mass and relative coordinates, denoted by $\mathbf{r}_{1/2} = \mathbf{R} \pm \mathbf{r}/2$, the centre of mass can be integrated out, reducing the problem of the 1D interactions to calculating

$$U_{1D}(z) = \frac{1}{2\pi l_\perp^2} \int_{-\infty}^{\infty} dx \int_{-\infty}^{\infty} dy U(\mathbf{r}) e^{-(x^2 + y^2)/2l_\perp^2}. \quad (5.4)$$

This integral is best handled using cylindrical polar coordinates. The first step is to calculate

$$U(z, \rho) = \int_0^{2\pi} d\phi U(z, \rho, \phi). \quad (5.5)$$

In order to perform this integral we can define the vector $\mathbf{r} = (x, y, z) = (\rho \cos \phi, \rho \sin \phi, z)$, where $\rho = \sqrt{x^2 + y^2}$ defines the radial coordinate. Assuming the dipoles lie in the x - z plane, we take $\mathbf{d}/d = (\cos \theta, 0, \sin \theta)$. Equation (5.5) can then be evaluated to yield

$$U(z, \rho) = \frac{C_{dd}[1 + 3 \cos(2\theta)]}{8} \left(\frac{\rho^2 - 2z^2}{(z^2 + \rho^2)^{5/2}} \right). \quad (5.6)$$

We can then proceed to write down an expression that will allow us to integrate out the

cylindrical variable ρ , noting that $dx dy = \rho d\rho$

$$U_{1D}(z) = \frac{C_{dd}[1 + 3 \cos(2\theta)]}{16\pi l_{\perp}^2} \int_0^{\infty} d\rho \rho \frac{\rho^2 - 2x^2}{(\rho^2 + x^2)^{5/2}} e^{-\rho^2/2l_{\perp}^2}. \quad (5.7)$$

Next, we use the transformation $u^2 = \rho^2 + z^2$, which after scaling the variable u by defining $v = u/[\sqrt{2}l_{\perp}]$ gives the following integral

$$U_{1D}(z) = \frac{C_{dd}[1 + 3 \cos(2\theta)]}{32\pi\sqrt{2}l_{\perp}^5} e^{\alpha^2} \int_{\alpha}^{\infty} dv \left\{ 2l_{\perp}^2 v^{-2} - 3z^2 v^{-4} \right\} e^{-v^2}, \quad (5.8)$$

where $\alpha = |z|/[\sqrt{2}l_{\perp}]$. In order to evaluate this integral we note the following useful recursive identity

$$I_n = \int_{\alpha}^{\infty} dv v^{-n} e^{-v^2} = \frac{e^{-\alpha^2}}{(n-1)\alpha^{n-1}} - \frac{2}{(n-1)} I_{n-2}, \quad (5.9)$$

where we note that $I_0 = \sqrt{\pi} \operatorname{erfc}(\alpha)/2$. This allows us to write

$$U_{1D}(z) = \frac{C_{dd}[1 + 3 \cos(2\theta)]}{32\pi\sqrt{2}l_{\perp}^5} e^{\alpha^2} \left[2l_{\perp}^2 I_2 - 3z^2 I_4 \right]. \quad (5.10)$$

Using the recursive identity given by Eq. (5.9) above, one can show that the 1D pseudo-potential for the DDI can be written as $U_{1D}(z) = U_{dd} \tilde{U}(|z|/l_{\perp})$ where

$$\tilde{U}(u) = 2u - \sqrt{2\pi}(1 + u^2)e^{u^2/2} \operatorname{erfc}(u/\sqrt{2}) + \frac{8}{3}\delta(u). \quad (5.11)$$

and $U_{dd} = C_{dd}[1 + 3 \cos(2\theta)]/[32\pi l_{\perp}^3]$. The term $8\delta(u)/3$ is a contact interaction contribution, and can be absorbed into the coefficient of the local nonlinear term in the GPE. The functional form of Eq. (5.11) is that given by the final equation in the appendix of Ref. [358]. If one makes the rescaling $u \rightarrow \sqrt{2}u$ in Eq. (5.11), we recover Eq. (2) of Ref. [356]. Finally, the DDI kernel obeys the important ‘normalisation’ condition

$$\int_{-\infty}^{\infty} dz \frac{1}{4l_{\perp}} \tilde{U}(|z|/l_{\perp}) = 1. \quad (5.12)$$

Consequently, the one-dimensional dipolar potential Φ_{1D} is defined as

$$\Phi_{1D}(z, t) = \int_{-\infty}^{\infty} dz' U_{1D}(z - z') |\Psi(z', t)|^2. \quad (5.13)$$

The numerical calculation of this integral is tricky, as it relies on information of the condensate far outside the region of the computational box. This leads us to finding the

pseudo potential in k -space, where use of the convolution theorem allows us to work around this fact.

Momentum space dipolar pseudo-potential

In Sec. 2.1.3 we derived the 3D momentum space dipolar pseudo-potential, which we state again here as

$$\tilde{U}_{\text{dd}}(\mathbf{k}) = \frac{C_{\text{dd}}}{3} (3 \cos^2 \theta_k - 1), \quad (5.14)$$

where $\cos \theta_k = \mathbf{k} \cdot \mathbf{d}/kd$. The dimensional reduction to 1D can be performed directly in Fourier space in an analogous way to the real-space reduction, again by assuming a harmonic ground state in the transverse directions: setting $\tilde{n}(\mathbf{k}) = \tilde{n}(k_z) \exp\{-l_\perp^2(k_x^2 + k_y^2)/4\}$. Performing the relevant integrals over the radial momenta yields the momentum space equivalent of Eq. (5.11) [258]

$$\frac{U_{1\text{D}}(k_z)}{l_\perp} = 4U_{\text{dd}} \frac{k_z^2 l_\perp^2}{2} e^{k_z^2 l_\perp^2/2} E_1\left(\frac{k_z^2 l_\perp^2}{2}\right) - \frac{4}{3} U_{\text{dd}}, \quad (5.15)$$

where $\hbar k_z$ is the momentum associated with the axial z -direction, while $E_1(x) = \int_x^\infty dt t^{-1} e^{-t}$ is the exponential integral, or equivalently $E_1(x) = \Gamma(0, x)$ where $\Gamma(0, x)$ is the incomplete Gamma function [356]. The dipolar potential can be calculated using Fourier transforms and the convolution theorem (appendix B). Denoting $\mathcal{F}[\cdot]$ as the Fourier transform and $n(k_z, t) = \mathcal{F}[|\psi(z, t)|^2]$ as the k -space density the dipolar potential can be calculated as

$$\Phi_{1\text{D}}(z, t) = \mathcal{F}^{-1}[U_{1\text{D}}(k_z)n(k_z, t)]. \quad (5.16)$$

Quasi-1D dipolar GPE

Now that we have obtained the one dimensional dipolar term, let us turn our attention to the full GPE. We generalise the radial harmonic potential to include a generic axial potential, $V_{\text{ext}}(\mathbf{r}) = m\omega_\perp^2 \rho^2/2 + V_{\text{ext}}(z)$, with transverse trapping frequency is ω_\perp . In cylindrical polar coordinates $\Psi \equiv \Psi(\rho, \theta, z, t)$ this reads

$$i\hbar \frac{\partial}{\partial t} \Psi = \left[-\frac{\hbar^2}{2m} \left(\frac{1}{\rho} \frac{\partial}{\partial \rho} \left(\rho \frac{\partial}{\partial \rho} \right) + \frac{1}{\rho^2} \frac{\partial^2}{\partial \theta^2} + \frac{\partial^2}{\partial z^2} \right) + \frac{1}{2} m \omega_\perp^2 \rho^2 + V_{\text{ext}}(z) + g|\Psi|^2 + \Phi_{\text{dd}} \right] \Psi. \quad (5.17)$$

We take the wavefunction for the condensate to be Eq. (5.1). To integrate out the x and y degrees of freedom, we plug this ansatz into Eq. (5.17) and pre-multiply the result with

$\psi_r(\rho)$. Then, by integrating over the area of the cloud we get

$$\begin{aligned}
 i\hbar \underbrace{\int_A dA \psi_r^2}_{=1} \frac{\partial}{\partial t} \psi = & -\frac{\hbar^2}{2m} \left[\int_A dA \psi_r \frac{1}{\rho} \frac{\partial}{\partial \rho} \left(\rho \frac{\partial \psi_r}{\partial \rho} \right) \psi + \underbrace{\int_A dA \psi_r^2}_{=1} \frac{\partial^2 \psi}{\partial z^2} \right] + \underbrace{\int_A dA \psi_r^2}_{=1} V_{\text{ext}}(z) \psi \\
 & + \frac{1}{2} m \omega_{\perp}^2 \int_A dA \rho^2 \psi_r^2 \psi + \frac{g}{2\pi l_{\perp}^2} \int_A dA \psi_r^4 |\psi|^2 \psi + \underbrace{\int_A dA \psi_r^2 \Phi_{\text{dd}} \psi}_{=\Phi_{\text{1D}} \psi} .
 \end{aligned} \tag{5.18}$$

After performing the Gaussian integrals above, and including the dipolar interaction term as per Eq. (5.16) we obtain the following form of the 1D Gross-Pitaevskii equation¹

$$i\hbar \frac{\partial}{\partial t} \psi(z, t) = \left[-\frac{\hbar^2}{2m} \frac{\partial^2}{\partial z^2} + V_{\text{ext}}(z) + \frac{g}{2\pi l_{\perp}^2} |\psi(z, t)|^2 + \Phi_{\text{1D}}(z, t) \right] \psi(z, t) . \tag{5.19}$$

To find time-independent solutions we separate the space and time dependencies from the wavefunction as $\psi(z, t) = \psi(z) \exp\{-i\mu t/\hbar\}$, where μ is the chemical potential (the energy eigenvalue of Eq. (5.19)). This gives the time-independent GPE

$$\mu \psi(z) = \left[-\frac{\hbar^2}{2m} \frac{\partial^2}{\partial z^2} + V_{\text{ext}}(z) + \frac{g}{2\pi l_{\perp}^2} |\psi(z)|^2 + \Phi_{\text{1D}}(z) \right] \psi(z) . \tag{5.20}$$

Our results will be presented in terms of the natural quantities of the homogeneous condensate. Taking n_0 as the uniform density, the chemical potential follows as

$$\mu_0 = \frac{n_0 g}{2\pi l_{\perp}^2} + \Phi_0 . \tag{5.21}$$

Here the first term represents the van der Waals contribution, and

$$\Phi_0 = -\frac{C_{\text{dd}} n_0 [1 + 3 \cos 2\theta]}{24\pi l_{\perp}^2} \tag{5.22}$$

is the dipolar contribution.

The natural units of length and speed are the dipolar healing length, $\xi = \hbar/\sqrt{m\mu_0}$, and the speed of sound, $c = \sqrt{\mu_0/m}$. A time unit follows as $\tau = \xi/c$. To parameterise the cross-over from three to one dimension we define $\sigma = l_{\perp}/\xi$; the quasi-one-dimensional limit is valid for $\sigma \lesssim 1$ [306]. It is worth noting that in dipolar systems the assumption of cylindrical symmetry breaks down when $\theta \neq 0$ due to magnetostriction. The effect of this is small, only slightly shifting the critical values of ε_{dd} at which we observe instability.

¹We are neglecting to include the constant contribution $\hbar\omega_{\perp}/2$ to the Hamiltonian. This arises from the zero-point energy in the radial oscillator, and can be ignored.

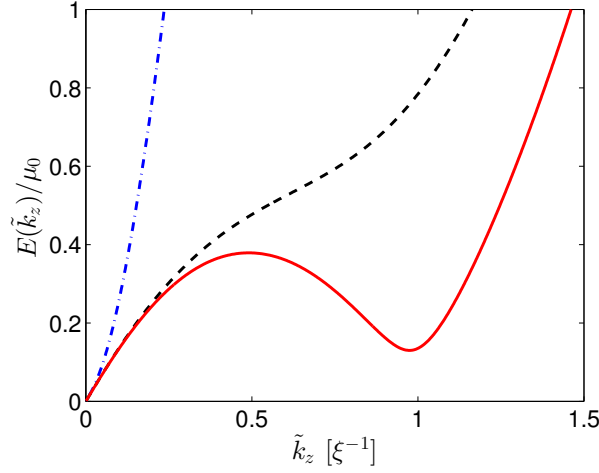


Figure 5.1: The Bogoliubov de Gennes spectrum, Eq. (5.23), plotted for three illustrative values of ε_{dd} : 0.95, -2 , -5 (dot-dashed blue, dashed black, solid red). These show, respectively, the conventional phonon/free-particle spectrum, the flattening off of the dispersion relation at intermediate k , and the emergence of a roton minimum. The condensate has arbitrary width $\sigma = 1$.

This is explored in Ch. 7 when we compare quasi-1D and 3D simulations.

5.2 Stability of the homogeneous system

Here we perform an analysis of the stability of the homogeneous quasi-1D dipolar condensate. This is a generalisation of the results of Refs. [258, 356] which only considered dipoles polarised along the long axis.

The stability of the condensate can be deduced from the fate of small perturbations whose energies are given by the Bogoliubov excitation spectrum. For a homogeneous system, the Bogoliubov spectrum depends on the momentum (Fourier) space interaction potential. The total one-dimensional pseudo-potential, including van der Waals and dipolar contributions, is $U_{\text{tot}}(k_z) = g/(2\pi l_{\perp}^2) + U_{1D}(k_z)$. Both Eq. (5.11) and (5.15) can be split into a non-local and local contribution; the former gives a contribution to the total contact interactions while the latter forms the important long-ranged part of the dipolar interaction. We note that in general the scattering length, and hence g , can be modified both by the dipolar interactions and confinement induced resonances (due to tight 1D trapping) and so may not take on their 3D dipole-free values [356]. Nevertheless, the general form of this pseudo-potential is expected to hold.

With the above results in hand, the Bogoliubov excitation spectrum for perturbations

of momentum $\hbar k_z$ from the background can be written as

$$E_k^2 = \epsilon_k^2 + 2n_0\epsilon_k \left[4l_\perp U_0 \tilde{U}_{1D}(k_z) + \frac{g}{2\pi l_\perp^2} \right], \quad (5.23)$$

where $\epsilon_k = \hbar^2 k_z^2 / 2m$ defines the free particle energy. The excitations associated with Eq. (5.23) are running waves of the form

$$\delta\psi(z, t) = u(k_z) e^{-i(k_z z - E_k t / \hbar)} + v^*(k_z) e^{i(k_z z - E_k^* t / \hbar)} \quad (5.24)$$

that constitute small amplitude fluctuations about the stationary condensate.

Figure 5.1 illustrates the dispersion relation corresponding to Eq. (5.23). For certain parameters, the dispersion relation has the same structure as for the non-dipolar case (dot-dashed blue line): for low k it is linear in k (the phonon regime), changing to a quadratic form at higher k (the free-particle regime). The system is prone to a phonon (long wavelength $k_z \rightarrow 0$) instability. In non-dipolar homogeneous condensates, this arises when the mean-field van der Waals interactions become attractive, $g < 0$. Examining the small k_z behaviour of the dispersion $E_k = \hbar\omega_k$ relation given by Eq. (5.23) yields

$$\omega_k = k_z \sqrt{\frac{1}{m} \left(-\frac{4n_0 U_0}{3} + \frac{n_0 g}{2\pi l_\perp^2} \right)} = k_z c_s, \quad (5.25)$$

where c_s is the speed of sound associated with this long-wavelength regime. We identify the phonon instability as occurring when the bracketed term (which corresponds to the homogeneous chemical potential μ_0) is less than zero. This leads to imaginary frequencies, signifying the unstable exponential growth of long-wavelength perturbations.

In other parameter regimes, the dipoles can change the form of the dispersion relation at intermediate k . In certain instances, it causes a flattening off of the dispersion spectrum, as shown in Fig. 5.1 (dashed black line), while in more extreme cases a minima can form in the dispersion relation at finite momentum, i.e. the roton. An example is shown in Fig. 5.1 (solid red line), with a pronounced dip appearing at $k_z \sim \xi^{-1}$. The associated local maximum in the dispersion relation is termed the maxon. If the roton minimum touches the zero-energy axis then the condensate undergoes the roton instability. The roton is predominantly driven by transverse (off-axis) effects of the dipole-dipole interaction, and becomes less pronounced in the one-dimensional limit ($\sigma \rightarrow 0$) [67].

We identify the roton instability as follows. The expression (5.23) for $E_k^2(k)$ is differentiated with respect to k_z and set equal to zero so as to identify the stationary points (which may correspond to the roton or the maxon). This is then combined with the dispersion relation (5.23) equated to zero (the maxon is automatically excluded from this result as it can never touch the zero energy axis). With some manipulation, the critical wavenumber

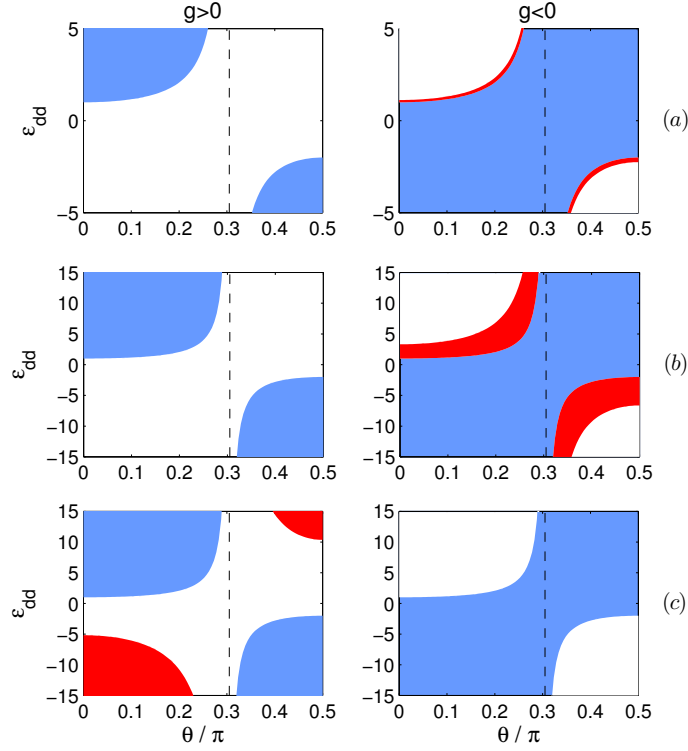


Figure 5.2: Stability diagrams corresponding to the homogeneous ground state of Eq. (5.20) in the $(\theta, \varepsilon_{dd})$ plane for $g > 0$ (left column) and $g < 0$ (right column). Rows (a), (b) and (c) correspond to $\sigma = 0.1, 0.5$ and 1.0 respectively. The blue (red) bands represent regions of phonon (roton) instability, while white regions are stable. The magic angle, $\theta_m \simeq 54^\circ$ is indicated in dashed black. Note that dipolar interactions can act to either destabilise or stabilise the BEC. The latter situation occurs when $g < 0$ but the net dipolar interactions are repulsive.

at which the roton touches zero energy is found to be

$$k_c^2 = -\frac{mn_0g}{\pi\hbar^2l_\perp^2\mu_0} \left\{ \left[1 + \frac{16\pi l_\perp^3 U_0}{3g} \right] - \sqrt{\left[1 + \frac{16\pi l_\perp^3 U_0}{3g} \right]^2 - \frac{4\pi l_\perp^2 \mu_0}{n_0 g \sigma^2} \left[1 - \frac{8\pi l_\perp^3 U_0}{g} \right]} \right\}.$$

While the above expression provides k_c for known system parameters, we wish to predict the onset of the instability as a function of the dipole-dipole interaction strength ε_{dd} . We can eliminate k_c by combining the above expression with a rearranged version of the dispersion relation (5.23) equated to zero:

$$k_c^2 + \frac{16n_0 m l_\perp U_0}{\hbar^2} U_{1D} \left(\frac{k_c^2 l_\perp^2}{2} \right) + \frac{2g n_0 m}{\pi l_\perp^2 \hbar^2} = 0. \quad (5.26)$$

These two equations can be solved iteratively to predict the critical ε_{dd} for the roton instability to occur as a function of θ and σ , as will be presented below.

In Figure 5.2 we map out stability diagrams in the $(\theta, \varepsilon_{dd})$ plane, showing the regions

of roton instability (shaded red) and phonon instability (shaded blue). To give insight into the role of the transverse condensate width, three values are considered: (a) $\sigma = 0.1$, (b) 0.5 and (c) 1. For each value, we distinguish between the $g > 0$ (left column) and $g < 0$ (right column) cases. The phonon instability is independent of σ throughout, and intuitively follows from the play-off between the van der Waals interactions and the dipolar contribution to the contact interactions. Consider, for example, the case of repulsive vdW interactions. For $\theta = 0$ the dipoles lie in the attractive end-to-end configuration, and when the dipoles are sufficiently strong ($\varepsilon_{dd} > 1$) they can overwhelm the repulsive vdW interactions, inducing phonon instability. Conversely, for $\theta = \pi/2$ the dipoles are side-by-side; conventionally this is a repulsive configuration, but in the regime of anti-dipoles ($C_{dd} < 0$) this configuration is attractive, and induces phonon instability when the anti-dipoles are sufficiently strong ($\varepsilon_{dd} < -2$).

The regions of roton instability are sensitive to σ . For low σ (cases (a) and (b) in Figure 5.2), the roton instability arises only for attractive vdWs interactions ($g < 0$). Deep in the 1D regime (case (a)) the roton instability arises only in a narrow band in the $(\theta, \varepsilon_{dd})$ plane; as σ is increased this band expands (case (b)). However once a critical value ($\sigma_{\text{crit}} \sim 0.8$) is exceeded, as per row (c), the roton instability shifts instead to appearing only for repulsive vdW interactions ($g > 0$). The value of σ_{crit} does not depend on the angle θ .

To further explore the shift of the roton instability from $g < 0$ to $g > 0$ for increasing σ , Fig. 5.3 depicts the roton instability in the $(\sigma, \varepsilon_{dd})$ plane for the extreme polarisation angles, (a) $\theta = 0$ and (b) $\theta = \pi/2$. In both cases it is seen that in the quasi-1D limit ($\sigma \ll 1$) the roton instability band narrows, approaching the onset of the phonon instability (horizontal dashed line). However as σ is gradually increased, the roton instability undergoes a change of sign at the critical value $\sigma = \sigma_{\text{crit}}$. Figure 5.3 (c) shows the critical wavelength defined as $\lambda_c = 2\pi/k_c$ plotted as a function of σ . It is seen that λ_c is monotonically increasing, and is always greater than σ (equivalently $\lambda_c > l_\perp$), indicating that our one-dimensional analysis is valid. The inset to Fig. 5.3 (c) shows a zoomed in portion of this graph centred around $\sigma = \sigma_c$, and clearly shows the discontinuity in λ_c , indicated by the dashed blue line.

5.3 Stability of the harmonically trapped system

Here we extend the above analysis with the inclusion of an external harmonic trapping potential. First, we explore the solutions to the dGPE in this regime. These can be categorised by introducing an effective local interaction parameter a_{eff} , defined as

$$a_{\text{eff}} = a_s \left[1 + \frac{\varepsilon_{dd}}{2} (1 - 3 \cos^2 \theta) \right]. \quad (5.27)$$

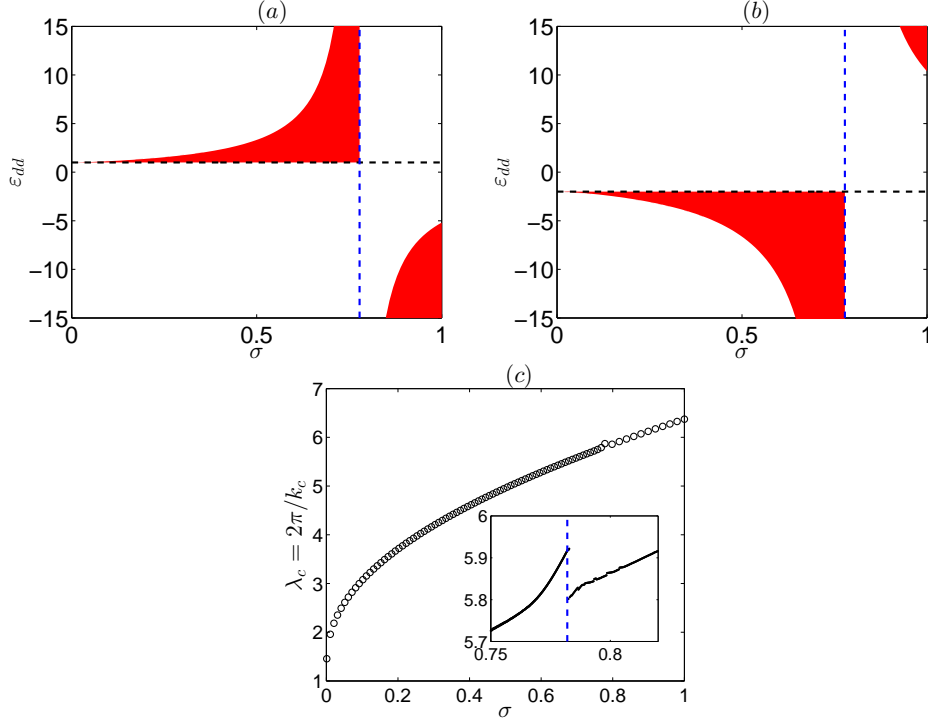


Figure 5.3: Stability diagram in the (θ, ϵ_{dd}) plane as a function of σ for $\theta = 0$ (a) and $\theta = \pi/2$ (b) with the position of the phonon instability indicated by the dashed black line. The critical wavelength, $\lambda_c = 2\pi/k_c$ at which the roton becomes unstable is shown as a function of σ in (c). The inset shows a zoomed portion of this figure displaying the discontinuity in λ_c at $\sigma_c \sim 0.78$.

If $a_{\text{eff}} > 0$ then the net local interactions are repulsive and the ground state is an inverted parabola as described in the Thomas-Fermi analysis. However, if $a_{\text{eff}} < 0$ the net local interactions are attractive and the ground state will be a bright soliton, which is the topic of Ch. 8. Of course, the stability of these states depends on the dipolar interaction.

We illustrate the ground state solutions using the case of dipoles polarised perpendicular to the z -axis ($\theta = \pi/2$). The criteria then reduces to $a_s(1 + \epsilon_{dd}/2) > 0$, or, in terms of ϵ_{dd} , $\epsilon_{dd} > -2$ for $a_s > 0$ and $\epsilon_{dd} < -2$ for $a_s < 0$. Figure 5.4 maps the density $n(z)$ of the quasi-1D BEC as a function of ϵ_{dd} . The vdW interactions, characterised by the dimensionless parameter $\beta = a_s N l_z / l_\perp^2$ with $l_z = \sqrt{\hbar/m\omega_z}$ the axial harmonic oscillator length, are fixed in amplitude throughout to two characteristic values; a low value $|\beta| = 61$, chosen to show stable solutions for $\epsilon_{dd} < -2$, and a larger value of $\beta = 1500$, where this region is roton unstable. The role of dimensionality is explored through two nominal values of σ . The choice $\sigma = 0.05$ shows stable regions for $a_s < 0$ and small β , and $\sigma = 1/8$ is an experimentally realistic quasi-1D value.

A trapped dipolar BEC can develop a roton (finite-momentum) minimum in its excitation spectrum which, for certain parameters, can touch zero energy, triggering an instability at finite momentum [294]. Our quasi-1D BEC has three roton unstable regimes.

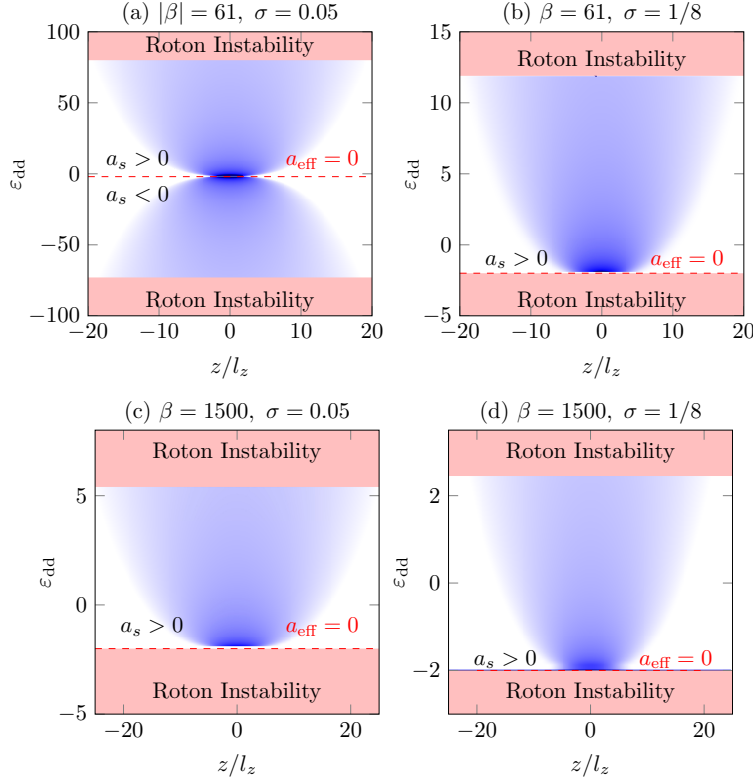


Figure 5.4: Density profile $n(z)$ of the quasi-1D dipolar BEC (polarisation perpendicular to the axis), as a function of ϵ_{dd} . Only the regimes satisfying $a_{\text{eff}} > 0$ are shown, with the line $a_{\text{eff}} = 0$ indicated (red dashed line). The roton-unstable regions extend to $\epsilon_{dd} = \pm\infty$.

The first also arises in the uniform system, as mapped out in the previous section; e.g., in Fig. 5.4(a) this occurs for $\epsilon_{dd} \gtrsim -2$ with $a_s < 0$. Two further roton unstable regimes arise for large $|\epsilon_{dd}|$ (red bands in Fig. 5.4(a) and (b)). For increasing magnitude of β , which can be achieved through a larger atom number, scattering length, or considering a more 3D system (increasing trap ratio ω_z/ω_\perp) these roton instability bands encroach towards $\epsilon_{dd} = 0$. Hence, in Figs. 5.4(b)-(d) there are no stable solutions for $a_s < 0$ ($\beta < 0$).

In order to show that these instabilities we observe are due to the roton we turn our attention to the BdG equations for a trapped gas. In Appendix A we have derived the BdG equations for an arbitrary potential, by taking perturbations to the ground state ψ_0 of the form

$$\delta\psi_j(z, t) = u_j(z)e^{-i\epsilon_j t/\hbar} - v_j^*(z)e^{i\epsilon_j t/\hbar}, \quad (5.28)$$

where $\epsilon_j = \hbar\omega_j$ are the eigenenergies for the j th excitation. Upon substitution of $\psi_j = \psi_0 + \delta\psi_j$ into the dGPE and linearising the fluctuations to lowest order leads us to a system of cou-

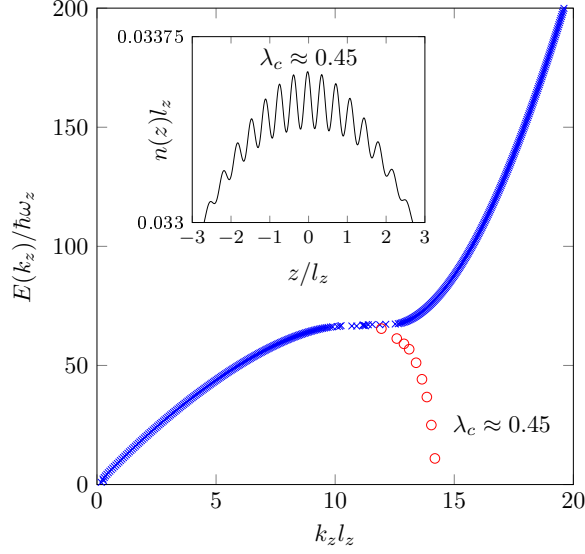


Figure 5.5: Excitation spectrum of an unstable gas. The emergence of the roton fingers (red circles) indicate the presence of density oscillations on the condensate density profile. Inset: Zoomed in density profile. Parameters: $\beta = 1500$, $\theta = \pi/2$ and $\sigma = 1/8$.

pled equations to solve

$$\begin{pmatrix} \hat{\mathcal{H}}_0 + 2\frac{g}{2\pi l_\perp^2}|\psi_0|^2 + \Phi_{dd} + \mathcal{X} & \frac{g}{2\pi l_\perp^2}|\psi_0|^2 + \mathcal{X} \\ -\frac{g}{2\pi l_\perp^2}|\psi_0|^2 - \mathcal{X} & -\hat{\mathcal{H}}_0 - 2\frac{g}{2\pi l_\perp^2}|\psi_0|^2 - \Phi_{dd} - \mathcal{X} \end{pmatrix} \begin{pmatrix} u_j \\ v_j \end{pmatrix} = \epsilon_j \begin{pmatrix} u_j \\ v_j \end{pmatrix}, \quad (5.29)$$

where $\hat{\mathcal{H}}_0$ is the single-particle Hamiltonian (Eq. (2.28)) and the operator

$$\mathcal{X}f(z) = \psi_0(z) \int_{-\infty}^{\infty} dz U_{1D}(z - z') f(z'). \quad (5.30)$$

Figure 5.5 shows the excitation spectrum of a condensate undergoing an instability. By taking a stable initial solution, in this instance with $\varepsilon_{dd} = 2.99$, $\beta = 1500$, $\theta = \pi/2$ and $\sigma = 1/8$, and dynamically increasing ε_{dd} into an unstable regime oscillations begin to grow on the background density profile (see inset *ibid.*). These oscillations appear in the excitation spectrum as *roton fingers*, as seen in quasi-2D purely dipolar condensates [359]. These fingers extend down to the zero energy axis and become unstable, triggering the growth of the density oscillations. By taking the end of the finger to be the critical wavelength λ_c we can compare this with the observed wavelength on the density oscillations and find excellent agreement.

The background BEC widens as ε_{dd} is varied away from the line $a_{\text{eff}} = 0$, caused by magnetostriction in the payoff between the vdW and DD interactions. This can be accounted for within the Thomas-Fermi approximation, valid for strong repulsive interac-

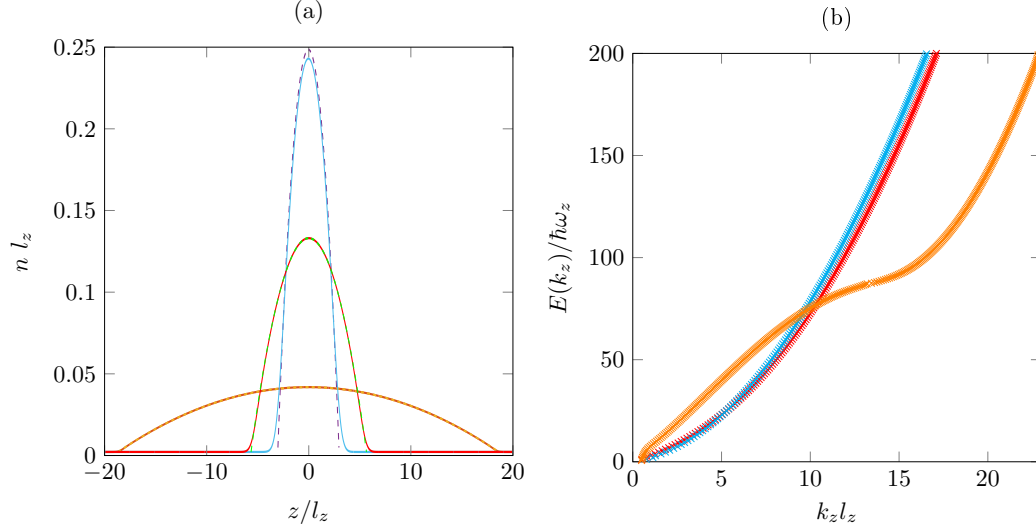


Figure 5.6: (a) Density profiles (solid lines) with the TF prediction of Eq. (5.31) overlaid (dotted). (b) The corresponding excitation spectrums for each density in (a). The parameters are $|\beta| = 61$, $\theta = \pi/2$, $\sigma = 0.05$, with $\varepsilon_{dd} = -1.7$ (blue lines), $\varepsilon_{dd} = -74$ (yellow lines) and $\varepsilon_{dd} = 0$ (red lines).

tions and based on neglecting density gradients. Generalizing previous derivations of the Thomas-Fermi profile of the quasi-1D trapped BEC [360, 355] to include dipoles aligned at an arbitrary angle θ leads to the Thomas-Fermi density [361],

$$n_{\text{TF}}(z) = \frac{(l_{\perp} R_z / 2l_z^2)^2}{a_{\text{eff}}} \left[1 - \frac{z^2}{R_z^2} \right], \quad (5.31)$$

for $z \leq R_z$, and $n_{\text{TF}} = 0$ elsewhere, where $R_z = [3a_{\text{eff}} N l_z^4 / l_{\perp}^2]^{1/3}$ defines the Thomas-Fermi half-width of the BEC. The angular dependence is intuitive: for axially-polarised dipoles (perpendicularly-polarised), R_z is smaller (larger) than the non-dipolar case, consistent with a head-to-tail (side-by-side) alignment shrinking (enlarging) the axial extent of the cloud. The TF prediction typically agrees very well with the true profiles, see Fig. 5.6(a), with significant deviations only when the net local interactions become small ($a_{\text{eff}} \rightarrow 0$) or the condensate becomes more 3D ($\sigma \rightarrow 1$).

While we have focussed on $\theta = \pi/2$, the behaviour is qualitatively similar for all $\theta > \theta_m$ (where θ_m is the magic angle relative to the z -axis), albeit with shifts in a_{eff} (according to Eq. (5.27)) and the onsets of the roton instability. Meanwhile, for $\theta < \theta_m$ the dependence on ε_{dd} is effectively flipped, as was discussed in Sec. 5.2.

5.4 Summary

We have given the derivation for the quasi-1D dipolar system for a general axial potential. By considering perturbations to the ground state we found that the quasi-1D system can become unstable due to phonon or roton instabilities.

For homogeneous systems this revealed the sensitivity of the roton to the transverse condensate size, σ , and the increase in the roton length scale as the dimensionality crossover, $\sigma \sim 1$, is approached. We mapped out the stability diagram as a function of the interaction parameters for this system, identifying suitable stable regions to explore possible soliton solutions in the next Chapter.

In trapped systems we found a similar picture to the homogeneous case, however there are two new roton instabilities associated with the competition between the potential and DDIs. By solving the BdG equations in these regions we found that the roton minimum occurs with the appearance of roton fingers, and becomes unstable when these touch the zero axis.

6

Dark solitons in homogeneous dipolar condensates

IN this Chapter we numerically obtain the family of static and moving dark solitons in a quasi-1D dipolar BEC as stationary solutions in static and moving frames. We map out the stability diagram and form of the soliton solutions as a function of the strength and polarisation direction of the dipoles, covering experimentally-relevant parameters. The dark solitons can acquire dramatically modified profiles, including ripples close to the roton instability. Moreover we show analytically that the absence of atoms in a dark soliton causes it to act like a giant anti-dipole [362]. This induces a non-local contribution to the soliton-soliton interactions which scales as $1/z^3$. This non-local contribution is effectively instantaneous and experimentally tunable in both strength and sign. When the non-local interaction between the solitons is attractive, the balance with the conventional repulsive soliton-soliton interaction supports bound states of two dark solitons, for which no analogue exists in conventional condensates. We show that these bound states themselves have soliton-like properties in that they emerge unscathed from collisions with each other.

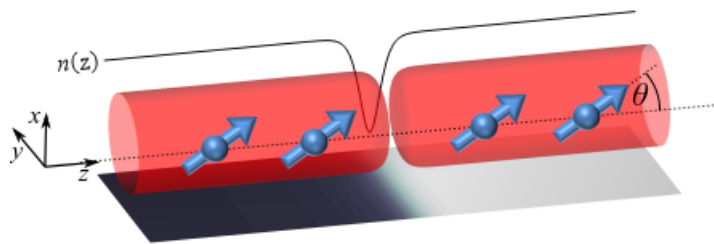


Figure 6.1: We consider an elongated Bose-Einstein condensate of atoms (shown as a density isosurface) with dipole moments (shown as arrows) which are co-polarised in a common direction. For suitable interaction parameters, a dark soliton can be supported, characterised by a 1D density notch and a non-trivial 1D phase slip.

6.1 Dark soliton solutions

6.1.1 Non-dipolar dark solitons

In the absence of dipolar interactions ($\varepsilon_{\text{dd}} = 0$) and for repulsive s -wave interactions ($g > 0$) it is well-known that the 1D GPE is integrable and supports dark soliton solutions of the form [177, 178]

$$\psi_s(z, z_0, t) = \sqrt{n_0} \left[\beta \tanh \frac{\beta(z - z_0 - vt)}{\xi} + i \frac{v}{c} \right] e^{-i\mu t/\hbar}. \quad (6.1)$$

Here $\beta = \sqrt{1 - v^2/c^2}$, where v is the velocity of the soliton, c is the sound speed in the condensate, and the dark soliton's centre of mass is initially placed at z_0 . The family of solitons commonly feature a density depression and a phase slip, with the depression density, n_d and total phase slip S related to the soliton speed, v , via $v/c = \sqrt{1 - (n_d/n_0)} = \cos(S/2)$. The $v = 0$ “black” soliton ($z = 0$) has zero density at its centre and a π phase slip, while the $v = c$ soliton is indistinguishable from the background density. Since dark solitons deplete the density profile, they are analogous to particles with negative mass [179].

6.1.2 Dipolar dark solitons

We now set about exploring the dipolar dark soliton solitons across the important parameters of soliton speed v , polarisation angle θ , dipolar strength ε_{dd} , and condensate width σ . We consider the dark solitons as stationary states in the moving frame, and obtain these solutions by numerically solving the 1D dipolar GPE in the moving frame. The details of this approach can be found in Sec. 3.3.

Figure 6.2(a,b) plots the spatial density profile $n(z)$ of the black ($v = 0$) soliton solutions as a function of ε_{dd} , for the extreme polarisation angles of (a) $\theta = 0$ and (b) $\theta = \pi/2$. The former represents the typical behaviour for all solutions in the range $\theta < \theta_m$, and the latter shows the converse. Figure 6.2(c,d) shows the corresponding plot for a finite speed case, $v = 0.5c$. The grey bands represent the range of ε_{dd} for which no stable condensate exists, consistent with the corresponding stability diagrams presented in row (a) of Fig. 5.2. Away from the unstable region, the density profiles resemble the \tanh^2 -density of the conventional dark solitons, with a width of the order of the healing length ξ (which should be noted is itself a function of ε_{dd} and θ). Near to the phonon instability (solid lines) the density profile diverges in width; this is due to a cancellation between the local interactions arising from the explicit van der Waals interactions and the implicit local contribution to the DDIs, with a similar effect seen for vortices in 2D dipolar condensates [363]. Meanwhile, as the roton instability (dashed lines) is approached, density ripples

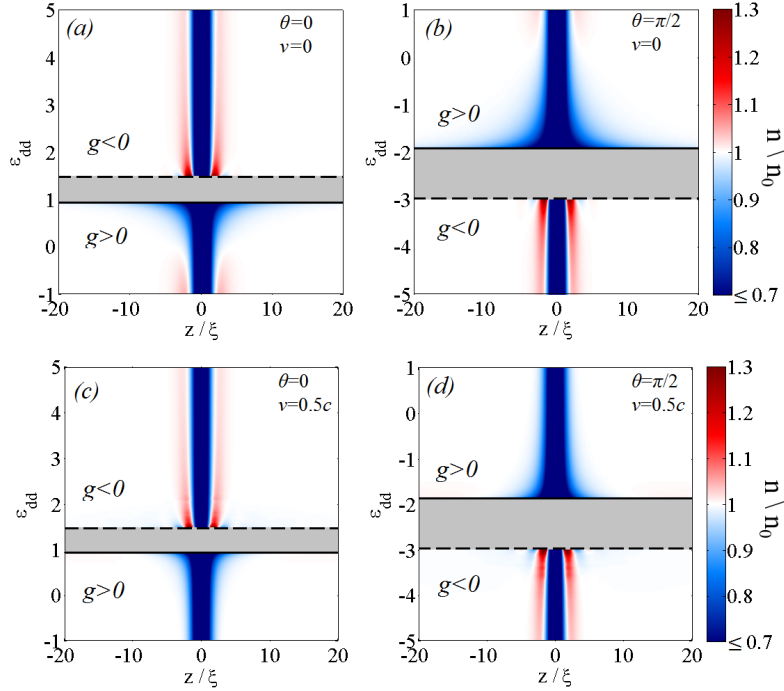


Figure 6.2: Density profiles $n(z)$ for (a) $v = 0$ and $\theta = 0$, (b) $v = 0$ and $\theta = \pi/2$, (c) $v = 0.5c$ and $\theta = 0$ and (d) $v = 0.5c$ and $\theta = \pi/2$, as a function of ε_{dd} with $\sigma = 0.1$. The band (grey) of instability is bounded by the onset of the roton (dashed) and phonon (solid) instabilities. Note that either side of this unstable band, the system is stable for only $g > 0$ or $g < 0$, as indicated.

form symmetrically around the soliton, decaying as they recede from the core. For the cases shown in Fig. 6.2, the ripples can rise to twice the background density with the most prominent parts being the two dominant lobes either side of the dark soliton (see also Fig. 6.3). They arise due to the soliton state mixing with the roton, an effect akin to that predicted for vortices in 2D [205, 364, 363]. The ripples can be understood from an energetic point of view by noticing that they occur when the dipolar interactions are repulsive along the axial direction meaning that the system can lower its energy by placing more dipoles near to the empty core. The repulsive dipolar interaction due to the lobes in turn causes a density reduction next to them, then another peak, and so on. The ripples are thus a direct effect of the long range nature of the dipolar interactions. Despite the density modulations, the soliton depth still follows the relation $n_d/n_0 = 1 - v^2/c^2$, familiar from non-dipolar dark solitons. We also find that the density modulations are slightly enhanced for slower solitons.

The soliton modifies the mean-field dipolar potential $\Phi_{1D}(z)$ in a non-local manner. We can glean some insight into this by considering the behaviour at long range. Expanding the real-space dipolar pseudo-potential Eq. (5.11) around infinity gives $U_{1D}(u) = U_0(4|u|^{-3} - 24|u|^{-5} + \dots)$ [365]. Then, taking the non-dipolar soliton (6.1) as an ansatz,

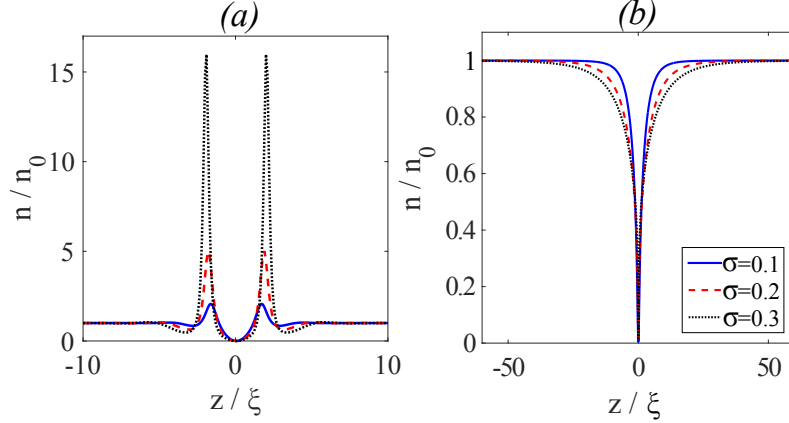


Figure 6.3: Density profiles of the black ($v = 0$) soliton close to the (a) roton instability and the phonon instability (b), for 3 values of σ . Since the roton instability shifts with σ , we consider different values of ε_{dd} in (a): $\varepsilon_{dd} = 1.46$ for $\sigma = 0.1$, $\varepsilon_{dd} = 2.68$ for $\sigma = 0.2$, and $\varepsilon_{dd} = 7.60$ for $\sigma = 0.3$. In (b) we take $\varepsilon_{dd} = 0.95$ throughout.

the asymptotic form of Φ_{1D} follows as,

$$\Phi_{1D}(z) \simeq \Phi_0 \left(1 - \frac{\beta n_0 \xi l_{\perp}^3}{e^{2\beta z_0/\xi} |z_0 - z|^3} \right), \quad (6.2)$$

where z_0 is a short-range cut-off to account for the asymptotic behaviour of the mean-field dipolar potential. The two terms represent the background and soliton contributions to Φ_{1D} , respectively. The $1/z^3$ decay of Φ_{1D} demonstrates that the soliton appears as a localised giant dipole, a key result of our work. This is intimately connected to the exponentially-fast decay of the soliton density profile; at large distances the soliton profile scales as $n(z) \simeq (n_0 - n_{\min})e^{-z/\xi}$. In contrast, a slow power-law-decaying density profile would render the object as an extended dipole at all scales, as for vortices in 2D [363]. The negative sign on the soliton contribution suggests that the soliton may be viewed as a collection of *anti-dipoles* superposed on a homogeneous background of conventional dipoles. This observation will help us below to interpret the modified form of the soliton-soliton collisions as due to the interaction of these anti-dipoles.

As previously discussed in Sec. 5.2, the roton and its instability is sensitive to the condensate width, σ . To determine the effect of σ on dark solitons, Fig. 6.3 compares the black soliton solution close to the (a) roton instability and (b) phonon instability, for different values of σ . Note that we maintain $\sigma < 1$ throughout so to satisfy the governing criteria for a quasi-1D condensate. As σ increases the system becomes less “1D” in nature and the effects of dipolar interactions become more pronounced. At the roton instability, the density ripples grow rapidly with σ , becoming as large as $15n_0$ for $\sigma = 0.3$ (dotted black line). The length scale of the ripples also increases with σ ; this is consistent with the earlier

homogeneous analysis, which showed the roton wavelength to increase with σ (Fig. 5.3 (c)). Meanwhile, at the phonon instability the soliton has a funnel shaped density profile, which widens with σ . Having explored the dependency of σ we will employ $\sigma = 0.1$ for the remainder of our work (the relevant homogeneous stability diagrams being shown in row (a) of Fig. 5.2).

We briefly comment on the manifestation of the phonon and roton instabilities on the soliton solutions. Imagine crossing the phonon instability threshold, from the stable side to the unstable side. The net interactions switch from repulsive to attractive, such that dark solitons are no longer stable. At the same time the background condensate undergoes a modulational instability, as per the non-dipolar attractive condensate [366], and fragments into bright soliton-like structures (the stable structures under net attractive interactions). Next consider crossing the roton instability, again from stable to unstable. The ripples surrounding the dark soliton grow and we find the BEC eventually collapses. However, in both cases, the sharp growth in density means that higher-order effects such as three-body losses [67] and quantum fluctuations [221] become important. Such physics is not contained within our dipolar GPE and is beyond the scope of this work.

6.1.3 Integrals of motion

The family of non-dipolar dark solitons [Eq. (6.1)] possess an infinite number of integrals of motion (viz. conserved quantities). The first three of these have a clear physical meaning: the soliton normalisation, momentum, and energy [178, 147]. In order to calculate finite values for each of these quantities, we compute their *renormalised* versions, that is, the difference between the quantity in the presence and absence of the soliton. In this subsection we generalise these quantities for dipolar dark solitons and explore their dependence on the dipolar parameters.

The renormalised norm and momentum of the dark soliton are defined as

$$N_{\text{sol}} = \int_{-\infty}^{\infty} dz (n_0 - |\psi|^2), \quad (6.3)$$

$$P_{\text{sol}} = \frac{i\hbar}{2} \int_{-\infty}^{\infty} dz \left[\psi \frac{\partial \psi^*}{\partial z} - \psi^* \frac{\partial \psi}{\partial z} \right] \left(1 - \frac{n_0}{|\psi|^2} \right), \quad (6.4)$$

where n_0 is the homogeneous background density. The renormalised soliton energy can be written as

$$E_{\text{sol}} = \int_{-\infty}^{\infty} dz \left[\frac{\hbar^2}{2m} \left| \frac{\partial \psi}{\partial z} \right|^2 + \frac{g}{4\pi l_{\perp}^2} (n_0 - |\psi|^2)^2 \right] + \frac{1}{4\pi} \int_{-\infty}^{\infty} dk_z n(-k_z) \tilde{U}_{1D}(k_z) n(k_z), \quad (6.5)$$

where $n(k_z) = \mathcal{F} [n_0 - |\psi|^2]$. In the absence of a soliton, for which $\Phi_{\text{dd}} = \Phi_0$ and $|\psi|^2 = n_0$, this expression correctly reduces to zero.

In the absence of dipoles and using the soliton solution (6.1), the renormalised norm, momentum and energy follow as

$$N_{\text{sol}}^0 = 2\xi n_0 \beta, \quad (6.6a)$$

$$P_{\text{sol}}^0 = -\frac{2\hbar n_0 v \beta}{c} + 2\hbar n_0 \arctan\left(\frac{c\beta}{v}\right), \quad (6.6b)$$

$$E_{\text{sol}}^0 = \frac{4}{3} n_0 \hbar c \beta^3, \quad (6.6c)$$

where, recall, $\beta = \sqrt{1 - v^2/c^2}$. Meanwhile the effective mass of the non-dipolar dark soliton is found from the relation $m_{\star}^0 = \partial P_{\text{sol}}^0 / \partial v$, and is given by

$$m_{\star}^0 = -\frac{4\hbar n_0 \beta}{c}. \quad (6.7)$$

We evaluate the norm, momentum and energy of the dipolar solitons numerically according to Eqs. (6.3-6.5). In the left rows of Fig. 6.4 (a-c) these conserved quantities are plotted as a function of the soliton speed for three values of ε_{dd} , with the polarisation angle fixed to $\theta = 0$. Note that these three values of ε_{dd} correspond to ^{168}Er parameters ($\varepsilon_{\text{dd}} = 0.4$) and near to the phonon ($\varepsilon_{\text{dd}} = 0.8$) and roton instabilities ($\varepsilon_{\text{dd}} = 5$). Throughout, the dipolar results show the same qualitative structure as the non-dipolar result (solid black line), but can be quite different quantitatively. The soliton norm N_{sol} [Fig. 6.4 (a), left] decreases monotonically with speed due to the reduction in the soliton depth for larger speeds, becoming zero for $v = c$ when the soliton is indistinguishable from the background. The soliton momentum P_{sol} [Fig. 6.4 (b), left] also decreases monotonically with v , due to the decreasing norm and decreasing phase gradient (the phase gradient determines the local fluid velocity according to $u(z) = (\hbar/m)\partial_z S(z)$, where $S(z)$ is the phase profile) across the soliton. It has a universal value for $v = 0$ of $P_{\text{sol}} = \pi\hbar n_0$ due to the π -phase-step profile of the $v = 0$ solitons. The momentum becomes zero for $v = c$ when the norm and phase gradient reach zero. The dipoles have the greatest effect on P_{sol} for intermediate velocities. Finally, the soliton energy E_{sol} [Fig. 6.4 (c), left] also decreases with v , associated with the decreasing interaction energy as the soliton gets increasingly shallow and the decreasing kinetic energy due to the reduced density and phase gradients, and at $v = c$ the energy $E_{\text{sol}} = 0$.

Close to the phonon instability (blue dashed lines) the integrals of motion tend to be larger than the non-dipolar case. This can be related to the wide funnel-shaped profile which develops close to this instability. This vastly increases the effective volume of the soliton core, i.e. the norm. This in turn raises the momentum and energy (in the latter case, due primarily to the increased interaction energy associated with the larger density depletion). The momentum and energy are also modified by density gradients. Mean-

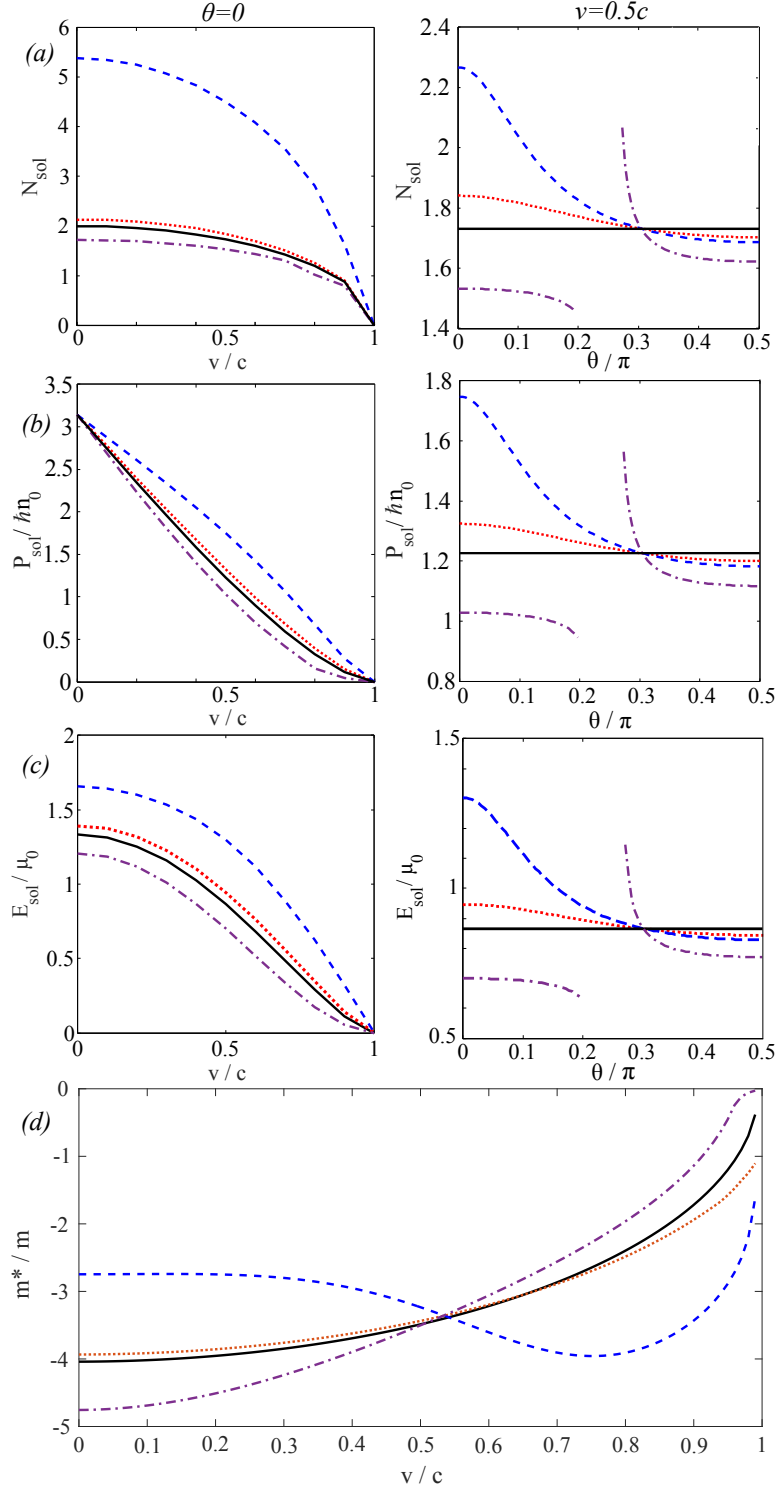


Figure 6.4: Three integrals of motion, the soliton (a) norm, (b) momentum, (c) energy, as a function of v/c (left column, with $\theta = 0$) and θ (right column, with $v = 0.5c$). (d) The soliton effective mass m^* as a function of soliton velocity. All plots contain four lines showing the non-dipolar solution (solid black), $\epsilon_{dd} = 0.4$ (dotted red), $\epsilon_{dd} = 0.8$ (dashed blue), and $\epsilon_{dd} = 5$ (purple dot-dashed).

while, close to the roton instability (purple dot-dashed line) the integrals of motion tend to be smaller. The density ripples which form here act to reduce the effective volume of the soliton core, which reduces the momentum and energy relative to the non-dipolar case.

Finally, in the right rows of Fig. 6.4 (a-c) the conserved quantities are plotted as a function of the polarisation angle for the three values of ε_{dd} , while keeping the soliton speed fixed ($v = 0.5c$). The non-dipolar result is constant in each plot. What is particularly prominent is that the θ dependence is the same for all 3 integrals of motion, with only the scale changing. At the magic angle, $\theta_{\text{m}} \approx 0.3\pi$, the integrals equal the non-dipolar result, due to the vanishing of the dipolar potential here. Note that the gap in the curve for $\varepsilon_{\text{dd}} = 5$ is due to the absence of stable solutions here, consistent with the stability diagram in Fig. 5.2 (a).

The effective mass of the soliton, defined as $m^* = \partial P_{\text{sol}} / \partial v$, is shown in Fig. 6.4 (d). The effective mass is negative throughout, tending towards zero effective mass when $v = c$, as expected. For most cases the effective mass increases monotonically with v . However, close to phonon instability it has a unusual form, being approximately constant for $v/c \lesssim 0.4$ and decreasing to a local minimum at $v/c \approx 0.75$.

6.2 Dynamics of dipolar dark solitons

In this section we explore the rudimentary dynamics of the dipolar dark solitons. In particular we seek to establish their soliton-like nature. We will approach this by reference to the general definition of a soliton given by Johnson and Drazin [149], which is of three key properties: (i) permanent form, (ii) localised within a region of space, and (iii) emergence from collisions unchanged, barring a phase shift. The results presented here are based on numerical propagation of the 1D (lab-frame) dipolar GPE using the Crank-Nicolson method, using a suitable initial condition featuring soliton solutions obtained from the BCGM method.

6.2.1 Propagation

Figure 6.5 shows the evolution of a $v = 0.5c$ dipolar dark soliton (with fixed $\theta = 0$) for three values of ε_{dd} : 0.4 (corresponding to ^{168}Er), 0.8 (close to the phonon instability) and 5 (close to the roton instability). Insets show the density and phase profiles across the soliton. For all three cases, the soliton maintains a permanent and localised form, with no radiative losses. It also undergoes centre-of-mass translation at the expected speed. As such, these states satisfy the soliton criteria (i) and (ii) above. It is also worth observing the phase profile across the soliton. For $\varepsilon_{\text{dd}} = 0.4$ [Fig. 6.5(a)], the phase profile is practically identical to that of the non-dipolar dark soliton, with a tanh-shaped step which relaxes

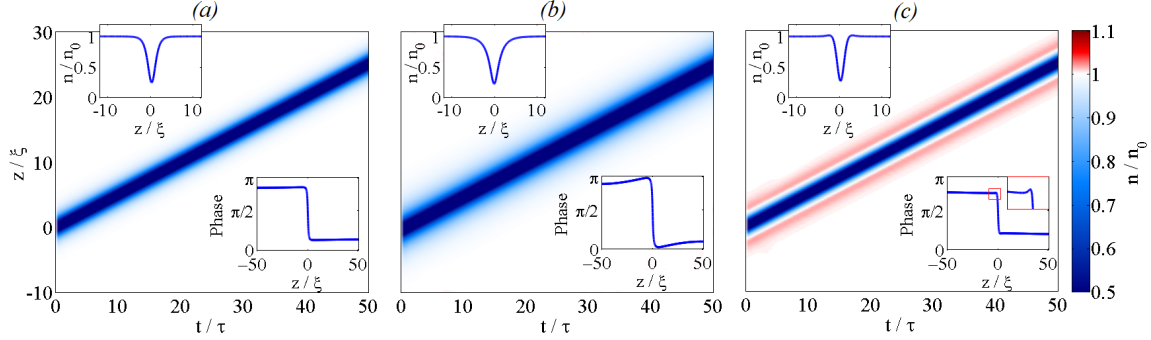


Figure 6.5: Single dipolar dark solitons propagating with unchanging form with speed $v = 0.5c$ (and $\theta = 0$) for (a) $\varepsilon_{dd} = 0.4$ (^{168}Er parameters), (b) $\varepsilon_{dd} = 0.8$ (close to the phonon instability), and (c) $\varepsilon_{dd} = 5$ (close to the roton instability). Top left insets show the soliton density profile and bottom right insets show the soliton phase profile.

to the asymptotic value over a short length scale of the order of the healing length. Close to the instabilities, the phase relaxes over a much larger length scale, of around $\sim 50\xi$ close to the phonon instability [Fig. 6.5(b)] and around 400ξ close to the roton instability [Fig. 6.5(c)]. In all cases the total asymptotic phase slip is the same as for the non-dipolar soliton (this is not directly evident from the inset in (c) due to the limited length range of this plot). Close to the instabilities the phase profile also features distinctive prominences. At the phonon instability these are broad, while at the roton instability they are of order of the roton length scale.

6.2.2 Collisions

In non-dipolar systems the interaction between multiple dark solitons has been experimentally observed and theoretically studied [187, 367]. In a symmetric collision for solitons satisfying $0 < v/c < 0.5$ the s-wave interactions create a repulsive force causing the solitons to appear to reflect at short distance. For velocities satisfying $0.5 \leq v/c < 1$ the solitons appear to pass through each other. In both cases the outgoing solitons are unchanged from the incoming form, barring a phase shift. Here we explore the soliton collisions further, exploring the role of the experimentally-tunable interaction parameter ε_{dd} and the soliton speed. We investigate the effect of the dipolar contribution near to the instabilities, for a system comprised of ^{168}Er atoms [16], with polarisation $\theta = 0$.

Figure 6.6 presents a series of dark soliton collisions for (left column) slow incoming solitons ($v = \pm 0.1c$) and (right column) faster solitons ($v = \pm 0.5c$), and for various values of ε_{dd} . For comparison, the non-dipolar collisions are also shown (row (a)); these confirm the apparent bouncing for low collisional speeds and apparent transmission for higher speeds. For relatively weak dipolar interactions (row (b), $\varepsilon_{dd} = 0.4$) the soliton collisions are virtually indistinguishable from the non-dipolar case, with a short-range-dominated

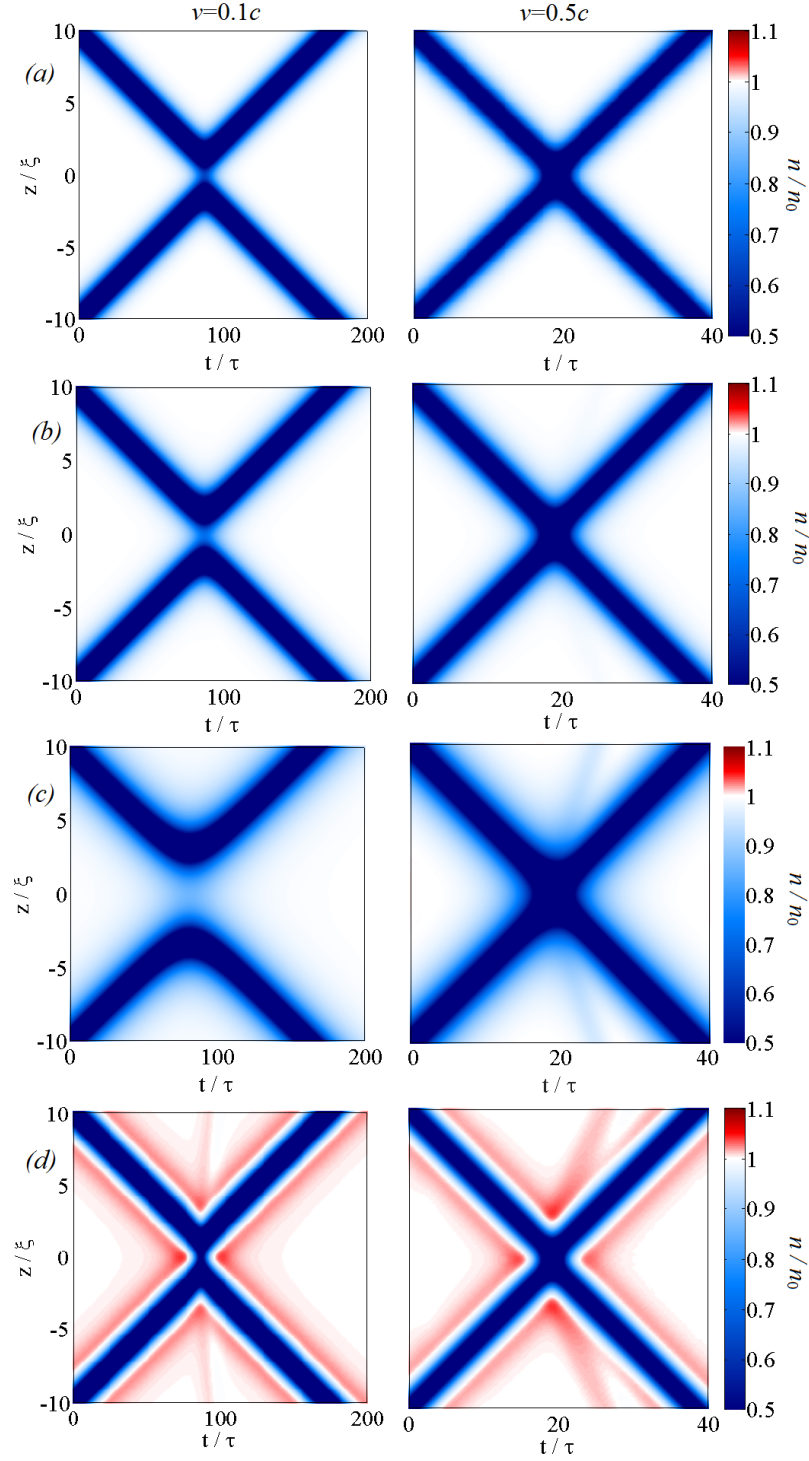


Figure 6.6: Collisions of two dark solitons at low speed ($v = \pm 0.1c$, left panels) and higher speed ($v = \pm 0.5c$, right panels) for (a) $\varepsilon_{dd} = 0$, (b) $\varepsilon_{dd} = 0.4$, (c) $\varepsilon_{dd} = 0.8$ and (d) $\varepsilon_{dd} = 5$. The polarisation angle is taken to be $\theta = 0$.

interaction and the solitons emerging unscathed.

For stronger dipolar interactions (row (c), $\varepsilon_{dd} = 0.8$), the dipolar interactions have a noticeable effect on the soliton interactions, particularly at low speeds. Here the solitons appear to bounce at a considerably greater separation than the non-dipolar case. This effect can be directly related to the dipolar interactions. Since $\theta = 0$ and $C_{dd} > 0$ for this case, the dipoles lie end-to-end and attract each other. However, the dark soliton is an object with negative effective mass, and thus experiences the opposite of this force, hence they repel each other¹. This repulsive contribution to the dark soliton interaction will arise whenever the dipoles are net repulsive, i.e. when $C_{dd} > 0$ with $\theta < \theta_m$ or when $C_{dd} < 0$ with $\theta > \theta_m$. The repulsive nature of the collision becomes washed out at higher incoming speeds (row (c), right panel). While the soliton collision is stable at low speed (left panel), at high speed the collision is inelastic, with energy lost from the solitons via the emission of sound waves (visible as bands propagating away from the collision at the speed of sound).

The case of $\varepsilon_{dd} = 5$ (row (d)) instead has $C_{dd} < 0$, i.e. repulsive dipoles. This in turn leads to an attractive contribution to the soliton interaction, and this is clearly observed in the corresponding soliton collisions. Note the distinctive sharp “pinching” of the solitons during their collision at low speed. More generally, this attractive contribution arises whenever the dipolar interactions are net attractive, i.e. when $C_{dd} < 0$ with $\theta < \theta_m$ or when $C_{dd} > 0$ with $\theta > \theta_m$. Here, for both low and higher incoming speeds, the collisions are inelastic through sound emission.

Note that when the dipoles are polarised at the magic angle θ_m the dynamics are equivalent to the non-dipolar case.

Away from the phonon and roton instabilities, the solitons collide elastically, and emerge unscathed from the collision. This satisfies the third soliton criteria outlined above. However, close to the instabilities, the collisions become dissipative, with sound being radiated away. This is particularly prevalent for higher speed collisions. We note, however, that the energy dissipated into sound waves during a single collision is typically very small, for example, in the maximally-dissipative case presented in Fig. 6.6 ((d), right panel), the energy loss is $\sim 10^{-3}\%E_{\text{sol}}$.

¹Consider Newton’s second law for a negative effective mass $m = -|m_\star|$,

$$F = ma = -|m_\star|a \implies a = \frac{1}{|m_\star|}\nabla V, \quad (6.8)$$

Thus the force exerted from an attractive potential will cause the “particle” to be repelled.

6.3 Two-soliton interaction potential and bound states

We can further understand the soliton-soliton interaction through an effective particle-like interaction potential. First, we state the analytic two-soliton solution to the non-dipolar 1D GPE [147],

$$\psi_{2s}(z, q) = \{F(z, q)/G(z, q)\} \exp(-i\mu t/\hbar) \quad (6.9)$$

with,

$$F(z, q) = 2\sqrt{n_0} \left[(1 - 2v^2/c^2) \cosh(2\beta q/\xi) - (v/c) \cosh(2\beta z/\xi) + i2(v/c)\beta \sinh(2\beta q/\xi) \right],$$

$$G(z, q) = 2\cosh(2\beta q/\xi) + 2(v/c)\cosh(2\beta z/\xi),$$

for separation between the two solitons q . Using this as an input to the energy equation Eq. (6.5), we find the interaction energy of two solitons at z_1 and z_2 (defined by their density minima), with separation $q = |z_1 - z_2|$, as,

$$V(q) = E_{\text{sol}}[\psi_{2s}(z, q)] - E_{\text{sol}}[\psi_s(z, z_1)] - E_{\text{sol}}[\psi_s(z, z_2)]. \quad (6.10)$$

This estimate $V(q)$ is calculated semi-analytically based on the non-dipolar two-soliton solution with small incoming speed (for larger speeds, the effective masses of the solitons change considerably during the collision, complicating this particle-like picture)². Figure 6.7(a) shows the soliton-soliton interaction potential, again for ¹⁶⁸Er parameters. The non-dipolar contribution V_0 (dashed red line) dominates only at short-range, consistent with the repulsive bouncing of two non-dipolar solitons [Fig. 6.6(a)].

For $\theta = 0$, the dipolar interaction potential V_{dd} (black dot-dashed line) is repulsive and non-local, consistent with the bouncing at increasing separation observed in Fig. 6.6(c). However, for $\theta = \pi/2$, V_{dd} (blue dotted line) is attractive at long-range. The payoff between this non-local attraction and the short-range repulsion from V_0 , conspires to form a total potential (solid black line) analogous to the Lennard-Jones inter-atomic potential: an energy minimum at finite q , with rapidly increasing potential at short-range and slowly increasing potential at larger range. This raises the prospect of forming a two-soliton bound state, analogous to a diatomic molecule.

The possibility of supporting a two-soliton bound state is probed through GPE simulations starting with two stationary solitons a distance q_0 apart, shown in Fig. 6.7(b)-(d). For sufficiently small q_0 (a), the solitons initially feel a strongly repulsive short-range interaction, repel and acquire sufficient kinetic energy to escape to infinity. For greater

²Note that the true $V(q)$ is flipped ($V(q) \rightarrow -V(q)$), but due to the negative effective mass of the solitons we have presented the data as it appears in Fig. 6.7(a) for visual ease.

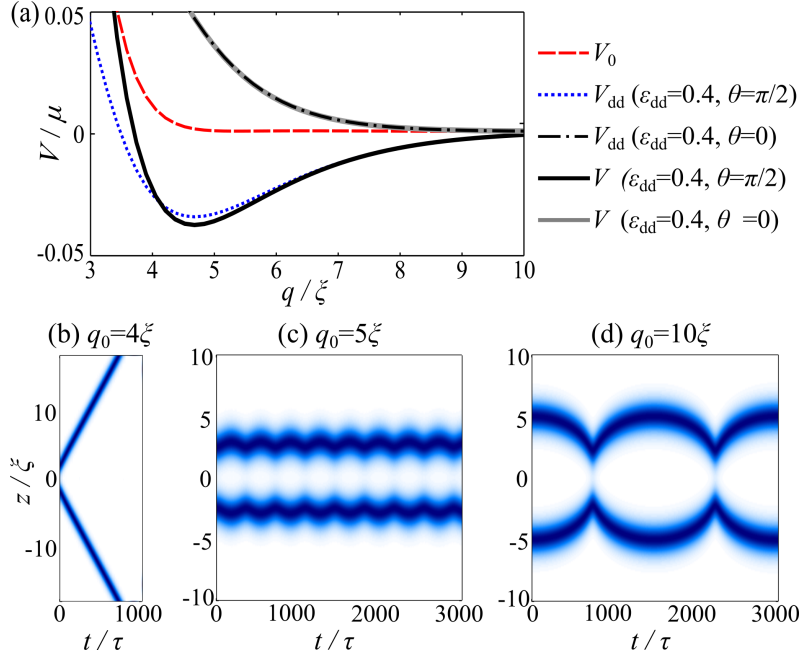


Figure 6.7: (a) Soliton-soliton interaction potential V as a function of separation q for $\epsilon_{dd} = 0.4$ and $\theta = \pi/2$ (estimated using the non-dipolar two-soliton solution in the low speed limit with arbitrary value $v = 0.001c$). The local minimum indicates a bound state. The non-dipolar V_0 and dipolar V_{dd} contributions are indicated. (b)-(d) Corresponding GPE dynamics starting from two stationary solitons a distance q_0 apart. For (a) $q_0 = 4\xi$, the solitons repel, while for (b) $q_0 = 5\xi$ and (c) $q_0 = 10\xi$, bound state oscillations are evident.

separations, e.g. (b) and (c), the solitons initially have negative potential energy and are restricted to execute oscillations in q about the potential minimum, analogous to vibrational modes of a diatomic molecule. For large initial separations $q_0 \gg q_{\min}$, the solitons experience a weak gradient in $V(q)$ and undergo slow oscillations.

Well away from the roton instability and phonon instability, these bound-state oscillations persist ad infinitum (within the zero-temperature GPE). However, close to these instabilities, repeated sound emission during the collisions leads to the counter-intuitive situation where the solitons *increase* their oscillation amplitude and ultimately *escape* the bound state by *losing* energy; this is related to the negative effective mass of the soliton and is analogous to anti-damping effects in external potentials [179].

We further investigate the properties of the bound state by considering its interaction with another bound state. Figure 6.8 depicts the collisions of two counter-propagating bound states at (a) low and (b) high speed. These moving bound states are formed by repeating the above method for forming bound states, but where both initial solitons have the same non-zero speed. First, it is worth observing from the plot that the bound states are stable to centre-of-mass motion at constant speed. For both low and high speed, the two bound states emerge unscathed from the collision, with their original speeds and

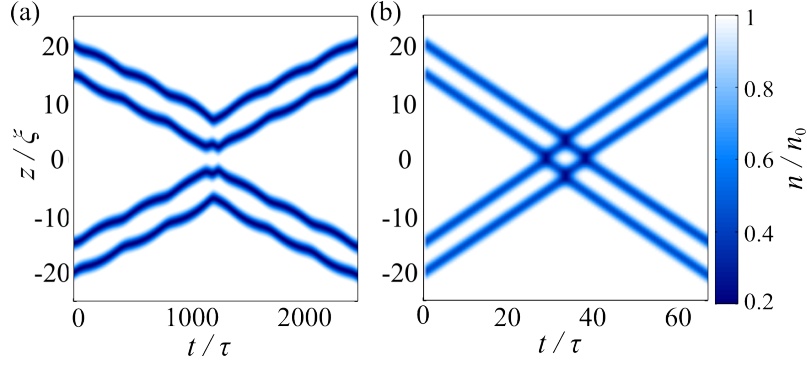


Figure 6.8: Collision of two counter-propagating bound states, with speeds (a) $v = 0.01c$ and (b) $v = 0.5c$. In both cases, the bound states emerge unscathed from the collision, with the only net effect being a phase shift of the outgoing waves (for the high speed case this phase shift is only just visible).

with no radiative losses. The only net difference is that the outgoing bound states both feature a translational offset, termed a phase shift. This is considerably larger for the low speed case, and is just visible in the high speed collision. At low speed, the bound states appear to bounce off each other, just like in the collision of two slow dark solitons [Fig. 6.6], while at high speed the bound states appear to pass through each other, again analogous to the corresponding behaviour of two fast colliding dark solitons [147]. Note that for the high speed case, the solitons in each bound state appear to move in parallel; this is simply because the period of the bound state oscillation is considerably longer than the timescale of the figure and the collision. We have repeated these simulations over a wider range of incoming speeds, and find the same qualitative soliton-like behaviour throughout. These results demonstrate the striking property that the bound states themselves behave like solitons in their interactions with other bound states.

Furthermore, analysing the collision between a bound state and a single incident dark soliton shows the same behaviour, with the single soliton and bound state emerging unscathed from the collision, barring a phase shift.

6.4 Summary

In this work the family of dark solitons supported in a quasi-one-dimensional dipolar Bose-Einstein condensate were studied. A bi-conjugate gradient method was implemented to numerically obtain these non-trivial solitons as stationary solutions in the moving frame, as a function of the dipole-dipole interaction strength (ε_{dd}), the polarisation angle θ and the soliton speed. The phonon and roton instabilities of the system play a key role in modifying the density and phase profiles of the solitons, which can deviate significantly from the non-dipolar form in these regimes. The dipolar dark solitons were characterised

in terms of their integrals of motion (norm, momentum and energy). Due to the modified profiles in the presence of dipolar interactions, these quantities differ from their non-dipolar form, particularly so close to the instabilities.

In isolation, the solitons propagate with unchanged form throughout the parameter space. Away from the instabilities their collisions are elastic, but become dissipative via emission of sound waves close to the instabilities. Thus, close to the instabilities these structures deviate from solitons in a strict sense, although it should be noted that the energy dissipated in a single collision is very small.

The solitons approximate giant localised dipoles, and have non-local soliton-soliton interactions, controllable through the direction of polarisation of the dipoles. When attractive, and in combination with the conventional short-range repulsive interaction, unconventional dark soliton bound states can be realised. These bound states are stable to centre-of-mass propagation at constant speed. Remarkably, they act themselves like solitons during collisions, emerging with unchanged form and speed.

The above soliton behaviour occurs robustly across a wide parameter space, accessible to dipolar BEC experiments [12, 65, 15, 16] and with current dark soliton generation and imaging capabilities [188, 186, 187]. These dipolar dark solitons extend the range of physics of dark solitons as mesoscopic probes of quantum physics [191] to include the interplay with magnetism. Moreover, the effectively instantaneous non-local soliton interaction, and its capacity to be experimentally tuned at will, offers intriguing possibilities for the controlled study of non-locality in complex networks [338], soliton gases [368] and super-solitons [369].

7

Dark solitons in confined dipolar condensates

REMARKABLY, the (non-dipolar) dark soliton, a collective excitation, behaves to first order as a classical particle with negative effective mass, acting under the external potential [178, 147]. For example, in harmonically-trapped BECs, the soliton oscillates at a characteristic ratio $\omega/\sqrt{2}$ of the trap frequency ω [179, 370–378], as confirmed experimentally [187]. This robust result, insensitive to the microscopic atomic interactions, is a signature of matter-wave dark solitons. In this Chapter we establish the form and dynamics of these fundamental structures in trapped BECs featuring dipole-dipole atomic interactions. Interestingly, the oscillations become strongly dependent on the strength and polarisation of the dipolar interactions, and an extended non-local characteristic is evident. We establish these solutions and their oscillatory behaviour, based on one- and three-dimensional mean-field models, and demonstrate that they are accessible to current experiments.

7.1 Dipolar dark solitons in a trapped BEC

We can specify a criterion for dark soliton to exist in the dipolar BEC. Within the local density approximation, the interaction terms in the 1D dipolar GPE reduce to $\hbar\omega_{\perp}[2a_s - a_{\text{dd}}(1 + 3\cos 2\theta)/2]n(z)$, where $n(z) = |\psi|^2$ is the axial density profile. Enforcing these net interactions to be repulsive (positive) leads to the rudimentary criterion to support dark solitons,

$$a_{\text{eff}} = a_s \left[1 + \frac{\varepsilon_{\text{dd}}}{2}(1 - 3\cos^2 \theta) \right] > 0, \quad (7.1)$$

where a_{eff} is an effective s -wave scattering.

Similarly to the soliton-free case Sec. 5.3 we illustrate the dark soliton solutions using the case of dipoles polarised perpendicular to the z -axis ($\theta = \pi/2$). The criteria (7.1) then reduces to $a_s(1 + \varepsilon_{\text{dd}}/2) > 0$, or, in terms of ε_{dd} , $\varepsilon_{\text{dd}} > -2$ for $a_s > 0$ and $\varepsilon_{\text{dd}} < -2$ for $a_s < 0$. We only consider the solutions in these ranges; stable dark solitons require positive

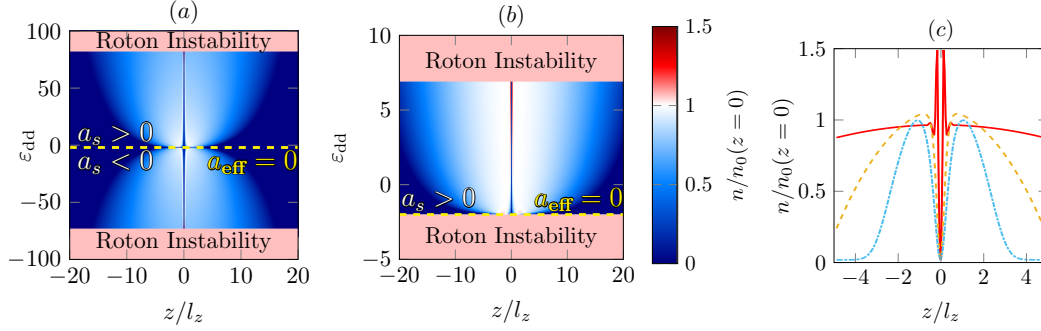


Figure 7.1: Density profile $n(z)$ of the quasi-1D dipolar BEC (polarisation perpendicular to the axis) featuring a central black soliton, as a function of ε_{dd} . The vdW interactions satisfy (a) $|\beta| = 61$, (b) $\beta = 1500$, and the trap frequency ratio $\omega_z/\omega_\perp = 0.0025$ ($\sigma = 0.05$). Only the regimes satisfying Eq. (7.1) are shown, with the line $a_{\text{eff}} = 0$ indicated (yellow dashed line). The color scale is normalised to the peak density of the soliton-free BEC, $n_0(z = 0)$ [see Fig. 5.4]. The roton-unstable regions extend to $\varepsilon_{dd} = \pm\infty$. (c) Example density profiles, for $\varepsilon_{dd} = -1.7$ (blue lines), $\varepsilon_{dd} = -74$ (red lines) and $\varepsilon_{dd} = 0$ (yellow lines).

chemical potential $\mu > 0$, the boundary for which remains close to the criteria specified based on the local density approximation, Eq. (7.1). Figure 7.1(a) maps the density $n(z)$ of the quasi-1D BEC featuring a central black soliton, as a function of ε_{dd} . As a reminder of the notation from Sec. 5.3 the vdW interactions, characterised by the dimensionless parameter $\beta = a_s N l_z / l_\perp^2$ with $l_z = \sqrt{\hbar / m \omega_z}$ the axial harmonic oscillator length, are fixed in amplitude throughout to two characteristic values; a low value $|\beta| = 61$, chosen to show stable solutions for $\varepsilon_{dd} < -2$, and a larger value of $\beta = 1500$ where this region is roton unstable. This black soliton state corresponds to the first excited state of the BEC [147], and is obtained by numerical integration of the 1D dipolar GPE in imaginary time (using a Crank-Nicolson scheme) subject to a π -phase step at the origin.

The black soliton appears as a density notch at the origin, set upon the background BEC. For $\varepsilon_{dd} = 0$ and with $a_s > 0$ the numerical solution (yellow line in Fig. 7.1(c)) closely approximates the product of the exact black soliton solution in a uniform system [177, 178] and the background density $n_b(z)$, i.e. $n(z) = n_b(z) \tanh^2(z/\xi)$, where $\xi = 1/\sqrt{4\pi n_0 a_s}$ is the healing length at the BEC centre. For $\varepsilon_{dd} \neq 0$, and away from $a_{\text{eff}} = 0$ and the roton instabilities, this approximate form holds, with a_s replaced by a_{eff} . However, close to a roton instability the dark soliton develops distinctive peripheral density ripples (e.g. red line in Fig. 7.1(c)), due to the mixing of the roton mode into this state, as reported in Sec. 5.3. Meanwhile, as $a_{\text{eff}} = 0$ is approached, the soliton broadens while the background BEC shrinks. This is expected from observing single solitons near to the phonon instability, for example Fig. 6.3.

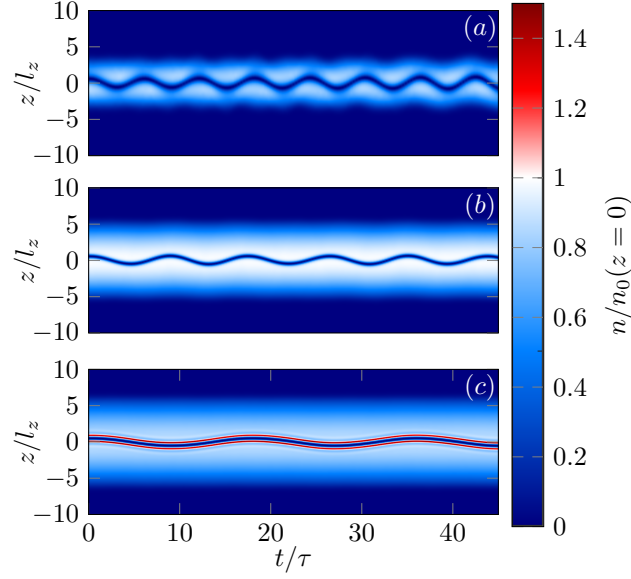


Figure 7.2: Density dynamics of a dark soliton in the quasi-1D dipolar condensate for (a) $\varepsilon_{dd} = -1.7$, (b) $\varepsilon_{dd} = 0$, and (c) $\varepsilon_{dd} = -5.5$. These values correspond to close to $a_{\text{eff}} = 0$, the non-dipolar case, and close to the roton instability, respectively. Remaining parameters as in Fig. 7.1. Time is expressed in units of $\tau = 1/\omega_z$.

7.2 Soliton dynamics

Next we study the oscillation dynamics of the dark soliton, from the initial condition of an off-centre black soliton at $z_0 = 0.5l_z$, although our findings are insensitive to the initial offset. Note that this choice of offset gives $0.01 < z_0/R_z < 0.15$, that is, that the soliton is located within the central region of the condensate, away from the edges. Identical results are obtained by using the product of the background BEC and a travelling dark soliton solution from the uniform system [197, 196]. Figure 7.2 shows three example cases with differing ε_{dd} (close to $a_{\text{eff}} = 0$, the non-dipolar case $\varepsilon_{dd} = 0$, and close to a roton instability). Throughout, the soliton oscillates sinusoidally and stably through the BEC, with preserved form and oscillation amplitude. These stable oscillations exist throughout the stable regime of the background condensate. It is clear, however, that the oscillation period changes with ε_{dd} (even for condensates with similar sizes and curvatures, c.f. Figs. 7.2(b) and (c)). Furthermore, in Fig. 7.2(a) there is evidence that the soliton-sound interactions are activating the dipole mode of the condensate, an effect which has been studied in non-dipolar condensates [379].

To explore the influence of dipolar interactions on the soliton oscillation frequency further, Fig. 7.3 plots the oscillation frequency ω_s of the soliton coordinate (defined as the point of minimum density) based on the 1D dipolar GPE for $|\beta| = 61$ (red triangles) and 1500 (red crosses). For $\varepsilon_{dd} = 0$ we recover the established result for the non-dipolar

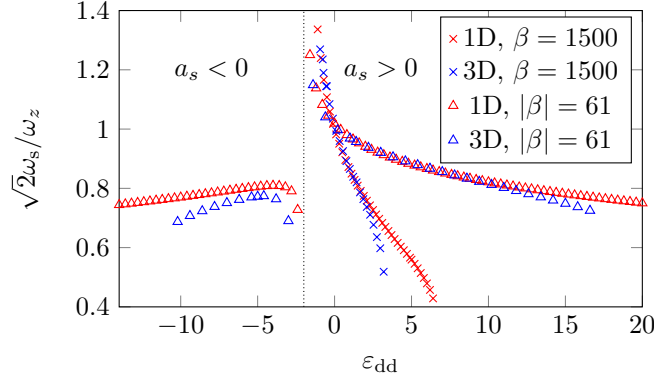


Figure 7.3: Oscillation frequency of the dark soliton (starting as an off-centre black soliton) based on the 1D dipolar GPE (red symbols), 3D dipolar GPE (blue symbols). The system parameters are as Fig. 7.1, but with two values of $|\beta| = 61, 1500$; the 3D system also assumes ^{164}Dy atoms, $\omega_{\perp} = 2\pi \times 16$ kHz and $|a_s| = 50a_0$, where a_0 is the Bohr radius. The 3D system is stable only in the range of markers.

system, $\omega_s \approx \omega_z/\sqrt{2}$ [179]. More generally, ω_s varies sensitively with ϵ_{dd} , deviating by up to 60% from the non-dipolar frequency. In comparison, for $\epsilon_{dd} = 0$, the deviation from $\omega_z/\sqrt{2}$ is only significant in the very weakly-interacting limit $\beta \lesssim 1$; for example, a non-dipolar system with comparable condensate and soliton sizes to Fig. 7.2(a) oscillates to within 5% of $\omega_z/\sqrt{2}$. The scale of this sensitivity is surprising given that the other collective oscillations - the shape oscillations - in elongated dipolar BECs vary much more weakly with ϵ_{dd} (see, e.g. Fig. 11(a) of Ref. [380]).

To assess the role of dimensionality, we have conducted the corresponding simulations using the full 3D dipolar GPE [381, 382]. The dimensional stability of the dark solitons in this system is confirmed. Moreover, the 3D oscillation frequencies (blue markers in Fig. 7.3) are similar to the 1D results, although the roton unstable regimes encroach to lower ϵ_{dd} in 3D. For example, the 3D BEC is stable for $-10 \lesssim \epsilon_{dd} \lesssim -3$ for $a_s < 0$ and $-2 \lesssim \epsilon_{dd} \lesssim 16$ for $a_s > 0$. The decreased stability in 3D is due to the role of transverse magnetostriction in facilitating the roton instability [294]; indeed, as the ratio ω_z/ω_{\perp} is decreased (system made more elongated), the roton instability is suppressed and approaches the 1D behaviour.

Finally, we use 3D simulations to examine the dark solitons achievable in the elongated system of a recent experiment [221] with ^{164}Dy atoms ($a_{dd} = 132a_0$), $\theta = \pi/2$ and $(\omega_{\perp}, \omega_z) = 2\pi \times (128, 2)$ Hz, with variations of ϵ_{dd} achieved through Feshbach tuning of a_s [383] (this is distinct to our previous results where β was fixed). Alongside introducing an off-centre black soliton into the initial condition (as done so far), we also imprint a π -phase step in real time, akin to experimental engineering of dark solitons [182, 188]. This generates a soliton plus sound waves. The oscillation frequency and phase diagram

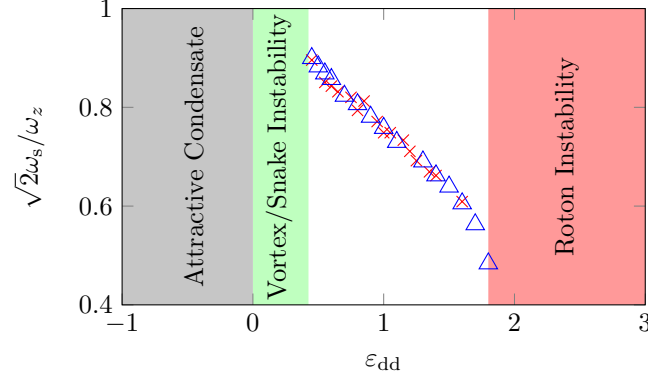


Figure 7.4: Oscillation frequency and phase diagram for a dark soliton in a ^{164}Dy BEC with Feshbach tuning of a_s , based on a recent experiment set-up [221]. Shown are cases where the soliton is imposed in the initial condition (blue triangles, as per Fig. 7.1) and imprinted in real time (red crosses). Outside of the dark soliton regime, the condensate is either roton unstable (red), an attractive condensate incapable of supporting dark solitons (grey), or the dark solitons are dimensionally unstable. Parameters: $\theta = \pi/2$, $(\omega_\perp, \omega_z) = 2\pi \times (128, 2)$ Hz, $a_{dd} = 132a_0$ and $N = 10000$.

is depicted in Fig. 7.4. Stable dark solitons are supported for $0.4 \lesssim \epsilon_{dd} \lesssim 1.8$; across this range ω_s changes by a factor of two. Above this range, the roton instability arises, matching the observed experimental value of condensate collapse for this system. Below this range, the dark solitons undergo the snake instability into vortex rings. This is because the regime of small positive ϵ_{dd} corresponds to large positive a_s and hence a small healing length; when this becomes smaller than the transverse system size, the condensate leaves the quasi-1D regime and becomes 3D in nature. For negative ϵ_{dd} , i.e. negative a_s , the large and attractive contact interactions dominate to form a net attractive trapped condensate, in which dark solitons are not supported.

7.3 Analytic consideration of the oscillation frequency

In this Section we extend the main analytical approaches for describing the particle-like motion of non-dipolar dark solitons in trapped condensates to include dipolar interactions.

The approach we consider follows that presented by Frantzeskakis [147] for the non-dipolar case, which we adapt to include the effect of the non-local dipolar interactions. This approach uses on the definition of the renormalised soliton energy, stated again here as

$$E_{\text{sol}} = \int_{-\infty}^{\infty} dz \left[\frac{\hbar^2}{2m} \left| \frac{\partial \psi}{\partial z} \right|^2 + \frac{g}{4\pi l_\perp^2} (n_0 - |\psi|^2)^2 \right] + \frac{1}{4\pi} \int_{-\infty}^{\infty} dk_z n(-k_z) \tilde{U}_{1D}(k_z) n(k_z), \quad (7.2)$$

and the non-dipolar dark soliton solution Eq. 6.1.

As reported in this thesis, away from the roton and phonon instabilities, the true dipolar dark soliton of the homogeneous system closely matches the (non-dipolar) Shabat-Zakharov soliton (6.1) with the modified scattering length a_{eff} (as defined in Eq. (7.1)). Within the local density approximation, these effective contact interactions account for the effect of the dipolar interactions on the healing length and speed of sound of the system, which in turn specify the absolute size and speed of the soliton. Thus we proceed by approximating the dipolar dark soliton solution as an ansatz given by the Zakharov-Shabat solution (6.1) but with $a_s \mapsto a_{\text{eff}}$. The mapping of the homogeneous chemical potential follows as $\mu = 2\hbar\omega_{\perp}n_0a_s \mapsto \mu = 2\hbar\omega_{\perp}n_0a_s[1 - \frac{1}{4}\varepsilon_{\text{dd}}(1 + 3\cos 2\theta)]$.

For this ansatz the Fourier transform of the renormalised density, $\tilde{f}(k_z) = \mathcal{F}[n_0 - |\psi_s|^2]$, is a function which decreases exponentially with momentum as $1/\xi$. Precisely, in our convention of the Fourier transform, $\tilde{f}(k_z) = -\pi k_z \xi^2 n_0 \text{cosech}\left(\frac{k_z \pi \xi}{2\beta_v}\right) e^{iz_0 k_z}$. The Fourier transform of the dipolar potential $\tilde{U}_{1D}(k_z)$ on the other hand is a function decreasing as $1/l_{\perp}$. Dimensional stability of the dark soliton requires $l_{\perp} < \xi$. Thus in the integral (7.2) one can approximate $\tilde{U}_{1D}(k_z)$ with its expansion around $k_z = 0$,

$$\begin{aligned}\tilde{U}_{1D}(q) &= 4U_0 l_{\perp} \left(q e^q E_1[q] - \frac{1}{3} \right) \\ &\approx -4U_0 l_{\perp} \left(q [\gamma + \log(q)] + \frac{1}{3} \right),\end{aligned}\quad (7.3)$$

where $q = k_z^2 l_{\perp}^2 / 2$, $U_0 = C_{\text{dd}}(1 + 3\cos 2\theta)/32\pi l_{\perp}^3$ and $\gamma \approx 0.56$ is the Euler-Mascheroni constant. Within these approximations, the renormalised energy of the dipolar dark soliton in a homogeneous system as per Eq. (7.2) is,

$$E_{\text{sol}} = \frac{4}{3}n_0\hbar c\beta_v^3 - \frac{C_{\text{dd}}n_0^2(1 + 3\cos 2\theta)}{2\pi^5\xi} \left\{ \frac{\pi^4}{15} \left[\gamma + \log\left(\frac{2\beta_v^2 l_{\perp}^2}{\pi^2 \xi^2}\right) \right] + \mathcal{K}_4 \right\} \beta_v^5, \quad (7.4)$$

where $\mathcal{K}_n = \int_{-\infty}^{\infty} du u^n \log(u^2) \text{cosech}^2 u$ and $\mathcal{K}_4 \approx 9.73$. In the absence of dipoles ($C_{\text{dd}}=0$) this reduces to the well-established result $E_{\text{sol}} = \frac{4}{3}n_0\hbar c\beta_v^3$ [147, 178]. The second, additional term accounts for the dipolar interactions.

Now, to extend this prediction for the soliton energy from a homogeneous condensate to a trapped condensate, we can adopt the method described by Frantzeskakis [384, 147] in which Eq. (7.4) is assumed to hold locally for a background density which varies slowly in space $n(z)$. We replace all density dependence in Eq. (7.4) with the varying density of the harmonically-trapped condensate. We write this density analytically in the Thomas-Fermi limit as $n(z) = n_0 - m\omega_z^2 z^2 / 4\hbar\omega_{\perp}a_{\text{eff}}$, with a_{eff} defined in the main paper, and make the replacement $n_0 \mapsto n(z)$, including $c \mapsto c(z)$ and $\xi \mapsto \xi(z)$, in Eq. (7.4).

Then, expanding the equation in the limit of slow solitons, and after some manipula-

tion, we write the result in the form,

$$E(z, v) = E_0 + \frac{1}{2}m_s v^2 + \frac{1}{4}m_s \omega_z^2 z^2. \quad (7.5)$$

This describes the soliton as a particle with effective mass m_s and rest mass energy E_0 . The effective mass is given by,

$$m_s = -\sqrt{\frac{2n_0}{a_s}} \frac{l_\perp m}{\left(1 - \frac{1}{4}\epsilon_{\text{dd}}(1 + 3\cos 2\theta)\right)} + \frac{5C_{\text{dd}}(1 + 3\cos 2\theta)n_0^{3/2}}{4\sqrt{2}\pi^5 l_\perp^3 \omega_\perp^2 a_s^{1/2} \left(1 - \frac{1}{4}\epsilon_{\text{dd}}(1 + 3\cos 2\theta)\right)^2} \left\{ \frac{\pi^4}{15} \left[\gamma + \frac{2}{5} + \log\left(\frac{4n_0 a_s}{\pi^2}\right) \right] + \mathcal{K}_4 \right\}. \quad (7.6)$$

and the rest mass energy is,

$$E_0 = \frac{4}{3} \left(\frac{2\hbar^3 n_0^3 a_s \omega_\perp}{m \left(1 - \frac{1}{4}\epsilon_{\text{dd}}(1 + 3\cos 2\theta)\right)^2} \right)^{1/2} - \frac{C_{\text{dd}}(1 + 3\cos 2\theta)n_0^{5/2} a_s^{1/2}}{\sqrt{2}\pi^5 l_\perp \left(1 - \frac{1}{4}\epsilon_{\text{dd}}(1 + 3\cos 2\theta)\right)^2} \left\{ \frac{\pi^4}{15} \left[\gamma + \log\left(\frac{4n_0 a_s}{\pi^2}\right) \right] + \mathcal{K}_4 \right\}. \quad (7.7)$$

This result tells us that the dipolar dark soliton behaves as a non-dipolar dark soliton with dipolar effective mass and predicts the soliton oscillation frequency to be,

$$\omega_s = \frac{\omega_z}{\sqrt{2}}. \quad (7.8)$$

This incorrect prediction tells us that the observed soliton oscillation frequency is not obtainable from the energy, with the assumptions used.

Note that if the true (numerically-obtained) dipolar dark soliton solution is employed, then the soliton energy, Eq. (7.4), gives close agreement with the prediction of Eq. (7.5), in the appropriate limit (small soliton oscillation amplitude, low speed, and a Thomas-Fermi-like background condensate).

We further explore the role of the local density approximation through the law of conservation of energy, removing the assumption of a stationary soliton from the previous analysis. We compare the energy of a soliton at two instances in time, denoted in Fig. 7.5 with A and B. Situation A corresponds to the initial condition, $t = 0$, when the soliton is at position $z = z_0$ with $v = 0$. Then the soliton accelerates in the harmonic potential and situation B is reached when the soliton passes the center of the trap - then its position is $z = 0$ with the maximal velocity. We observed numerically that the soliton is moving

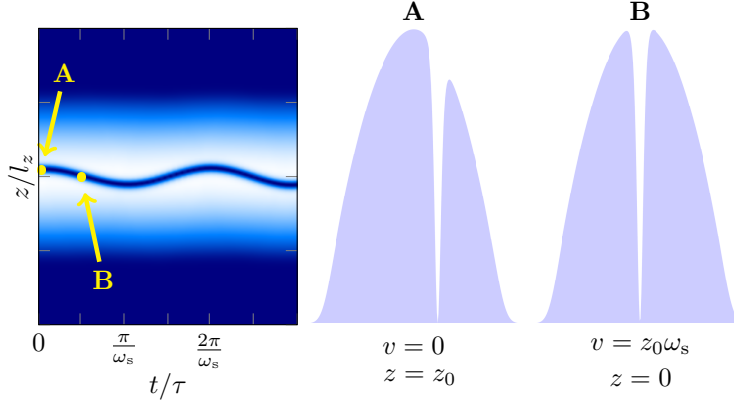


Figure 7.5: Left: Density of the atomic cloud with soliton as a function of time and position. Right: Schematic cut through density profile at two instances of times: $t = 0$, situation A, when the soliton is displaced from the trap center by z_0 and it has a zero velocity, and $t = \pi/(2\omega_s)$, situation B, when the soliton is at a quarter of period, passing the center of the trap with the velocity $\omega_s z_0$.

periodically in the potential (see example in the left panel of Fig. 7.5). Hence, at situation B, the velocity of the soliton should be equal to $z_0\omega_s$. In what follows we rewrite the estimation of the energy, Eq. (7.5), in terms of the chemical potential and velocity of a dipolar soliton:

$$E(\mu, v) = A_0(\mu - mv^2)^{3/2} + A_1(\mu - mv^2)^{5/2} + B_1(\mu - mv^2) \log\left(\frac{\mu - mv^2}{\hbar\omega_\perp}\right). \quad (7.9)$$

The exact form of the coefficients A_0 , A_1 and B_1 do not play any role in the derivation below. If we assume the Thomas-Fermi profile of the gas, then: $\mu(z) = \mu_0(1 - z^2/R_z^2)$, where $R_z = \frac{3}{2} \frac{N\tilde{g}}{\hbar\omega_z}$, $\mu_0 = \frac{3N\tilde{g}}{4R_z^2}$ and $\tilde{g} = 2\hbar\omega_\perp a_s(1 - \epsilon_{dd}(1 + 3\cos 2\theta)/4)$. The energies in both situations, A and B, read:

$$\begin{aligned} E_A &= E(\mu(z_0), v = 0) \\ &= A_0\mu(z_0)^{3/2} + A_1(\mu(z_0))^{5/2} + B_1(\mu(z_0)) \log\left(\frac{\mu(z_0)}{\hbar\omega_\perp}\right), \\ E_B &= E(\mu_0, v = z_0\omega_s) \\ &= A_0(\mu - m(z_0\omega_s)^2)^{3/2} + A_1(\mu - m(z_0\omega_s)^2)^{5/2} + B_1(\mu - m(z_0\omega_s)^2) \log\left(\frac{\mu - m(z_0\omega_s)^2}{\hbar\omega_\perp}\right). \end{aligned}$$

The comparison between both energies is done only in the limit $\epsilon = z_0/R_z \ll 1$, so for solitons relatively close to the trap center. We expand the identity $E_A = E_B$ to the second

order of ϵ . Simple algebra gives

$$\omega_s^2 = \frac{\mu_0}{mR_z^2} \implies \omega_s^2 = \frac{\omega_z^2}{2}. \quad (7.10)$$

The derivation is based on the following approximations:

1. Approximate formula for the soliton energy
2. Local density approximation
3. Expansion with respect to the small parameter z_0/R_z

The last approximation seems to be very reasonable - even for the gas with van der Waals interaction only we expect that the sinusoidal oscillation with frequency $\omega_z/\sqrt{2}$ is valid for solitons localised close to the center of the trap.

We believe the inaccuracy of the local density approximation is due to the long-range interactions between the soliton and background fluid, negating the applicability of the separation of the two.

This discrepancy is not accounted for by the effective mass of the soliton: the denominator of $\sqrt{2}$ in the predicted non-dipolar oscillation frequency is related to the soliton having an effective mass of $M_s = 2m$. We have evaluated, and corrected for, the effective mass of the soliton and find no significant effect. The incapability of conventional methods describing solitons in terms of a particle model, so successful for non-dipolar dark solitons, used to describe the observed oscillations leads us to conclude that the dipolar dark solitons are inherently extended and non-particle-like excitations, which cannot be decomposed from the background BEC.

7.4 Summary

In conclusion, dark solitons are supported in trapped quasi-1D dipolar BECs, providing the background BEC is itself stable and net repulsively-interacting. These excitations are accessible to current experiments. While dark solitons in non-dipolar trapped BECs oscillate at a robust, characteristic ratio of the trap frequency, the oscillations in dipolar condensates become strongly dependent on the atomic interactions, and remarkably more sensitive than the collective surface modes. Similar anomalous oscillations have been predicted across the BEC-BCS crossover in Fermi gases [385]. Analytical models derived from previously successful methods do not capture the interaction-dependent behaviour. The dark soliton is strictly an extended excitation, not amenable to analytical treatment as a (local) particle, decomposable from the background. These states offer a novel platform to study non-local dark solitons, to date observed in optics [342] and liquid crystals [341],

with the immense control afforded by the atomic physics toolbox. Finally, our results show that this species of quantum canary [191] is particularly sensitive to the interactions, suggesting their use to probe the mesoscopic details of the quantum field, such as current open questions over quantum fluctuations in dipolar BECs [223, 222, 228, 296].

8

Dipolar bright solitons

THIS Chapter is organised as follows: we begin by discussing the relevant parameter regimes for finding bright solitons in dipolar condensates confined to a quasi-one-dimensional waveguide. In Sec. 8.1, we procure the dipolar bright soliton solutions as a function of the dipole-dipole strength and polarisation angle, for attractive and repulsive van der Waals interactions. Subsequently in Sec. 8.2 we focus on the interplay of the relative phase with the dipole-dipole interaction strength on soliton-soliton collisions, highlighting regimes of free collisions, bound state formation and soliton fusion, as well as the effect of noise on such collisions. In Sec. 8.3 we characterise the stability of the bright solitons in three dimensions, revealing the parameter regimes where the solitons are stable to collapse and expansion. Our findings are then summarised in Sec. 8.4.

We consider an ensemble of weakly-interacting atoms forming a BEC at zero temperature confined to a quasi-one-dimensional waveguide. The effective 1D dipolar GPE is written as

$$i\hbar \frac{\partial \psi}{\partial t} = \left[-\frac{\hbar^2}{2m} \partial_z^2 + \frac{g}{2\pi l_\perp^2} |\psi|^2 + \Phi_{1D}(z, t) \right] \psi, \quad (8.1)$$

where the one-dimensional dipolar potential is obtained via the convolution theorem as $\Phi_{1D}(z, t) = \mathcal{F}^{-1}[\tilde{U}_{1D}(k_z) \tilde{n}_z(k_z, t)]$, where $\mathcal{F}^{-1}[\dots]$ denotes the inverse Fourier transform.

To obtain the solutions to Eq. (8.1) we work in momentum space using a split operator method. In what follows we adopt the so-called ‘soliton’ units [168, 169], where length, time and energy are measured in terms of $l_z = \hbar/mv$, $\tau = l_z/v$, and $E = mv^2$ respectively, where $v = |g_{1D}|N/\hbar$ and $g_{1D} = g/(2\pi l_\perp^2)$ defines the units of velocity and one-dimensional van der Waals interaction strength respectively. We quantify how one-dimensional the system is through the ratio $\sigma = l_\perp/l_z$. To be in the true one-dimensional limit one must have $\sigma \ll 1$.

8.1 Single dipolar solitons

The local cubic nonlinear Schrödinger equation (Eq. (8.1) in the limit $\varepsilon_{dd} = 0$) is known to possess bright soliton solutions for $a_s < 0$ (corresponding to when the chemical potential

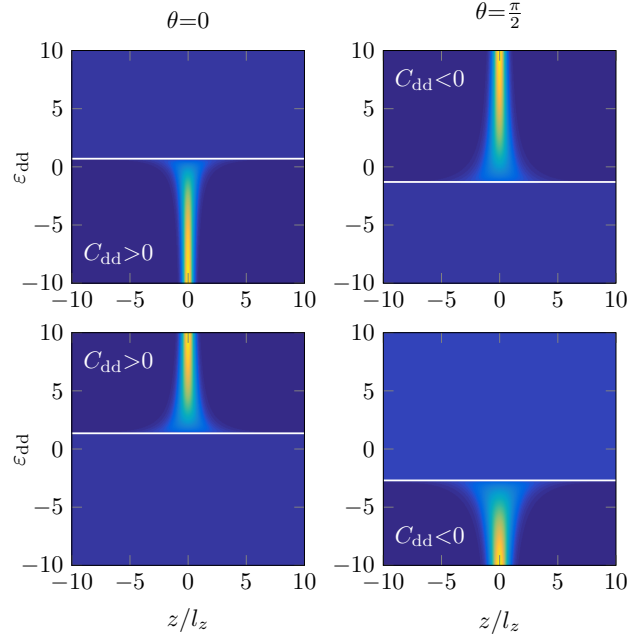


Figure 8.1: Ground state density profiles obtained numerically from Eq. (8.1) as a function of $\text{varepsilon}_{\text{dd}}$. The top (bottom) row corresponds to $\text{sgn}(a_s) < 0$ ($\text{sgn}(a_s) > 0$). The left (right) column corresponds to $\theta = 0$ ($\theta = \pi/2$). The solid white line in each figure indicates the borderline between homogeneous and soliton solutions. Solutions are for $\sigma = 0.2$.

$\mu < 0$). The single soliton solution, which for simplicity we take to be initially positioned at the origin is

$$\psi(z, t) = \frac{1}{2\sqrt{l_z}} \text{sech}\left(\frac{z - ut}{2l_z}\right) \exp\left[i\left\{\frac{m}{\hbar}\left(uz + \frac{u^2 t}{2} + \frac{\omega_{\perp}^2 |a_s|^2 N^2 t}{2}\right) + \phi\right\}\right], \quad (8.2)$$

where u defines the velocity of the bright soliton, while ϕ is the phase. This solution describes a sech-shaped profile which propagates at constant velocity. Here, we explore the family of dipolar bright solitons across the full parameter space afforded by the quasi-one-dimensional model. For a single bright soliton, we can independently vary four key parameters: $\text{varepsilon}_{\text{dd}}$, θ , $\text{sgn}(a_s)$ and also σ . Meanwhile the normalisation is given by $\int dz |\psi(z, t)|^2 = N$. Despite the additional dipolar term present in Eq. (8.1), we will see that the allowed dipolar bright soliton solutions are still sech-shaped. Throughout this work we take $\sigma = 0.2$.

Figure 8.1 shows the ground state densities obtained by solving Eq. (8.1) numerically in imaginary time. Each individual plot is divided into two regions: a flat homogeneous region, corresponding to regimes of net repulsive interactions, and a second region showing the inhomogeneous dipolar bright soliton solutions. The solid white line in each figure shows the crossover between these two parts, which corresponds to when the 1D chem-

ical potential of the ground state solution crosses from positive (homogeneous state) to negative (bright soliton). The top (bottom) rows in Fig. 8.1 correspond to $\text{sgn}(a_s) < 0$ (> 0). Fixing both the sign and value of the van der Waals interactions reveals that altering the polarisation angle of the dipoles between $\theta = 0$ and $\theta = \pi/2$ has the effect of shifting the soliton solutions from $C_{dd} > 0$ ($\theta = 0$) to $C_{dd} < 0$ ($\theta = \pi/2$). The parameter regimes where $C_{dd} < 0$, corresponding to anti-dipoles are found to support soliton solutions as the net interactions are attractive for dipoles polarised perpendicular to the z -axis. We note that in each of the cases presented in Fig. 8.1 the borderline between the homogeneous and soliton solutions does not coincide with $\varepsilon_{dd} = 0$. This can be understood from the form of the dimensionally-reduced pseudo-potential, Eq. (5.11) which comprises both a non-local and local contribution, whose net effect is to shift the value of ε_{dd} at which the chemical potential μ changes sign.

8.2 Collisions

In the absence of dipolar interactions and within the one-dimensional nonlinear Schrödinger equation, bright solitons are known to collide elastically, emerging from the collision with their original speed and form. The net effect of soliton-soliton interaction is a position and phase shift in the outgoing solitons. In this section we study the collisions of two dipolar bright solitons, exploring the role the relative phase plays in collisions as a function of the dipole-dipole interaction and the initial kinetic energy of the solitons. In what follows we simulate two-counter-propagating solitons with equal speed v_i , and take $\text{sgn}(a_s) = 1$ and $C_{dd} > 0$, i.e. the soliton solutions shown in the lower left figure of Fig. 8.1.

8.2.1 In-phase collisions

We consider the collision dynamics of bright solitons with zero initial phase difference, $\Delta\phi = 0$. As we shall see, the collisions of the dipolar solitons can be inelastic. In order to quantify the elasticity of the soliton dynamics, we compute the coefficient of restitution, defined as

$$\eta = \frac{v_1(t_f) - v_2(t_f)}{v_1(t_i) - v_2(t_i)}, \quad (8.3)$$

where v_j is the velocity of soliton j , and t_i and t_f are the initial and final times, respectively. The coefficient of restitution is a measure of the amount of kinetic energy before and after a collision event. If $\eta = 1$ the incoming and outgoing speeds are identical and a collision is perfectly elastic. For $\eta < 1$ the outgoing speeds are less than the incoming speeds, and the collision is deemed inelastic. As we shall see it is also possible to realise $\eta > 1$, corresponding to the outgoing speeds exceeding the incoming speeds, and which can occur, for example, when interaction (van der Waals plus dipolar) energy is transformed

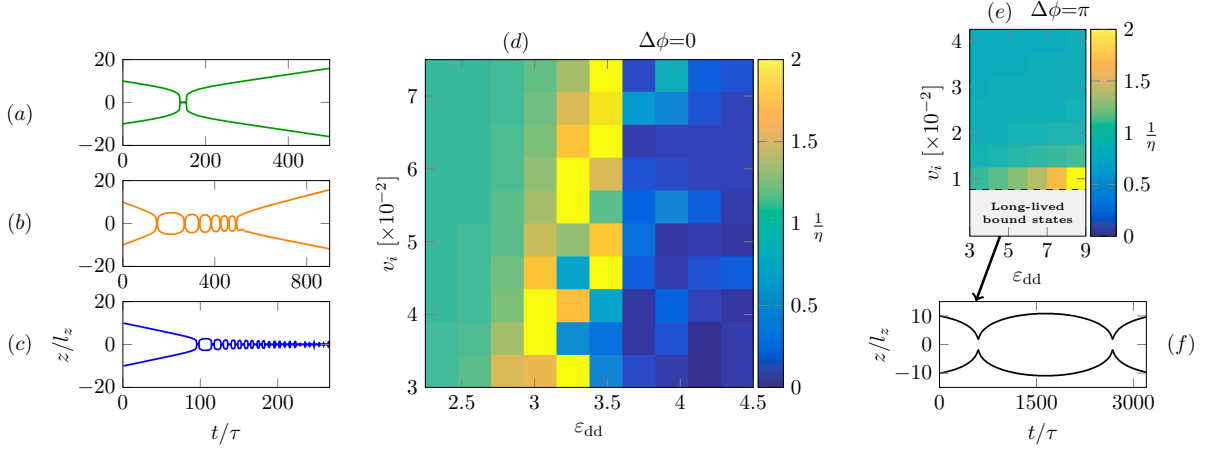


Figure 8.2: Collision dynamics of in-phase and out-of-phase solitons. For in-phase collisions three regimes of dynamics are shown: (a) elastic, (b) bound-state and (c) inelastic dynamics. The coefficient of restitution (Eq. (8.3)) is mapped out as a function of the initial speed v_i and ϵ_{dd} in (d). The corresponding restitution data is computed for the out-of-phase collisions in (e). (f) shows a typical long-lived bound state for out-of-phase dynamics, corresponding to $v_i = 5 \times 10^{-3}$ and $\epsilon_{dd} = 8$.

into kinetic energy during the collision.

The coefficient of restitution η is mapped out in the (ϵ_{dd}, v_i) plane in Fig. 8.2 (d). Each pixel represents an individual simulated collision between two bright solitons, with the color representing the value of the inverse of the coefficient of restitution (we plot $1/\eta$ as this quantity's scale evolves at a slower rate over the parameter range considered). Three different regimes of dynamics can then be identified. For relatively weak dipole-dipole interactions $\epsilon_{dd} \leq 2.5$, the collisions are almost perfectly elastic ($\eta \sim 1$), independent of the initial velocity. Figure 8.2 (a) shows a typical set of collision trajectories in this limit. Here the incoming solitons scatter elastically with each other and escape at longer times. In the intermediate regime, short-lived (meta-stable) bound states are found, whose dynamics are inelastic. Here, the balance of the initial kinetic energy of the solitons to the dipole-dipole strength is favourable to the formation of a short-lived bound state; again a simulation typical of this situation is shown in Fig. 8.2 (b). We note that similar dynamics were reported by Ref. [386] for kink solutions to the sine-Gordon equation, which also exhibited short-lived bound-states. In the limit where the dipole-dipole interactions are large, we instead observe soliton fusion with $1/\eta \ll 1$. A trajectory plot indicative of this limit is shown in Fig. 8.2 (c), showing the collision and eventual merging of the two solitons. Here the individual solitons do not re-emerge at long times.

We can gain an understanding of the short-lived bound state by considering the effect of the in-phase collision on the soliton's kinetic and potential energies. After the bound state has initially formed, each successive collision event causes a redistribution of some interaction (van der Waals and dipolar) energy into kinetic energy, causing the effective

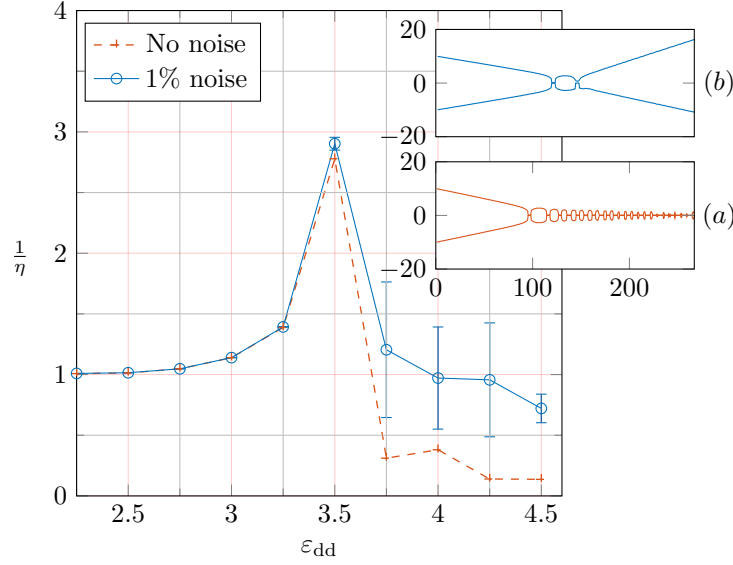


Figure 8.3: Comparison of $1/\eta$ with and without noise for in-phase soliton collisions. The initial velocity in all simulations was $v_i = 7.5 \times 10^{-2}$, corresponding to a line scan along the top row of Fig. 8.2 (d). The two insets (a) and (b) show trajectories associated with $\epsilon_{dd} = 4.5$ without and with noise respectively.

oscillation frequency of the soliton molecule to increase. Eventually, this is enough to cause the bind to break, releasing the two solitons. Note that the total energy remains constant throughout the simulations.

8.2.2 Out-of-phase collisions

It is also pertinent to consider the equivalent dynamics for out-of-phase dipolar bright solitons, with Fig. 8.2 (e) plotting $1/\eta$ in the (ϵ_{dd}, v_i) plane. For relatively large incoming speed, the dynamics are almost elastic ($\eta \sim 1$), while for increasing dipole strength or decreasing incoming velocity, the dynamics are instead found to be increasingly inelastic. This system has a regime of long-lived bound states occurring for low incoming speeds, with example collision trajectories shown in the panel Fig. 8.2 (f).

The binding of two out-of-phase dipolar bright solitons, has been studied previously by Refs. [272, 271]. Unlike their in-phase counterparts, the π phase difference preserves long-lived bound states. One cannot assign a value of η to the collisions in this regime.

8.2.3 Noise

In order to quantify the collisional sensitivity of the dipolar bright solitons, we calculate the coefficient of restitution in the presence of noise. The noise is implemented by introducing a random term to the phase with mean zero whose amplitude $\mathcal{N}_{\text{noise}}$ is a given

fraction of the initial peak density of the soliton density such that

$$\mathcal{N}_{\text{noise}} = \mathcal{N}_0 \max(n(z)) , \quad (8.4)$$

where $0 < \mathcal{N}_0 \leq 1$, and $\max(n(z))$ is the peak soliton density. As an example we consider $1/\eta$ versus ε_{dd} , for a fixed incoming speed and for in-phase collisions. Figure 8.3 shows a comparison of $1/\eta$ with $\mathcal{N}_0 = 0$ (no noise) and $\mathcal{N}_0 = 10^{-2}$. In the presence of noise, each data point was obtained by averaging over 10 individual simulations. The error bars represent the standard deviation. For low values of ε_{dd} , the value of $1/\eta$ follows very closely the value obtained in the absence of noise. This is attributed to the elastic dynamics being insensitive to the phase noise. On the other hand, for stronger dipolar interactions, there is a marked deviation from the no-noise case, resulting in a larger value of $1/\eta$. In this regime, the presence of noise introduces an apparent repulsion between the solitons, which is large enough to make the collisions shown in Fig. 8.3 elastic. Such an effect has also been noted in non-dipolar bright soliton collisions [387]. We see qualitatively the same behaviour for different strengths of noise, with increasing amounts of noise causing the bound-states to break sooner, until no bound-states are formed.

A corollary of the phase noise is that the bound state dynamics in the presence of noise show fewer oscillations before escaping their bind. This effect is illustrated in the soliton trajectories with/without noise in insets Fig. 8.3 (a) and (b). The presence of only small amounts of noise demonstrates how sensitive the binding dynamics are: Fig. 8.3 (b) illustrates that only one oscillation can occur in this example before the solitons escape. For larger amounts of noise the bound states are no longer present, even at these larger values of ε_{dd} . On the other hand, the collisions for out-of-phase solitons, in contrast, are insensitive to noise. The effective repulsion in these collisions serves to stabilise the collisions against the noise.

Although the analysis presented here is rudimentary, it nonetheless allows one to comment on the effect of dissipative processes that are present in a real system, especially those at finite temperature. For example, for small changes in temperature, it is expected that the formation of bound states would be unfavourable. The dipolar interactions would play an increasingly diminished role in the system dynamics, since this term fundamentally depends on the condensate density, which is reduced due to the presence of the non-condensate [27].

8.3 3D stability

A repercussion of attractive interactions between particles is that, for sufficiently large number of particles and/or interaction strength, the mean-field wave function of a 3D condensate is unstable to collapse. For systems possessing only short-ranged isotropic

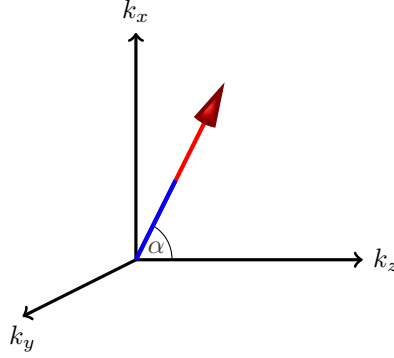


Figure 8.4: Schematic of the dipoles polarisation with respect to the Cartesian momentum axis. The polarised dipoles make an angle α with the k_z axis.

van der Waals type interactions, the critical point of collapse has been extensively studied in Refs. [388–392], and gives insight into the parameter regimes where one can expect stable soliton dynamics [393]. The presence of dipole-dipole interactions are expected to modify the collapse point significantly [294], which has recently been explored for lower dimensional systems in Refs. [394–396] as well as for two-dimensional dipolar bright solitons using 3D simulations [397, 279]. As well as this, the presence of the dipolar interaction can lead to the spectacular d -wave collapse of the condensate in three dimensions [292]. Understanding when the dipolar bright soliton is unstable to collapse in turn allows us to identify regimes of stability applicable to the quasi-one-dimensional dynamics described earlier in Sec. 8.2.

8.3.1 Gaussian variational approach

We employ a variational approach that approximates the wave function of the dipolar soliton as a 3D Gaussian packet with variable width in each dimension [388–391]. This approach has provided important insight into the stability of non-dipolar bright solitons, predicting thresholds for instability which agree closely with experiments [392]. Under general conditions an appropriate variational ansatz is given by

$$\psi(\mathbf{r}) = \sqrt{\frac{N}{\pi^{\frac{3}{2}} \sigma_x \sigma_y \sigma_z \bar{l}^3}} \exp \left[-\frac{1}{2\bar{l}^2} \left(\frac{x^2}{\sigma_x^2} + \frac{y^2}{\sigma_y^2} + \frac{z^2}{\sigma_z^2} \right) \right], \quad (8.5)$$

where the lengthscale $\bar{l} = \sqrt{\hbar/m\bar{\omega}}$ is based on the geometric mean of the transverse trapping frequencies $\bar{\omega} = (\omega_x \omega_y)^{1/2}$ and $\sigma_{x,y,z}$ are the dimensionless variational widths of the packet. Equation (8.5) is normalised to the total number of atoms, $\int d\mathbf{r} |\psi(\mathbf{r})|^2 = N$.

We seek to calculate the total energy of the packet in terms of the above parameters. We write the total energy as $E = E_0 + E_{dd}$, where E_{dd} is the dipolar interaction energy,

while

$$E_0 = \int d\mathbf{r} \left[\frac{\hbar^2}{2m} |\nabla \psi|^2 + V(x, y) |\psi|^2 + \frac{g}{2} |\psi|^4 \right] \quad (8.6)$$

constitutes the remaining energy contributions arising from kinetic energy, potential energy (from the transverse trapping $V(x, y) = \frac{1}{2}m(\omega_x^2 x^2 + \omega_y^2 y^2)$) and van der Waals interaction energy. These contributions to the energy are handled in real space. Meanwhile, the dipolar contribution E_{dd} is evaluated in momentum space, using the convolution theorem. We consider the case where the atoms forming the condensate are polarised by an external magnetic field such that their individual dipole moments form an angle α with the z axis, as shown schematically in Fig. 8.4. This configuration leads to a momentum space pseudo-potential

$$\tilde{U}_{dd}(\mathbf{k}) = \frac{C_{dd}}{3} \left[3 \frac{(k_x \sin \alpha + k_z \cos \alpha)^2}{k_x^2 + k_y^2 + k_z^2} - 1 \right], \quad (8.7)$$

where k_i is the component of the momentum in the i^{th} coordinate direction. The dipolar interaction energy is then

$$E_{dd} = \frac{1}{2} \frac{1}{(2\pi)^3} \int d^3\mathbf{k} \tilde{U}_{dd}(\mathbf{k}) \tilde{n}(\mathbf{k}) \tilde{n}(-\mathbf{k}). \quad (8.8)$$

We perform the integrations appearing in Eq. (8.8) in spherical polar coordinates, and assume the dipoles are polarised parallel to the z axis of the condensate so that $\alpha = 0$. Then, using Eqs. (8.5)-(8.8), we can write a general expression for the variational energy of the system as

$$\frac{E}{N\hbar\omega} = \frac{1}{4} \left[\frac{1}{\sigma_x^2} + \frac{1}{\sigma_y^2} + \frac{1}{\sigma_z^2} \right] + \frac{1}{4\lambda} \left[\sigma_x^2 + \lambda^2 \sigma_y^2 \right] + \frac{\beta}{\sigma_x \sigma_y \sigma_z} \left[1 - \varepsilon_{dd} \int_0^{2\pi} \frac{d\phi}{2\pi} f[\kappa(\phi)] \right], \quad (8.9)$$

where ϕ denotes the azimuthal angles and $f[\kappa(\phi)]$ is defined as

$$f[\kappa(\phi)] = \frac{1 + 2\kappa^2(\phi)}{1 - \kappa^2(\phi)} \frac{\kappa_x \kappa_y}{\kappa^2(\phi)} - 3\kappa_x \kappa_y \frac{\text{atanh} \sqrt{1 - \kappa^2(\phi)}}{(1 - \kappa^2(\phi))^{3/2}}, \quad (8.10)$$

and $\kappa^2(\phi) = (\kappa_x^2 - \kappa_y^2) \cos^2 \phi + \kappa_y^2$ defines the anisotropic aspect ratio function. Equations (8.9) and (8.10) also introduce the trap aspect ratio $\lambda = \omega_y/\omega_x$, the dimensionless interaction parameter $\beta = Na_s/(l_\perp \sqrt{2\pi})$ and the variational aspect ratios $\kappa_{x,y} = \sigma_{x,y}/\sigma_z$.

8.3.2 Stability analysis

For a given set of system parameters (β , ε_{dd} and λ), Eq. (8.9) defines an energy landscape as a function of the dimensionless length scales σ_x , σ_y and σ_z . A stable variational solu-

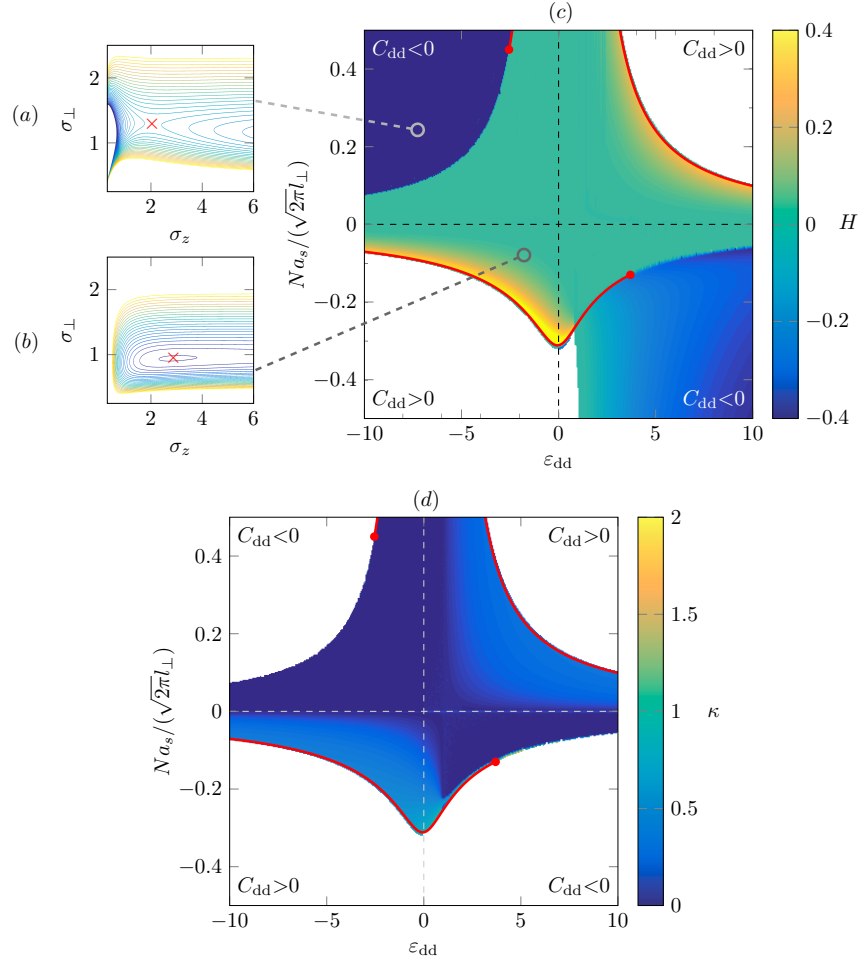


Figure 8.5: Stability analysis of the three-dimensional dipolar soliton. (a, b) Typical plots of the variational energy landscape (corresponding to the parameters annotated in plot (c)). (c) Stability diagram in the $(\varepsilon_{dd} - \beta)$ plane. White regions correspond to an absence of a stationary point in the variational energy landscape. Elsewhere, a stationary point exists, and the color denotes the value of the Hessian at that point. The solid red lines indicate the threshold at which the soliton becomes unstable to collapse. (d) Stability diagram, which in white regions correspond to unstable states and coloured regions to stable states; in the latter case the color indicates the aspect ratio κ of the variational solution. The dashed lines in (c) and (d) indicate the axes $\varepsilon_{dd} = 0$ and $\beta = 0$.

tion is an energy minimum (local or global minimum) in this landscape. It is instructive to consider the non-dipolar case as a pedagogical example, which has previously been studied numerically [392] and using a variational approach [398] to determine the parameter regimes where the bright soliton is stable to collapse. For moderate attractive van der Waals interactions ($N|a_s|/l_\perp \lesssim 0.7$), the energy landscape has a global minimum at the origin ($\sigma_z = \sigma_\perp = 0$), representing a collapsed state, and a local minimum at finite σ_z and σ_\perp , representing the 3D bright soliton solution. This local energy minimum is preserved by a delicate balance between the kinetic and interaction energy. A saddle point separates the local and global minimum. For $N|a_s|/l_\perp \approx 0.7$ the saddle point and local minimum merge; this marks the threshold at which the 3D bright solitons become unstable to a runaway collapse. Meanwhile, for repulsive van der Waals interactions, the energy landscape decreases monotonically towards $\sigma_z \rightarrow \infty$; any wavepacket will disperse axially and no stable solutions exist (unless axial trapping is applied, which we do not consider here). It is the goal of this section to obtain and analyse the nature of the critical points of the full 3D dipolar bright soliton as a function of the interaction parameters β and ε_{dd} .

We seek the points in the energy landscape defined by Eq. (8.9) at which an instability manifests. This analysis in principle requires us to solve the set of equations defined by $\partial E / \partial \sigma_{x,y,z} = 0$ simultaneously with the determinant of the Hessian matrix set equal to zero [393], which are in general a set of four coupled algebraic equations in four unknowns. In order to simplify the general Eqs. (8.9) and (8.10) but still gain useful insight, we consider the axially-symmetric case for which $\omega_x = \omega_y$ and $\sigma_\perp = \sigma_i$ for $i \in \{x, y\}$. The integral over the azimuthal angle ϕ appearing in Eq. (8.9) can then be evaluated as the ϕ dependency of $\kappa^2(\phi)$ is removed in this limit. Although we have assumed the bright soliton is well-described by a Gaussian wave function (Eq. (8.5)), it is worth contrasting the value at which the instability manifests found from the equivalent analysis for $\varepsilon_{\text{dd}} = 0$ assuming either a sech or Gaussian like variational wave function. If β^* denotes the dimensionless critical collapse parameter, then one finds that $\beta_s^* / \beta_g^* = \sqrt{3/\pi}$, which means that the difference between the two approaches is $\sim 2\%$, supporting our choice of a Gaussian variational ansatz. Proceeding, we wish to solve $\partial_{\sigma_z} E = 0$, $\partial_{\sigma_\perp} E = 0$ and $H = \det(\mathbf{J}(\nabla E)) \equiv 0$, where $\nabla = (\partial_{\sigma_z}, \partial_{\sigma_\perp})$, and the matrix elements of the Jacobian \mathbf{J} are defined as

$$J_{ij} = \frac{\partial E}{\partial \sigma_j}, \quad (8.11)$$

in the space $\{\sigma_z, \sigma_\perp\}$. The value of the Hessian H determines the nature of the extrema. For $H < 0$ the extrema is a saddle point; for $H > 0$ it is necessary to evaluate either $\partial_{\sigma_i}^2 E$ at the critical point to determine if the extrema is a minimum ($\partial_{\sigma_i}^2 E > 0$) or a maximum ($\partial_{\sigma_i}^2 E < 0$).

We employ an iterative procedure to obtain numerical solutions for the collapse point

in the $(\beta, \varepsilon_{dd})$ parameter space, using the exact analytical result for $\varepsilon_{dd} = 0$ at which the bright soliton collapses as the initial point to start the numerical calculation from. Figure 8.5 (c) shows the collapse points (solid red), computed numerically. The colouring of each of the four quadrants is found from the Hessian H , evaluated from Eq. (8.11) for a given value of β and ε_{dd} , evaluated at the extrema point. The Hessian gives us insight into the nature of the extrema close to and away from the collapse points of the bright soliton. The white areas of this figure are where there are no extrema, and the bright soliton is unstable to collapse.

The collapse dynamics can be categorised based on the sign of the dipole-dipole interaction parameter C_{dd} . For $C_{dd} > 0$ (bottom left and top right quadrants) the dipoles attract each other in a head-to-tail configuration, and beyond the critical point of collapse no stable dipolar bright soliton can exist (white areas, Fig. 8.5 (c)). On the other hand, when the Hessian $H < 0$, there is a saddle point in the energy surface, and no stable bright soliton can form. These regions are found in both the $C_{dd} < 0$ parts of the parameter space. Alternatively for $C_{dd} < 0$, (bottom right and top left quadrants) the dipoles repel each other in the head-to-tail arrangement, which precludes the bright soliton from collapsing. Instead, one can have a runaway expansion, where the repulsive nature of the dipoles overcomes any attractive forces present. Interestingly, the solutions in these two quadrants do not continue indefinitely, but rather terminate at a point, as indicated by red circles.

Contour plots of the energy surfaces found from Eqs. (8.9)-(8.10) in the σ_z, σ_\perp parameter space accompany Fig. 8.5 (c), Fig. 8.5 (a) and (b). Figure 8.5 (a) shows a typical energy contour in a region where the Hessian $H < 0$, i.e. a saddle point. Meanwhile, a typical ‘bowl’ configuration that the energy takes in stable regions of the $(\beta, \varepsilon_{dd})$ parameter space is shown in Fig. 8.5 (b). This particular plot shows a stable minima indicative of regions where the bright soliton is stable. Figure 8.5 (d) shows a shaded plot of the stable regions where one can expect a bright soliton to form. In comparison with Fig. 8.5 (c), the two regions with $H < 0$ ($C_{dd} < 0$) have been removed, showing how the stable regions are bound by the collapse or runaway expansion curves (solid red). For $C_{dd} > 0$ condensation occurs with $\kappa \lesssim 1$, giving a three-dimensional character to the solitons in these regions of the parameter space. For $C_{dd} < 0$ however, one finds instead that $\kappa \ll 1$, indicative of a very elongated (cigar) like cloud. Here the solitons exist closer to the one-dimensional limit. Finally, we note that close to the unstable boundary (red lines) the bright soliton can pass through a region where $\kappa > 1$. Such states would be challenging to observe, as the system would preferentially wish to collapse due to the presence of thermal or quantum fluctuations.

Although our presented results only consider a particular choice of dipole polarisation, one can still comment on the stability of the dipolar bright soliton when the dipoles

are, say, polarised perpendicular to the axis of the waveguide. As was noted in Sec. 8.1, altering the polarisation of the dipoles from $\theta = 0$ to $\theta = \pi/2$ has the effect of swapping the regimes of ε_{dd} where one obtains bright soliton solutions. We can speculate that a similar effect would occur when examining the stability of the dipolar system, except here we would see the regions associated with collapse and runaway expansion switch. However, this case breaks cylindrical symmetry, requiring a fully anisotropic ansatz to capture the stability of the system. This greatly complicates the analysis, as one has three variational width parameters to consider.

8.4 Summary

We have analysed the solutions, quasi-one-dimensional dynamics and full three-dimensional stability of dipolar bright solitons. The bright soliton solutions obtained from the dipolar Gross-Pitaevskii equation exhibit a number of novel features, including collisions which have regimes of elastic behaviour, bound state formation and soliton fusion. These regimes were shown to depend sensitively on the dipolar interactions and the presence of noise, which modify the phase shifts of the solitons. We quantified the collisional behaviour in terms of the coefficient of restitution. Analysis of soliton dynamics in terms of the coefficient of restitution could then provide important insight for systems where the full scattering phase shifts may be difficult to obtain analytically.

The stability of the full three-dimensional dipolar system was explored; in particular it emerged that the dipolar interactions can destabilise the bright soliton in two distinct ways, either through a traditional collapse, or instead through a runaway expansion along the axis. For axially-polarised dipoles the former occurs when the dipole-dipole interaction is positive, while the latter is associated with regimes of anti-dipoles for which the dipole-dipole interaction is instead negative.

Our results provide a benchmark for future experimental studies of non-local soliton in dipolar condensates. In turn, this system offers unique opportunities to explore the fundamental properties of non-local solitons in general with the immense tunability of atomic physics.

III

Rotation and turbulence

Accessing the anti-dipole regime

9

Stability analysis of a rotationally tuned dipolar BEC

DIPOLAR quantum gas experiments to date have largely relied on exploiting Feshbach resonances to tune the s-wave interaction strength relative to the inherent DDI strength. However, the realisation of a theory from 2002 recently came to reality, where the DDI strength is tuned through rapid rotation of the dipoles [see Sec. 2.1.2], thereby allowing access to a regime of a repulsive contact interaction and an effective ‘head-to-tail’ repulsion between the dipolar condensed bosons [217, 218]. However, to our knowledge, the GPE has not been solved in the presence of continuous rotation of the dipole moments to obtain vorticity-free solutions for an arbitrary dipole moment angular velocity.

Tuning of the DDI has applications in quantum gases, including the modulation of Faraday patterns [399]. In optical lattice systems, scaling of the DDI could lead to the observation of quasi-crystallisation in one-dimensional systems [400], fractional quantum Hall states [401], and Luttinger-liquids [356, 402]. Condensation in the anti-dipole regime opens the door to some exotic new phenomena, including molecular bound states in dark solitons [197], multi-dimensional dark [280] and bright [275] solitons, and stratified turbulence (see Ch. 10). Tuning the DDI in dipolar Fermi gases could also lead to the observation of Weyl superfluidity [403].

Previous analyses of rotationally tuned dipolar BECs have involved solving the dipolar GPE in the laboratory frame, by substituting the time averaged DDI pseudo-potential,

$$\langle U_{dd}(\mathbf{r}) \rangle = \frac{C_{dd}}{4\pi} \left(\frac{1 - 3 \cos^2 \theta}{r^3} \right) \left[\frac{3 \cos^2 \varphi - 1}{2} \right]. \quad (9.1)$$

for the usual DDI in the dipolar GPE, with dipoles pointing along z . In this limit, the density is cylindrically symmetric about z . In this work, we focus on the special case $\varphi = \pi/2$, and demonstrate that for all finite dipole rotation frequencies, this cylindrical symmetry about z is not exhibited by stationary solutions to the GPE with the exact, non-time-averaged DDI, and is seen to result in an associated dynamical instability. These results are explored via two distinct approaches, the first being based on a semi-analytical anal-

ysis in the Thomas-Fermi limit, and the second being numerical solutions of the dipolar GPE.

9.1 Hydrodynamic equations in a rotating frame

The hydrodynamic formalism has previously been successfully employed to predict the onset of instability in a rotating non-dipolar condensate. Since a cylindrically symmetric trap set into rotation applies no torque to the condensate, the trap is made anisotropic in the plane of rotation. Instead a weakly elliptical trap of the form [109, 111] $V_{\text{ext}}(\mathbf{r}) = (1/2)m\omega_{\perp}^2 ((1 - \epsilon)x^2 + (1 + \epsilon)y^2 + \gamma^2 z^2)$, with weak ellipticity ϵ , is employed where rotation is performed about the z -axis. The trap ratio is defined as $\gamma = \omega_z/\omega_{\perp}$. Typically, in the absence of dipolar effects, the condensate profile is elongated along the z -axis when $\gamma \ll 1$, and is flattened along the z -axis when $\gamma \gg 1$.

In the absence of dipolar interactions, vortices become energetically favourable under rotation frequencies $\Omega \sim 0.3\omega_{\perp}$. However, BEC experiments observed that the nucleation of vortices occurred at much larger rotation frequencies $\Omega \sim 0.7\omega_{\perp}$. This extra stability is garnered by the collective modes of the condensate, whose important role is elucidated in the hydrodynamic equations. Specifically, for $\Omega \lesssim 0.7\omega_{\perp}$ low-lying collective modes are excited via elliptical deformation. The seeding of vortices, at higher rotation frequencies, arises when one or more of these modes becomes unstable [404, 405]. The evidence for this interpretation comes from the comparison between experiments [111, 406] and GPE simulations [407–410].

Including dipolar interactions into the above analysis has been explored. In Refs. [236, 411] the stability diagram was mapped out for dipoles pointing along z . For the cylindrically symmetric case ($\epsilon = 0$) the stability becomes ϵ_{dd} -dependent, with the largest stable frequency $\Omega \sim 0.7\omega_{\perp}$ being reduced by 20% to $\Omega \approx 0.55\omega_{\perp}$ when $\epsilon_{\text{dd}} = 0.99$. The inclusion of a small ellipticity $\epsilon = 0.025$ (chosen to match the experiment from Madison *et al.* [109]) in non-dipolar condensates increases the largest stable frequency, however in dipolar gases was found to reduce this stability for $\epsilon_{\text{dd}} > 0$.

In order to explore the rotational tuning of the DDI requires dipoles to be tilted relative to the polarisation axis. Hence this requires a more advanced treatment than seen previously. In this work we use the dipolar GPE model in a harmonic trap, in a rotating frame with frequency Ω around the z -axis and with dipole moments aligned along the x -axis. Under these criteria the dipolar GPE, Eq. (2.31), reads

$$i\hbar \frac{\partial \psi(\mathbf{r}, t)}{\partial t} = \left[-\frac{\hbar^2 \nabla^2}{2m} + V_{\text{ext}}(\mathbf{r}) + gn(\mathbf{r}, t) + \Phi_{\text{dd}}(\mathbf{r}, t) - i\hbar\Omega \left(x \frac{\partial}{\partial y} - y \frac{\partial}{\partial x} \right) \right] \psi(\mathbf{r}, t). \quad (9.2)$$

To ensure that V_{ext} is invariant under rotation about the z -axis, and thus time-independent

in both the laboratory and rotating frames, we assume cylindrical symmetry, i.e.

$$V_{\text{ext}}(\mathbf{r}) = \frac{1}{2}m\omega_{\perp}^2 (x^2 + y^2 + \gamma^2 z^2) . \quad (9.3)$$

For $C_{\text{dd}} > 0$, it is thus generally energetically favourable for the condensate to be elongated along \hat{x} in the co-rotating frame. The situation where $C_{\text{dd}} < 0$, which corresponds to a head-to-tail dipole-dipole repulsion, is referred to, henceforth, as the ‘*anti-dipolar*’ regime. We shall always consider the s-wave interactions to be repulsive, i.e. $g > 0$, such that $\varepsilon_{\text{dd}} < 0$ implies $C_{\text{dd}} < 0$.

In what follows we work in the hydrodynamic formalism, obtained by employing the Madelung transformation Eq. (2.44), and work in the Thomas-Fermi approximation. This is equivalent to the work we showed in Sec. 2.3.3 but now we are working in the rotating frame and have fixed the dipole polarisation to the x -axis. The main results to take away from this slightly modified analysis are the rotating hydrodynamic equations, which read

$$m \frac{\partial \mathbf{v}}{\partial t} = -\nabla \left[\frac{1}{2}m\mathbf{v}^2 + V_{\text{ext}} + gn + \Phi_{\text{dd}} - m\mathbf{v} \cdot (\boldsymbol{\Omega} \times \mathbf{r}) \right] , \quad (9.4)$$

$$\frac{\partial n}{\partial t} = \nabla \cdot [n(\mathbf{v} - \boldsymbol{\Omega} \times \mathbf{r})] . \quad (9.5)$$

Initially, we seek to find stationary solutions to Eq. (9.4) and (9.5), these being solutions obeying $\partial_t \mathbf{v} = \partial_t n = 0$. Combining this condition with the relation for stationary solutions $\psi = \sqrt{n} \exp(-i\mu t/\hbar)$ and the relation equating velocity and phase, $\mathbf{v} = (\hbar/m)\nabla S$, yields

$$\mu = \frac{m}{2} \left[\mathbf{v}^2 + \omega_{\perp}^2 (x^2 + y^2 + \gamma^2 z^2) \right] + gn + \Phi_{\text{dd}} - m\mathbf{v} \cdot (\boldsymbol{\Omega} \times \mathbf{r}) , \quad (9.6)$$

$$0 = \nabla \cdot [n(\mathbf{v} - \boldsymbol{\Omega} \times \mathbf{r})] . \quad (9.7)$$

In the TF limit, the density, n_{TF} , is of the form

$$n_{\text{TF}}(\mathbf{r}) = n_0 \left(1 - \frac{x^2}{\kappa_x^2 R_z^2} - \frac{y^2}{\kappa_y^2 R_z^2} - \frac{z^2}{R_z^2} \right) , \quad (9.8)$$

$$n_0 = \frac{15N}{8\pi\kappa_x\kappa_y R_z^3} , \quad (9.9)$$

valid for $n_{\text{TF}} > 0$ and the aspect ratios are defined as $\kappa_x = R_x/R_z$ and $\kappa_y = R_y/R_z$. Stationary solutions for the velocity satisfy a quadrupolar ansatz of the form [404, 405]

$$\mathbf{v} = \alpha \nabla(xy) = \alpha(y\hat{x} + x\hat{y}) , \quad (9.10)$$

where an example solution of the phase profile obtained with Eq. (9.10) can be seen in Fig. 9.3 (bottom left). Substituting Eq. (9.8) and (9.10) into (9.7) yields a stationary solution

condition for the velocity field amplitude, α , in terms of κ_x and κ_y ,

$$\frac{\alpha + \Omega}{\kappa_x^2} + \frac{\alpha - \Omega}{\kappa_y^2} = 0 \Rightarrow \alpha = \frac{\kappa_x^2 - \kappa_y^2}{\kappa_x^2 + \kappa_y^2} \Omega. \quad (9.11)$$

Recasting the dipolar potential in the form of an electrostatic potential (Eq. (2.62)) polarised along x ,

$$\Phi_{\text{dd}}(\mathbf{r}, t) = -g \varepsilon_{\text{dd}} \left[n(\mathbf{r}, t) + 3 \partial_x^2 \phi(\mathbf{r}, t) \right], \quad (9.12)$$

$$\phi(\mathbf{r}, t) = \frac{1}{4\pi} \int d^3 \mathbf{r}' \frac{n(\mathbf{r}', t)}{|\mathbf{r} - \mathbf{r}'|}, \quad (9.13)$$

allows for an elegant solution for the self-interaction potential corresponding to a TF density profile, for which $\phi(\mathbf{r})$ has been found to be given by [231, 232, 411]

$$\begin{aligned} \frac{4\phi(x, y, z)}{n_0 \kappa_y \kappa_z} = & \frac{\beta_{000}}{2} - x^2 \beta_{100} - y^2 \beta_{010} - z^2 \beta_{001} + \frac{x^4 \beta_{200}}{2R_z^2} \\ & + \frac{y^4 \beta_{020} + z^4 \beta_{002} + 2(x^2 y^2 \beta_{110} + y^2 z^2 \beta_{011} + x^2 z^2 \beta_{101})}{2R_z^2}, \end{aligned} \quad (9.14)$$

where β_{ijk} are functions of κ_x and κ_y , and are specified via

$$\beta_{ijk}(\kappa_x, \kappa_y) = \int_0^\infty \frac{ds}{(\kappa_x^2 + s)^{i+1/2} (\kappa_y^2 + s)^{j+1/2} (1+s)^{k+1/2}}. \quad (9.15)$$

The solution of Eq. (9.6), via Eq. (9.8), (9.12) and (9.14), yields the stationary state Thomas-Fermi density,

$$\begin{aligned} n(\mathbf{r}) = & \frac{\mu - \frac{m}{2} (\tilde{\omega}_x^2 x^2 + \tilde{\omega}_y^2 y^2 + \gamma^2 \omega_\perp^2 z^2)}{g(1 - \varepsilon_{\text{dd}})} \\ & + \frac{3\varepsilon_{\text{dd}} n_0 \kappa_x \kappa_y (3\beta_{200} x^2 + \beta_{110} y^2 + \beta_{101} z^2 - \beta_{100} R_z^2)}{2(1 - \varepsilon_{\text{dd}}) R_z^2}, \end{aligned} \quad (9.16)$$

with dressed trapping frequencies, $\tilde{\omega}_x$ and $\tilde{\omega}_y$, given by

$$\tilde{\omega}_x^2 = \omega_\perp^2 + \alpha^2 - 2\alpha\Omega, \quad (9.17)$$

$$\tilde{\omega}_y^2 = \omega_\perp^2 + \alpha^2 + 2\alpha\Omega. \quad (9.18)$$

By comparing the coefficients of x^2, y^2, z^2 in Eq. (9.8) and (9.16), we find that

$$\kappa_x^2 = \frac{1}{\zeta} \left(\frac{\omega_\perp \gamma}{\tilde{\omega}_x} \right)^2 \left[1 + \varepsilon_{\text{dd}} \left(\frac{9}{2} \kappa_x^3 \kappa_y \beta_{200} - 1 \right) \right], \quad (9.19)$$

$$\kappa_y^2 = \frac{1}{\zeta} \left(\frac{\omega_\perp \gamma}{\tilde{\omega}_y} \right)^2 \left[1 + \varepsilon_{\text{dd}} \left(\frac{3}{2} \kappa_y^3 \kappa_x \beta_{110} - 1 \right) \right], \quad (9.20)$$

$$R_z^2 = \frac{2gn_0}{m\gamma^2\omega_\perp^2} \zeta, \quad (9.21)$$

$$\zeta = 1 + \varepsilon_{\text{dd}} \left(\frac{3}{2} \kappa_x \kappa_y \beta_{101} - 1 \right). \quad (9.22)$$

Substituting Eq. (9.19) and (9.20) into Eq. (9.11) also yields

$$\begin{aligned} 0 = & (\alpha + \Omega) \left[\tilde{\omega}_x^2 - \frac{9}{2} \varepsilon_{\text{dd}} \frac{\omega_\perp^2 \kappa_x \kappa_y \gamma^2}{\zeta} \beta_{200} \right] \\ & + (\alpha - \Omega) \left[\tilde{\omega}_y^2 - \frac{3}{2} \varepsilon_{\text{dd}} \frac{\omega_\perp^2 \kappa_x \kappa_y \gamma^2}{\zeta} \beta_{110} \right]. \end{aligned} \quad (9.23)$$

Equations (9.19), (9.20) and (9.23), together with Eq. (9.22), fully specify the shape of the stationary TF density, via κ_x & κ_y , and the corresponding laboratory-frame velocity field, via α .

9.2 Stationary solutions

We follow the conventional procedure of visualising stationary states in the hydrodynamical formalism by plotting α as a function of $\{\gamma, \varepsilon_{\text{dd}}, \Omega/\omega_\perp\}$, noting that, from Eq. (9.23), a positive (negative) α implies for a finite Ω that κ_x is greater (lesser) than κ_y , and thus encapsulates the planar anisotropy of the condensate density in the stationary state. To explore the dependence of this anisotropy on Ω , we thus plot α as a function of Ω/ω_\perp , with $\gamma = 1$, $\varepsilon_{\text{dd}} \in \{0, 0.1, 0.4, 0.8\}$ in Fig. 9.1 (a) and (c), and $\gamma \in \{0.1, 1, 10\}$, $\varepsilon_{\text{dd}} = 0.4$ in Fig. 9.1 (b) and (d). From Fig. 9.1, the stationary solutions are qualitatively independent of γ . Although a finite $\varepsilon_{\text{dd}} > 0$ results in a planar ellipticity, viz. $\kappa_x > \kappa_y$, Eq. (9.23) implies that $\alpha(\Omega = 0) = 0$ always. At a certain bifurcation frequency, $\Omega \equiv \Omega_b$, the system undergoes a bifurcation from one to three distinct stationary states. For $\varepsilon_{\text{dd}} = 0$, $\alpha = 0$ is always a solution, and two $\alpha \neq 0$ solutions, which are symmetric about the Ω -axis, exist when $\Omega_b \leq \Omega < \omega_\perp$. However, when $\varepsilon_{\text{dd}} > 0$, $\alpha > 0$ for $0 < \Omega < \Omega_b$; this solution persists for $\Omega_b \leq \Omega < \omega_\perp$, with two additional $\alpha < 0$ solutions, simply connected at $\Omega = \Omega_b$, appearing when $\Omega \geq \Omega_b$. This behaviour is an expected feature of BECs in the Thomas-Fermi limit, as viewed in a rotating reference frame. A similar bifurcation in α has been predicted by theory [404], and confirmed via experiment [406], to occur in a con-

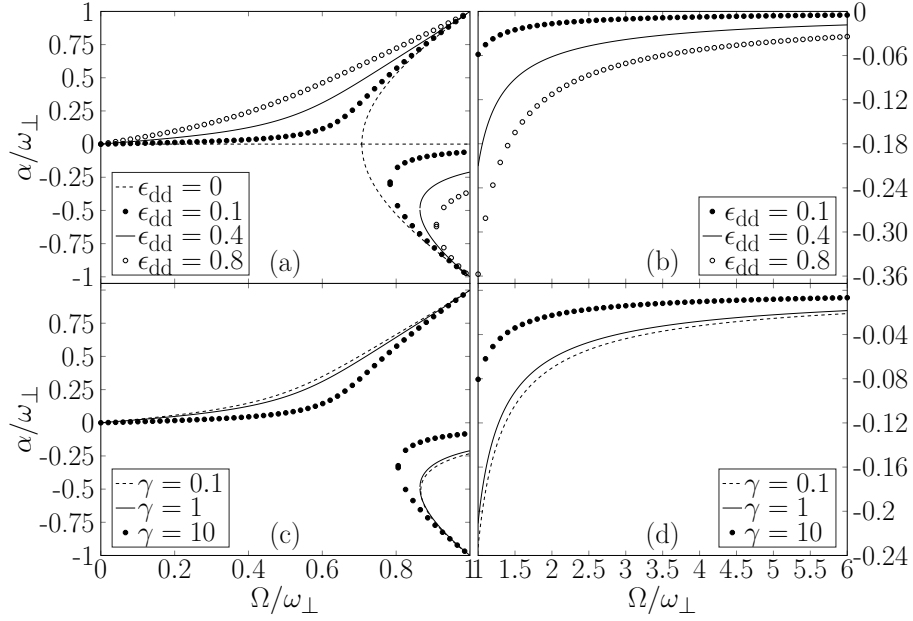


Figure 9.1: α as a function of Ω , with $\gamma = 1$ and $\epsilon_{dd} = 0.4$ unless otherwise specified.

densate rotating about the z -axis, with a planar trapping ellipticity, both with [236, 411] and without the existence of z -polarised dipoles. The existence of this bifurcation has been attributed to the $L_z = 2$ quadrupole mode being energetically unstable for $\Omega > \omega_b$ [45].

A slow convergence of the condensate density towards axial symmetry in the $\Omega \gg \omega_\perp$ limit is evident in Fig. 9.1. Agreement with previous predictions would suggest the stationary solutions in this limit to be those obtained from time-averaging the DDI, over one rotation cycle, in the laboratory frame [217]. The time-average of the DDI, where \hat{e} rotates about the z -axis while offset from this axis by the angle φ , is

$$\langle U_{dd}(\mathbf{r}) \rangle = \frac{C_{dd}}{4\pi} \left(\frac{3 \cos^2 \varphi - 1}{2} \right) \left[\frac{1 - 3(\hat{z} \cdot \mathbf{r})^2}{|\mathbf{r}|^3} \right]. \quad (9.24)$$

For $\varphi > \arccos(1/\sqrt{3})$, the time-averaged DDI boasts a negative effective ϵ_{dd} , thereby allowing emulation of the anti-dipolar regime of a dipolar BEC. In our system, the stationary solutions corresponding to the time-averaged DDI may be found by writing $\epsilon_{dd} \rightarrow -\epsilon_{dd}/2$, $\Omega = 0$ and $\hat{e} \equiv \hat{z}$ in Eq. (9.6) and (9.7). These stationary solutions are necessarily axially symmetric about \hat{z} , with the corresponding aspect ratio $\kappa_\parallel = R_x/R_z = R_y/R_z$

specified by the positive solution to [231, 232]

$$0 = 3\varepsilon_{\text{dd}}\kappa_{\parallel}^2 \left[\left(1 + \frac{\gamma^2}{2} \right) \frac{f(\kappa_{\parallel})}{1 - \kappa_{\parallel}^2} - 1 \right] + (\varepsilon_{\text{dd}} + 2)(\kappa_{\parallel}^2 - \gamma^2), \quad (9.25)$$

$$f(\kappa_{\parallel}) = \frac{1 + 2\kappa_{\parallel}^2}{1 - \kappa_{\parallel}^2} - \frac{3\kappa_{\parallel}^2 \operatorname{arctanh} \sqrt{1 - \kappa_{\parallel}^2}}{(1 - \kappa_{\parallel}^2)^{3/2}}. \quad (9.26)$$

This result may be compared with the true time-averaged condensate density by transforming Eq. (9.8) to the laboratory frame coordinates, denoted by \mathbf{r}' . As the dipole moments boast an angular velocity $\boldsymbol{\Omega} = \Omega \hat{z}$, the transformation is given by

$$\begin{pmatrix} x \\ y \\ z \end{pmatrix} = \begin{pmatrix} \cos(\Omega t) & \sin(\Omega t) & 0 \\ -\sin(\Omega t) & \cos(\Omega t) & 0 \\ 0 & 0 & 1 \end{pmatrix} \begin{pmatrix} x' \\ y' \\ z' \end{pmatrix}. \quad (9.27)$$

In the laboratory frame, the time-average of the TF density, Eq. (9.8), over one rotation cycle, is simply

$$\langle n(\mathbf{r}') \rangle = \frac{n_0}{R_z^2} \left[R_z^2 - \left(\frac{1}{\kappa_x^2} + \frac{1}{\kappa_y^2} \right) \frac{x'^2 + y'^2}{2} - z'^2 \right], \quad (9.28)$$

and so the true time-averaged aspect ratio, $\langle \kappa \rangle$,

$$\kappa_{\perp} \equiv \langle \kappa \rangle = \sqrt{\frac{2\kappa_x^2 \kappa_y^2}{\kappa_x^2 + \kappa_y^2}}, \quad (9.29)$$

Consequently, we have computed κ_{\perp} , as determined from Eq. (9.19), (9.20), (9.23) & (9.29), as a function of ε_{dd} , for $\gamma \in \{0.1, 1, 10\}$ and $\Omega = 50\omega_{\perp}$. At the same values of ε_{dd} and γ , we have also computed κ_{\parallel} as specified by the real, positive roots of Eq. (9.25), which is compared with κ_{\perp} in Fig. 9.2. Here, a high degree of agreement between the two methodologies is evident. In particular, the consequence of an effective anti-dipolar regime, that when $\gamma = 1$, the condensate is flattened with respect to the z -axis, is demonstrated by the fact that $\kappa_{\perp} \gg 1$.

9.3 Comparison to GPE simulations

To verify the stationary solutions specified through Eq. (9.19) – (9.23), we also solve the GPE, numerically, on a spatial grid. This numerical procedure is briefly outlined as follows. At $t = 0$, the stationary state for $\varepsilon_{\text{dd}} = 0$, and fixed $\{\Omega/\omega_{\perp}, \gamma, N\}$, is obtained by evolving the dipolar GPE in imaginary time [412]. For $t > 0$, the real-time evolution of the

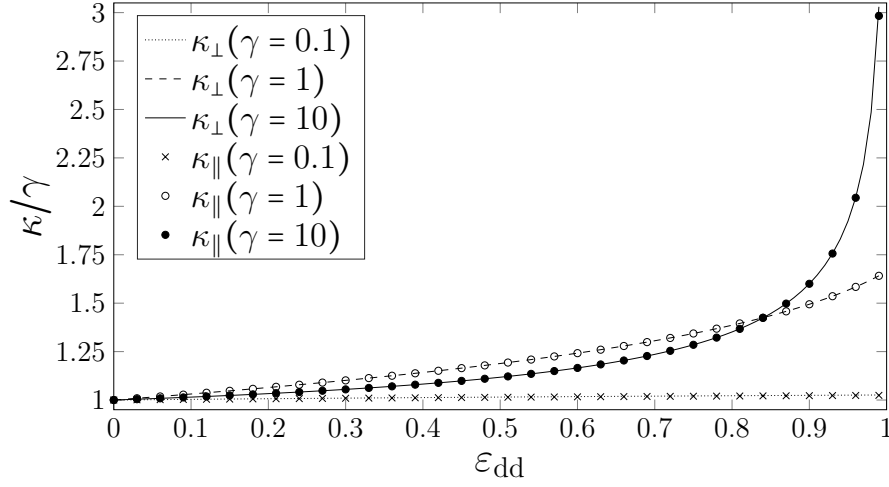


Figure 9.2: Comparison of $\kappa_{\perp}(\Omega = 50\omega_{\perp})$ (solid lines), as a function of ε_{dd} , and κ_{\parallel} (with $\varepsilon_{dd} \rightarrow -\varepsilon_{dd}/2$; unfilled circles). The incidence of the circles on the solid lines illustrates the high degree of convergence of the rotating-frame stationary states to those from the time-averaged DDI when $\Omega \gg \omega_{\perp}$.

dipolar GPE is accompanied by an increase of ε_{dd} increased at a rate $d\varepsilon_{dd}/dt = 10^{-3}\omega_{\perp}$, allowing the realisation of stationary solutions at finite values of ε_{dd} . To model random external symmetry-breaking perturbations, which may shift the condensate state away from the stationary state in an experimental scenario, the condensate density is modified at the initial timestep by a random, local, multiplicative perturbation of up to 5%.

Taking $\Omega = 3\omega_{\perp}$, $N = 10^5$, and $\gamma = 1$ we simulate this adiabatic ramp of ε_{dd} . A few select density and phase profiles of this simulation are shown in Fig. 9.3. After $t = 50\omega_{\perp}^{-1}$ the condensate density is slightly oval in shape, and matches the quadrupolar velocity ansatz specified in Eq. 9.10. However, this state is highly unstable and undergoes large density oscillations leading to a collapse instability around $t \approx 150\omega_{\perp}^{-1}$. By $t = 200\omega_{\perp}^{-1}$ the condensate is in a highly non-equilibrium state and the Thomas-Fermi approximation is no longer appropriate to describe the solution.

From this simulation, and a second with $N = 10^4$, we extract α as a function of ε_{dd} and compare to the analytic solutions of Eq. (9.19) – (9.23), shown in Fig. 9.4. This figure demonstrates that when $N = 10^4$, the numerical solutions diverge considerably from the analytical Thomas-Fermi predictions; we attribute this to the condensate atom number, N , being insufficient for the Thomas-Fermi approximation to be valid. When $N = 10^5$, the analytical predictions for α agree closely with the numerical simulation for $\varepsilon_{dd} \leq 0.075$, but the numerical value experiences large fluctuations as the ramp procedure continues for $\varepsilon_{dd} \geq 0.075$. As ε_{dd} is ramped up beyond 0.17, the numerical solution diverges from the analytical one entirely.

The stable, but large, fluctuations of α in Fig. 9.4 may be interpreted as evidence for the

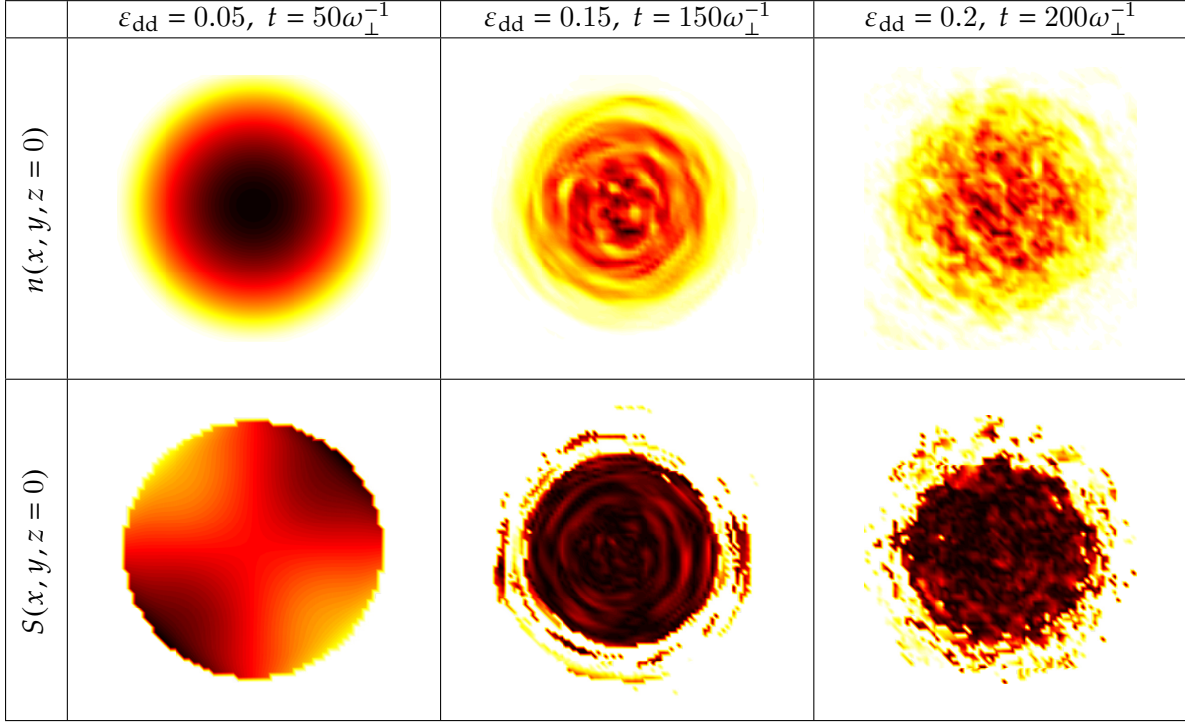


Figure 9.3: Density (top row) and phase (bottom row) profiles taken from a numerical simulation of the dipolar GPE. A slow linear ramp of ε_{dd} is introduced to break cylindrical symmetry. Parameters: $\Omega = 3\omega_{\perp}^{-1}$, $\gamma = 1$, $N = 10^5$.

existence of collective modes of the condensate [86], seeded by the random perturbations of the numerical procedure, and the divergence of α from the analytical value as being due to an associated *dynamical instability*.

9.4 Stability analysis

To investigate this notion further, we linearise the fully time-dependent hydrodynamic equations, Eq. (9.4) and (9.5), about their stationary Thomas-Fermi solutions [413, 405]. We note that other formalisms for determining the nature of collective modes in BECs, such as the determination of scaling perturbations to the Thomas-Fermi density [231, 414] and the solution of the Bogoliubov equations governing order parameter fluctuations [415, 209], have been previously been employed. However, we are interested in a larger class of perturbations than mere scaling of the density and phase, and have expressed our stationary solutions in terms of n and \mathbf{v} and not ψ , and so neither of these formalisms are used. Instead, the hydrodynamic equations themselves are linearised, a method which has previously been utilised in the context of rotating dipolar BECs with z -polarised dipoles [411].

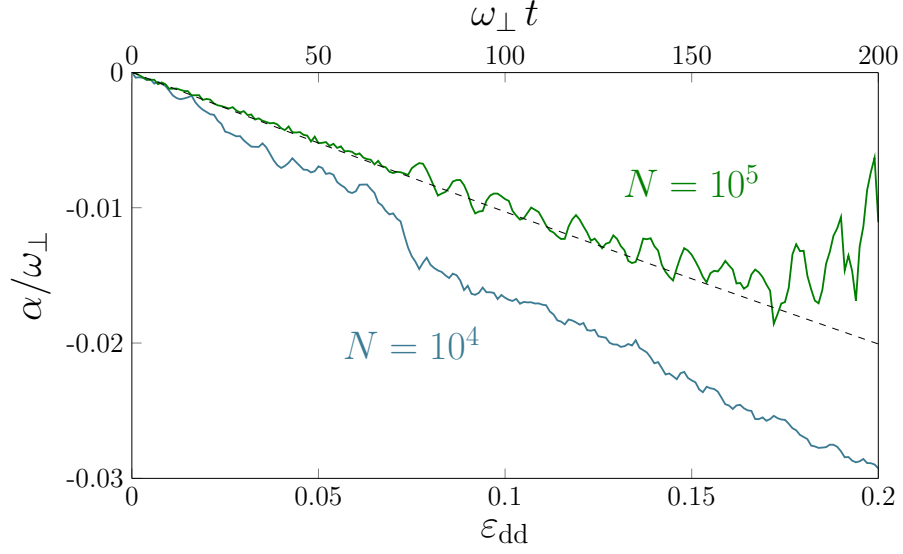


Figure 9.4: Plot of α as a function of ε_{dd} at $\Omega = 3\omega_{\perp}$ and $\gamma = 1$, determined via (9.19) – (9.23) (dashed line) and a numerical solution of the dipolar GPE for $N = 10^4$ (blue solid line) and $N = 10^5$ (green solid line).

We write the time-dependent density and phase as fluctuations about the respective stationary state values

$$n(\mathbf{r}, t) = n_{\text{TF}}(\mathbf{r}) + \delta n(\mathbf{r}, t), \quad (9.30)$$

$$S(\mathbf{r}, t) = (\alpha m x y - \mu t)/\hbar + \delta S(\mathbf{r}, t). \quad (9.31)$$

Subsequently, Eq. (9.30) and (9.31) are substituted into Eq. (9.4) and (9.5), which are linearised by discarding all terms of order $O((\delta n)^2)$ and $O((\delta S)^2)$. This results in the following system of coupled, first-order equations

$$\frac{\partial}{\partial t} \begin{pmatrix} \delta S \\ \delta n \end{pmatrix} = \mathcal{L} \begin{pmatrix} \delta S \\ \delta n \end{pmatrix}, \quad (9.32)$$

where the operator \mathcal{L} and its components are defined as

$$\mathcal{L} = - \begin{pmatrix} \mathbf{v}_c \cdot \nabla & \frac{g}{\hbar} (1 + \varepsilon_{dd} \widehat{K}) \\ \frac{\hbar}{m} \nabla \cdot (n_{\text{TF}} \nabla) & \mathbf{v}_c \cdot \nabla \end{pmatrix}, \quad (9.33)$$

$$\mathbf{v}_c = \alpha \nabla(x y) - \Omega \times \mathbf{r}, \quad (9.34)$$

$$\widehat{K}[\delta n] = \frac{-3}{4\pi} \frac{\partial^2}{\partial x^2} \int_{\Gamma} d^3 \mathbf{r}' \frac{\delta n(\mathbf{r}', t)}{|\mathbf{r} - \mathbf{r}'|} - \delta n, \quad (9.35)$$

Note that Eq. (9.35), Γ is defined as the domain in which $n_{\text{TF}} > 0$, i.e. $\Gamma = \{\mathbf{r} \in \mathbb{R}^3 : n_{\text{TF}} > 0\}$.

Defining the condition $n_{\text{TF}} + \delta n > 0$ would amount to including quadratic effects in δn [380].

The solutions of Eq. (9.33) are collective oscillations, and their respective eigenvalues, obeying

$$\begin{pmatrix} \delta S(\mathbf{r}, t) \\ \delta n(\mathbf{r}, t) \end{pmatrix} = \exp(\lambda t) \mathbf{W}(\mathbf{r}) : \mathcal{L} \mathbf{W}(\mathbf{r}) = \lambda \mathbf{W}(\mathbf{r}). \quad (9.36)$$

A qualitative understanding of the stability of the condensate, with respect to collective oscillations, may thus be found by examining the spectra of Eq. (9.36). If *any* collective mode, indexed by i , features $\text{Re}(\lambda_i) > 0$, its amplitude will grow exponentially and ultimately overwhelm the stationary Thomas-Fermi solution. Within this formalism, the stationary states are stable against perturbations only if $\forall i, \text{Re}(\lambda_i) \leq 0$.

Equation (9.36) is diagonalised numerically via polynomial *ansätze* for the collective modes of the form [405, 411]

$$\mathbf{W}(\mathbf{r}) \equiv \begin{pmatrix} \delta S(\mathbf{r}) \\ \delta n(\mathbf{r}) \end{pmatrix} = \sum_{p+q+r \leq N_{\text{max}}} \begin{pmatrix} a_{pqr} \\ b_{pqr} \end{pmatrix} x^p y^q z^r. \quad (9.37)$$

Fluctuations of order $p + q + r = 2, 3, 4$ represent quadrupolar, hexapolar and octupolar modes respectively, and so on; a rich variety of collective modes, including breathing and scissors modes, have been observed in several dipolar BEC experiments. Note that due to computational constraints, we truncate the Hilbert space of available modes to $N_{\text{max}} = 14$. However, reducing the degree of the Hilbert space truncation, i.e. increasing N_{max} , does not have the effect of modifying any eigenvalues corresponding to modes with an order less than N_{max} , but merely increases the dimension of the truncated spectrum of modes available to us. If, at a given point in parameter space, the diagonalisation of Eq. (9.36) with respect to fluctuations of order less than N_{max} yields at least one eigenvalue with a positive real component, it is thus sufficient to claim that the condensate is dynamically unstable up to linear order in fluctuations.

To analyse the regions of parameter space explored in Figs. 9.1 and 9.4, we compute the spectrum of modes associated with the domain $\varepsilon_{\text{dd}} \in [0, 1)$, $\Omega/\omega_{\perp} \in [1, 6]$ and $\gamma = 1$. As several modes might be unstable at a given point in parameter space, we merely work with the eigenvalue with the largest positive, real component. In Fig. 9.5 (left), we plot the real component of the eigenvalue, λ , with the largest positive real component, as a function of both ε_{dd} and Ω . In addition, by taking a cross-section of this plot at a fixed $\Omega = 3\omega_{\perp}$, we plot $\max \{\text{Re}(\lambda) : \text{Re}(\lambda) > 0\}$ as a function of ε_{dd} , in Fig. 9.5(right), for the purpose of a direct comparison with the GPE simulation. Interestingly, we always find that the eigenvalues of \mathcal{L} are either purely real, or purely imaginary, with each eigenvalue

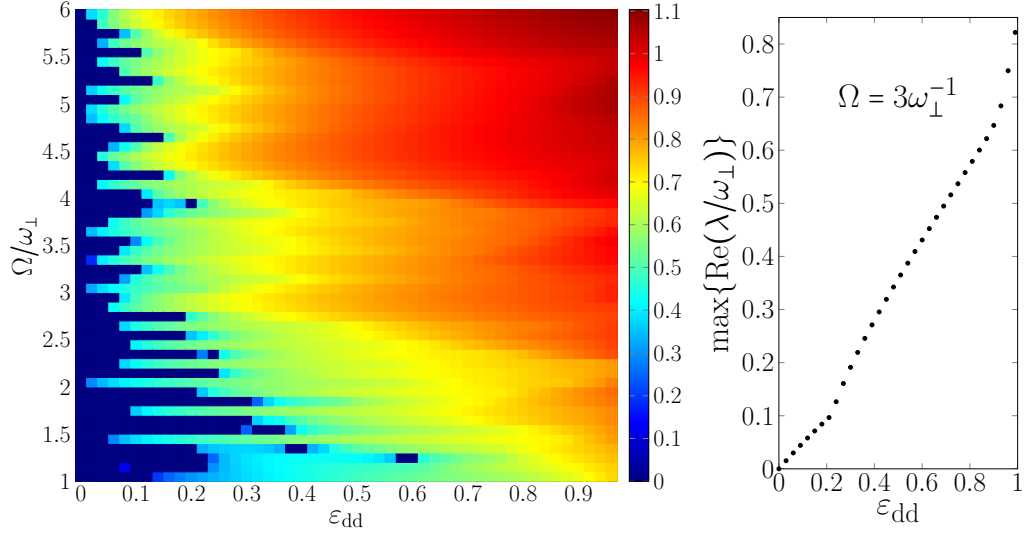


Figure 9.5: False colour plot of $\max\{[\text{Re}(\lambda/\omega_\perp)]^{1/4} : \text{Re}(\lambda) > 0\}$, as a function of Ω and ε_{dd} , with $\gamma = 1$ and $N_{\max} \leq 14$. The prevalence of real, positive eigenvalues for $\varepsilon_{dd} > 0$ indicates that the stationary solutions are dynamically unstable. On the right, a cross-section is taken at $\Omega = 3\omega_\perp^{-1}$, corresponding to Fig. 9.4, showing positive, real eigenvalues $\forall \varepsilon_{dd} > 0$.

λ associated with another eigenvalue $-\lambda$. Thus, without loss of generality, we simply denote the real, positive eigenvalues in Fig. 9.5 by λ .

In Fig. 9.5, we may see that as $\varepsilon_{dd} \rightarrow 1$, more regions of parameter space become dynamically unstable to collective modes of polynomial order less than 14. In addition, the region that remains stable against these modes becomes smaller for larger Ω . We also note that while a mode, associated with a real, positive eigenvalue λ , increases in amplitude with an associated exponential timescale equivalent to $\Omega/(2\pi\lambda)$ rotation cycles, the formalism employed here does not provide information on the initial amplitude, and thus cannot predict the time taken for a dynamical instability to overwhelm the condensate stationary state, as observed in the GPE simulation. Nonetheless, from the inset to Fig. 9.5, it is evident that for all non-zero ε_{dd} , with $\Omega = 3\omega_\perp$ and $\gamma = 1$, the corresponding stationary suffer one or more dynamical instabilities, with the corresponding maximum real eigenvalue growing as $\varepsilon_{dd} \rightarrow 1$. This result would appear to assert that the instability observed in the GPE simulation is dynamical, and not numerical.

We have assumed that the harmonic confinement of the condensate is axially symmetric about the field rotation axis, as a trapping anisotropy about this axis prevents the identification of a reference frame in which the GPE is separable into the density and chemical potential contributions. However, realistic experiments often exhibit precisely such an anisotropy [218], in which case our results cannot be applied. In addition, our formalism must be modified substantially in order to account for an alignment of the dipole moments at an arbitrary angle φ to the z -axis; for the special case $\Omega = 0$, stationary states

and their associated collective modes have been previously been discussed in the literature [416].

9.5 Summary

In conclusion, we have outlined a semi-analytical formalism for obtaining Thomas-Fermi stationary states of a dipolar BEC, with its dipoles rotating about an axis normal to their alignment plane, in a harmonic trap that is symmetric about this axis. Numerical GPE simulations of this scenario confirm the validity of the semi-analytically determined Thomas-Fermi solutions which, in the high rotation frequency limit, converge to those predicted for a dipolar BEC subject to the corresponding, time-averaged, dipolar potential. However, we also find that, in this limit, the stationary solutions are found to be unstable with respect to collective oscillations induced by external perturbations. Crucially, the timescale for the onset of these instabilities is found to be on the order of 10^2 rotation cycles, suggesting that the experiments involving the rotational tuning of ε_{dd} must be carefully designed to avoid seeding these instabilities before meaningful measurements are taken.

Quantum ferrofluid turbulence

CONVENTIONAL ferrofluids, colloidal suspensions of permanently magnetised particles, exhibit unique fluid properties due to the dipole-dipole inter-particle interaction, such as the normal field instability and flow characteristics which can be varied through an external magnetic field [69]. The ability to direct the fluid using magnetic fields has led to broad applications from tribology to targeted medicine [417]. Remarkably, turbulence in ferrofluids has been limited to only a few studies [418–420]; this may be attributed to difficulties in achieving turbulent regimes (due to their high viscosity) and in characterising the flow (due to their opacity). Typical parameters for ferrofluid experiments are a fluid density of 800 (3500) kgm^{-3} for water- (oil-) based carrier solution, flow velocity up to 3 ms^{-1} , system length of 2250 mm (and diameter 25 mm), a magnetic field dependent viscosity varying from $1\text{--}12 \times 10^{-3} \text{ kgm}^{-1}\text{s}^{-1}$ [421]. These parameters give a typical Reynolds number of $\text{Re} \sim 7000$. As such the manner in which the anisotropic, long-range interactions modify the turbulent state remains an open question. Nonetheless, theoretical work has predicted that the coupling with ferrohydrodynamics leads to new turbulent phenomena such as control over the onset of turbulence through the applied magnetic field [422] and new modes of energy dissipation and conversion [423].

In combining ferrohydrodynamics with superfluidity, quantum ferrofluids embody a prototype system for studying ferrofluid turbulence due to the absence of viscosity and the quantisation of vorticity. As demonstrated experimentally for conventional condensates, states of such quantum turbulence can be formed and imaged [136, 138, 424], and can show both direct analogies to its counterpart in everyday viscous fluids (for example, Kolmogorov scaling [425, 426] and the transition from the von Kármán vortex street [121]) and distinct quantum effects (for example, ultra-quantum regimes [425, 426] and non-classical velocity statistics [427]), depending on the details of the turbulent state. As well as the simplified fluid characteristics, these systems have the facet that the fluid parameters (*viz.* atomic interactions) can be tuned at will. As such, quantum ferrofluids stand to shed light on general aspects of ferrofluid turbulence, as well as phenomena specific to the quantum nature of the fluid, such as quantised vortex line dynamics, reconnections and inviscid dissipation mechanisms [127].

While various aspects of vortices in quantum ferrofluids have been theoretically ex-

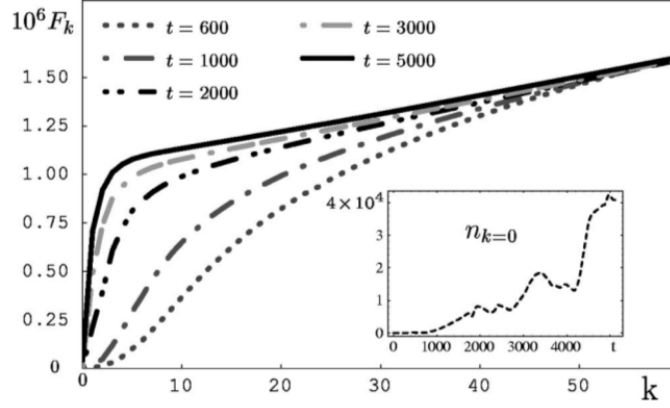


Figure 10.1: The temporal evolution of the integral distribution of particles F_k . At later times a “shoulder” appears at low k , indicating the presence of the quasi-condensate fraction. The inset shows the evolution of the $n_{k=0}$ mode, which at late times becomes macroscopically occupied. (Copyright (2002) by The American Physical Society [132]).

plored, e.g. their generation, profiles and lattice structures [269], the behaviour of quantum ferrofluid turbulence remains at large. Here we study turbulence in quantum ferrofluids through the scenario of a homogeneous dipolar Bose gas freely evolving from highly non-equilibrium conditions. There are many different ways to generate turbulence in a condensate, e.g. stirring and shaking, but these tend to ‘bias’ the turbulence which is generated. A quench is the most favourable method since it produces essentially randomised vortices. This scenario, representative of a sudden quench from a thermal gas through the BEC transition, is known to generate unstructured quantum turbulence which decays over time [132, 428]. This setting, free from boundaries and artefacts that may be introduced by external forcing, allows us to unambiguously identify the effects of the dipolar interactions.

10.1 Classical field method in non-dipolar gases

The seminal works on the classical field method were undertaken by Svistunov and co-workers in the early 1990s [429–431]. They studied the relaxation of a highly non-equilibrium initial state

$$\psi(\mathbf{r}, t = 0) = \sum_{\mathbf{k}} a_{\mathbf{k}} \exp(i\mathbf{k} \cdot \mathbf{r}) , \quad (10.1)$$

where the phases of the complex amplitudes $a_{\mathbf{k}}$ are distributed randomly. The occupation of a single \mathbf{k} mode is $n_{\mathbf{k}} = |a_{\mathbf{k}}|^2$.

Work by Berloff and Svistunov [132] showed that the initially uniformly distributed $n_{\mathbf{k}}$

evolve to a state with macroscopic population for $k < k_c$, and low occupation for the high k modes. This is illustrated through the cumulative density distribution $F_k = \sum_{k' \leq k} n_{\mathbf{k}'}$ shown in Fig. 10.1. The densely occupied low- k region ($k < k_c$) is identified as the quasi-condensate, whereas the high- k region ($k > k_c$) is identified as the thermal cloud. In Ref. [132] they chose a dynamic value of the dimensionless cut-off wavenumber $k_c = 9 - t/1000$.

Stagg, Parker and Barenghi [428] showed that the ensuing vortex tangle from the turbulent initial condition does not contain coherent structures or exhibit a Kolmogorov kinetic energy cascade indicative of classical turbulence. Instead, the thermally quenched turbulence has similar properties to ultraquantum turbulence, which is akin to a random disorganised flow.

10.2 Polarised turbulence

We adopt the classical field methodology of the weakly-interacting, finite-temperature Bose gas [432, 313, 433, 132, 434, 310, 435–437], extending it to include dipolar interactions. Contrary to the presentation in the earlier parts of this thesis the gas is described by a classical field $\psi(\mathbf{r}, t)$ (a valid assumption providing the modes are highly occupied), describing the dynamics of the condensate density and the thermal field. The theory we have established in Ch. 2 still holds, and the dynamics of this classical field follow the Gross-Pitaevskii equation Eq. (2.31). Thus, in this work we solve the homogeneous 3D dipolar GPE, stated here as

$$i\hbar \frac{\partial \psi(\mathbf{r}, t)}{\partial t} = \left[-\frac{\hbar^2 \nabla^2}{2m} + g n(\mathbf{r}, t) + \Phi_{\text{dd}}(\mathbf{r}, t) \right] \psi(\mathbf{r}, t), \quad (10.2)$$

for the highly non-equilibrium initial condition $\psi(\mathbf{r}, 0)$ generated from Eq. (10.1).

For $g > 0$ and $-0.5 \leq \varepsilon_{\text{dd}} \leq 1$ the ground state of the dipolar Bose gas is the uniform solution $\psi = \sqrt{n_0} e^{iS_0}$, where n_0 is the uniform density and S_0 an arbitrary uniform phase, and chemical potential $\mu_0 = n_0 g (1 - \varepsilon_{\text{dd}})$. According to Bogoliubov theory (see Sec. 2.4.1), perturbations to this state of momentum \mathbf{p} have energy

$$E_{\text{B}}(\mathbf{p}) = \sqrt{c^2(\theta_k) p^2 + (p^2/2m)^2}, \quad (10.3)$$

where

$$c^2(\theta_k) = (g n_0 / m) \left[1 + \varepsilon_{\text{dd}} (3 \cos^2 \theta_k - 1) \right], \quad (10.4)$$

and θ_k is that between \mathbf{p} and the polarisation direction [67]. For small p the spectrum corresponds to oscillatory excitations in the form of phonons with anisotropic phase velocity

$c(\theta)$. Note that outside of the regime of $g > 0$, $-0.5 \leq \varepsilon_{dd} \leq 1$, the excitations develop imaginary energy components, signifying unstable growth (the “phonon instability”) and the instability of this homogeneous state.

We express length in units of the dipolar healing length $\xi = \hbar/\sqrt{m\mu_0}$ and time in terms of the unit $\tau = \hbar/\mu_0$. The GPE is evolved numerically using a split step Fourier method [334, 335] on a 192^3 periodic grid with spacing $d = 0.5\xi$. Our findings are insensitive to these numerical parameters. The time step $\Delta t = 0.001\tau$ is two orders of magnitude smaller than the timescale of the fastest modes supported¹. Following previous approaches [132, 428] we initialise the system with the non-equilibrium state $\psi(\mathbf{r}, 0) = \sum_{\mathbf{k}} a_{\mathbf{k}} \exp(i\mathbf{k} \cdot \mathbf{r})$, where \mathbf{k} is the wavevector (defined up to the maximum amplitude allowed by the numerical box [132, 310]), the coefficients $a_{\mathbf{k}}$ are uniformly valued (up to a certain wave vector amplitude set by the choice of system parameters), and the phases are distributed randomly². We illustrate the key behaviours through case studies of $\varepsilon_{dd} = 0.8$ and $\varepsilon_{dd} = -0.4$, as well as the non-dipolar case $\varepsilon_{dd} = 0$ for comparison; the more general behaviour will also be described.

At very early times, there is a rapid self-ordering of the field, akin to the non-dipolar case [132, 310]. From the initially uniform distribution across modes, the low k modes grow to develop macroscopic occupation, forming a quasi-condensate. The high k modes develop low occupations and are associated with thermal excitations. Within of the order of 100 time units, this bimodal distribution across the modes has effectively saturated. Unlike the non-dipolar case, the mode occupations are anisotropic in momentum space. The quasi-condensate has superfluid ordering and features a tangle of quantised vortices. To visualise the superfluid vortices for $t > 0$, we follow Ref. [132] in defining a “quasi-condensate” density n_q of the low-lying modes $k \leq k_c$, where k_c is identified from the condensate-thermal crossover in the mode distribution³. Here we identify $k_c = 0.46\xi^{-1}$. Vortices are then identified as tubes of low quasi-condensate density, $n_q < 0.05\langle n_q \rangle$, where $\langle \dots \rangle$ denotes the ergodic average. Our results are insensitive to the precise values of k_c and the density threshold.

In the non-dipolar Bose gas [Fig. 10.2 (top row)], this tangle is randomised in space, with no large-scale structure [132, 310], and the density fluctuations, representative of the high k component of the field, are isotropic in space.

For the dipolar Bose gas the spatial isotropy is broken. For $\varepsilon_{dd} > 0$ [$\varepsilon_{dd} = 0.8$, Fig. 10.2 (middle row)] the density fluctuations become columnar, aligned along the polarisation

¹The maximum wavevector supported by the cubic grid has amplitude $k_{\max} = \sqrt{3}\pi/d \approx 11\xi^{-1}$ [428]. From the dispersion relation, the corresponding period is of the order of 0.1τ .

²While this isotropic initial condition is an approximation to the (anisotropic) pure thermal state of the dipolar gas, the system very rapidly evolves to an anisotropic thermal state. This occurs on much shorter timescales than the vortex dynamics of interest.

³The identification of the quasi-condensate vortices is meaningful only for $t > 0$. At $t = 0$ there is no quasi-condensate.

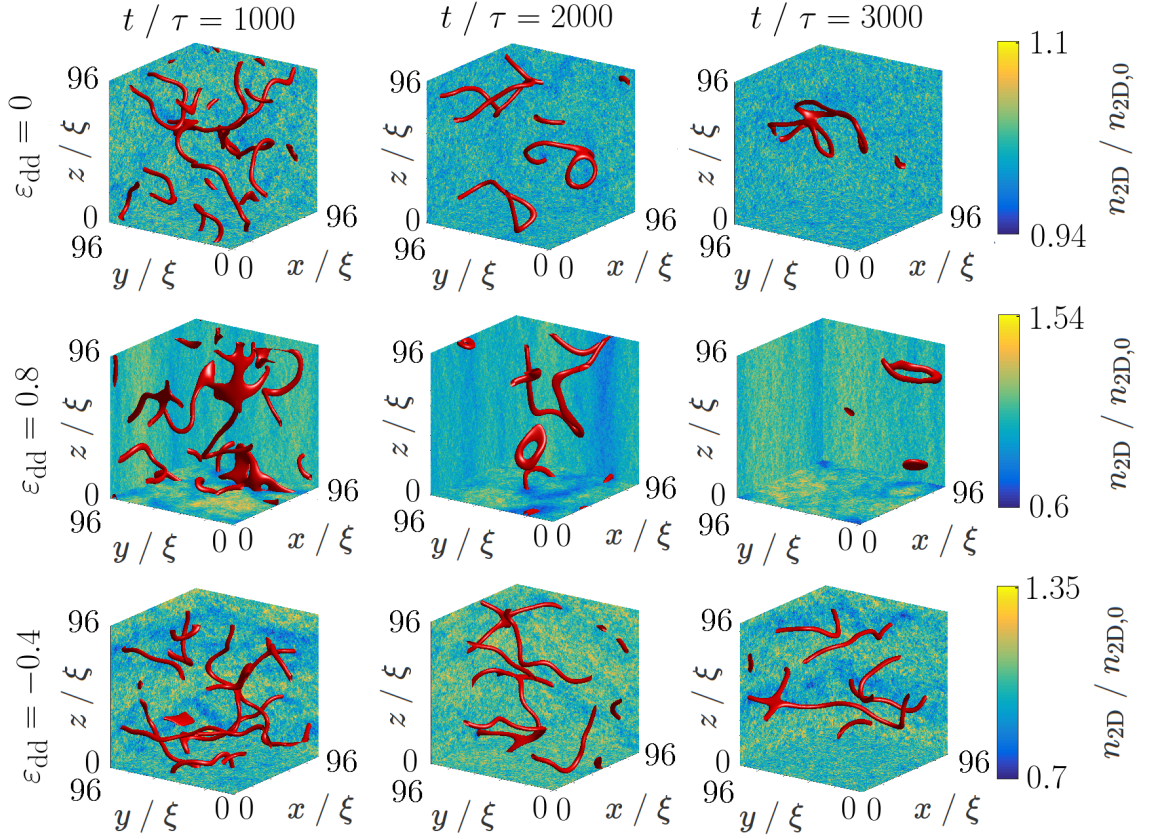


Figure 10.2: Turbulence in the quantum ferrofluid, for three values of ε_{dd} . Vortices are shown through isosurfaces (red tubes) of the quasi-condensate density at the $0.05\langle n_q \rangle$ level (angled brackets denote ergodic average). The walls of the box show 2D density profiles, corresponding to integrating the density, $|\psi|^2$, over the dimension perpendicular to their face.

direction, as seen in the integrated density profiles. This is because these modes have lower energy, as seen in the earlier dispersion relation $E_B(\mathbf{p})$, due to the lower energy configuration of dipoles to a head-to-tail configuration. These fluctuations are sizeable in amplitude, ranging from around 0.6 to 1.5 of the mean density, and are dynamic. The vortices visibly tend to orient along z .

For $\varepsilon_{dd} < 0$ (*viz.* $C_{dd} < 0$) [$\varepsilon_{dd} = -0.4$, Fig. 10.2 (bottom row)] the density fluctuations become planar, in accord with $E_B(\mathbf{p})$ and driven by the attraction of side-by-side dipoles, again with a large density amplitude. The vortices in this case prefer to align in these low density planes.

For all cases, the vortices decay in time, through reconnections, Kelvin wave decay and thermal dissipation, and by $t \approx 2000\tau$ only a few vortex loops are left in the gas. The columnar (planar) density fluctuations arise generically for $\varepsilon_{dd} > 0$ ($\varepsilon_{dd} < 0$), growing in amplitude with $|\varepsilon_{dd}|$. For larger $|\varepsilon_{dd}|$ values than shown, however, the dominance of the columnar (planar) density fluctuations makes it challenging to visualise the vortices.

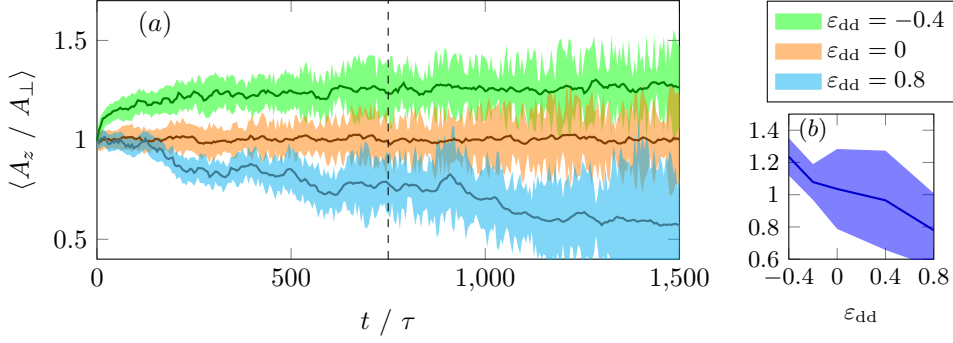


Figure 10.3: (a) Polarisation of the vortex tangle over time, shown through the area ratio of vortices, A_z/A_{\perp} , for three ϵ_{dd} values. Lines and shaded regions represent the mean and one standard deviation over five realisations with different randomised initial conditions. (b) Snapshot of the area ratio over more detailed range of ϵ_{dd} at $t = 750\tau$ (dotted line in (a)).

10.3 Quantifying the polarisation

We project the quasi-condensate vortex tubes in the x , y and z directions, denoting the areas cast as A_x , A_y and A_z , respectively. The ratio A_z/A_{\perp} , where $A_{\perp} = \frac{1}{2}(A_x + A_y)$, then quantifies the axial-to-perpendicular anisotropy of the vortices. Figure 10.3(a) shows the evolution of A_z/A_{\perp} , over five initial conditions for each ϵ_{dd} , up to $t = 1500\tau$. By this time, the number of vortices has decreased to the order of unity; beyond this the area ratio is no longer a meaningful characteristic of the tangle, with the fluctuations becoming excessive. Moreover, at this stage the dynamics are no longer multi-scaled, a key characteristic of hydrodynamic turbulence. Due to the isotropic initial conditions, all cases begin being isotropic with $A_z/A_{\perp} \approx 1$. For $\epsilon_{dd} = 0$, the tangle remains isotropic throughout. However, for $\epsilon_{dd} \neq 0$ the tangle evidently becomes polarised, seen by the statistically significant deviation of A_z/A_{\perp} from unity. For $\epsilon_{dd} = 0.8$, A_z/A_{\perp} decreases by up to 25%; for $\epsilon_{dd} = -0.4$ it increases up by 40%. In Fig. 10.3(b) a more thorough parameter sweep of ϵ_{dd} is displayed, focussing on the asymptotic value of A_z/A_{\perp} obtained at $t/\tau = 750$, where, within errorbars, this quantity decreases approximately with ϵ_{dd} .

The area ratio is plotted over longer timescales in Fig. 10.4. The fluctuations become dominant beyond around $t = 1500\tau$. Indeed, this is the time at which the averaged inter-vortex spacing becomes comparable to the size of the box, in other words, when only one or two vortices are left. We do not believe any useful information can be gleaned at these late times, due to the excessive fluctuations, and so we limited Fig. 10.3 to $t = 1500/\tau$.

To further understand the polarisation of the vortices, Fig. 10.5 shows the location of the vortex lines (red isosurface tubes) and regions of high quasi-condensate density (blue isosurface regions). It is evident that, firstly, the system is threaded with vertical tube-like structures of high density; the intervening regions being of low density. Secondly, the

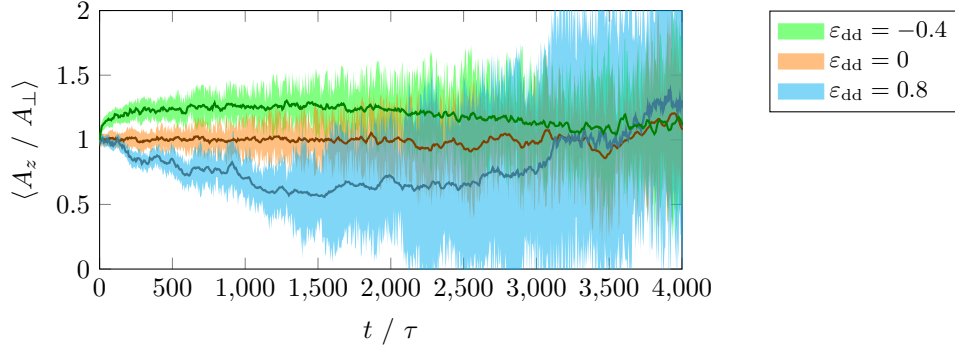


Figure 10.4: An extended plot of Fig. 10.3. At later times only one or two vortices remain in the system and our adopted measure is no longer valid.

vortices avoid the high density regions; by maximising their overlap with the low density regions they reduce their kinetic energy. For $\varepsilon_{dd} < 0$ the high density regions are planar strata, with the vortices tending to locate in the intervening low density layers.

The preference of the vortices to align in the low density regions is particularly prominent at the late stages of the decay, when only one or a few vortex loops remain. Here we observe situations, for example, in which vortex loops become heavily pinned across two planar regions of low density, as in Fig. 10.6. Considerable vortex line length lies in these planes, while two vortex segments connect between these planes to form the overall loop. The pinned segments move with the low density region. This large loop is metastable but decays eventually via a reconnection, forming two small loops, each of which is heavily pinned within each low density plane. We observe such pinning of vortices to the low density region to be a general occurrence for moderate to large values of ε_{dd} .

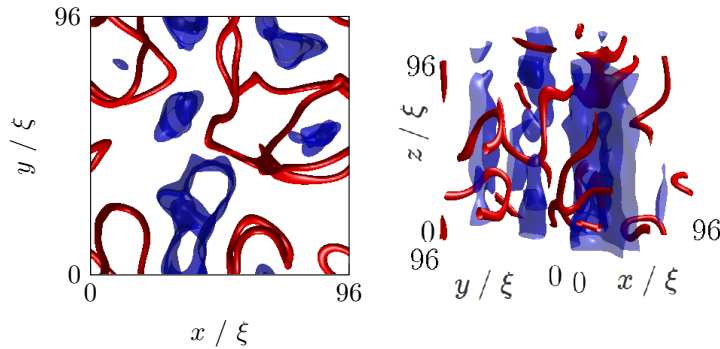


Figure 10.5: A representative snapshot (left: top view; right: angled view) for $\varepsilon_{dd} = 0.8$ ($t/\tau = 1000$) highlighting the location of the high density regions (blue isosurfaces, plotted at $0.8 \max(\langle n_q \rangle)$) and the vortices (red isosurfaces, plotted at $0.05 \langle n_q \rangle$).

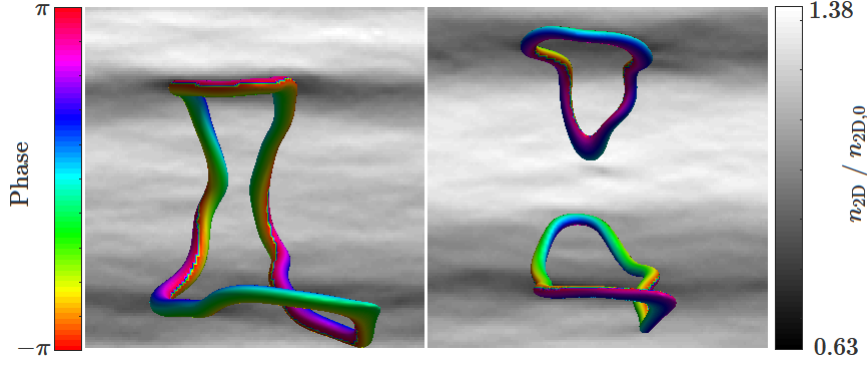


Figure 10.6: Coupling between vortices and the dipolar-driven density fluctuations. One large loop spreads across two planar density regions, which act as pinning layers. The observed dynamics are indicative of simulations for relative dipolar strength $\varepsilon_{dd} < 0$ and the times of the images shown are $t/\tau = 50$ apart from left to right. The phase is evaluated and displayed on the quasi-condensate density at the $0.05\langle n_q \rangle$ level, the back wall of the box shows the 2D density profiles, corresponding to integrating the density over the dimension perpendicular to its face.

10.4 Line-length decay

Having identified an additional ‘organisation’ of the vortices driven by the dipolar interactions we now seek to understand how this affects the nature of the turbulence itself. In contrast with classical turbulence, two distinct regimes of quantum turbulence have been identified [129]. In the quasi-classical regime, motions over a wide range of scales are observed, and many of the statistical properties of classical turbulence (such as Kolmogorov’s energy spectrum) are observed [438]. However quantum fluids also give rise to another form of turbulence, the ultraquantum or Vinen regime, which is associated with a random tangle of quantised vortices and no large-scale structure. In the quasi-classical regime energy dissipation is dictated by the lifetime of the largest scales of motion, and one can construct a classical argument that the rate of the decay of the vortex line density, L , follows a power law scaling $L \sim t^{-3/2}$. The Vinen regime can be distinguished from the quasi-classical regime because different dissipation mechanisms dominate its decay, which leads to a different power-law scaling, with L decaying as t^{-1} .

The turbulence arising from a thermally quenched (non-dipolar) Bose gas has been linked to ultra-quantum turbulence [428]. Here we estimate the vortex line length L as the volume occupied by the vortex tubes divided by their typical cross-sectional area [428]; its evolution is shown in Fig. 10.7. We interpret the behaviour above the horizontal line; below this, the number of vortices becomes of the order of unity. For $\varepsilon_{dd} = 0$ we recover the t^{-1} behaviour of ultra-quantum turbulence. The dynamics for $\varepsilon_{dd} = -0.4$ also closely follow this trend. However, what is particularly striking is that for $\varepsilon_{dd} = 0.8$ we see a faster decay, akin to $t^{-3/2}$.

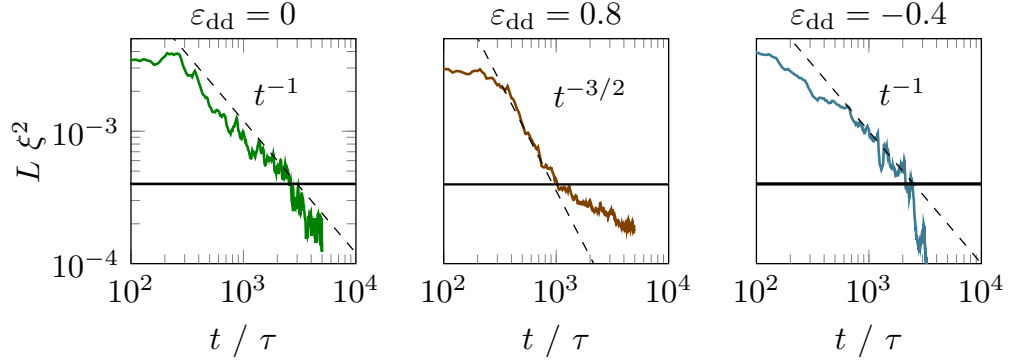


Figure 10.7: Decay of the vortex tangles. Vortex line length L for the three ε_{dd} values shown, averaged over five simulations. For reference, t^{-1} and $t^{-3/2}$ lines are shown (dashed lines) where appropriate. The horizontal line shows when the average intervortex spacing $\ell = 1/\sqrt{L}$ equals the box half-width, representing the level at which the number of vortices becomes of the order of unity.

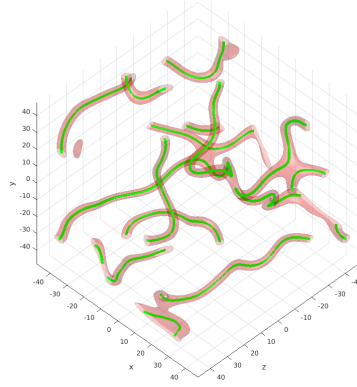


Figure 10.8: Density-threshold regions (pink) used to identify vortices in the previous analyses. Superimposed are the vortex lines (green) identified using pseudo-vorticity tracking. Image courtesy of L. Galantucci.

We have compared our density-threshold method of calculating vortex line length to the method of following the lines of pseudo-vorticity presented by Villois *et al.* [439]. An example of this is shown in Fig. 10.8. We find that the methods differ by at most around 10% throughout the vortex line decay, and improves over time. This is at odds with the results of Villois *et al.* [439], who found the discrepancy to become as large as a factor of 10 difference at late times. We speculate that the difference may be due to the different regimes of the GPE - the work of Villois *et al.* used the GPE in the zero temperature regime whereas we are in the classical-field regime, where thermal dissipation and fluctuations are present. Note that the density-threshold method is consistently larger than the pseudo-vorticity method. The reason for this is that the density-threshold method occasionally captures the low density regions between two closely-positioned vortices, as seen in Fig. 10.8. This effect diminishes over time, as the vortex line density decreases. Importantly, the difference between these methods is sufficiently small that it does not significantly affect our calculation of vortex line length, and does not affect our conclusions on the scaling of the vortex line density.

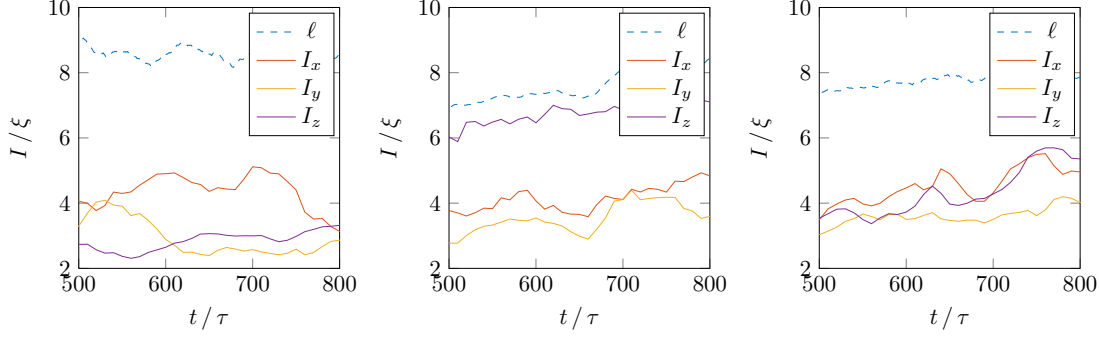


Figure 10.9: Comparison of the inter-vortex spacing $\ell = 1/\sqrt{L}$ and the integral length scale I_j , calculated along the r_j axis. From left to right $\varepsilon_{dd} = 0, 0.8, -0.4$.

At first glance, the results in Fig. 10.7 suggest that the turbulence enters the quasi-classical regime. To test this, we examine the lengthscale of the velocity correlations. We first calculate the longitudinal velocity correlation function,

$$f_j(r, t) = \langle v_j(\mathbf{r}, t) v_j(\mathbf{r} + r\hat{\mathbf{e}}_j, t) \rangle / \langle v_j(\mathbf{r}, t)^2 \rangle, \quad (10.5)$$

along each direction $j = x, y, z$, where \mathbf{v} is the quasi-condensate velocity and the ensemble average is performed over positions \mathbf{r} . From this, we calculate the integral lengthscale

$$I_j(t) = \int_0^\infty dr f_j(r, t) \quad (10.6)$$

a convenient measure of the distance over which velocities are correlated [123, 428]. The results of this calculation are presented in Fig. 10.9. For all cases of ε_{dd} , the integral lengthscales are significantly less than the average distance between vortices $\ell = 1/\sqrt{L}$: this confirms that there are no large-scale motions and that the turbulence is of the ultraquantum/Vinen form. Furthermore, for $\varepsilon_{dd} = 0$ and $\varepsilon_{dd} = -0.4$, we find that the integral lengthscale is isotropic ($I_x \approx I_y \approx I_z$) to within statistical fluctuations. However, for $\varepsilon_{dd} = 0.8$ we find that $I_z \approx 2I_x \approx 2I_y$, indicative of significant extension of the velocity correlations along the polarisation direction. This strong anisotropy in the velocity correlations may be responsible for the $t^{-3/2}$ scaling; however, a dimensional derivation of this situation which confirms this decay law remains outstanding.

10.5 Summary

To summarise, for the first time we have numerically studied turbulence in a quantum ferrofluid. In the absence of dipolar interactions the rapid quench of a thermal gas through the transition temperature generates a random unstructured tangle with no significant

large scale motions, that is, ultraquantum/Vinen turbulence. We find that for values of ε_{dd} approaching unity, where the dipolar atomic interaction is comparable to the isotropic van der Waals interactions, the quantum turbulence that emerges is strongly polarised, both in the orientation of the vortex lines and the velocity correlations of the flow. Whereas polarised quantum turbulence has been predicted in rotating superfluids [440], here the origin is very different, arising naturally from the inter-particle interactions without external forcing. In contrast for large negative values of ε_{dd} the vortices arrange into sheets; this has the potential to lead to stratified quantum turbulence, which as yet is unexplored.

We believe that turbulence in a quantum ferrofluid will allow both experimental and theoretical studies of new and interesting aspects of fluid dynamics. For example the inverse cascade has received much attention in quantum fluids recently [441], and it is entirely conceivable that new regimes of two dimensional turbulence can be realised by the presence of dipolar interactions within the gas. Finally whilst numerous mechanisms for continuously forcing three-dimensional turbulence in a BEC have been put forward [134, 136, 424], most follow James Bond's lead and shake, rather than stir the condensate, generating significant phonon excitations [424]. By using a time dependent external magnetic field, or changing the effective value of ε_{dd} (through modulation of the local van der Waals force g for example) in both space and time one could stir the fluid in a method analogous to the magnetic stirring of a classical electrically conducting fluid [442].

IV

Conclusions, outlook, and appendices

11

Conclusions and future work

In this chapter, we summarise the conclusions of the work presented throughout the thesis, and suggest relevant directions in which the work can be extended in the future.

11.1 Conclusions

In Part I we presented a history of dilute, weakly interacting dipolar Bose-Einstein condensates and introduced the mean-field theory that allows for their accurate modelling. We described the dipolar GPE, a nonlinear Schrödinger equation used to model condensates at zero temperature, and gave a detailed account of the solutions found to date. We assessed the stability of these systems by determining the fate of small perturbations to the ground state solutions and showed the presence of the roton in these systems. We also described the theory and practice of various numerical procedures we have used throughout the thesis.

Stability of the quasi-1D dipolar condensate

In Chapter 5 we derived the quasi-1D system and assessed its stability. We found that small scale perturbations become unstable for parameters when the interactions are dominantly attractive (phonon) and for specific parameters allowing for roton instability. The sensitivity of the roton was assessed for homogeneous and trapped systems. Under harmonic confinement the parameter regions of stability heavily reduce for $\sigma \rightarrow 1$. Remarkably, in homogeneous systems the regions of roton instability can flip from being 1D-like to 3D-like for a critical measure of lengthscales σ_c .

Dark solitons in homogeneous dipolar condensates

In Chapter 6 the family of dark solitons supported in quasi-1D dipolar BECs were studied. The phonon and roton instabilities of the system play a key role in modifying the density and phase profiles of the solitons, which can deviate significantly from the non-dipolar form in these regimes. We investigated the variations in the integrals of motion due to dipolar interactions and found significant deviations from the non-dipolar values, particularly so close to the instabilities.

In isolation, the solitons propagate with unchanged form throughout the parameter space. Away from the instabilities their collisions are elastic, but become dissipative via emission of sound waves close to the instabilities. Thus, close to the instabilities these structures are solitary waves rather than solitons, although it should be noted that the energy dissipated in a single collision is very small.

The solitons approximate giant localised dipoles, and have non-local soliton-soliton interactions, controllable through the direction of polarisation of the dipoles, DDI strength, and trap ratio. When attractive, and in combination with the conventional short-range repulsive interaction, unconventional dark soliton bound states can be realised. These bound states are stable to centre-of-mass propagation at constant speed. Remarkably, they act themselves like solitons during collisions, emerging with unchanged form and speed.

Dark solitons in confined dipolar condensates

In Chapter 7 we studied dark solitons in trapped quasi-1D dipolar BECs. The results were presented in experimentally relevant scenarios. While dark solitons in non-dipolar trapped BECs oscillate at a robust, characteristic ratio of the trap frequency, the oscillations in dipolar condensates become strongly dependent on the atomic interactions, and remarkably more sensitive than the collective surface modes.

Analytical models derived from previously successful methods do not capture the interaction-dependent behaviour. The dark soliton is strictly an extended excitation, not amenable to analytical treatment as a (local) particle, decomposable from the background.

Dipolar bright solitons

In Chapter 8 we found bright soliton solutions and dynamics of the quasi-1D dipolar GPE and undertook a full three-dimensional stability analysis. The bright soliton solutions obtained from the dipolar GPE exhibit a number of novel features, including collisions which have regimes of elastic behaviour, bound state formation and soliton fusion. These regimes were shown to depend sensitively on the dipolar interactions and the presence of noise, which modify the phase shifts of the solitons. We quantified the collisional behaviour in terms of the coefficient of restitution.

To better quantify the inelasticity of the solitons dynamics, we computed the coefficient of restitution, finding that the solitons exhibited sensitive bound-state dynamics, which was found to increase with the strength of the dipole-dipole interaction in the presence of noise. The origin of the variation of the coefficient of restitution with dipole-dipole interaction strength stems accordingly from the presence of the dipolar interactions which modify the phase shifts of the solitons.

The stability of the full three-dimensional dipolar system was explored; in particular

it emerged that the dipolar interactions can destabilise the bright soliton in two distinct ways, either through a traditional collapse, or instead through a runaway expansion along the axis.

Stability analysis of a rotationally tuned dipolar BEC

In Chapter 9 we outlined a semi-analytical formalism for obtaining Thomas-Fermi stationary states of a dipolar BEC, polarised perpendicularly to the rotation axis, in a harmonic trap that is symmetric about the rotation axis. Numerical GPE simulations of this scenario confirm the validity of the semi-analytically determined Thomas-Fermi solutions which, in the high atom number limit, converge to those predicted for a dipolar BEC subject to the corresponding, time-averaged, dipolar potential. However, we also find that, in this limit, the stationary solutions are found to be unstable with respect to collective oscillations induced by external perturbations. Crucially, the timescale for the onset of these instabilities is found to be on the order of 10^2 rotation cycles, suggesting that the experiments involving the rotational tuning of ε_{dd} must be carefully designed to avoid seeding these instabilities before meaningful measurements are taken.

Quantum ferrofluid turbulence

In Chapter 10 we numerically studied turbulence in a quantum ferrofluid. In the absence of dipolar interactions the rapid quench of a thermal gas through the transition temperature generates a random unstructured tangle with no significant large scale motions, that is, ultraquantum/Vinen turbulence. We find that for values of ε_{dd} approaching unity, where the dipolar atomic interaction is comparable to the isotropic van der Waals interactions, the quantum turbulence that emerges is strongly polarised, both in the orientation of the vortex lines and the velocity correlations of the flow. In contrast for large negative values of ε_{dd} the vortices arrange into sheets; this has the potential to lead to stratified quantum turbulence, which as yet is unexplored.

11.2 Further work

The work we have completed opens many avenues that could be explored in the future.

In homogeneous quasi-1D dipolar systems we could investigate the breakdown of superfluidity. In non-dipolar quasi-1D systems it has been shown that a flow past an obstacle induces solitons into the system [116] (similarly, 2D flow past a cylinder nucleates vortices, in 3D the flow past a sphere nucleates vortex rings). In dipolar systems these excitations still arise, however there is also the added nucleation of the roton, which may occur at lower critical velocities than necessary for the generation of solitons.

In two component systems, where both components are dipolar in nature, there exist two distinct roton minima, k_{c1} and k_{c2} . At the point of a roton instability we have seen that a dipolar system undergoes a phase transition into a series of droplets, separated by a distance $\lambda_{cj} = 2\pi/k_{cj}$, for each component $j = 1, 2$. If the critical wavelength ratio $\lambda_{c1}/\lambda_{c2}$ is irrational then the spacing between the droplets will be in a quasi-crystalline structure - with no repeating pattern in any region of space.

Our work on quantum ferrofluid turbulence was undertaken in an infinite homogeneous system. Unfortunately, real experimental conditions limit us to finite-sized condensates confined in traps. As previously discussed, recent experiments have employed box-like traps, which would allow for quasi-homogeneity, and our results will only be changed by the inclusion of a barrier. However, inclusion of a trapping potential will also induce a roton minimum in the excitation spectrum, which may change the dynamics we observe.



Derivation of the dipolar Bogoliubov-de Gennes equations

In 1947 Bogoliubov proposed splitting the mean-field wavefunction into two contributions: the macroscopically occupied condensate described by a complex mean-field $\psi_0(\mathbf{r})$ and weak perturbations describing small-scale excitations to the background $\delta\psi_j(\mathbf{r}, t)$ [36], a theory later applied to superconductivity of metals by de Gennes [252]. This gives a trial wavefunction

$$\psi_j(\mathbf{r}, t) = [\psi_0(\mathbf{r}) + \delta\psi_j(\mathbf{r}, t)] e^{-i\mu t/\hbar}. \quad (\text{A.1})$$

Substitution of (A.1) into the dipolar GPE (2.31) evaluates as

$$i\hbar \frac{\partial \psi_j}{\partial t} = \left(\mu \psi_0 + \mu \delta\psi_j + i\hbar \frac{\partial \delta\psi_j}{\partial t} \right) e^{-i\mu t/\hbar} \quad (\text{A.2})$$

for the left hand side, and the right hand side becomes

$$\begin{aligned} (\hat{\mathcal{H}}_0 + g|\psi_j|^2 + \Phi_{\text{dd}}[\psi])\psi = & \left\{ \hat{\mathcal{H}}_0(\psi_0 + \delta\psi_j) + g[|\psi_0|^2(\psi_0 + 2\delta\psi_j) + \psi_0^2\delta\psi_j^*] \right. \\ & \left. + \Phi_{\text{dd}}[\psi_0](\psi_0 + \delta\psi_j) + \mathcal{X}(\psi_0^*\delta\psi_j + \psi_0\delta\psi_j^*) \right\} e^{-i\mu t/\hbar}, \end{aligned} \quad (\text{A.3})$$

where only linear terms in $\delta\psi_j$ remain, the operator \mathcal{X} is defined as

$$\mathcal{X}f(\mathbf{r}) = \psi_0(\mathbf{r}) \int_{-\infty}^{\infty} d^3\mathbf{r}' U_{\text{dd}}(\mathbf{r} - \mathbf{r}') f(\mathbf{r}') \quad (\text{A.4})$$

for test function $f(\mathbf{r})$, and $\hat{\mathcal{H}}_0$ is the single-particle Hamiltonian Eq. (2.28).

Identifying that ψ_0 is the groundstate solution to the stationary dipolar GPE with chemical potential μ the linearised governing equation for the fluctuations is

$$i\hbar \frac{\partial \delta\psi_j}{\partial t} = (\hat{\mathcal{H}}_0 + 2g|\psi_0|^2 - \mu)\delta\psi_j + g\psi_0^2\delta\psi_j^* + \Phi_{\text{dd}}\delta\psi_j + \mathcal{X}(\psi_0^*\delta\psi_j + \psi_0\delta\psi_j^*). \quad (\text{A.5})$$

The fluctuations are decomposed according to

$$\delta\psi_j(\mathbf{r}, t) = u_j(\mathbf{r})e^{-i\omega_j t} - v_j^*(\mathbf{r})e^{i\omega_j t}, \quad (\text{A.6})$$

where the amplitude functions $u_j(\mathbf{r})$ and $v_j(\mathbf{r})$ are complex and the perturbation is time-dependent with characteristic frequency ω_j . Inserting Eq. (A.6) into (A.5) gives two equations, identified by equating terms in $e^{-i\omega_j t}$

$$\epsilon_j u_j = \hat{\mathcal{H}}_0 u_j + 2g|\psi_0|^2 u_j + g\psi_0^2 v_j + \Phi_{\text{dd}}[\psi_0] u_j + \mathcal{X}(u_j + v_j), \quad (\text{A.7})$$

and terms in $e^{i\omega_j t}$

$$-\epsilon_j v_j = \hat{\mathcal{H}}_0 v_j + 2g|\psi_0|^2 v_j + g\psi_0^2 u_j + \Phi_{\text{dd}}[\psi_0] v_j + \mathcal{X}(u_j + v_j), \quad (\text{A.8})$$

where $\epsilon_j = \hbar\omega_j$ is the eigenenergy of the j th excitation. In matrix form these read

$$\begin{pmatrix} \hat{\mathcal{H}} + g|\psi_0|^2 + \mathcal{X} & g|\psi_0|^2 + \mathcal{X} \\ -g|\psi_0|^2 - \mathcal{X} & -\hat{\mathcal{H}} - g|\psi_0|^2 - \mathcal{X} \end{pmatrix} \begin{pmatrix} u_j \\ v_j \end{pmatrix} = \epsilon_j \begin{pmatrix} u_j \\ v_j \end{pmatrix}, \quad (\text{A.9})$$

where we define $\hat{\mathcal{H}} = \hat{\mathcal{H}}_0 + g|\psi_0|^2 + \Phi_{\text{dd}}[\psi_0]$ as the ground-state Hamiltonian. These are the Bogoliubov-de Gennes equations for the dilute dipolar Bose gas. Solutions to these equations are found by diagonalising the matrix, however in a dipolar gas analytical solutions are limited. Solutions to the homogeneous system are discussed in Ch. 2. In a homogeneous system with background density $|\psi_0(\mathbf{r})|^2 = n_0$, $V(\mathbf{r}) = 0$ and $\mu = n_0 g$ the eigenenergies are continuous, i.e. $\epsilon_j \rightarrow \epsilon(\mathbf{k})$ and after taking Fourier transforms of both Eqs (A.7) and (A.8) the eigenvalues can be found analytically as

$$\epsilon(\mathbf{k}) = \sqrt{\frac{\hbar^2 k^2}{2m} \left(\frac{\hbar^2 k^2}{2m} + 2n_0(g + \tilde{U}_{\text{dd}}(\mathbf{k})) \right)}. \quad (\text{A.10})$$

For the general case solutions must be found numerically, however first the equations must be rewritten in a spectral basis. Following the derivation from [327] we define $\psi_j^\pm(\mathbf{r}) = u_j(\mathbf{r}) \pm v_j(\mathbf{r})$ and adding or subtracting Eqs. (A.7) and (A.8) and making the assumption that the groundstate is real gives

$$[\hat{\mathcal{H}} - \mu]\psi^+ = \epsilon_j \psi^- \quad (\text{A.11})$$

$$[\hat{\mathcal{H}} + 2g\psi_0^2 + 2\mathcal{X} - \mu]\psi^- = \epsilon_j \psi^+. \quad (\text{A.12})$$

Sequentially applying (A.11) and (A.12) leads to the decoupled equations

$$[\hat{\mathcal{H}} + 2g\psi_0^2 + 2\mathcal{X} - \mu][\hat{\mathcal{H}} - \mu]\psi^+ = \epsilon_j^2 \psi^+ \quad (\text{A.13})$$

$$[\hat{\mathcal{H}} - \mu][\hat{\mathcal{H}} + 2g\psi_0^2 + 2\mathcal{X} - \mu]\psi^- = \epsilon_j^2 \psi^- . \quad (\text{A.14})$$

Choosing the dipolar GPE spectral basis with orthonormal modes $\phi_j(\mathbf{r})$ and energies ϵ_j^{GP} defined by

$$[\hat{\mathcal{H}} - \mu]\phi_j = \epsilon_j^{\text{GP}} \phi_j . \quad (\text{A.15})$$

The excited GP modes are used, with the condensate mode removed, so that quasiparticle modes constructed from such a basis are automatically orthogonal to the condensate. The basis modes are obtained by diagonalising Eq. (A.15) using the matlab function `eigs` for the smallest amplitude N_G eigenenergies.

Making the expansion

$$\psi_j^+(\mathbf{r}) = \sum_{\alpha} c_{\alpha}^j \phi_{\alpha}(\mathbf{r}) , \quad (\text{A.16})$$

multiplying Eq. (A.13) on the left by $\phi_{\gamma}^*(\mathbf{r})$ then integrating gives the matrix equation

$$\sum_{\alpha} \int d^3\mathbf{r} \phi_{\gamma}^*(\mathbf{r}) \underbrace{[\hat{\mathcal{H}} - \mu + 2g\psi_0^2 + 2\mathcal{X}]}_{\epsilon_{\alpha}^{\text{GP}} \delta_{\gamma\alpha}} \underbrace{[\hat{\mathcal{H}} - \mu]\phi_{\alpha}(\mathbf{r})}_{\epsilon_{\alpha}^{\text{GP}} \phi_{\alpha}(\mathbf{r})} c_{\alpha}^j = \sum_{\alpha} \epsilon_j^2 \underbrace{\int d^3\mathbf{r} \phi_{\gamma} \phi_{\alpha}}_{\delta_{\gamma\alpha}} c_{\alpha}^j , \quad (\text{A.17})$$

which simplifies to

$$\sum_{\alpha} H_{\gamma\alpha} c_{\alpha}^j \equiv \sum_{\alpha} [\epsilon_{\alpha}^{\text{GP}} \delta_{\gamma\alpha} + 2M_{\gamma\delta}] \epsilon_{\alpha}^{\text{GP}} c_{\alpha}^j = \epsilon_j^2 c_{\gamma}^j , \quad (\text{A.18})$$

where

$$M_{\gamma\alpha} = g \int d^3\mathbf{r} \phi_{\gamma}^* \psi_0^2 \phi_{\alpha} + \frac{1}{(2\pi)^3} \int d^3\mathbf{k} \varphi_{\gamma}^*(-\mathbf{k}) U_{\text{dd}}(\mathbf{k}) \varphi_{\alpha}(\mathbf{k}) , \quad (\text{A.19})$$

with $\varphi_j(\mathbf{k}) = \mathcal{F}[\phi_j(\mathbf{r})\psi_0(\mathbf{r})]$.

Thus, the algorithm to find the excitation spectrum is as follows

1. Solve the dipolar GPE in imaginary time to find the groundstate ψ_0 .
2. Calculate the first N_G spectral basis modes $\phi_j(\mathbf{r})$ and energies ϵ_j^{GP} through diagonalisation of Eq. (A.15).
3. Form the exchange matrix $M_{\gamma\alpha}$.

4. Construct $H_{\gamma\alpha}$ and diagonalise to find ϵ_j^2 and coefficients c_α^j , and accept some $N_B < N_G$ modes as correct.

5. Reconstruct $u_j(\mathbf{r})$ and $v_j(\mathbf{r})$ through

$$u_j(\mathbf{r}) = \frac{1}{2} \sum_{\alpha} \left[1 + \frac{\epsilon_{\alpha}^{\text{GP}}}{\epsilon_j} \right] c_{\alpha}^j \phi_{\alpha}(\mathbf{r}) , \quad (\text{A.20})$$

$$v_j(\mathbf{r}) = \frac{1}{2} \sum_{\alpha} \left[1 - \frac{\epsilon_{\alpha}^{\text{GP}}}{\epsilon_j} \right] c_{\alpha}^j \phi_{\alpha}(\mathbf{r}) . \quad (\text{A.21})$$

6. The obtained eigenvalues are only sorted in ascending order, so we sort them based on $|\mathbf{k}|$, so the momentum of the j th eigenvalue is

$$k_j = \sqrt{\frac{\int d^3\mathbf{k} k^2 (|\tilde{u}_j(\mathbf{k})|^2 + |\tilde{v}_j(\mathbf{k})|^2)}{\int d^3\mathbf{k} |\tilde{u}_j(\mathbf{k})|^2 + |\tilde{v}_j(\mathbf{k})|^2}} . \quad (\text{A.22})$$

B

Convolution theorem

The convolution of two well behaved functions, f and g , can be defined as

$$(f * g)(x) = \int dx' f(x - x')g(x') = \int dx' f(x')g(x - x'). \quad (\text{B.1})$$

Consider the quasi-1D dipolar potential integral

$$\Phi_{1D} = \int_{-\infty}^{\infty} dx' V(x - x')n(x') = (V * n)(x). \quad (\text{B.2})$$

This integral can be more readily calculated in momentum space. We define the Fourier transform, $\mathcal{F}[\cdot]$, and inverse Fourier transform, $\mathcal{F}^{-1}[\cdot]$, respectively, as follows

$$\hat{f}(k) = \mathcal{F}[f(x)] = \int dx f(x)e^{ikx} \quad (\text{B.3})$$

$$f(x) = \mathcal{F}^{-1}[\hat{f}(k)] = \int \frac{dk}{2\pi} \hat{f}(k)e^{-ikx} \quad (\text{B.4})$$

By inputting these relations into our dipolar potential equation we can rewrite this as

$$\begin{aligned} \int dx' V(x - x')n(x') &= \int dx' \left(\int \frac{dk}{2\pi} \hat{V}(k)e^{-ik(x-x')} \right) \left(\int \frac{dq}{2\pi} \hat{n}(q)e^{-iqx'} \right) \\ &= \int \frac{dk}{2\pi} \int \frac{dq}{2\pi} \hat{V}(k)e^{-ikx} \hat{n}(q) \int dx' e^{-i(q-k)x'} \\ &= \int \frac{dk}{2\pi} \int dq \hat{V}(k)e^{-ikx} \hat{n}(q) \delta(q - k) \\ &= \int \frac{dk}{2\pi} \hat{V}(k) \hat{n}(k) e^{-ikx}. \end{aligned}$$

Therefore, the convolution of V and n has been reduced down to the inverse Fourier transform of the product of the function's Fourier transforms, or mathematically

$$\int dx' V(x - x')n(x') = \mathcal{F}^{-1} \left[\hat{V}(k) \hat{n}(k) \right]. \quad (\text{B.5})$$



Derivation of the Gross-Pitaevskii equation

In this appendix we apply the Heisenberg equation of motion to the second quantised Hamiltonian (2.27), stated again here as

$$\hat{\mathcal{H}} = \int d^3\mathbf{r} \hat{\Psi}^\dagger(\mathbf{r}) \hat{\mathcal{H}}_0 \hat{\Psi}(\mathbf{r}) + \frac{1}{2} \int d^3\mathbf{r} \int d^3\mathbf{r}' \hat{\Psi}^\dagger(\mathbf{r}) \hat{\Psi}^\dagger(\mathbf{r}') V_{\text{int}}(\mathbf{r}, \mathbf{r}') \hat{\Psi}(\mathbf{r}') \hat{\Psi}(\mathbf{r}), \quad (\text{C.1})$$

where $V_{\text{int}}(\mathbf{r}, \mathbf{r}')$ is the two-body interaction potential, and

$$\hat{\mathcal{H}}_0 = -\frac{\hbar^2}{2m} \nabla^2 + V_{\text{ext}}(\mathbf{r}), \quad (\text{C.2})$$

is the single-particle Hamiltonian, and $V_{\text{ext}}(\mathbf{r})$ is the external potential. The Bose field operators follow the commutation relations

$$[\hat{\Psi}(\mathbf{r}), \hat{\Psi}^\dagger(\mathbf{r}')] = \delta(\mathbf{r} - \mathbf{r}'), \quad (\text{C.3})$$

$$[\hat{\Psi}(\mathbf{r}), \hat{\Psi}(\mathbf{r}')] = 0, \quad (\text{C.4})$$

$$[\hat{\Psi}^\dagger(\mathbf{r}), \hat{\Psi}^\dagger(\mathbf{r}')] = 0. \quad (\text{C.5})$$

Note that the Bose field operators also depend on time, $\hat{\Psi}(\mathbf{r}) \equiv \hat{\Psi}(\mathbf{r}, t)$, which is suppressed throughout this derivation for legibility. Now we state and use the Heisenberg equation of motion to derive the system's dynamics, this equation describes a system where the state vector remains stationary and the operators evolve in time, giving

$$\begin{aligned} i\hbar \frac{\partial \hat{\Psi}(\mathbf{r})}{\partial t} &= [\hat{\Psi}(\mathbf{r}), \hat{\mathcal{H}}], \\ &= \hat{\Psi}(\mathbf{r}) \hat{\mathcal{H}} - \hat{\mathcal{H}} \hat{\Psi}(\mathbf{r}), \\ &= \hat{\Psi}(\mathbf{r}) \hat{\mathcal{H}} - \int d^3\mathbf{r}' \hat{\Psi}^\dagger(\mathbf{r}') \hat{\mathcal{H}}_0 \hat{\Psi}(\mathbf{r}') \hat{\Psi}(\mathbf{r}) \\ &\quad - \frac{1}{2} \int d^3\mathbf{r}' \int d^3\mathbf{r}'' \hat{\Psi}^\dagger(\mathbf{r}') \hat{\Psi}^\dagger(\mathbf{r}'') V_{\text{int}}(\mathbf{r}', \mathbf{r}'') \hat{\Psi}(\mathbf{r}') \hat{\Psi}(\mathbf{r}'') \hat{\Psi}(\mathbf{r}). \end{aligned}$$

The commutation relations allow us to move the $\hat{\Psi}(\mathbf{r})$ term to the left-hand side of the integrals by using the following two rules:

$$\hat{\Psi}(\mathbf{r}')\hat{\Psi}(\mathbf{r}) = \hat{\Psi}(\mathbf{r})\hat{\Psi}(\mathbf{r}') \quad \text{and} \quad \hat{\Psi}^\dagger(\mathbf{r}')\hat{\Psi}(\mathbf{r}) = \hat{\Psi}(\mathbf{r})\hat{\Psi}^\dagger(\mathbf{r}') - \delta(\mathbf{r} - \mathbf{r}'). \quad (\text{C.6})$$

$$\begin{aligned} i\hbar \frac{\partial \hat{\Psi}(\mathbf{r})}{\partial t} &= \hat{\Psi}(\mathbf{r})\hat{\mathcal{H}} - \int d^3\mathbf{r}' \left[\hat{\Psi}(\mathbf{r})\hat{\Psi}^\dagger(\mathbf{r}') - \delta(\mathbf{r}' - \mathbf{r}) \right] \hat{\mathcal{H}}_0 \hat{\Psi}(\mathbf{r}') \\ &\quad - \frac{1}{2} \int d^3\mathbf{r}' \left[\left(\hat{\Psi}(\mathbf{r})\hat{\Psi}^\dagger(\mathbf{r}') - \delta(\mathbf{r}' - \mathbf{r}) \right) \Psi^\dagger(\mathbf{r}') - \Psi^\dagger(\mathbf{r}')\delta(\mathbf{r}' - \mathbf{r}) \right] V_{\text{int}}(\mathbf{r}', \mathbf{r}'') \hat{\Psi}(\mathbf{r}')\hat{\Psi}(\mathbf{r}''), \\ &= \hat{\Psi}(\mathbf{r})\hat{\mathcal{H}} - \hat{\Psi}(\mathbf{r}) \left[\int d^3\mathbf{r}' \hat{\Psi}^\dagger(\mathbf{r}')\hat{\mathcal{H}}_0 \hat{\Psi}(\mathbf{r}') \right. \\ &\quad \left. - \frac{1}{2} \int d^3\mathbf{r}' \int d^3\mathbf{r}'' \hat{\Psi}^\dagger(\mathbf{r}')\hat{\Psi}^\dagger(\mathbf{r}'') V_{\text{int}}(\mathbf{r}', \mathbf{r}'') \hat{\Psi}(\mathbf{r}')\hat{\Psi}(\mathbf{r}'') \right] \\ &\quad + \int d^3\mathbf{r}' \hat{\mathcal{H}}_0 \hat{\Psi}(\mathbf{r}')\delta(\mathbf{r}' - \mathbf{r}) + \int d^3\mathbf{r}' \int d^3\mathbf{r}'' \hat{\Psi}^\dagger(\mathbf{r}'')\delta(\mathbf{r}' - \mathbf{r}) V_{\text{int}}(\mathbf{r}', \mathbf{r}'') \hat{\Psi}(\mathbf{r}')\hat{\Psi}(\mathbf{r}'') \\ &= \hat{\Psi}(\mathbf{r})\hat{\mathcal{H}} - \hat{\Psi}(\mathbf{r})\hat{\mathcal{H}} + \hat{\mathcal{H}}_0 \hat{\Psi}(\mathbf{r}) + \int d^3\mathbf{r}'' \hat{\Psi}^\dagger(\mathbf{r}'') V_{\text{int}}(\mathbf{r}, \mathbf{r}'') \hat{\Psi}(\mathbf{r}'')\hat{\Psi}(\mathbf{r}). \end{aligned}$$

Finally after reinserting the time dependence this gives Eq. (2.29),

$$i\hbar \frac{\partial \hat{\Psi}(\mathbf{r}, t)}{\partial t} = \hat{\mathcal{H}}_0 \hat{\Psi}(\mathbf{r}, t) + \int d^3\mathbf{r}' \hat{\Psi}^\dagger(\mathbf{r}', t) V_{\text{int}}(\mathbf{r}, \mathbf{r}') \hat{\Psi}(\mathbf{r}', t) \hat{\Psi}(\mathbf{r}, t). \quad (\text{C.7})$$

After applying the mean-field approximation $\hat{\Psi} \rightarrow \psi$, and applying the pseudo-potential,

$$V_{\text{int}}(\mathbf{r}, \mathbf{r}') \rightarrow U(\mathbf{r}, \mathbf{r}') = g\delta(\mathbf{r} - \mathbf{r}') + \frac{C_{\text{dd}}}{4\pi} \left(\frac{1 - 3\cos^2\theta}{|\mathbf{r} - \mathbf{r}'|^3} \right), \quad (\text{C.8})$$

leads to the dipolar Gross-Pitaevskii equation, Eq. (2.31),

$$i\hbar \frac{\partial \psi(\mathbf{r}, t)}{\partial t} = \left(-\frac{\hbar^2 \nabla^2}{2m} + V_{\text{ext}}(\mathbf{r}, t) + gn(\mathbf{r}, t) + \Phi_{\text{dd}}(\mathbf{r}, t) \right) \psi(\mathbf{r}, t). \quad (\text{C.9})$$

D

Probing quasi-integrability of the Gross-Pitaevskii equation in the harmonic oscillator potential

Previous simulations of the one-dimensional Gross-Pitaevskii equation (GPE) with repulsive nonlinearity and a harmonic-oscillator trapping potential hint towards the emergence of quasi-integrable dynamics – in the sense of quasi-periodic evolution of a moving dark soliton without any signs of ergodicity – although this model does not belong to the list of integrable equations. To investigate this problem, we replace the full GPE by a suitably truncated expansion over harmonic oscillator eigenmodes (the Galerkin approximation), which accurately reproduces the full dynamics, and then analyse the system’s dynamical spectrum. The analysis enables us to interpret the observed quasi-integrability as the fact that the finite-mode dynamics always produces a *quasi-discrete* power spectrum, with no visible continuous component, the presence of the latter being a necessary manifestation of ergodicity. This conclusion remains true when a strong random-field component is added to the initial conditions. On the other hand, the same analysis for the GPE in an infinitely deep potential box leads to a clearly continuous power spectrum, typical for ergodic dynamics.

This work is presented as a standalone Chapter, and is based on the work published in Ref. [202].

D.1 Introduction

Integrability, relaxation, and thermalisation of many-body systems are intricately-linked key topics of the modern theory of non-equilibrium dynamical systems. Although, strictly speaking, a closed quantum system should exhibit no thermalisation in the usual sense, non-integrable closed systems can nonetheless mimic relaxation to thermal equilibrium through dephasing occurring within the eigenstate thermalisation hypothesis [443, 444].

The investigation of these issues has recently become a core activity in studies of dynamics of ultracold gases [445], due to the uniquely precise experimental control achieved

in this field. Such settings can be engineered in both weak- and strong-interaction regimes, the effectively one-dimensional (1D) realisations being of particular relevance, as the respective model equations may be able to support integrable dynamics. In this context, pioneering experiments with ultracold atoms in the effectively 1D regime have revealed evidence for a long-term absence of thermalisation [446], attributed to the expected integrability of the underlying (Lieb-Liniger) model of strong interactions. Subsequent works, however, have predicted timescales for the breakdown of integrability in experimentally relevant geometries, with thermalisation possible through virtual excitation of higher radial modes [447, 448]. These findings were reported to be consistent with both the previous experiments [446] and other relevant observations [449], subsequent work also addressing the emergence of pre-thermalisation [450], in which a closed system loses part of its initial information.

In the idealised setting described by an integrable equation, which possesses an infinite number of conserved quantities, the trajectories are weakly sensitive to initial conditions, lying on invariant tori in the phase space, realistic systems often exhibit “weak integrability breaking”, in the sense that one can construct and probe “quasi-conserved” quantities. One should here distinguish between two different issues: the perceived presence of (quasi-)integrability of a given physical system as probed in experiments, and the emergence of integrability in the equations believed to accurately describe the physical system, which is usually probed through numerical simulations. The fundamental equation describing ultracold atoms in the weakly-interacting regime is the nonlinear Schrödinger equation (NLSE), with cubic nonlinearity arising from inter-atomic collisions, alias the Gross-Pitaevskii equation (GPE). This equation is the workhorse of the theoretical studies of ultracold atoms, with an impressive portfolio of successes in predicting experimental phenomena to high accuracy, including the static characteristics of the ultracold gases, their modes, nonlinear waves, dynamical instabilities, etc. [44, 45, 451]. The most common case to which we limit our study here is when the effective interactions are repulsive (i.e., the respective nonlinearity is defocusing). Such an equation is known to be integrable in the 1D free space (including the case of periodic boundary conditions) [177, 452–454], but not in the presence of the harmonic oscillator confining potential, which is relevant for modelling actual experiments. Even in this case, however, long-time simulations of the 1D GPE have revealed no conclusive evidence of chaotisation [455, 456], which is believed to originate in the experiment from the coupling to transverse degrees of freedom, beyond the limits of the 1D approximation [448]. On the other hand, a single particle in the harmonic oscillator trap is commonly known to be integrable. The question then arises under what conditions, and to what extent, features of the integrability may be approximately preserved in many-body systems trapped by this potential.

The closest many-body state which exhibits some particle-like properties is a soli-

tonic excitation – specifically, a dark soliton in the case of repulsive interactions, which is thus a natural candidate to use as a probe of the integrability. Importantly, previous studies of the motion of dark solitons in the harmonic oscillator-trapped 1D GPE lead to a quasi-periodic evolution, revealing no evidence of chaotisation (ergodicity) in the evolution of the mean-field wavefunction, unlike certainly non-integrable settings, corresponding to other (anharmonic) probed trapping potentials [457, 458]. This observation suggests an “apparent quasi-integrability” of the 1D GPE in the harmonic oscillator trap, with regard to the motion of a dark soliton, which was predicted to perform shuttle motion, as a classical particle, with a well-defined oscillation amplitude and frequency [384, 459, 179, 370, 375, 147, 379]. This behaviour is consistent with experiments which have generated dark solitons and demonstrated their motion in elongated quasi-1D BECs [181, 182, 113, 115, 183, 116, 184–189]. However, the presence of any potential, *including* the harmonic oscillator trap, is known to break the integrability of the underlying GPE, and, in particular, to trigger the emission of small-amplitude excitations (“sound waves”) from dark solitons moving with acceleration [179, 370, 379, 457, 373, 460, 461]. This mechanism of the decay of dark solitons into radiation is similar to that known for optical dark solitons governed by the NLSE [462, 178, 344].

To reconcile these apparently contrasting predictions, one implying the presence of the effective quasi-integrability, and the other referring to the non-integrability of the GPE with the harmonic oscillator potential, it was proposed that the emission of sound waves might be reversible, i.e., that the dark soliton may reabsorb the emitted waves, thus stabilizing itself against the systematic decay [458, 379, 460]. This effect may even be employed to preferentially stabilise dark solitons in states with selected energies [463]. The reversibility effect has been shown to be crucial over timescales shorter than those imposed by other non-integrability factors (for example, those related to thermal dissipation and coupling to the transverse dimensions) in harmonic oscillator-trapped BECs [384, 459, 344, 464, 366, 357, 465–471]. In turn, the sound-emission reversibility suggests that the harmonic oscillator potential may maintain quasi-integrability of the system. Further evidence to support this conjecture comes from simulations which reveal a systematic decay when the harmonic oscillator potential is altered, and the quasi-integrability is clearly broken, e.g., by the addition of dimple traps [179, 379], an optical lattice [457, 472], or a localised obstacle [473, 344]. Another sign of the quasi-integrability in the presence of the harmonic oscillator confinement is an essentially elastic character of collisions between two trapped dark solitons, observed in direct simulations and verified experimentally [187, 367].

To gain insight into the presumably quasi-integrable dynamics, we here develop a finite-mode approximation for the 1D GPE with the harmonic oscillator potential, known as the *Galerkin approximation* [474]: the wave field is expanded over the full set of eigen-

modes of the linear Schrödinger equation with the harmonic oscillator potential, thus replacing the underlying cubic GPE by a chain of nonlinearly coupled ordinary differential equations for the evolution of amplitudes of the eigenmode expansion. The chain is truncated for a finite set of M modes, sufficient to provide an accurate approximation for the global evolution of the mean-field wave function governed by the GPE, including relevant features such as the above-mentioned sound emission and absorption by the dark soliton. A similar expansion approach was developed for various nonlinear models [475–477], including multi-component and multi-dimensional GPE systems [478, 479].

The finite-mode Galerkin expansion is also at the heart of the projected Gross-Pitaevskii equation (PGPE) [437], which has been extensively applied to model Bose gases at finite temperatures. However, there are several contextual differences between our study and those using the PGPE. Specifically, we seek to approximate the zero-temperature GPE wave field, not a thermal field, with the key point being that we can very accurately capture the soliton dynamics and aspects of quasi-integrability by employing $M = 16$ modes.

The aim of our analysis, performed in the framework of the suitably truncated finite-mode dynamical system, is to highlight the degree of the quasi-integrability of the underlying cubic GPE including the harmonic oscillator potential. Specifically, we find, with high numerical accuracy, that the power spectrum of all dynamical trajectories remains *quasi-discrete* in the course of the indefinitely long evolution, corresponding to a quasi-periodic motion, rather than to chaotic dynamics. This observation strongly suggests that the Galerkin-approximation system with a finite number of the degrees of freedom has almost all its trajectories spanning invariant tori, in accordance with the Kolmogorov-Arnold-Moser theorem [480, 481]. Such a finding provides an adequate explanation of the effective quasi-integrability featured by the underlying harmonically-trapped GPE in the previously reported direct simulations [379].

Although the analysis reveals strong evidence of the repeated reversible cycles of the emission/absorption of radiation from/by the dark soliton, there is no straightforward way to isolate the soliton and sound modes through the Galerkin approximation in the condensate trapped in the harmonic oscillator potential. To demonstrate the role of this process in a more explicit form, we also develop a similar analysis for the GPE in a potential box with zero boundary conditions (i.e., an infinitely deep rectangular potential, which can be experimentally realised using electromagnetic fields [50–53], although the box walls in the experiment are softer than the ideal impenetrable ones). The Galerkin approximation for the potential box can be naturally built on the basis of the underlying sine and cosine eigenfunctions [482]. Systematic simulations of the GPE in the infinitely deep box show that a moving dark soliton shuttles back and forth in a stable manner (although the soft walls may cause an instability and sound emission [483]). Interestingly, and perhaps somewhat unexpectedly, we find in this case that the power spectrum of generic

trajectories is continuous, in direct contrast to the quasi-discrete spectrum found in the harmonic oscillator potential, which clearly suggests chaotisation (ergodicity) of the dynamics in the box, rather than evolution guided by invariant tori. Such behaviour is also wholly captured by our finite-mode expansion (without the need for using the known exact box eigenstates of the nonlinear equation [484]).

It is relevant to mention that, strictly speaking, the NLSE in a finite interval with zero boundary conditions belongs to the class of integrable equations [485–488]. This fact seems to be in contradiction with the above-mentioned ergodicity revealed by the Galerkin approximation for the potential box. However, it is known that there are two types of integrability, *strong* and *weak* [489]. The contradistinction between them is based on the relation between the numbers of degrees of freedom and dynamical invariants. Indeed, a Liouville-integrable dynamical system with a finite number of degrees of freedom must have it equal to the number of dynamical invariants [490]. In the limit of the infinite number of degrees of freedom (integrable PDEs), the set of dynamical invariants is also infinite, but in the case of weak integrability the set is incomplete (not “sufficiently infinite”), which allows the system to feature non-integrable dynamics, such as fission and merger of solitons in the weakly integrable three-wave system [491, 492], another known example of weak integrability being provided by the Kadomtsev-Petviashvili-I equation. Models of this type, in spite of their formal integrability, readily admit chaotic dynamics – in particular, in the form of wave turbulence in the free space [489]. Of course, the finite-mode truncation most plausibly breaks the strong and weak integrability of the underlying partial differential equation alike, but the concept of the weak integrability suggests a possible explanation to the fact that the truncation, derived for a weakly integrable model, may feature ergodicity: if the underlying model admits chaotic dynamics, the truncated version may feature it too. Concerning the GPE in the finite-size box, the issue of its strong/weak integrability is not explored yet, to the best of our knowledge. This issue may be a subject for a separate study, which is definitely beyond the scope of the present work.

The rest of the Chapter is organised as follows. In Sec. D.2, we summarise the Galerkin approximation for both the harmonic oscillator and box traps and demonstrate its success in capturing both the ground-state solutions and dark-soliton motion, with only a small number of modes in the truncation. This finding enables us to use the motion of the dark soliton, Sec. D.3 as a probe for the quasi-integrability of the 1D harmonically-confined GPE, focusing in Sec. D.4 on the distinction between the quasi-discrete and continuous spectra of the evolution of complex amplitudes of the Galerkin truncation, which are found, respectively, in the harmonic oscillator and box traps. Our findings are summarised in Sec. D.5.

D.2 The Galerkin approximation and its validity

Our analysis starts from the well-known 1D GPE, written in the presence of an arbitrary time-independent potential, $V(x)$ [44, 45],

$$i\hbar \frac{\partial \Psi}{\partial t} = -\frac{\hbar^2}{2m} \frac{\partial^2 \Psi}{\partial x^2} + g|\Psi|^2\Psi + V(x)\Psi. \quad (\text{D.1})$$

Here $\Psi(x, t)$ is the mean-field wave function of the BEC, normalised to the number of particles $\mathcal{N} = \int |\Psi|^2 dx$, and g is the coefficient of the cubic nonlinearity, induced by the van der Waals interactions between atoms which make up the BEC. The characteristic energy, length and time scales are the chemical potential μ of the BEC, the healing length $\xi = \hbar/\sqrt{m\mu}$, and $\tau = \xi/c$, where $c = \sqrt{\mu/m}$ is the speed of sound, and m is the atomic mass. Using these scales to define dimensionless energy, position and time variables, Eq. (D.1) can be rewritten as

$$i \frac{\partial \psi}{\partial \tilde{t}} = -\frac{1}{2} \frac{\partial^2 \psi}{\partial \tilde{x}^2} + \sigma |\psi|^2 \psi + \tilde{V}(\tilde{x})\psi, \quad (\text{D.2})$$

where $\psi = \sqrt{2|a_s|/\xi^2}\Psi$ and $\sigma = +1$ and -1 corresponds to the repulsive and attractive nonlinearities, respectively. The dimensionless wave function $\psi \equiv \psi(\tilde{x}, \tilde{t})$ is subject to normalisation $N = \int |\psi|^2 d\tilde{x}$, where $\mathcal{N} = \mu \xi N/g$. Thus, for typical experimental parameters the atom number will correspond to $\mathcal{N} \sim 10^4 N$. From this point on, we drop the tilde notation for dimensionless variables; the exception is in figures, where x and t are presented in the dimensional form.

In this work, we are interested in repulsive interactions which admit dark solitons trapped in the external potential [179], therefore we fix $\sigma = 1$. We consider harmonic oscillator and box potentials, which are defined, respectively, as

$$V(x) = \frac{1}{2}\omega_x^2 x^2, \quad \omega_x \equiv 1, \quad \text{or} \quad V(x) = \begin{cases} 0, & \text{at } 0 < x < L, \\ \infty, & \text{elsewhere.} \end{cases} \quad (\text{D.3})$$

In the former case, $\omega_x \equiv 1$ is fixed by rescaling. It is relevant to note that the infinite-box potential, which gives rise to zero boundary conditions, $\psi(x=0) = \psi(x=L) = 0$, directly applies, in addition to BEC, as the model of a metallic conduit for microwaves [493].

The Galerkin approximation takes two different forms, depending on the potential considered. In each case, the wave field is approximated by an M -mode linear combination of time-dependent eigenmodes of the corresponding linear Schrödinger equation, with each eigenmode subject to the unitary normalisation. In the harmonic oscillator case,

the corresponding ansatz is

$$\psi_{\text{GA}}(x, t) = \sum_{n=0}^{M-1} a_n(t) \exp\left(-\frac{x^2}{2} - i\left(\frac{1}{2} + n\right)t\right) \frac{H_n(x)}{\pi^{1/4} \sqrt{2^n n!}}, \quad (\text{D.4})$$

where $a_n(t)$ are complex amplitudes, which are slowly varying functions of time, in comparison with $\exp\left(-i\left(\frac{1}{2} + n\right)t\right)$, and $H_n(x)$ are the Hermite polynomials. In the case of the box potential, the expansion is built as

$$\psi_{\text{GA}}(x, t) = \sum_{n=0}^{M-1} a_n(t) \sqrt{\frac{2}{L}} \sin\left(\frac{(n+1)\pi x}{L}\right) e^{-iE_n t}, \quad (\text{D.5})$$

with $E_n = \pi^2 (n+1)^2 / 2L^2$, and amplitudes $a_n(t)$ being slowly varying functions in comparison with $\exp(-iE_n t)$.

Note that it would also be possible to conduct the expansion using the nonlinear modes of the system. However, while the nonlinear solutions in the 1D box potential are known [484], they are not known in analytical form for the harmonic potential. Moreover, the nonlinear box solutions would give rise to extremely cumbersome differential equations. Hence for the purpose of this work we focus on expansion into linear modes, which are clearly demonstrated to capture the key features of the underlying GPE they are approximating.

Evolution equations for amplitudes a_n can be readily derived by means of the variational principle [494, 495]. To this end, we use the Lagrangian of Eq. (D.2),

$$L = \int_{-\infty}^{+\infty} \left(i\psi^* \frac{\partial \psi}{\partial t} - \frac{1}{2} \left| \frac{\partial \psi}{\partial x} \right|^2 - \frac{\sigma}{2} |\psi|^4 - V(x) |\psi|^2 \right) dx. \quad (\text{D.6})$$

The substitution of *ansätze* defined by Eqs. (D.4) and (D.5) into the Lagrangian leads to the following result,

$$L = i \sum_{n=0}^{M-1} a_n^* \frac{da_n}{dt} - H, \quad (\text{D.7})$$

where the Hamiltonian is

$$H = f(a_0, \dots, a_{M-1}, a_0^*, \dots, a_{M-1}^*, t), \quad (\text{D.8})$$

and function f is a combination of quartic terms, depending on the number of modes kept in the Galerkin approximation. Accordingly, the dynamics are governed by the Euler-

Lagrange equations derived from the Lagrangian,

$$\frac{da_n}{dt} = -i \frac{\partial H}{\partial a_n^*} . \quad (\text{D.9})$$

This is a mechanical system with M degrees of freedom and two dynamical invariants, H and the total norm,

$$N = \sum_{n=0}^{M-1} |a_n|^2 . \quad (\text{D.10})$$

D.2.1 The four-mode truncated Hamiltonian and dynamical equations

An explicit form of the Hamiltonian and dynamical equations for the Galerkin approximation with $M = 4$ are given below. Similar equations have been explicitly derived up to $M = 16$ (they are not included here, as they seem too cumbersome, but, nevertheless, they are tractable, for the purposes of the current analysis.) The Hermite polynomials required to construct the corresponding Galerkin approximation ansatz are

$$H_0(x) = 1, \quad H_1(x) = 2x, \quad H_2(x) = 2(2x^2 - 1), \quad H_3(x) = 4x(2x^2 - 3) .$$

Calculation of the quartic term in the corresponding Lagrangian (D.6) leads to Hamiltonian (D.8) in the following form:

$$\begin{aligned}
 H = \frac{\sigma}{2\sqrt{2\pi}} \left[\right. & |a_0|^4 + \frac{3}{4} |a_1|^4 + \frac{41}{64} |a_2|^4 + \frac{147}{256} |a_3|^4 + 2|a_0|^2|a_1|^2 + \frac{3}{2}|a_0|^2|a_2|^2 + \frac{7}{4}|a_1|^2|a_2|^2 \\
 & + \frac{5}{4}|a_0|^2|a_3|^2 + \frac{11}{8}|a_1|^2|a_3|^2 + \frac{51}{32}|a_2|^2|a_3|^2 + \frac{\sqrt{3}}{4} (a_1 a_2 a_0^* a_3^* + a_0 a_1^* a_2^* a_3) \\
 & + \frac{5\sqrt{3}}{16\sqrt{2}} (a_2^2 a_1^* a_3^* + a_1 (a_2^*)^2 a_3) + \frac{1}{2\sqrt{2}} (a_1^2 a_0^* a_2^* + a_0 a_2 (a_1^*)^2) \\
 & + \frac{5}{16} (a_0^2 (a_3^*)^2 + (a_0^*)^2 a_3^2) + \frac{11}{32} (e^{4it} a_1^2 (a_3^*)^2 + e^{-4it} (a_1^*)^2 a_3^2) \\
 & + \frac{51}{128} (e^{2it} a_2^2 (a_3^*)^2 + e^{-2it} (a_2^*)^2 a_3^2) + \frac{1}{16\sqrt{2}} (e^{4it} a_0 a_2 (a_3^*)^2 + e^{-4it} a_0^* a_2^* a_3^2) \\
 & + \frac{3\sqrt{3}}{32\sqrt{2}} (e^{2it} a_1 a_3^* |a_3|^2 + e^{-2it} a_1^* |a_3|^2 a_3) + \frac{1}{2} (e^{2it} a_0^2 (a_1^*)^2 + e^{-2it} a_1^2 (a_0^*)^2) \\
 & + \frac{1}{\sqrt{2}} (e^{2it} a_0 |a_1|^2 a_2^* + e^{-2it} |a_1|^2 a_2 a_0^*) - \frac{1}{\sqrt{2}} (e^{2it} |a_0|^2 a_0 a_2^* + e^{-2it} |a_0|^2 a_2 a_0^*) \\
 & - \sqrt{\frac{3}{2}} (e^{2it} a_1 |a_0|^2 a_3^* + e^{-2it} |a_0|^2 a_1^* a_3) + \frac{7}{16} (e^{2it} a_1^2 (a_2^*)^2 + e^{-2it} a_2^2 (a_1^*)^2) \\
 & + \frac{1}{8\sqrt{2}} (e^{2it} a_0 |a_2|^2 a_2^* + e^{-2it} |a_2|^2 a_2 a_0^*) - \frac{\sqrt{3}}{2\sqrt{2}} (e^{4it} a_0^2 a_1^* a_3^* + e^{-4it} a_1 (a_0^*)^2 a_3) \\
 & + \frac{5\sqrt{3}}{8\sqrt{2}} (e^{2it} a_1 |a_2|^2 a_3^* + e^{-2it} |a_2|^2 a_1^* a_3) - \frac{\sqrt{3}}{4\sqrt{2}} (e^{2it} |a_1|^2 a_1 a_3^* + e^{-2it} |a_1|^2 a_1^* a_3) \\
 & + \frac{\sqrt{3}}{4} (e^{4it} a_0 a_1 a_2^* a_3^* + e^{-4it} a_2 a_0^* a_1^* a_3) + \frac{3}{8} (e^{4it} a_0^2 (a_2^*)^2 + e^{-4it} a_2^2 (a_0^*)^2) \\
 & \left. + \frac{\sqrt{3}}{4\sqrt{2}} (e^{2it} a_0 a_2 a_1^* a_3^* + e^{-2it} a_1 a_0^* a_2^* a_3) + \frac{1}{8\sqrt{2}} (e^{2it} a_0 a_2^* |a_3|^2 + e^{-2it} a_2 a_0^* |a_3|^2) \right].
 \end{aligned}$$

Finally, substituting this Hamiltonian in Euler-Lagrange equations (D.9), we arrive at the following dynamical system with four degrees of freedom:

$$\begin{aligned}
 i\frac{2\sqrt{2\pi}}{\sigma}\frac{da_0}{dt} &= 2a_0^*a_0^2 - \frac{1}{\sqrt{2}}a_2^*e^{2it}a_0^2 - \sqrt{2}a_2a_0^*e^{-2it}a_0 - \sqrt{\frac{3}{2}}a_3a_1^*e^{-2it}a_0 - \sqrt{\frac{3}{2}}a_1a_3^*e^{2it}a_0 \\
 &\quad + 2a_1a_1^*a_0 + \frac{3}{2}a_2a_2^*a_0 + \frac{5}{4}a_3a_3^*a_0 + \frac{5}{8}a_3^2a_0^*e^{-6it} + \frac{3}{4}a_2^2a_0^*e^{-4it} - \sqrt{\frac{3}{2}}a_1a_3a_0^*e^{-4it} \\
 &\quad + \frac{1}{4}\sqrt{3}a_2a_3a_1^*e^{-4it} + \frac{1}{16\sqrt{2}}a_3^2a_2^*e^{-4it} + a_1^2a_0^*e^{-2it} + \frac{1}{\sqrt{2}}a_1a_2a_1^*e^{-2it} \\
 &\quad + \frac{1}{8\sqrt{2}}a_2^2a_2^*e^{-2it} + \frac{1}{4}\sqrt{3}a_1a_3a_2^*e^{-2it} + \frac{1}{8\sqrt{2}}a_2a_3a_3^*e^{-2it} + \frac{1}{2\sqrt{2}}a_1^2a_2^* + \frac{1}{4}\sqrt{3}a_1a_2a_3^*, \\
 i\frac{2\sqrt{2\pi}}{\sigma}\frac{da_1}{dt} &= a_1^*e^{2it}a_0^2 - \frac{1}{2}\sqrt{\frac{3}{2}}a_3^*e^{4it}a_0^2 - \sqrt{\frac{3}{2}}a_3a_0^*e^{-2it}a_0 + \frac{1}{\sqrt{2}}a_1a_2^*e^{2it}a_0 \\
 &\quad + \frac{1}{4}\sqrt{3}a_2a_3^*e^{2it}a_0 + 2a_1a_0^*a_0 + \frac{1}{\sqrt{2}}a_2a_1^*a_0 + \frac{1}{4}\sqrt{3}a_3a_2^*a_0 + \frac{1}{4}\sqrt{3}a_2a_3a_0^*e^{-4it} \\
 &\quad + \frac{11}{16}a_3^2a_1^*e^{-4it} + \frac{1}{\sqrt{2}}a_1a_2a_0^*e^{-2it} + \frac{7}{8}a_2^2a_1^*e^{-2it} - \frac{1}{2}\sqrt{\frac{3}{2}}a_1a_3a_1^*e^{-2it} \\
 &\quad + \frac{5}{8}\sqrt{\frac{3}{2}}a_2a_3a_2^*e^{-2it} + \frac{3}{32}\sqrt{\frac{3}{2}}a_3^2a_3^*e^{-2it} - \frac{1}{4}\sqrt{\frac{3}{2}}a_1^2a_3^*e^{2it} + \frac{3}{2}a_1^2a_1^* \\
 &\quad + \frac{7}{4}a_1a_2a_2^* + \frac{5}{16}\sqrt{\frac{3}{2}}a_2^2a_3^* + \frac{11}{8}a_1a_3a_3^*, \\
 i\frac{2\sqrt{2\pi}}{\sigma}\frac{da_2}{dt} &= \frac{3}{4}a_2^*e^{4it}a_0^2 - \frac{1}{\sqrt{2}}a_0^*e^{2it}a_0^2 + \frac{1}{\sqrt{2}}a_1a_1^*e^{2it}a_0 + \frac{1}{4\sqrt{2}}a_2a_2^*e^{2it}a_0 \\
 &\quad + \frac{1}{8\sqrt{2}}a_3a_3^*e^{2it}a_0 + \frac{1}{4}\sqrt{3}a_1a_3^*e^{4it}a_0 + \frac{3}{2}a_2a_0^*a_0 + \frac{1}{4}\sqrt{3}a_3a_1^*a_0 + \frac{1}{16\sqrt{2}}a_3^2a_0^*e^{-4it} \\
 &\quad + \frac{1}{8\sqrt{2}}a_2^2a_0^*e^{-2it} + \frac{1}{4}\sqrt{3}a_1a_3a_0^*e^{-2it} + \frac{5}{8}\sqrt{\frac{3}{2}}a_2a_3a_1^*e^{-2it} + \frac{51}{64}a_3^2a_2^*e^{-2it} \\
 &\quad + \frac{7}{8}a_1^2a_2^*e^{2it} + \frac{5}{8}\sqrt{\frac{3}{2}}a_1a_2a_3^*e^{2it} + \frac{1}{2\sqrt{2}}a_1^2a_0^* + \frac{7}{4}a_1a_2a_1^* + \frac{41}{32}a_2^2a_2^* \\
 &\quad + \frac{5}{8}\sqrt{\frac{3}{2}}a_1a_3a_2^* + \frac{51}{32}a_2a_3a_3^*, \\
 i\frac{2\sqrt{2\pi}}{\sigma}\frac{da_3}{dt} &= -\frac{1}{2}\sqrt{\frac{3}{2}}a_1^*e^{4it}a_0^2 + \frac{5}{8}a_3^*e^{6it}a_0^2 - \sqrt{\frac{3}{2}}a_1a_0^*e^{2it}a_0 + \frac{1}{4}\sqrt{3}a_2a_1^*e^{2it}a_0 \\
 &\quad + \frac{1}{8\sqrt{2}}a_3a_2^*e^{2it}a_0 + \frac{1}{4}\sqrt{3}a_1a_2^*e^{4it}a_0 + \frac{1}{8\sqrt{2}}a_2a_3^*e^{4it}a_0 + \frac{5}{4}a_3a_0^*a_0 + \frac{1}{8\sqrt{2}}a_2a_3a_0^*e^{-2it} \\
 &\quad + \frac{3}{32}\sqrt{\frac{3}{2}}a_3^2a_1^*e^{-2it} - \frac{1}{4}\sqrt{\frac{3}{2}}a_1^2a_1^*e^{2it} + \frac{5}{8}\sqrt{\frac{3}{2}}a_1a_2a_2^*e^{2it} + \frac{51}{64}a_2^2a_3^*e^{2it} \\
 &\quad + \frac{3}{16}\sqrt{\frac{3}{2}}a_1a_3a_3^*e^{2it} + \frac{11}{16}a_1^2a_3^*e^{4it} + \frac{1}{4}\sqrt{3}a_1a_2a_0^* + \frac{5}{16}\sqrt{\frac{3}{2}}a_2^2a_1^* \\
 &\quad + \frac{11}{8}a_1a_3a_1^* + \frac{51}{32}a_2a_3a_2^* + \frac{147}{128}a_3^2a_3^*.
 \end{aligned}$$

D.2.2 Exploring the accuracy of the Galerkin approximation

We employ a Crank-Nicolson method to find stationary and dynamic solutions to the GPE in MATLAB. Typical simulation parameters are (in the scaled units): spatial discretisation $\Delta x = 0.05$, simulation-box length $L = 20$, and time step $\Delta t = 0.001$. The finite-mode dynamical system based on Eq. (D.9) was also solved with the help of MATLAB. The largest mode number considered in this work is $M = 16$, the consideration of still larger M being technically possible, but not really necessary, as shown by the results presented below.

Here we characterise the ability of the Galerkin approximation to capture the stationary ground state of the system, as a function of the mode number M and norm N . Using a stationary solution ψ_{GPE} of the GPE (obtained by means of the imaginary-time propagation [451]), Galerkin approximation amplitudes a_j (see Eqs. (D.4) and (D.5)) are calculated by projecting ψ_{GPE} onto the set of eigenstates of the respective linearised Schrödinger equation,

$$a_j(0) = \int_{\mathcal{V}} dx \, \psi_j(x) \psi_{\text{GPE}}(x), \quad (\text{D.11})$$

where \mathcal{V} is the actual range of x for the harmonic oscillator potential, and interval $0 < x < L$ for the box. Using the amplitudes given by Eq. (D.11) to construct the Galerkin approximation wave function $\psi_{\text{GA}}(x, 0)$, as per Eqs. (D.4) and (D.5), we define the *fidelity* F of the approximation as

$$F = \frac{1}{N} \int_{\mathcal{V}} dx \, \psi_{\text{GA}}(x, 0) \psi_{\text{GPE}}(x), \quad (\text{D.12})$$

where $F = 1$ ($F = 0$) corresponds to two identical (mutually orthogonal) wave functions.

Figure D.1 (top row) shows how the number of modes affects the fidelity of the initial Galerkin approximation wave function, for different norms N . In the case of the harmonic oscillator trap and $M = 16$, the fidelity is virtually exactly $F = 1$, implying an almost perfect GPE-Galerkin approximation overlap for all norms considered. For the box trap, the fidelity is still good but poorer than for the harmonic oscillator; even in the case of $N = 1$ (weak nonlinearity), ψ_{GPE} for the box is not perfectly approximated by the truncation with $M < 10$.

Finally we explore the validity of the Galerkin model for recreating dynamical simulations of the GPE. Figure D.1 (bottom row) explores the role of the mode truncation in the Galerkin approximation, by direct comparison of dark soliton oscillation frequencies (see Sec. D.3), extracted from the GPE simulations, and their counterparts, predicted by the Galerkin approximation, as a function of the total norm. The results clearly show that the increasing number of modes, M , improves the Galerkin approximation accuracy for all norms considered.

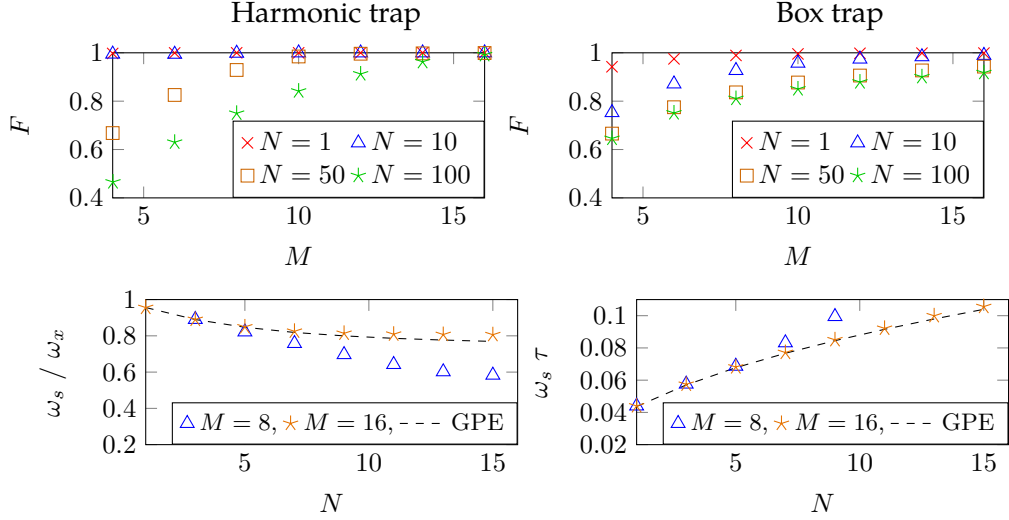


Figure D.1: (Top row) Fidelity of the ground-state wave function vs. the number of modes, M , kept in the Galerkin approximation, shown for the harmonic oscillator (left) and box (right) traps, with different values of norm N . (Bottom row) Effect of the increasing number of modes in the Galerkin approximation on its accuracy, estimated by the comparison of the frequency of the shuttle oscillations of the dark soliton with results of the GPE simulations (see Sec. D.3). Other parameters used here are the same as in Fig. D.2.

D.3 Dark-soliton dynamics as the testbed for the validity of the Galerkin approximation

Next we test the validity of the Galerkin approximation for the dark soliton through its comparison to the numerically exact GPE solution. In the case of the repulsive nonlinearity ($\sigma > 0$), which we deal with in this work, the free-space GPE (no trap) has a commonly known family of dark-soliton solutions, written here in the unscaled units [177],

$$\psi_{\text{ds}}(x, t) = \sqrt{n_0} \left[\beta \tanh \left(\frac{x - x_0 + vt}{\xi} \beta \right) + i \left(\frac{v}{c} \right) \right] e^{-i\mu t/\hbar}. \quad (\text{D.13})$$

Here $\beta = \sqrt{1 - v^2/c^2}$, x_0 is the initial position and v the soliton's velocity. Stationary (alias black) solitons, with $v = 0$, have a zero-density notch with a phase slip of π across it. The soliton's energy decreases with increasing speed [178], emulating a particle with a negative effective mass [179].

Figure D.2 shows oscillations of a dark soliton in the harmonic oscillator and box trapping potentials (left and right columns, respectively). The first row displays the evolution predicted by the Galerkin approximation, as produced by the solution of Eq. (D.9), with $M = 16$ modes. In the box trapping potential, the soliton trajectory closely approximates a triangular wave, as would be expected. In the harmonic oscillator potential, one might

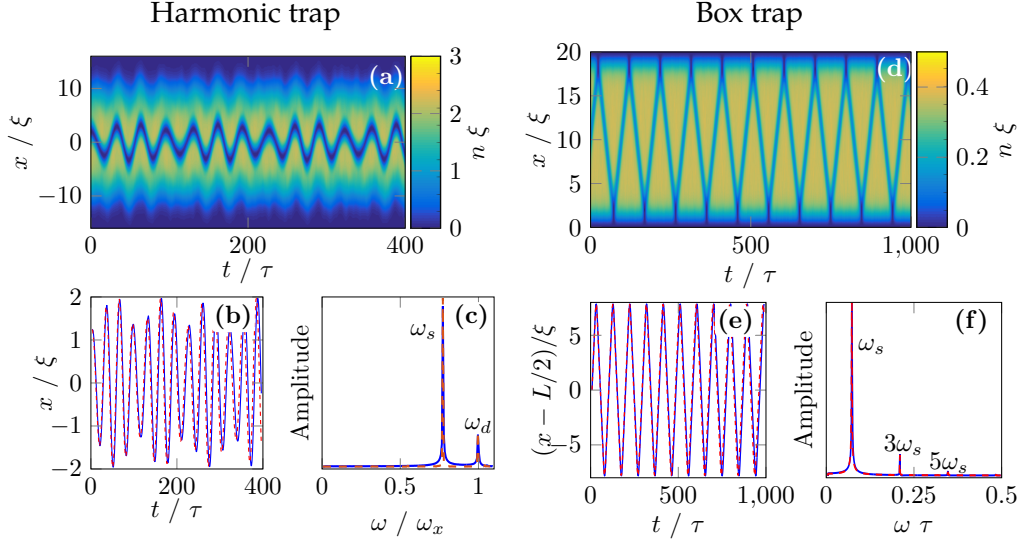


Figure D.2: The motion of an initially off-center black soliton ($v = 0$) in the harmonic oscillator (left column) or gray soliton ($v = 0.6$) in the box (right column) traps. Panel (a) depicts the evolution of the complex amplitudes as per the Galerkin approximation for the ansatz with 16 modes, with similar results for the box trap shown in (d). Panels (b) and (e) display the corresponding center-of-mass oscillations of the dark soliton, as produced by simulations of the GPE (blue solid lines) and by the Galerkin approximation (red dashed lines), while their Fourier transforms are shown in (c) and (f). Parameters are $N = 15$, $v = 0$ and $x_0 = 1$ (see Eq. (D.13)) for the harmonic oscillator trap; $N = 5$, $L = 20$, $v = 0.6$ and $x_0 = 10$ for the box.

expect that the soliton would closely follow a sinusoidal trajectory; however, the interaction of the soliton with the dynamical background condensate significantly distorts the trajectory. The deformation of the background field reveals evidence for the interaction of the soliton with the sound (propagating excitations), whereas, in the potential box, we observe chaotisation of the soliton dynamics at very long evolution times.

It is relevant to mention that the above-mentioned oscillations of the background condensate trapped in the harmonic oscillator potential (panel (a)) are excited by the sound emission from the accelerating soliton. The wavelength of the sound is comparable to the system size, hence it becomes visible as a dipole oscillation of the cloud (note that the direct visualisation of the sound pulse is challenging due to the immediate reflection of the sound from boundaries and re-interaction with the soliton, motivating the use of dimple traps elsewhere to overcome this issue [458, 379]). A quasi-steady state is thus established, wherein the background modes and soliton maintain constant average amplitude. This equilibrium is attributed to the balance between emission and reabsorption of sound by the soliton [458, 379]. Fluctuations in this energy balance are evident in the quasi-periodic acceleration and deceleration of the soliton, visible in the panel (a).

Figures D.2(b) and (e) display the soliton's center-of-mass motion, with overlaid re-

sults produced by the predictions of the Galerkin approximation with $M = 16$ and GPE simulations. The Fourier transform of these center-of-mass oscillations is displayed in Figs. D.2(c) and (f), where the oscillation frequency of the soliton, ω_s , is highlighted, along with frequency ω_d [in panel (b)] corresponding to the dipole mode of small excitations of the condensate as a whole. The latter mode, with

$$\omega_d = \omega_x \equiv 1, \quad (\text{D.14})$$

[see Eq. (D.3) for the definition of ω_x], is excited by the motion and sound emission of the dark soliton traversing the condensate [379].

The dark soliton in the harmonic oscillator potential is known to oscillate at frequency

$$\omega_s = \omega_x / \sqrt{2}, \quad (\text{D.15})$$

as shown theoretically [179] and experimentally [187], deep in the Thomas-Fermi limit, corresponding to large N in our notation. The role of the total number of modes, M , of the Galerkin approximation is addressed in Fig. D.1, demonstrating perfect dynamical accuracy of the approximation for $M = 16$ modes. Moreover, the dark soliton's oscillation frequency in the harmonic oscillator potential indeed approaches, as expected, the value $\omega_x / \sqrt{2}$ as N increases.

D.4 Probing quasi-integrability in the 1D harmonic oscillator potential

In this section, we address the challenging issue of detecting quasi-integrability of the GPE with the harmonic oscillator potential, which is the main reason why the above analysis was undertaken. As is well known, in strictly integrable dynamical systems the power spectrum of the time dependence of dynamical variables (the complex amplitudes, in the present case), $\tilde{a}_j(\omega) = \mathcal{F}[|a_j(t)|^2]$, where \mathcal{F} stands for the Fourier transform, is truly discrete, corresponding to the generic quasi-periodic motion on a surface of an invariant torus, while non-integrable systems feature a conspicuous continuous component in the spectrum, as a result of destruction of the tori [480, 496]. We have applied this criterion of the integrability, by analysing the motion displayed in Fig. D.2, extending the computation of the spectra to a hundred oscillations of the dark soliton. Figure D.3 depicts our main findings, both for the evidently discrete spectrum in the harmonic oscillator trap, and the case of the box potential (left and right images, respectively). The results are represented by power spectra $\tilde{a}_0(\omega)$ [top panels] and $\tilde{a}_1(\omega)$ [bottom panels] of the first and second amplitudes of the Galerkin expansion, which are overlaid on the corresponding results of the GPE simulations. The GPE spectra were produced by computing the corresponding

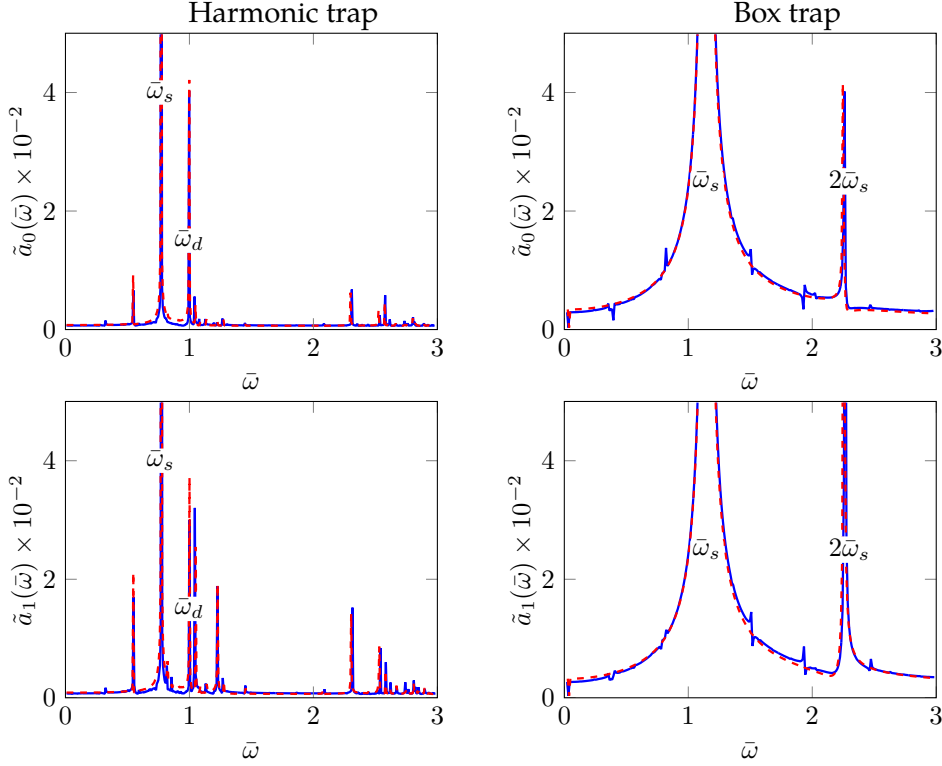


Figure D.3: Generic examples of power spectra for the first (top row) and second (bottom row) amplitudes of the Galerkin expansion in the models with the harmonic oscillator (left) and box (right) potentials. Parameters are the same as in Fig. D.2 with $M = 16$. In each case, the simulations comprised 100 full periods of shuttle oscillations of the dark soliton. As in Figs. D.2(b,c,e,f), we show results produced by both the GPE simulations (solid blue lines) and Galerkin approximation with 16 modes (red dashed lines), which reveals excellent agreement between both.

amplitudes as per Eq. (D.11), and then calculating their power spectra. In both cases, the agreement between the Galerkin approximation and full GPE simulations is impressive, a feature which is also true for higher-order $\tilde{a}_j(\omega)$ coefficients (not shown here).

A crucial finding is the stark difference in the results for the dark soliton's motion in the two potentials: In the harmonic oscillator case (left) we obtain a spectrum consisting of extremely sharp peaks, which may be definitely categorised as a *practically discrete* spectrum, thus representing *quasi-integrable dynamics*. The tallest peaks in the spectrum can be immediately identified as located at the above-mentioned frequencies ω_d and ω_s of the dipole mode of the excitations of the condensate as a whole [see Eq. (D.15)], and shuttle oscillations of the dark soliton [see Eq. (D.14)]. The surrounding peaks can be readily identified as combinational frequencies produced by mixing of these two modes. In stark contrast to this, the spectrum in the box trap exhibits a broad peak, which clearly represents a continuous spectrum, typical to non-integrable systems, that give rise to dy-

namical chaos and ergodicity [496]. Simulations of the dynamical Galerkin system for the potential-box model with $M < 16$ produce a similar behaviour, but with a growing noise component.

The finite width of the peaks representing the harmonic oscillator potential is attributed to numerical accuracy, the inherent frequency resolution of the discrete Fourier transform for total simulation time T being $\Delta\omega = 2\pi/T$. In the present case, $\Delta\omega \approx 0.0005$, and, indeed, the width of the peaks is equal to $2\Delta\omega$.

A physically relevant situation, when a random initial condition is generated for each coefficient $j = 1, \dots, M$ such that $a_j(0) = x_j \exp(iy_j)$, where x_j is an observation from the random variable $X \sim U(-1, 1)$ and y_j from $Y \sim U(0, 2\pi)$ (taking care to renormalise according to Eq. (D.10)), has been tested too. Typical examples of power spectra found in this case are displayed, for both the harmonic oscillator and box traps, in Fig. D.4. It is seen that both models keep the character of their dynamics, corresponding to the quasi-discrete and continuous spectra, respectively, in the presence of the strong random component in the input. Thus, the quasi-integrability of the GPE with the harmonic oscillator potential is a robust property. Figure D.4 also shows the density and phase profiles of the initial condition for both wave-fields. This initial condition is akin to a soliton-gas configuration, generated by summation of several dark soliton solutions with random position, phase and velocity. Using this comparison we can describe the nature of the arising peaks. Considering the dynamics in the harmonic oscillator case, shallow (fast) solitons have an oscillation frequency close to $\omega_s \approx \omega_x$, whereas deep (slow) solitons near the condensate centre have an oscillation frequency near to $\omega_s \approx \omega_x/\sqrt{2}$, as shown previously. In the dynamics ensuing from this highly nonequilibrium initial state the power spectra displays a complicated mixing of these modes, with an envelope of spectra centred around their average, $\omega \approx 0.85 \omega_x$. Similar to Fig. D.3 the envelopes at larger ω are due to mixing of these frequencies.

D.5 Summary

Previous numerical simulations based on the 1D GPE have revealed shuttle oscillations of dark solitons in the harmonic oscillator potential. In the course of the periodic motion, the dark soliton reversibly emits small-amplitude waves ("sound"), being able to fully re-absorb them. No chaotisation was observed in the course of indefinitely long simulations of this model. On the contrary to that, GPE simulations with other types of trapping potentials exhibit irreversible evolution and an eventual trend to the onset of dynamical chaos (wave-function "turbulence") [458, 483]. To explain this phenomenology, we have first derived a finite-mode dynamical system, in the form of the Galerkin approximation, based on the truncated expansion of the wave function, governed by the GPE (Gross-

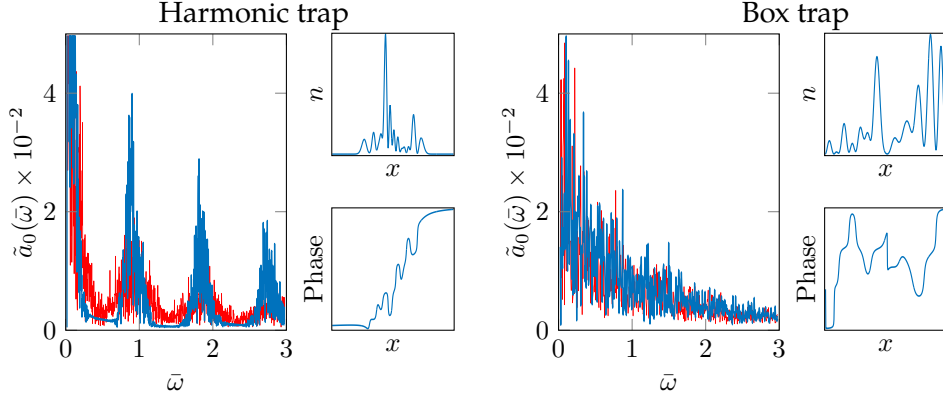


Figure D.4: The first amplitude of the Galerkin expansion, with a set of random-field amplitudes generated for the initial condition in both models, with the harmonic oscillator (left) and box (right) trapping potentials. The power spectra are produced by the projection of the GPE simulations (blue) onto the first eigenmode of the Galerkin basis. Simulations of the the Galerkin system produced similar results, which are consistent with the findings produced by the full GPE simulations (red). Other parameters are the same as in Fig. D.3.

Pitaevskii equation) with the repulsive cubic nonlinearity, over the set of eigenmodes of the corresponding linear Schrödinger equation. The comparison of results produced by the Galerkin approximation to those of full GPE simulations shows that the Galerkin approximation for the model with the harmonic oscillator potential, with $M = 16$ modes, reproduces the full solutions virtually exactly (with fidelity indistinguishable from 1, see Fig. D.1) for indefinitely long evolution times. In the case of the box potential, the Galerkin approximation with $M = 16$ also provides a high accuracy, although, eventually, there emerges a deviation from the GPE solutions at large evolution times. The main finding is that generic trajectories of the Galerkin approximation derived for the model with the harmonic oscillator potential produce a discrete power spectrum (up to the accuracy of the numerically implemented Fourier transform), which is a remarkable manifestation of the conjectured quasi-integrability. This finding (which remains true in the presence of a strong random-noise component in the input) strongly suggests that, in the underlying dynamical system, virtually all trajectories wind upon invariant tori, only an extremely small share of the tori (if any) being destroyed. It remains a challenge to understand the quasi-integrability of the GPE with the harmonic oscillator potential at a deeper mathematical level than the explanation offered by the present analysis.

On the other hand, both direct simulations of the GPE and the Galerkin approximation for the model with the box potential produce a continuous power spectrum, in the form of a very broad peak, which clearly implies that the latter system is subject to the (rather slow) onset of chaotisation. Thus, this work puts forward an open question concerning the

nature of the non-integrable dynamics in the truncated version of the formally integrable system [485–488].

It may also be interesting to perform a similar analysis to the one performed here for the case of *attractive* nonlinearity ($\sigma = -1$ in Eq. (D.6)) focussing on shuttle oscillations of a trapped bright soliton (see also the related work in Ref. [169]), as well as for recurrent collisions between two (or several) solitons (the latter setting was experimentally realised in the self-attracting BEC [164]). Furthermore, for both cases of the self-repulsion and attraction, the analysis may be extended to a two-component GPE with equal strengths of the self- and cross-interactions, which, in the free space, corresponds to the integrable Manakov’s system [497]. This system remains integrable too if it includes the Rabi coupling, i.e., linear interconversion between the components [498], which is thus also an appropriate subject for the consideration. The Manakov’s system finds the well-known realisation in terms of the two-component BEC mixtures [45].

Interesting questions are also expected to arise in the development of the Galerkin approximation for the two-dimensional (2D) GPE with an isotropic harmonic oscillator potential (see also Ref. [479] for multidimensional Schrödinger equations with generalised nonlinearities and damping). In particular, it is known that the 2D model with the attractive nonlinearity and harmonic oscillator trapping potential makes the trapped fundamental solitons completely stable (against the critical collapse in the 2D space [499, 500]), and provides for partial stabilisation of vortex solitons with topological charge 1 against the collapse and splitting [501–505]. The investigation of the 2D model may be interesting also for the reason that the 2D GPE in the free space is not integrable, the question being if the harmonic oscillator confinement may induce a quasi-integrability in this case.

Bibliography

- [1] S. N. Bose, Z. Phys. **26**, 178 (1924).
- [2] A. Einstein, Sitzber. Kgl. Preuss. Akad. Wiss. **23**, 3 (1925).
- [3] M. H. Anderson, J. R. Ensher, M. R. Matthews, C. E. Wieman, and E. A. Cornell, Science **269**, 198 (1995).
- [4] K. B. Davis, M. O. Mewes, M. R. Andrews, N. J. van Druten, D. S. Durfee, D. M. Kurn, and W. Ketterle, Phys. Rev. Lett. **75**, 3969 (1995).
- [5] C. C. Bradley, C. A. Sackett, J. J. Tollett, and R. G. Hulet, Phys. Rev. Lett. **75**, 1687 (1995).
- [6] C. C. Bradley, C. A. Sackett, and R. G. Hulet, Phys. Rev. Lett. **78**, 985 (1997).
- [7] D. G. Fried, T. C. Killian, L. Willmann, D. Landhuis, S. C. Moss, D. Kleppner, and T. J. Greytak, Phys. Rev. Lett. **81**, 3811 (1998).
- [8] A. Robert, O. Sirjean, A. Browaeys, J. Poupard, S. Nowak, D. Boiron, C. I. Westbrook, and A. Aspect, Science **292**, 461 (2001).
- [9] G. Modugno, G. Ferrari, G. Roati, R. J. Brecha, A. Simoni, and M. Inguscio, Science **294**, 1320 (2001).
- [10] T. Weber, J. Herbig, M. Mark, H.-C. Nägerl, and R. Grimm, Science **299**, 232 (2003).
- [11] Y. Takasu, K. Maki, K. Komori, T. Takano, K. Honda, M. Kumakura, T. Yabuzaki, and Y. Takahashi, Phys. Rev. Lett. **91**, 040404 (2003).
- [12] A. Griesmaier, J. Werner, S. Hensler, J. Stuhler, and T. Pfau, Phys. Rev. Lett. **94**, 160401 (2005).
- [13] S. Kraft, F. Vogt, O. Appel, F. Riehle, and U. Sterr, Phys. Rev. Lett. **103**, 130401 (2009).
- [14] S. Stellmer, M. K. Tey, B. Huang, R. Grimm, and F. Schreck, Phys. Rev. Lett. **103**, 200401 (2009).

-
- [15] M. Lu, N. Q. Burdick, S. H. Youn, and B. L. Lev, *Phys. Rev. Lett.* **107**, 190401 (2011).
 - [16] K. Aikawa, A. Frisch, M. Mark, S. Baier, A. Rietzler, R. Grimm, and F. Ferlaino, *Phys. Rev. Lett.* **108**, 210401 (2012).
 - [17] B. DeMarco and D. S. Jin, *Science* **285**, 1703 (1999).
 - [18] F. Schreck, L. Khaykovich, K. L. Corwin, G. Ferrari, T. Bourdel, J. Cubizolles, and C. Salomon, *Phys. Rev. Lett.* **87**, 080403 (2001).
 - [19] A. G. Truscott, K. E. Strecker, W. I. McAlexander, G. B. Partridge, and R. G. Hulet, *Science* **291**, 2570 (2001).
 - [20] J. McNamara, T. Jelts, A. Tychkov, W. Hogervorst, and W. Vassen, *Phys. Rev. Lett.* **97**, 080404 (2006).
 - [21] M. K. Tey, S. Stellmer, R. Grimm, and F. Schreck, *Phys. Rev. A* **82**, 011608 (2010).
 - [22] S. Sugawa, K. Inaba, S. Taie, R. Yamazaki, M. Yamashita, and Y. Takahashi, *Nat. Phys.* **7**, 642 (2011).
 - [23] M. Lu, N. Q. Burdick, and B. L. Lev, *Phys. Rev. Lett.* **108**, 215301 (2012).
 - [24] K. Aikawa, A. Frisch, M. Mark, S. Baier, R. Grimm, and F. Ferlaino, *Phys. Rev. Lett.* **112**, 010404 (2014).
 - [25] B. Naylor, A. Reigue, E. Maréchal, O. Gorceix, B. Laburthe-Tolra, and L. Vernac, *Phys. Rev. A* **91**, 011603 (2015).
 - [26] K. Huang, *Statistical Mechanics* (Wiley, 1987).
 - [27] N. Proukakis, *Quantum Gases: Finite temperature and non-equilibrium dynamics*, vol. 1 (World Scientific, 2013).
 - [28] D. Tilley and J. Tilley, *Superfluidity and Superconductivity* (Taylor & Francis, 1990).
 - [29] P. Kapitza, *Nature* **141**, 74 (1938).
 - [30] J. F. Allen and A. D. Misener, *Nature* **141**, 75 (1938).
 - [31] F. London, *Nature* **141**, 643 (1938).
 - [32] F. London, *Phys. Rev.* **54**, 947 (1938).
 - [33] L. Tisza, *Nature* **141**, 913 (1938).
 - [34] L. D. Landau, *J. Phys. (USSR)* **5**, 71 (1941).

-
- [35] L. D. Landau, Phys. Rev. **75**, 884 (1949).
- [36] N. N. Bogoliubov, J. Phys. (USSR) **11**, 23 (1947).
- [37] O. Penrose, Phil. Mag. **42**, 1373 (1951).
- [38] O. Penrose and L. Onsager, Phys. Rev. **104**, 576 (1956).
- [39] S. Balibar, J. Low Temp. Phys. **146**, 441 (2007).
- [40] A. Acín, I. Bloch, H. Buhrman, T. Calarco, C. Eichler, J. Eisert, D. Esteve, N. Gisin, S. J. Glaser, F. Jeletzko, et al., New J. Phys. **20**, 080201 (2018).
- [41] F. Dalfovo, S. Giorgini, L. P. Pitaevskii, and S. Stringari, Rev. Mod. Phys. **71**, 463 (1999).
- [42] A. J. Leggett, Rev. Mod. Phys. **73**, 307 (2001).
- [43] I. Bloch, J. Dalibard, and W. Zwerger, Rev. Mod. Phys. **80**, 885 (2008).
- [44] C. Pethick and H. Smith, *Bose-Einstein Condensation in Dilute Gases* (Cambridge University Press, 2002).
- [45] L. P. Pitaevskii and S. Stringari, *Bose-Einstein Condensation* (Oxford University Press, Oxford, 2003).
- [46] E. Gross, Nuovo Cimento **20**, 454 (1961).
- [47] E. P. Gross, J. Math. Phys. **4**, 195 (1963).
- [48] L. P. Pitaevskii, Zh. Eksp. Teor. Fiz. **40**, 646 (1961).
- [49] L. Pitaevskii, Sov. Phys. JETP **13**, 451 (1961).
- [50] T. Meyrath, F. Schreck, J. Hanssen, C.-S. Chuu, and M. Raizen, Phys. Rev. A **71**, 041604 (2005).
- [51] J. Van Es, P. Wicke, A. Van Amerongen, C. Rétif, S. Whitlock, and N. Van Druten, J. Phys. B **43**, 155002 (2010).
- [52] A. L. Gaunt, T. F. Schmidutz, I. Gotlibovych, R. P. Smith, and Z. Hadzibabic, Phys. Rev. Lett. **110**, 200406 (2013).
- [53] L. Chomaz, L. Corman, T. Bienaimé, R. Desbuquois, C. Weitenberg, S. Nascimbène, J. Beugnon, and J. Dalibard, Nat. Comm. **6**, 6162 (2015).
- [54] S. Inouye, M. R. Andrews, J. Stenger, H.-J. Miesner, D. M. Stamper-Kurn, and W. Ketterle, Nature **392**, 151 (1998).

-
- [55] E. Madelung, Z. Phys. A **40**, 322 (1927).
- [56] H. Stoof and M. Bijlsma, J. Low Temp. Phys. **124**, 431 (2001).
- [57] C. Gardiner and M. Davis, J. Phys. B **36**, 4731 (2003).
- [58] S. Cockburn and N. Proukakis, Laser Phys. **19**, 558 (2009).
- [59] H. Büchler, A. Micheli, and P. Zoller, Nat. Phys. **3**, 726 (2007).
- [60] A. Micheli, Phys. Rev. A **76**, 043604 (2007).
- [61] H. P. Büchler, E. Demler, M. Lukin, A. Micheli, N. Prokof'ev, G. Pupillo, and P. Zoller, Phys. Rev. Lett. **98**, 060404 (2007).
- [62] M. Chalony, J. Barré, B. Marcos, A. Olivetti, and D. Wilkowski, Phys. Rev. A **87**, 013401 (2013).
- [63] R. Mottl, F. Brennecke, K. Baumann, R. Landig, T. Donner, and T. Esslinger, Science **336**, 1570 (2012).
- [64] Y.-J. Lin, K. Jiménez-García, and I. B. Spielman, Nature **471**, 83 (2011).
- [65] Q. Beaufils, R. Chicireanu, T. Zanon, B. Laburthe-Tolra, E. Maréchal, L. Vernac, J.-C. Keller, and O. Gorceix, Phys. Rev. A **77**, 061601 (2008).
- [66] Y. Tang, N. Q. Burdick, K. Baumann, and B. L. Lev, New J. Phys. **17**, 045006 (2015).
- [67] T. Lahaye, C. Menotti, L. Santos, M. Lewenstein, and T. Pfau, Rep. Prog. Phys. **72**, 126401 (2009).
- [68] T. Koch, T. Lahaye, J. Metz, B. Fröhlich, A. Griesmaier, and T. Pfau, Nat. Phys. **4**, 218 (2008).
- [69] R. E. Rosensweig, *Ferrohydrodynamics* (Courier Corporation, 2013).
- [70] S. Papell and O. Faber Jr, *On the influence of nonuniform magnetic fields on ferromagnetic colloidal sols* (National Aeronautics and Space Administration, 1968).
- [71] C. Scherer and A. M. Figueiredo Neto, Braz. J. Phys. **35**, 718 (2005).
- [72] A. J. Dickstein, S. Erramilli, R. E. Goldstein, D. P. Jackson, and S. A. Langer, Science **261**, 1012 (1993).
- [73] G. Maxwell (2006), URL https://upload.wikimedia.org/wikipedia/commons/2/21/Ferrofluid_Magnet_under_glass_edit.jpg.

- [74] M. Zahn, *J. Nanopart. Res.* **3**, 73 (2001).
- [75] Y. Shilo, K. Cohen, B. Laikhtman, K. West, L. Pfeiffer, and R. Rapaport, *Nat. Comm.* **4**, 2335 (2013).
- [76] K. Cohen, Y. Shilo, K. West, L. Pfeiffer, and R. Rapaport, *Nano Lett.* **16**, 3726 (2016).
- [77] M. Stern, V. Umansky, and I. Bar-Joseph, *Science* **343**, 55 (2014).
- [78] M. Combescot, O. Betbeder-Matibet, and R. Combescot, *Phys. Rev. Lett.* **99**, 176403 (2007).
- [79] S. Misra, M. Stern, A. Joshua, V. Umansky, and I. Bar-Joseph, *Phys. Rev. Lett.* **120**, 047402 (2018).
- [80] Y. Mazuz-Harpaz, M. Khodas, and R. Rapaport (2018), [arXiv:1803.03918](https://arxiv.org/abs/1803.03918).
- [81] W. Li, M. W. Noel, M. P. Robinson, P. J. Tanner, T. F. Gallagher, D. Comparat, B. L. Tolra, N. Vanhaecke, T. Vogt, N. Zahzam, et al., *Phys. Rev. A* **70**, 042713 (2004).
- [82] H. Bernien, S. Schwartz, A. Keesling, H. Levine, A. Omran, H. Pichler, S. Choi, A. S. Zibrov, M. Endres, M. Greiner, et al., *Nature* **551**, 579 (2017).
- [83] G. Quémener and J. L. Bohn, *Phys. Rev. A* **93**, 012704 (2016).
- [84] M. L. González-Martínez, J. L. Bohn, and G. Quémener, *Phys. Rev. A* **96**, 032718 (2017).
- [85] T. Karman and J. M. Hutson, *Phys. Rev. Lett.* **121**, 163401 (2018).
- [86] G. Bismut, B. Pasquiou, E. Maréchal, P. Pedri, L. Vernac, O. Gorceix, and B. Laburthe-Tolra, *Phys. Rev. Lett.* **105**, 040404 (2010).
- [87] B. Pasquiou, E. Maréchal, G. Bismut, P. Pedri, L. Vernac, O. Gorceix, and B. Laburthe-Tolra, *Phys. Rev. Lett.* **106**, 255303 (2011).
- [88] G. Bismut, B. Laburthe-Tolra, E. Maréchal, P. Pedri, O. Gorceix, and L. Vernac, *Phys. Rev. Lett.* **109**, 155302 (2012).
- [89] S. Lepoutre, L. Gabardos, K. Kechadi, P. Pedri, O. Gorceix, E. Marechal, L. Vernac, and B. Laburthe-Tolra, *Phys. Rev. Lett.* **121**, 013201 (2018).
- [90] A. De Paz, A. Sharma, A. Chotia, E. Marechal, J. Huckans, P. Pedri, L. Santos, O. Gorceix, L. Vernac, and B. Laburthe-Tolra, *Phys. Rev. Lett.* **111**, 185305 (2013).
- [91] A. de Paz, P. Pedri, A. Sharma, M. Efremov, B. Naylor, O. Gorceix, E. Maréchal, L. Vernac, and B. Laburthe-Tolra, *Phys. Rev. A* **93**, 021603 (2016).

-
- [92] T. Fukuhara, S. Sugawa, and Y. Takahashi, *Phys. Rev. A* **76**, 051604 (2007).
- [93] J. J. McClelland and J. L. Hanssen, *Phys. Rev. Lett.* **96**, 143005 (2006).
- [94] A. J. Berglund, J. L. Hanssen, and J. J. McClelland, *Phys. Rev. Lett.* **100**, 113002 (2008).
- [95] H. Kadau, M. Schmitt, M. Wenzel, C. Wink, T. Maier, I. Ferrier-Barbut, and T. Pfau, *Nature* **530**, 194 (2016).
- [96] E. Lucioni, L. Tanzi, A. Fregosi, J. Catani, S. Gozzini, M. Inguscio, A. Fioretti, C. Gabbanini, and G. Modugno, *Phys. Rev. A* **97**, 060701 (2018).
- [97] P. Ilzhöfer, G. Durastante, A. Patscheider, A. Trautmann, M. Mark, and F. Ferlino, *Phys. Rev. A* **97**, 023633 (2018).
- [98] A. Trautmann, P. Ilzhöfer, G. Durastante, C. Politi, M. Sohmen, M. J. Mark, and F. Ferlino (2018), [arXiv:1807.07555](#).
- [99] D. Sukachev, A. Sokolov, K. Chebakov, A. Akimov, S. Kanorsky, N. Kolachevsky, and V. Sorokin, *Phys. Rev. A* **82**, 011405 (2010).
- [100] J. Miao, J. Hostetter, G. Stratis, and M. Saffman, *Phys. Rev. A* **89**, 041401 (2014).
- [101] D. M. Stamper-Kurn and M. Ueda, *Rev. Mod. Phys.* **85**, 1191 (2013).
- [102] B. Pasquiou, G. Bismut, Q. Beaufils, A. Crubellier, E. Maréchal, P. Pedri, L. Vernac, O. Gorceix, and B. Laburthe-Tolra, *Phys. Rev. A* **81**, 042716 (2010).
- [103] Y. Tang, A. Sykes, N. Q. Burdick, J. L. Bohn, and B. L. Lev, *Phys. Rev. A* **92**, 022703 (2015).
- [104] T. Maier, I. Ferrier-Barbut, H. Kadau, M. Schmitt, M. Wenzel, C. Wink, T. Pfau, K. Jachymski, and P. S. Julienne, *Phys. Rev. A* **92**, 060702 (2015).
- [105] A. Frisch, Ph.D. thesis (2014).
- [106] S. Baier, M. J. Mark, D. Petter, K. Aikawa, L. Chomaz, Z. Cai, M. Baranov, P. Zoller, and F. Ferlino, *Science* **352**, 201 (2016).
- [107] T. Karman, M. D. Frye, J. D. Reddel, and J. M. Hutson (2018), [arXiv:1808.07723](#).
- [108] M. R. Matthews, B. P. Anderson, P. C. Haljan, D. S. Hall, C. E. Wieman, and E. A. Cornell, *Phys. Rev. Lett.* **83**, 2498 (1999).
- [109] K. W. Madison, F. Chevy, W. Wohlleben, and J. Dalibard, *Phys. Rev. Lett.* **84**, 806 (2000).

-
- [110] B. P. Anderson, P. C. Haljan, C. E. Wieman, and E. A. Cornell, Phys. Rev. Lett. **85**, 2857 (2000).
- [111] E. Hodby, G. Hechenblaikner, S. A. Hopkins, O. M. Maragò, and C. J. Foot, Phys. Rev. Lett. **88**, 010405 (2002).
- [112] J. R. Abo-Shaeer, C. Raman, J. M. Vogels, and W. Ketterle, Science **292**, 476 (2001).
- [113] P. Engels, I. Coddington, P. C. Haljan, V. Schweikhard, and E. A. Cornell, Phys. Rev. Lett. **90**, 170405 (2003).
- [114] W. J. Kwon, G. Moon, S. W. Seo, and Y. Shin, Phys. Rev. A **91**, 053615 (2015).
- [115] B. P. Anderson, P. C. Haljan, C. A. Regal, D. L. Feder, L. A. Collins, C. W. Clark, and E. A. Cornell, Phys. Rev. Lett. **86**, 2926 (2001).
- [116] Z. Dutton, M. Budde, C. Slowe, and L. V. Hau, Science **293**, 663 (2001).
- [117] D. V. Freilich, D. M. Bianchi, A. M. Kaufman, T. K. Langin, and D. S. Hall, Science **329**, 1182 (2010).
- [118] S. Serafini, L. Galantucci, E. Iseni, T. Bienaimé, R. N. Bisset, C. F. Barenghi, F. Dalfovo, G. Lamporesi, and G. Ferrari, Phys. Rev. X **7**, 021031 (2017).
- [119] A. L. Fetter and A. A. Svidzinsky, J. Phys. Condens. Matter **13**, R135 (2001).
- [120] P. Nozières and D. Pines, *Theory of quantum liquids* (Hachette UK, 1999).
- [121] W. J. Kwon, J. H. Kim, S. W. Seo, and Y.-i. Shin, Phys. Rev. Lett. **117**, 245301 (2016).
- [122] V. Bretin, S. Stock, Y. Seurin, and J. Dalibard, Phys. Rev. Lett. **92**, 050403 (2004).
- [123] P. Davidson, *Turbulence: an introduction for scientists and engineers* (Oxford University Press, 2015).
- [124] D. I. Bradley, S. N. Fisher, A. M. Guenault, R. P. Haley, G. R. Pickett, D. Potts, and V. Tsepelin, Nat. Phys. **7**, 473 (2011).
- [125] L. Skrbek and K. R. Sreenivasan, Phys. Fluids **24**, 011301 (2012).
- [126] L. Boué, V. L'vov, A. Pomyalov, and I. Procaccia, Phys. Rev. Lett. **110**, 014502 (2013).
- [127] C. F. Barenghi, L. Skrbek, and K. R. Sreenivasan, Proc. Natl. Acad. Sci. **111**, 4647 (2014).
- [128] D. E. Zmeev, P. M. Walmsley, A. I. Golov, P. V. E. McClintock, S. N. Fisher, and W. F. Vinen, Phys. Rev. Lett. **115**, 155303 (2015).

-
- [129] P. M. Walmsley and A. I. Golov, Phys. Rev. Lett. **100**, 245301 (2008).
- [130] C. Nore, M. Abid, and M. E. Brachet, Phys. Rev. Lett. **78**, 3896 (1997).
- [131] M. Kobayashi and M. Tsubota, Phys. Rev. Lett. **94**, 065302 (2005).
- [132] N. G. Berloff and B. V. Svistunov, Phys. Rev. A **66**, 013603 (2002).
- [133] N. Parker and C. Adams, Phys. Rev. Lett. **95**, 145301 (2005).
- [134] M. Kobayashi and M. Tsubota, Phys. Rev. A **76**, 045603 (2007).
- [135] M. Tsubota and M. Kobayashi, J. Low Temp. Phys. **150**, 402 (2008).
- [136] E. Henn, J. Seman, G. Roati, K. M. F. Magalhães, and V. S. Bagnato, Phys. Rev. Lett. **103**, 045301 (2009).
- [137] T. Neely, E. Samson, A. Bradley, M. Davis, and B. Anderson, Phys. Rev. Lett. **104**, 160401 (2010).
- [138] W. J. Kwon, G. Moon, J.-y. Choi, S. W. Seo, and Y.-i. Shin, Phys. Rev. A **90**, 063627 (2014).
- [139] S. P. Johnstone, A. J. Groszek, P. T. Starkey, C. J. Billington, T. P. Simula, and K. Helmerson (2018), arXiv:1801.06952.
- [140] G. Gauthier, M. T. Reeves, X. Yu, A. S. Bradley, M. Baker, T. A. Bell, H. Rubinsztein-Dunlop, M. J. Davis, and T. W. Neely (2018), arXiv:1801.06951.
- [141] J. Yepez, G. Vahala, L. Vahala, and M. Soe, Phys. Rev. Lett. **103**, 084501 (2009).
- [142] T. Dauxois and M. Peyrard, *Physics of solitons* (Cambridge University Press, 2006).
- [143] N. Manton and P. Sutcliffe, *Topological solitons* (Cambridge University Press, 2004).
- [144] G. I. Stegeman and M. Segev, Science **286**, 1518 (1999).
- [145] P. Kevrekidis, D. Frantzeskakis, and R. Carretero-González, *Emergent Nonlinear Phenomena in Bose-Einstein Condensates: Theory and Experiment*, Springer Series on Atomic, Optical, and Plasma Physics (Springer Berlin Heidelberg, 2007).
- [146] F. Kh. Abdullaev, A. Gammal, A. M. Kamchatnov, and L. Tomio, Int. J. Mod. Phys. B **19**, 3415 (2005).
- [147] D. J. Frantzeskakis, J. Phys. A **43**, 213001 (2010).
- [148] T. Billam, A. Marchant, S. Cornish, S. Gardiner, and N. Parker, in *Spontaneous Symmetry Breaking, Self-Trapping, and Josephson Oscillations* (Springer, 2012), pp. 403–455.

-
- [149] P. Drazin and R. Johnson, *Solitons: An Introduction*, Cambridge Computer Science Texts (Cambridge University Press, 1989).
- [150] G. Agrawal, *Nonlinear Fiber Optics*, Optics and Photonics (Elsevier Science, 2001).
- [151] K. Naugolnykh and L. Ostrovsky, *Nonlinear Wave Processes in Acoustics*, Cambridge Texts in Applied Mathematics (Cambridge University Press, 1998).
- [152] H.-H. Chen and C.-S. Liu, Phys. Rev. Lett. **37**, 693 (1976).
- [153] H. C. Kim, R. L. Stenzel, and A. Y. Wong, Phys. Rev. Lett. **33**, 886 (1974).
- [154] J. S. Russell, Report of the fourteenth meeting of the British Association for the Advancement of Science, Plates XLVII-LVII p. 311 (1865).
- [155] K. E. Strecker, G. B. Partridge, A. G. Truscott, and R. G. Hulet, Nature **417**, 150 (2002).
- [156] L. Khaykovich, F. Schreck, G. Ferrari, T. Bourdel, J. Cubizolles, L. D. Carr, Y. Castin, and C. Salomon, Science **296**, 1290 (2002).
- [157] B. Eiermann, T. Anker, M. Albiez, M. Taglieber, P. Treutlein, K.-P. Marzlin, and M. Oberthaler, Phys. Rev. Lett. **92**, 230401 (2004).
- [158] S. L. Cornish, S. T. Thompson, and C. E. Wieman, Phys. Rev. Lett. **96**, 170401 (2006).
- [159] A. Marchant, T. Billam, T. Wiles, M. Yu, S. Gardiner, and S. Cornish, Nat. Comm. **4**, 1865 (2013).
- [160] G. D. McDonald, C. C. Kuhn, K. S. Hardman, S. Bennetts, P. J. Everitt, P. A. Altin, J. E. Debs, J. D. Close, and N. P. Robins, Phys. Rev. Lett. **113**, 013002 (2014).
- [161] P. Medley, M. Minar, N. Cizek, D. Berryrieser, and M. Kasevich, Phys. Rev. Lett. **112**, 060401 (2014).
- [162] S. Lepoutre, L. Fouché, A. Boissé, G. Berthet, G. Salomon, A. Aspect, and T. Bourdel, Phys. Rev. A **94**, 053626 (2016).
- [163] A. Marchant, T. Billam, M. Yu, A. Rakonjac, J. Helm, J. Polo, C. Weiss, S. Gardiner, and S. Cornish, Phys. Rev. A **93**, 021604 (2016).
- [164] J. H. Nguyen, P. Dyke, D. Luo, B. A. Malomed, and R. G. Hulet, Nat. Phys. **10**, 918 (2014).
- [165] J. Helm, S. Cornish, and S. Gardiner, Phys. Rev. Lett. **114**, 134101 (2015).
- [166] J. Gordon, Opt. Lett. **8**, 596 (1983).

-
- [167] R. Scharf and A. Bishop, Phys. Rev. A **46**, R2973 (1992).
- [168] A. Martin, C. Adams, and S. Gardiner, Phys. Rev. Lett. **98**, 020402 (2007).
- [169] A. Martin, C. Adams, and S. Gardiner, Phys. Rev. A **77**, 013620 (2008).
- [170] A. Martin, Phys. Rev. A **93**, 023631 (2016).
- [171] N. Parker, A. Martin, S. Cornish, and C. Adams, J. Phys. B **41**, 045303 (2008).
- [172] N. Parker, A. Martin, C. Adams, and S. Cornish, Physica D **238**, 1456 (2009).
- [173] B. B. Baizakov, B. A. Malomed, and M. Salerno, Phys. Rev. A **70**, 053613 (2004).
- [174] U. Al Khawaja, H. Stoof, R. Hulet, K. Strecker, and G. Partridge, Phys. Rev. Lett. **89**, 200404 (2002).
- [175] T. Billam, S. Cornish, and S. Gardiner, Phys. Rev. A **83**, 041602 (2011).
- [176] U. Al Khawaja and H. Stoof, New J. Phys. **13**, 085003 (2011).
- [177] V. Zakharov and A. Shabat, Sov. Phys. JETP **37**, 823 (1973).
- [178] Y. S. Kivshar and B. Luther-Davies, Phys. Rep. **298**, 81 (1998).
- [179] T. Busch and J. Anglin, Phys. Rev. Lett. **84**, 2298 (2000).
- [180] P. Emplit, J. P. Hamaide, F. Reynaud, G. Froehly, and A. Barthelemy, Opt. Commun. **62**, 374 (1987).
- [181] S. Burger, K. Bongs, S. Dettmer, W. Ertmer, K. Sengstock, A. Sanpera, G. V. Shlyapnikov, and M. Lewenstein, Phys. Rev. Lett. **83**, 5198 (1999).
- [182] J. Denschlag, J. E. Simsarian, D. L. Feder, C. W. Clark, L. A. Collins, J. Cubizolles, L. Deng, E. W. Hagley, K. Helmerson, W. P. Reinhardt, et al., Science **287**, 97 (2000).
- [183] I. Shomroni, E. Lahoud, S. Levy, and J. Steinhauer, Nat. Phys. **5**, 193 (2009).
- [184] G.-B. Jo, J.-H. Choi, C. A. Christensen, T. Pasquini, Y.-R. Lee, W. Ketterle, and D. E. Pritchard, Phys. Rev. Lett. **98**, 180401 (2007).
- [185] J. J. Chang, P. Engels, and M. Hoefer, Phys. Rev. Lett. **101**, 170404 (2008).
- [186] S. Stellmer, C. Becker, P. Soltan-Panahi, E.-M. Richter, S. Dörscher, M. Baumert, J. Kronjäger, K. Bongs, and K. Sengstock, Phys. Rev. Lett. **101**, 120406 (2008).
- [187] A. Weller, J. P. Ronzheimer, C. Gross, J. Esteve, M. K. Oberthaler, D. J. Frantzeskakis, G. Theocharis, and P. G. Kevrekidis, Phys. Rev. Lett. **101**, 130401 (2008).

-
- [188] C. Becker, S. Stellmer, P. Soltan-Panahi, S. Dörscher, M. Baumert, E.-M. Richter, J. Kronjäger, K. Bongs, and K. Sengstock, *Nat. Phys.* **4**, 496 (2008).
- [189] C. Hamner, J. Chang, P. Engels, and M. Hoefer, *Phys. Rev. Lett.* **106**, 065302 (2011).
- [190] A. Hasegawa and Y. Kodama, *Solitons in optical communications*, Oxford series in optical and imaging sciences (Clarendon Press, 1995).
- [191] J. Anglin, *Nat. Phys.* **4**, 437 (2008).
- [192] A. Negretti and C. Henkel, *J. Phys. B* **37**, L385 (2004).
- [193] S. Cornish, N. Parker, A. Martin, T. Judd, R. Scott, T. Fromhold, and C. Adams, *Physica D* **238**, 1299 (2009).
- [194] M. Lewenstein and B. A. Malomed, *New J. Phys.* **11**, 113014 (2009).
- [195] M. I. Shaukat, E. V. Castro, and H. Terças, *Phys. Rev. A* **95**, 053618 (2017).
- [196] M. Edmonds, T. Bland, D. O'Dell, and N. Parker, *Phys. Rev. A* **93**, 063617 (2016).
- [197] T. Bland, M. Edmonds, N. Proukakis, A. Martin, D. O'Dell, and N. Parker, *Phys. Rev. A* **92**, 063601 (2015).
- [198] T. Bland, K. Pawłowski, M. Edmonds, K. Rzażewski, and N. Parker, *Phys. Rev. A* **95**, 063622 (2017).
- [199] M. Edmonds, T. Bland, R. Doran, and N. Parker, *New J. Phys.* **19**, 023019 (2017).
- [200] S. Prasad, T. Bland, B. Mulkerin, N. Parker, and A. Martin (2018), [arXiv:1810.09041](#).
- [201] T. Bland, G. Stagg, L. Galantucci, A. Baggageley, and N. Parker, *Phys. Rev. Lett.* **121**, 174501 (2018).
- [202] T. Bland, N. G. Parker, N. P. Proukakis, and B. A. Malomed, *J. Phys. B* **51**, 205303 (2018).
- [203] T. Bland, J. Tong, B. Ward, and N. Parker, *J. Phys.: Conf. Ser.* **797** (2017).
- [204] L. D. Landau and E. M. Lifshitz, *Quantum mechanics: non-relativistic theory*, vol. 3 (Elsevier, 2013).
- [205] S. Yi and L. You, *Phys. Rev. A* **63**, 053607 (2001).
- [206] M. Marinescu and L. You, *Phys. Rev. Lett.* **81**, 4596 (1998).

- [207] S. Yi and L. You, *Phys. Rev. A* **61**, 041604 (2000).
- [208] D. Bortolotti, S. Ronen, J. Bohn, and D. Blume, *Phys. Rev. Lett.* **97**, 160402 (2006).
- [209] S. Ronen, D. C. Bortolotti, D. Blume, and J. L. Bohn, *Phys. Rev. A* **74**, 033611 (2006).
- [210] I. Mazets and G. Kurizki, *Phys. Rev. Lett.* **98**, 140401 (2007).
- [211] W. C. Stwalley, *Phys. Rev. Lett.* **37**, 1628 (1976).
- [212] P. Courteille, R. Freeland, D. Heinzen, F. Van Abeelen, and B. Verhaar, *Phys. Rev. Lett.* **81**, 69 (1998).
- [213] J. Roberts, N. Claussen, J. P. Burke Jr, C. H. Greene, E. A. Cornell, and C. Wieman, *Phys. Rev. Lett.* **81**, 5109 (1998).
- [214] V. Vuletić, A. J. Kerman, C. Chin, and S. Chu, *Phys. Rev. Lett.* **82**, 1406 (1999).
- [215] C. Chin, R. Grimm, P. Julienne, and E. Tiesinga, *Rev. Mod. Phys.* **82**, 1225 (2010).
- [216] A. Moerdijk, B. Verhaar, and A. Axelsson, *Phys. Rev. A* **51**, 4852 (1995).
- [217] S. Giovanazzi, A. Görlitz, and T. Pfau, *Phys. Rev. Lett.* **89**, 130401 (2002).
- [218] Y. Tang, K. Wil, K.-Y. Li, and B. L. Lev, *Phys. Rev. Lett.* **120**, 230401 (2018).
- [219] K. Góral, K. Rzażewski, and T. Pfau, *Phys. Rev. A* **61**, 051601 (2000).
- [220] T. Winiecki, B. Jackson, J. F. McCann, and C. S. Adams, *J. Phys. B* **33**, 4069 (2000).
- [221] I. Ferrier-Barbut, H. Kadau, M. Schmitt, M. Wenzel, and T. Pfau, *Phys. Rev. Lett.* **116**, 215301 (2016).
- [222] M. Schmitt, M. Wenzel, F. Böttcher, I. Ferrier-Barbut, and T. Pfau, *Nature* **539**, 259 (2016).
- [223] L. Chomaz, S. Baier, D. Petter, M. Mark, F. Wächtler, L. Santos, and F. Ferlaino, *Phys. Rev. X* **6**, 041039 (2016).
- [224] F. Wächtler and L. Santos, *Phys. Rev. A* **93**, 061603 (2016).
- [225] T. D. Lee, K. Huang, and C. N. Yang, *Phys. Rev.* **106**, 1135 (1957).
- [226] A. R. Lima and A. Pelster, *Phys. Rev. A* **84**, 041604 (2011).
- [227] A. R. Lima and A. Pelster, *Phys. Rev. A* **86**, 063609 (2012).
- [228] R. Bisset, R. Wilson, D. Baillie, and P. Blakie, *Phys. Rev. A* **94**, 033619 (2016).

- [229] D. Schumayer and B. Apagyí, Phys. Rev. A **65**, 053614 (2002).
- [230] D. P. Craig and T. Thirunamachandran, *Molecular quantum electrodynamics: an introduction to radiation-molecule interactions* (Courier Corporation, 1984).
- [231] D. H. O'Dell, S. Giovanazzi, and C. Eberlein, Phys. Rev. Lett. **92**, 250401 (2004).
- [232] C. Eberlein, S. Giovanazzi, and D. H. O'Dell, Phys. Rev. A **71**, 033618 (2005).
- [233] F. Dyson, QJ Pure Appl. Math **25**, 259 (1891).
- [234] N. Ferrers, QJ Pure Appl. Math **14**, 1 (1877).
- [235] M. Levin and R. Muratov, Astrophys. J. **166**, 441 (1971).
- [236] R. Van Bijnen, D. O'dell, N. Parker, and A. Martin, Phys. Rev. Lett. **98**, 150401 (2007).
- [237] S. Ronen, D. C. Bortolotti, and J. L. Bohn, Phys. Rev. Lett. **98**, 030406 (2007).
- [238] O. Dutta and P. Meystre, Phys. Rev. A **75**, 053604 (2007).
- [239] A. Martin and P. Blakie, Phys. Rev. A **86**, 053623 (2012).
- [240] H.-Y. Lu, H. Lu, J.-N. Zhang, R.-Z. Qiu, H. Pu, and S. Yi, Phys. Rev. A **82**, 023622 (2010).
- [241] H. Saito, Y. Kawaguchi, and M. Ueda, Phys. Rev. Lett. **102**, 230403 (2009).
- [242] R. M. Wilson, C. Ticknor, J. L. Bohn, and E. Timmermans, Phys. Rev. A **86**, 033606 (2012).
- [243] D. Petrov, Phys. Rev. Lett. **115**, 155302 (2015).
- [244] A. Bulgac, Phys. Rev. Lett. **89**, 050402 (2002).
- [245] H. Saito, J. Phys. Soc. Jpn **85**, 053001 (2016).
- [246] C. Cabrera, L. Tanzi, J. Sanz, B. Naylor, P. Thomas, P. Cheiney, and L. Tarruell, Science **359**, 301 (2018).
- [247] G. Semeghini, G. Ferioli, L. Masi, C. Mazzinghi, L. Wolswijk, F. Minardi, M. Modugno, G. Modugno, M. Inguscio, and M. Fattori, Phys. Rev. Lett. **120**, 235301 (2018).
- [248] V. Cikojević, K. Dželalija, P. Stipanović, L. V. Markić, and J. Boronat, Phys. Rev. B **97**, 140502 (2018).
- [249] D. Baillie, R. Wilson, R. Bisset, and P. Blakie, Phys. Rev. A **94**, 021602 (2016).

-
- [250] D. Baillie, R. Wilson, and P. Blakie, *Phys. Rev. Lett.* **119**, 255302 (2017).
- [251] I. Ferrier-Barbut, M. Wenzel, F. Böttcher, T. Langen, M. Isoard, S. Stringari, and T. Pfau, *Phys. Rev. Lett.* **120**, 160402 (2018).
- [252] P. De Gennes, *Superconducting of metals and alloys* (1966).
- [253] M. Wenzel, F. Böttcher, J.-N. Schmidt, M. Eisenmann, T. Langen, T. Pfau, and I. Ferrier-Barbut, *Phys. Rev. Lett.* **121**, 030401 (2018).
- [254] R. P. Feynman, *Phys. Rev.* **94**, 262 (1954).
- [255] S. Balibar, in *AIP Conf. Proc.* (AIP, 2006), vol. 850, pp. 18–25.
- [256] L. Santos, G. Shlyapnikov, and M. Lewenstein, *Phys. Rev. Lett.* **90**, 250403 (2003).
- [257] R. M. Wilson, S. Ronen, and J. L. Bohn, *Phys. Rev. Lett.* **104**, 094501 (2010).
- [258] S. Giovanazzi and D. H. O'Dell, *The European Physical Journal D-Atomic, Molecular, Optical and Plasma Physics* **31**, 439 (2004).
- [259] L. Chomaz, R. Bijnen, D. Petter, G. Faraoni, S. Baier, J. H. Becher, M. J. Mark, F. Waechtler, L. Santos, and F. Ferlaino, *Nat. Phys.* **14**, 442 (2018).
- [260] C. Ticknor, R. M. Wilson, and J. L. Bohn, *Phys. Rev. Lett.* **106**, 065301 (2011).
- [261] B. Mulkerin, D. O'Dell, A. Martin, and N. Parker, in *Journal of Physics: Conference Series* (IOP Publishing, 2014), vol. 497, p. 012025.
- [262] R. M. Wilson, S. Ronen, and J. L. Bohn, *Phys. Rev. A* **79**, 013621 (2009).
- [263] A. Cidrim, F. E. dos Santos, E. A. Henn, and T. Macrì, *Phys. Rev. A* **98**, 023618 (2018).
- [264] R. K. Kumar, T. Sriraman, H. Fabrelli, P. Muruganandam, and A. Gammal, *J. Phys. B* **49**, 155301 (2016).
- [265] L. Jia, A.-B. Wang, and S. Yi, *Phys. Rev. A* **97**, 043614 (2018).
- [266] S. Sabari, in *AIP Conference Proceedings* (AIP Publishing, 2018), vol. 1942, p. 030028.
- [267] X.-F. Zhang, L. Wen, C.-Q. Dai, R.-F. Dong, H.-F. Jiang, H. Chang, and S.-G. Zhang, *Sci. Rep.* **6**, 19380 (2016).
- [268] L.-X. Wang, B. Dong, G.-P. Chen, W. Han, S.-G. Zhang, Y.-R. Shi, and X.-F. Zhang, *Phys. Lett. A* **380**, 435 (2016).
- [269] A. Martin, N. Marchant, D. O'Dell, and N. Parker, *J. Phys. Condens. Matter* **29**, 103004 (2017).

- [270] J. Cuevas, B. A. Malomed, P. Kevrekidis, and D. Frantzeskakis, *Phys. Rev. A* **79**, 053608 (2009).
- [271] B. Baizakov, S. Al-Marzoug, and H. Bahlouli, *Phys. Rev. A* **92**, 033605 (2015).
- [272] B. Umarov, N. Aklan, B. Baizakov, and F. K. Abdullaev, *J. Phys. B* **49**, 125307 (2016).
- [273] K. Pawłowski and K. Rzażewski, *New J. Phys.* **17**, 105006 (2015).
- [274] S. Adhikari, *Phys. Rev. A* **89**, 043615 (2014).
- [275] P. Pedri and L. Santos, *Phys. Rev. Lett.* **95**, 200404 (2005).
- [276] I. Tikhonenkov, B. Malomed, and A. Vardi, *Phys. Rev. Lett.* **100**, 090406 (2008).
- [277] M. Raghunandan, C. Mishra, K. Lakomy, P. Pedri, L. Santos, and R. Nath, *Phys. Rev. A* **92**, 013637 (2015).
- [278] H. Chen, Y. Liu, Q. Zhang, Y. Shi, W. Pang, and Y. Li, *Phys. Rev. A* **93**, 053608 (2016).
- [279] S. K. Adhikari, *Phys. Rev. A* **90**, 055601 (2014).
- [280] R. Nath, P. Pedri, and L. Santos, *Phys. Rev. Lett.* **101**, 210402 (2008).
- [281] P. Cheiney, C. Cabrera, J. Sanz, B. Naylor, L. Tanzi, and L. Tarruell, *Phys. Rev. Lett.* **120**, 135301 (2018).
- [282] A. Cappellaro, T. Macrì, and L. Salasnich, *Phys. Rev. A* **97**, 053623 (2018).
- [283] P. Ruprecht, M. Holland, K. Burnett, and M. Edwards, *Phys. Rev. A* **51**, 4704 (1995).
- [284] B. Esry, C. H. Greene, Y. Zhou, and C. Lin, *J. Phys. B* **29**, L51 (1996).
- [285] F. Dalfovo and S. Stringari, *Phys. Rev. A* **53**, 2477 (1996).
- [286] M. Houbiers and H. Stoof, *Phys. Rev. A* **54**, 5055 (1996).
- [287] T. Bergeman, *Phys. Rev. A* **55**, 3658 (1997).
- [288] Y. Kagan, A. Muryshev, and G. Shlyapnikov, *Phys. Rev. Lett.* **81**, 933 (1998).
- [289] E. A. Donley, N. R. Claussen, S. L. Cornish, J. L. Roberts, E. A. Cornell, and C. E. Wieman, *Nature* **412**, 295 (2001).
- [290] J. L. Roberts, N. R. Claussen, S. L. Cornish, E. A. Donley, E. A. Cornell, and C. E. Wieman, *Phys. Rev. Lett.* **86**, 4211 (2001).
- [291] E. A. Cornell and C. E. Wieman, *Rev. Mod. Phys.* **74**, 875 (2002).

-
- [292] T. Lahaye, J. Metz, B. Froehlich, T. Koch, M. Meister, A. Griesmaier, T. Pfau, H. Saito, Y. Kawaguchi, and M. Ueda, *Phys. Rev. Lett.* **101**, 080401 (2008).
- [293] J. Metz, T. Lahaye, B. Fröhlich, A. Griesmaier, T. Pfau, H. Saito, Y. Kawaguchi, and M. Ueda, *New J. Phys.* **11**, 055032 (2009).
- [294] J. L. Bohn, R. M. Wilson, and S. Ronen, *Laser Phys.* **19**, 547 (2009).
- [295] A. Macia, J. Sánchez-Baena, J. Boronat, and F. Mazzanti, *Phys. Rev. Lett.* **117**, 205301 (2016).
- [296] F. Wächtler and L. Santos, *Phys. Rev. A* **94**, 043618 (2016).
- [297] I. Ferrier-Barbut, M. Schmitt, M. Wenzel, H. Kadau, and T. Pfau, *J. Phys. B* **49**, 214004 (2016).
- [298] M. Wenzel, F. Böttcher, T. Langen, I. Ferrier-Barbut, and T. Pfau, *Phys. Rev. A* **96**, 053630 (2017).
- [299] E. Zaremba, T. Nikuni, and A. Griffin, *J. Low Temp. Phys.* **116**, 277 (1999).
- [300] M. Bijlsma, E. Zaremba, and H. Stoof, *Phys. Rev. A* **62**, 063609 (2000).
- [301] R. Walser, J. Williams, J. Cooper, and M. Holland, *Phys. Rev. A* **59**, 3878 (1999).
- [302] N. Proukakis, *J. Phys. B* **34**, 4737 (2001).
- [303] T. Kirkpatrick and J. Dorfman, *Phys. Rev. A* **28**, 2576 (1983).
- [304] T. Kirkpatrick and J. Dorfman, *J. Low Temp. Phys.* **58**, 301 (1985).
- [305] T. Kirkpatrick and J. Dorfman, *J. Low Temp. Phys.* **58**, 399 (1985).
- [306] A. Görlitz, J. M. Vogels, A. E. Leanhardt, C. Raman, T. L. Gustavson, J. R. Abo-Shaeer, A. P. Chikkatur, S. Gupta, S. Inouye, T. Rosenband, et al., *Phys. Rev. Lett.* **87**, 130402 (2001).
- [307] H. Ott, J. Fortagh, G. Schlotterbeck, A. Grossmann, and C. Zimmermann, *Phys. Rev. Lett.* **87**, 230401 (2001).
- [308] Z. Hadzibabic, P. Krüger, M. Cheneau, B. Battelier, and J. Dalibard, *Nature* **441**, 1118 (2006).
- [309] P. B. Blakie and M. J. Davis, *Phys. Rev. A* **72**, 063608 (2005).
- [310] C. Connaughton, C. Josserand, A. Picozzi, Y. Pomeau, and S. Rica, *Phys. Rev. Lett.* **95**, 263901 (2005).

-
- [311] R. Pattinson, N. Parker, and N. Proukakis, in *Journal of Physics: Conference Series* (IOP Publishing, 2014), vol. 497, p. 012029.
- [312] S. Nazarenko, M. Onorato, and D. Proment, *Phys. Rev. A* **90**, 013624 (2014).
- [313] M. J. Davis, S. A. Morgan, and K. Burnett, *Phys. Rev. Lett.* **87**, 160402 (2001).
- [314] M. J. Davis and P. B. Blakie, *Phys. Rev. Lett.* **96**, 060404 (2006).
- [315] T. M. Wright, N. P. Proukakis, and M. J. Davis, *Phys. Rev. A* **84**, 023608 (2011).
- [316] T. P. Simula and P. B. Blakie, *Phys. Rev. Lett.* **96**, 020404 (2006).
- [317] N. G. Berloff and A. J. Youd, *Phys. Rev. Lett.* **99**, 145301 (2007).
- [318] N. Berloff and C. Yin, *J. Low Temp. Phys.* **145**, 187 (2006).
- [319] H. Salman and N. G. Berloff, *Physica D* **238**, 1482 (2009).
- [320] R. W. Pattinson, N. P. Proukakis, and N. G. Parker, *Phys. Rev. A* **90**, 033625 (2014).
- [321] M. Steel, M. Olsen, L. Plimak, P. Drummond, S. Tan, M. Collett, D. Walls, and R. Graham, *Phys. Rev. A* **58**, 4824 (1998).
- [322] S. Ronen and J. L. Bohn, *Phys. Rev. A* **76**, 043607 (2007).
- [323] C. Ticknor, *Phys. Rev. A* **85**, 033629 (2012).
- [324] S. Cormack and D. Hutchinson, *Phys. Rev. A* **86**, 053619 (2012).
- [325] R. Bisset, D. Baillie, and P. Blakie, *Phys. Rev. A* **83**, 061602 (2011).
- [326] R. Bisset, D. Baillie, and P. Blakie, *Phys. Rev. A* **86**, 033609 (2012).
- [327] R. N. Bisset, Ph.D. thesis, University of Otago (2013).
- [328] M. L. Chiofalo, S. Succi, and M. P. Tosi, *Phys. Rev. E* **62**, 7438 (2000).
- [329] W. H. Press, S. A. Teukolsky, W. T. Vetterling, and B. P. Flannery, *Numerical Recipes in FORTRAN; The Art of Scientific Computing* (Cambridge University Press, New York, NY, USA, 1993), 2nd ed.
- [330] T. Winiecki, J. F. McCann, and C. S. Adams, *Europhys. Lett.* **48**, 475 (1999).
- [331] T. Winiecki, Ph.D. thesis, The University of Durham (2001).
- [332] G. Evans, J. Blackledge, and P. Yardley, *Numerical methods for partial differential equations* (Springer Science & Business Media, 2012).

-
- [333] A. Goldberg, H. M. Schey, and J. L. Schwartz, *Am. J. Phys.* **35**, 177 (1967).
- [334] J. Fleck, J. Morris, and M. Feit, *Appl. Phys.* **10**, 129 (1976).
- [335] J. Fleck, J. Morris, and E. Bliss, *IEEE J. Quantum Electron* **14**, 353 (1978).
- [336] J. Javanainen and J. Ruostekoski, *J. Phys. A* **39**, L179 (2006).
- [337] W. Bao and H. Wang, *J. Comp. Phys.* **217**, 612 (2006).
- [338] C. Rotschild, B. Alfassi, O. Cohen, and M. Segev, *Nat. Phys.* **2**, 769 (2006).
- [339] M. Peccianti, K. A. Brzdękiewicz, and G. Assanto, *Opt. Lett.* **27**, 1460 (2002).
- [340] C. Long-Gui, Z. Ya-Jian, H. Wei, Y. Ping-Bao, and G. Qi, *Chin. Phys. Lett.* **26**, 064209 (2009).
- [341] A. Piccardi, A. Alberucci, N. Tabiryan, and G. Assanto, *Opt. Lett.* **36**, 1356 (2011).
- [342] A. Dreischuh, D. N. Neshev, D. E. Petersen, O. Bang, and W. Królikowski, *Phys. Rev. Lett.* **96**, 043901 (2006).
- [343] J. K. Jang, M. Erkintalo, S. G. Murdoch, and S. Coen, *Nat. Phot.* **7**, 657 (2013).
- [344] N. P. Proukakis, N. G. Parker, D. J. Frantzeskakis, and C. S. Adams, *J. Opt. B* **6**, S380 (2004).
- [345] N. I. Nikolov, D. Neshev, O. Bang, and W. Z. Królikowski, *Phys. Rev. E* **68**, 036614 (2003).
- [346] Q. Kong, Q. Wang, O. Bang, and W. Królikowski, *Opt. Lett.* **35**, 2152 (2010).
- [347] W. Królikowski, O. Bang, N. I. Nikolov, D. Neshev, J. Wyller, J. J. Rasmussen, and D. Edmundson, *J. Opt. B* **6**, S288 (2004).
- [348] N. I. Nikolov, D. Neshev, W. Królikowski, O. Bang, J. J. Rasmussen, and P. L. Christiansen, *Opt. Lett.* **29**, 286 (2004).
- [349] W. Chen, M. Shen, Q. Kong, J. Shi, Q. Wang, and W. Królikowski, *Opt. Lett.* **39**, 1764 (2014).
- [350] C. Conti, A. Fratalocchi, M. Peccianti, G. Ruocco, and S. Trillo, *Phys. Rev. Lett.* **102**, 083902 (2009).
- [351] Y. S. Kivshar and B. A. Malomed, *Rev. Mod. Phys.* **61**, 763 (1989).
- [352] B. A. Malomed, D. Mihalache, F. Wise, and L. Torner, *J. Opt. B* **7**, R53 (2005).

-
- [353] Q. Kong, Q. Wang, O. Bang, and W. Królikowski, Phys. Rev. A **82**, 013826 (2010).
- [354] S. Pu, C. Hou, K. Zhan, C. Yuan, and Y. Du, Opt. Commun **285**, 3631 (2012).
- [355] N. G. Parker and D. H. J. O'Dell, Phys. Rev. A **78**, 041601 (2008).
- [356] S. Sinha and L. Santos, Phys. Rev. Lett. **99**, 140406 (2007).
- [357] A. Muryshv, G. Shlyapnikov, W. Ertmer, K. Sengstock, and M. Lewenstein, Phys. Rev. Lett. **89**, 110401 (2002).
- [358] F. Deuretzbacher, J. C. Cremon, and S. Reimann, Phys. Rev. A **81**, 063616 (2010).
- [359] R. Bisset, D. Baillie, and P. Blakie, Phys. Rev. A **88**, 043606 (2013).
- [360] C. Menotti and S. Stringari, Phys. Rev. A **66**, 043610 (2002).
- [361] Y. Cai, M. Rosenkranz, Z. Lei, and W. Bao, Phys. Rev. A **82**, 043623 (2010).
- [362] M. Klawunn, R. Nath, P. Pedri, and L. Santos, Phys. Rev. Lett. **100**, 240403 (2008).
- [363] B. Mulkerin, R. van Bijnen, D. O'Dell, A. Martin, and N. Parker, Phys. Rev. Lett. **111**, 170402 (2013).
- [364] R. M. Wilson, S. Ronen, J. L. Bohn, and H. Pu, Phys. Rev. Lett. **100**, 245302 (2008).
- [365] M. Abramowitz and I. A. Stegun, *Handbook of Mathematical Functions with Formulas, Graphs, and Mathematical Tables* (Selected Government Publications. John Wiley & Sons, Inc., New York, 1984).
- [366] J. Brand and W. P. Reinhardt, Phys. Rev. A **65**, 043612 (2002).
- [367] G. Theocharis, A. Weller, J. Ronzheimer, C. Gross, M. Oberthaler, P. Kevrekidis, and D. Frantzeskakis, Phys. Rev. A **81**, 063604 (2010).
- [368] G. El and A. Kamchatnov, Phys. Rev. Lett. **95**, 204101 (2005).
- [369] D. Novoa, B. A. Malomed, H. Michinel, and V. M. Pérez-García, Phys. Rev. Lett. **101**, 144101 (2008).
- [370] G. Huang, J. Szeftel, and S. Zhu, Phys. Rev. A **65**, 053605 (2002).
- [371] V. V. Konotop and L. Pitaevskii, Phys. Rev. Lett. **93**, 240403 (2004).
- [372] V. Brazhnyi, V. Konotop, and L. Pitaevskii, Phys. Rev. A **73**, 053601 (2006).
- [373] D. E. Pelinovsky, D. Frantzeskakis, and P. Kevrekidis, Phys. Rev. E **72**, 016615 (2005).

-
- [374] D. Frantzeskakis, P. Kevrekidis, and N. Proukakis, *Phys. Lett. A* **364**, 129 (2007).
- [375] G. Theocharis, P. Kevrekidis, M. Oberthaler, and D. Frantzeskakis, *Phys. Rev. A* **76**, 045601 (2007).
- [376] D. Pelinovsky and P. Kevrekidis, *AMS Contemp. Math* **473**, 159 (2008).
- [377] A. M. Kamchatnov and M. Salerno, *J. Phys. B* **42**, 185303 (2009).
- [378] G. Astrakharchik and L. Pitaevskii, *Europhys. Lett.* **102**, 30004 (2013).
- [379] N. Parker, N. Proukakis, M. Leadbeater, and C. Adams, *Phys. Rev. Lett.* **90**, 220401 (2003).
- [380] R. Van Bijnen, N. Parker, S. Kokkelmans, A. Martin, and D. O'Dell, *Phys. Rev. A* **82**, 033612 (2010).
- [381] V. Lončar, A. Balaž, A. Bogojević, S. Škrbić, P. Muruganandam, and S. K. Adhikari, *Comput. Phys. Commun.* **200**, 406 (2016).
- [382] R. K. Kumar, L. E. Young-S, D. Vudragović, A. Balaž, P. Muruganandam, and S. K. Adhikari, *Comput. Phys. Commun.* **195**, 117 (2015).
- [383] Y. Tang, A. G. Sykes, N. Q. Burdick, J. M. DiSciacca, D. S. Petrov, and B. L. Lev, *Phys. Rev. Lett.* **117**, 155301 (2016).
- [384] P. Fedichev, A. Muryshv, and G. V. Shlyapnikov, *Phys. Rev. A* **60**, 3220 (1999).
- [385] R. Scott, F. Dalfovo, L. Pitaevskii, and S. Stringari, *Phys. Rev. Lett.* **106**, 185301 (2011).
- [386] D. K. Campbell, M. Peyrard, and P. Sodano, *Physica D* **19**, 165 (1986).
- [387] B. Dabrowska-Wüster, S. Wüster, and M. Davis, *New J. Phys.* **11**, 053017 (2009).
- [388] V. M. Pérez-García, H. Michinel, J. Cirac, M. Lewenstein, and P. Zoller, *Phys. Rev. A* **56**, 1424 (1997).
- [389] V. M. Pérez-García, H. Michinel, and H. Herrero, *Phys. Rev. A* **57**, 3837 (1998).
- [390] A. Gammal, T. Frederico, and L. Tomio, *Phys. Rev. A* **64**, 055602 (2001).
- [391] L. Salasnich, *Phys. Rev. A* **70**, 053617 (2004).
- [392] N. Parker, S. Cornish, C. Adams, and A. Martin, *J. Phys. B* **40**, 3127 (2007).
- [393] L. Carr and Y. Castin, *Phys. Rev. A* **66**, 063602 (2002).
- [394] R. Eichler, J. Main, and G. Wunner, *Phys. Rev. A* **83**, 053604 (2011).

- [395] K. Łakomy, R. Nath, and L. Santos, *Phys. Rev. A* **86**, 013610 (2012).
- [396] D. Baillie and P. Blakie, *New J. Phys.* **17**, 033028 (2015).
- [397] P. Köberle, D. Zajec, G. Wunner, and B. A. Malomed, *Phys. Rev. A* **85**, 023630 (2012).
- [398] B. A. Malomed, F. Lederer, D. Mazilu, and D. Mihalache, *Phys. Lett. A* **361**, 336 (2007).
- [399] R. Nath and L. Santos, *Phys. Rev. A* **81**, 033626 (2010).
- [400] X. Deng, S. Ray, S. Sinha, G. Shlyapnikov, and L. Santos (2018), [arXiv:1808.03585](https://arxiv.org/abs/1808.03585).
- [401] M. Hafezi, A. S. Sørensen, E. Demler, and M. D. Lukin, *Phys. Rev. A* **76**, 023613 (2007).
- [402] R. Citro, E. Orignac, S. De Palo, and M. L. Chiofalo, *Phys. Rev. A* **75**, 051602 (2007).
- [403] B. Liu, X. Li, L. Yin, and W. V. Liu, *Phys. Rev. Lett.* **114**, 045302 (2015).
- [404] A. Recati, F. Zambelli, and S. Stringari, *Phys. Rev. Lett.* **86**, 377 (2001).
- [405] S. Sinha and Y. Castin, *Phys. Rev. Lett.* **87**, 190402 (2001).
- [406] K. W. Madison, F. Chevy, V. Bretin, and J. Dalibard, *Phys. Rev. Lett.* **86**, 4443 (2001).
- [407] E. Lundh, J.-P. Martikainen, and K.-A. Suominen, *Phys. Rev. A* **67**, 063604 (2003).
- [408] C. Lobo, A. Sinatra, and Y. Castin, *Phys. Rev. Lett.* **92**, 020403 (2004).
- [409] N. Parker, R. van Bijnen, and A. Martin, *Phys. Rev. A* **73**, 061603 (2006).
- [410] I. Corro, N. Parker, and A. Martin, *J. Phys. B* **40**, 3615 (2007).
- [411] R. M. W. van Bijnen, A. J. Dow, D. H. J. O'Dell, N. G. Parker, and A. M. Martin, *Phys. Rev. A* **80**, 3 (2009).
- [412] W. Bao and Y. Cai, *Kinet. Relat. Mod.* **6**, 1 (2013).
- [413] S. Stringari, *Phys. Rev. Lett.* **77**, 2360 (1996).
- [414] S. Giovanazzi, P. Pedri, L. Santos, A. Griesmaier, M. Fattori, T. Koch, J. Stuhler, and T. Pfau, *Phys. Rev. A* **74**, 013621 (2006).
- [415] F. Dalfovo, S. Giorgini, M. Guilleumas, L. Pitaevskii, and S. Stringari, *Phys. Rev. A* **56**, 3840 (1997).
- [416] I. Sapina, T. Dahm, and N. Schopohl, *Phys. Rev. A* **82**, 053620 (2010).

-
- [417] C. Alexiou, R. Schmid, R. Jurgons, C. Bergemann, W. Arnold, and F. Parak, in *Ferrofluids* (Springer, 2002), pp. 233–251.
- [418] A. I. Anton, J. Magn. Mater **85**, 137 (1990).
- [419] B. Berkovski and V. Bashtovoy, *Magnetic fluids and applications handbook* (1996).
- [420] K. R. Schumacher, I. Sellien, G. S. Knoke, T. Cader, and B. A. Finlayson, Phys. Rev. E **67**, 026308 (2003).
- [421] R. Rosensweig, R. Kaiser, and G. Miskolczy, J. Colloid Interface Sci. **29**, 680 (1969).
- [422] S. Altmeyer, Y. Do, and Y.-C. Lai, Sci. Rep. **5**, 10781 (2015).
- [423] K. R. Schumacher, J. J. Riley, and B. A. Finlayson, J. Fluid Mech. **599**, 1 (2008).
- [424] N. Navon, A. L. Gaunt, R. P. Smith, and Z. Hadzibabic, Nature **539**, 72 (2016).
- [425] A. C. White, B. P. Anderson, and V. S. Bagnato, Proc. Natl. Acad. Sci. **111**, 4719 (2014).
- [426] M. C. Tsatsos, P. E. Tavares, A. Cidrim, A. R. Fritsch, M. A. Caracanhas, F. E. A. dos Santos, C. F. Barenghi, and V. S. Bagnato, Phys. Rep. **622**, 1 (2016).
- [427] A. White, C. Barenghi, N. Proukakis, A. Youd, and D. Wacks, Phys. Rev. Lett. **104**, 075301 (2010).
- [428] G. Stagg, N. Parker, and C. Barenghi, Phys. Rev. A **94**, 053632 (2016).
- [429] B. Svistunov, J. Moscow Phys. Soc **1**, 373 (1991).
- [430] Y. Kagan, B. Svistunov, and G. Shlyapnikov, Sov. Phys. JETP **75**, 387 (1992).
- [431] Y. Kagan and B. Svistunov, Sov. Phys. JETP **78**, 187 (1994).
- [432] Y. Kagan and B. V. Svistunov, Phys. Rev. Lett. **79**, 3331 (1997).
- [433] A. Sinatra, C. Lobo, and Y. Castin, Phys. Rev. Lett. **87**, 210404 (2001).
- [434] M. J. Davis, S. A. Morgan, and K. Burnett, Phys. Rev. A **66**, 053618 (2002).
- [435] M. Brewczyk, M. Gajda, and K. Rzażewski, J. Phys. B **40**, R1 (2007).
- [436] N. P. Proukakis and B. Jackson, J. Phys. B **41**, 203002 (2008).
- [437] P. Blakie, A. Bradley, M. Davis, R. Ballagh, and C. Gardiner, Adv. Phys. **57**, 363 (2008).
- [438] A. W. Baggaley, J. Laurie, and C. F. Barenghi, Phys. Rev. Lett. **109**, 205304 (2012).
- [439] A. Vilhois, G. Krstulovic, D. Proment, and H. Salman, J. Phys. A **49**, 415502 (2016).

-
- [440] M. Tsubota, C. Barenghi, and T. Araki, J. Low Temp. Phys. **134**, 471 (2004).
- [441] M. T. Reeves, T. P. Billam, B. P. Anderson, and A. S. Bradley, Phys. Rev. Lett. **110**, 104501 (2013).
- [442] P. Tabeling, S. Burkhart, O. Cardoso, and H. Willaime, Phys. Rev. Lett. **67**, 3772 (1991).
- [443] M. Srednicki, Phys. Rev. E **50**, 888 (1994).
- [444] M. Rigol, V. Dunjko, and M. Olshanii, Nature **452**, 854 (2008).
- [445] T. Langen, R. Geiger, and J. Schmiedmayer, Annu. Rev. Condens. Matter Phys. **6**, 201 (2015).
- [446] T. Kinoshita, T. Wenger, and D. S. Weiss, Nature **440**, 900 (2006).
- [447] I. Mazets, T. Schumm, and J. Schmiedmayer, Phys. Rev. Lett. **100**, 210403 (2008).
- [448] I. Mazets and J. Schmiedmayer, New J. Phys. **12**, 055023 (2010).
- [449] S. Hofferberth, I. Leshanovsky, B. Fischer, T. Schumm, and J. Schmiedmayer, Nature **449**, 324 (2007).
- [450] D. A. Smith, M. Gring, T. Langen, M. Kuhnert, B. Rauer, R. Geiger, T. Kitagawa, I. Mazets, E. Demler, and J. Schmiedmayer, New J. Phys. **15**, 075011 (2013).
- [451] C. F. Barenghi and N. G. Parker, *A primer on quantum fluids* (Springer, 2017).
- [452] S. Kichenassamy, *Nonlinear wave equations*, vol. 194 (CRC Press, 1995).
- [453] Y.-C. Ma and M. J. Ablowitz, Stud. Appl. Math. **65**, 113 (1981).
- [454] R. Dodd, *Solitons and nonlinear wave equations* (Academic Press, 1982).
- [455] S. Cockburn, A. Negretti, N. Proukakis, and C. Henkel, Phys. Rev. A **83**, 043619 (2011).
- [456] P. Grisins and I. E. Mazets, Phys. Rev. A **84**, 053635 (2011).
- [457] N. Parker, N. Proukakis, C. Barenghi, and C. Adams, J. Phys. B **37**, S175 (2004).
- [458] N. Parker, N. Proukakis, and C. Adams, Phys. Rev. A **81**, 033606 (2010).
- [459] A. Muryshev, H. v. L. van den Heuvel, and G. Shlyapnikov, Phys. Rev. A **60**, R2665 (1999).
- [460] A. Allen, D. Jackson, C. Barenghi, and N. Proukakis, Phys. Rev. A **83**, 013613 (2011).

-
- [461] A. Radouani, Phys. Rev. A **68**, 043620 (2003).
- [462] D. E. Pelinovsky, Y. S. Kivshar, and V. V. Afanasjev, Phys. Rev. E **54**, 2015 (1996).
- [463] N. Proukakis, N. Parker, C. Barenghi, and C. Adams, Phys. Rev. Lett. **93**, 130408 (2004).
- [464] D. L. Feder, M. S. Pindzola, L. A. Collins, B. I. Schneider, and C. W. Clark, Phys. Rev. A **62**, 053606 (2000).
- [465] L. D. Carr, M. A. Leung, and W. P. Reinhardt, J. Phys. B **33**, 3983 (2000).
- [466] J. Dziarmaga, Z. P. Karkuszewski, and K. Sacha, J. Phys. B **36**, 1217 (2003).
- [467] B. Jackson, N. Proukakis, and C. Barenghi, Phys. Rev. A **75**, 051601 (2007).
- [468] B. Jackson, C. Barenghi, and N. Proukakis, J. Low Temp. Phys. **148**, 387 (2007).
- [469] A. Martin and J. Ruostekoski, Phys. Rev. Lett. **104**, 194102 (2010).
- [470] D. Gangardt and A. Kamenev, Phys. Rev. Lett. **104**, 190402 (2010).
- [471] S. Cockburn, H. Nistazakis, T. Horikis, P. Kevrekidis, N. Proukakis, and D. Frantzeskakis, Phys. Rev. Lett. **104**, 174101 (2010).
- [472] P. Kevrekidis, R. Carretero-González, G. Theocharis, D. Frantzeskakis, and B. Malomed, Phys. Rev. A **68**, 035602 (2003).
- [473] D. J. Frantzeskakis, G. Theocharis, F. Diakonov, P. Schmelcher, and Y. S. Kivshar, Phys. Rev. A **66**, 053608 (2002).
- [474] B. G. Galerkin, Vestn. Inzh. Tekh **19**, 897 (1915).
- [475] S. Brenner and R. Scott, *The mathematical theory of finite element methods*, vol. 15 (Springer Science & Business Media, 2007).
- [476] J.-L. Guermond, P. Mineev, and J. Shen, Comput. Methods in Appl. Mech. Eng. **195**, 6011 (2006).
- [477] X. Liu, J. Wang, and Y. Zhou, Nonlinear Dyn. **90**, 599 (2017).
- [478] R. Driben, V. Konotop, B. Malomed, and T. Meier, Phys. Rev. E **94**, 012207 (2016).
- [479] J. Wang, Y. Zhou, and X. Liu, Math. Probl. Eng. **2017** (2017).
- [480] V. I. Arnol'd, *Mathematical methods of classical mechanics*, vol. 60 (Springer Science & Business Media, 2013).

- [481] J. You, J. Differ. Equ. **152**, 1 (1999).
- [482] E. Shamriz, N. Dror, and B. A. Malomed, Phys. Rev. E **94**, 022211 (2016).
- [483] M. Sciacca, C. Barengi, and N. Parker, Phys. Rev. A **95**, 013628 (2017).
- [484] L. D. Carr, C. W. Clark, and W. P. Reinhardt, Phys. Rev. A **62**, 063610 (2000).
- [485] E. K. Sklyanin, Funct. Anal. Appl. **21**, 164 (1987).
- [486] R. Bikbaev and A. R. Its, Math. Notes. **45**, 349 (1989).
- [487] A. Fokas and A. Its, J. Phys. A **37**, 6091 (2004).
- [488] M. Olshanii and S. G. Jackson, New J. Phys. **17**, 105005 (2015).
- [489] V. E. Zakharov, Stud. Appl. Math. **122**, 219 (2009).
- [490] M. Lakshmanan and S. Rajaseekar, *Nonlinear Dyn.: integrability, chaos and patterns* (Springer Science & Business Media, 2012).
- [491] V. Zakharov and S. Manakov, Zh. Eksp. Teor. Fiz. Pisma Red **18**, 413 (1973).
- [492] D. Kaup, Stud. Appl. Math. **55**, 9 (1976).
- [493] F. Xu, Y. Zhang, W. Hong, K. Wu, and T. J. Cui, IEEE Trans. Microw. Theory Tech. **51**, 2221 (2003).
- [494] D. Anderson, Phys. Rev. A **27**, 3135 (1983).
- [495] B. A. Malomed, Prog. Optics **43**, 71 (2002).
- [496] F. C. Moon, *Chaotic vibrations: An introduction for applied scientist and engineers* (1987).
- [497] S. V. Manakov, J. Exp. Theor. Phys. **38**, 248 (1974).
- [498] M. Tratnik and J. Sipe, Phys. Rev. A **38**, 2011 (1988).
- [499] L. Bergé, Phys. Rep. **303**, 259 (1998).
- [500] G. Fibich, *The nonlinear Schrödinger equation* (Springer, 2015).
- [501] T. J. Alexander and L. Bergé, Phys. Rev. E **65**, 026611 (2002).
- [502] H. Saito and M. Ueda, Phys. Rev. Lett. **89**, 190402 (2002).
- [503] H. Saito and M. Ueda, Phys. Rev. A **69**, 013604 (2004).
- [504] L. Carr and C. W. Clark, Phys. Rev. Lett. **97**, 010403 (2006).
- [505] D. Mihalache, D. Mazilu, B. A. Malomed, and F. Lederer, Phys. Rev. A **73**, 043615 (2006).